TECHNISCHE UNIVERSITÄT DRESDEN

Millimeter Wave Line-of-Sight Spatial Multiplexing: Antenna Topology and Signal Processing

Xiaohang Song

der Fakultät Elektrotechnik und Informationstechnik
der Technischen Universität Dresden

zur Erlangung des akademischen Grades eines

Doktoringenieurs

(Dr.-Ing.)

genehmigte Dissertation

Vorsitzender:	Prof. Dr. rer. nat. Stefan Mannsfeld
Gutachter:	Prof. Dr.-Ing. Dr. h.c. Gerhard Fettweis
	Prof. Giuseppe Caire, Ph.D.
Tag der Einreichung:	29. 06. 2018
Tag der Verteidigung:	30. 10. 2018

Acknowledgment

First, I would like to express my deepest gratitude to Prof. Gerhard Fettweis who gave me continuous supports and advices during my work and study in Vodafone Chair Mobile Communications Systems at TU Dresden. He provided me with the opportunity to work on interesting research topics while helping me discover my potentials. Without his kind guidance and tremendous help, this work would have not been possible. I would also like to thank Prof. Giuseppe Caire for reviewing this work as my second supervisor and providing his valuable feedback.

I am highly indebted to my group leader Dr. Wolfgang Rave for sharing his knowledge and wisdom on the signal processing and MIMO technologies. Many of the results in this work were inspired during our fruitful discussions. Dr. Wolfgang Rave, Dr. Dan Zhang, Dr. Meik Dörpinghaus, and Mr. Mostafa Marandi also deserve my sincere thanks for reviewing my thesis and giving me criticism and feedback, which significantly improved the quality of the description. Furthermore, I appreciate all colleagues in the chair I worked and spent pleasant moments with.

My special thanks goes to my project partners, Prof. Berthold Lankl, Prof. Eckhard Grass, Mr. Tim Hälsig, and Mr. Darko Cvetkovski, in MaximumMIMO project which has been supported by German Science Foundation. Based on our discussions about channel measurement results, my understanding of practical systems is quite better built. Especially, Tim Hälsig and Darko Cvetkovski shared their recorded experimental data with me in the framework of our cooperation. This data including hardware effects is used for evaluating the signal processing architecture proposed in Chapter 5. In addition, I would like to thank Mr. Nithin Babu and Prof. Sudhan Majhi for discussions on the channel model used in Chapter 6.

I further express my thanks to Prof. Gerhard Kramer who supported me during my master study at TU Munich and Dr. Matthias Wagner, my research director during my time at NTT DOCOMO Euro-Labs, for their recognitions and recommendations at the early stage of my career.

Last but by no means least, I could not thank more the unconditional love from my family. With the moral and emotional support from my beloved wife Qiaoman Wang, I could follow and focus on my interests with her company. My mother, Qian Qiao, and my father, Gang Song, have supported me unconditionally throughout my life. With their encouragements, I came to Germany and started my study together with world-leading researchers. Especially, my dear father, who really hoped to see me in the doctoral gown, sadly and suddenly passed away and left us on my first day on board to this journey. Therefore, this work is also written in honor of him.

Dresden, December 2018 Xiaohang Song

Abstract

Fixed wireless communication is a cost-efficient solution for flexible and rapid front-/backhaul deployments. Technologies including dual polarization, carrier aggregation, and higher order modulation schemes have been developed for enhancing its throughput. In order to better support the massive traffic increment during network evolution, novel wireless backhaul solutions with possible new dimensions in increasing the spectral efficiency are needed. Line-of-Sight (LoS) Multiple-Input-Multiple-Output (MIMO) communication is such a promising candidate allowing the throughput to scale linearly with the deployed antenna pairs. Spatial multiplexing with sub-channels having approximately equal quality exists within a single LoS direction. In addition, operating at millimeter wave (mmWave) frequencies or higher, the abundantly available bandwidth can further enhance the throughput of LoS MIMO communication. The mmWave LoS MIMO communication in this work exploits the spatial multiplexing from the structured phase couplings of a single path direction, while most of the state-of-the-art works in mmWave communication focus on the spatial multiplexing from the spatial signature of multiple path directions.

Challenges: The performance of a LoS MIMO system is highly dependent on the antenna topology. Topologies resulting in theoretically orthogonal channels are considered as optimal arrangements. The general topology solution from a unified viewpoint is unknown. The known optimal arrangements in the literature are rather independently derived and contain restrictions on their array planes. Moreover, operating at mmWave frequencies with wideband signals introduces additional challenges. On one hand, high pathloss is one limiting factor of the received signal power. On the other hand, high symbol rates and relatively high antenna numbers create challenges in signal processing, especially the required complexity for compensating hardware imperfections and applying beamforming.

Targets: In this thesis, we focus on antenna topologies and signal processing schemes to effectively handle the complexity challenge in LoS MIMO communications. Considering the antenna topology, we target a general solution of optimal arrangements on any arbitrarily curved surface. Moreover, we study the antenna topologies with which the system gains more streams and better received signals. Considering the signal processing, we look for low complexity schemes that can effectively compensate the hardware impairments and can cope with a large number of antennas.

Main Contributions: The following models and algorithms are developed for understanding mmWave LoS spatial multiplexing and turning it into practice. First, after analyzing the relation

between the phase couplings and the antenna positions in three dimensional space, we derive a channel factorization model for LoS MIMO communication. Based on this, we provide a general topology solution from a projection point of view and show that the resulting spatial multiplexing is robust against moderate displacement errors. In addition, we propose a multi-subarray LoS MIMO system for jointly harvesting the spatial multiplexing and array gains. Then, we propose a novel algorithm for LoS MIMO channel equalization, which is carried out in the reverse order w.r.t. the channel factorization model. The number of multiplications in both digital and analog implementations of the proposed solution is found to increase approximately linearly w.r.t. the number of antennas. The proposed algorithm thus potentially reduces complexity for equalizing the channel during the system expansion with more streams. After this, we focus on algorithms that can effectively estimate and compensate the hardware impairments. A systolic/pipelined processing architecture is proposed in this work to achieve a balance between computational complexity and performance. The proposed architecture is a viable approach that scales well with the number of MIMO streams. With the recorded data from a hardware-in-the-loop demonstrator, it is shown that the proposed algorithms can provide reliable signal estimates at a relatively low complexity level. Finally, a channel model is derived for mmWave systems with multiple widely spaced subarrays and multiple paths. The spatial multiplexing gain from the spatial signature of multiple path directions and the spatial multiplexing gain from the structured phase couplings of a single path direction are found simultaneously at two different levels of the antenna arrangements. Attempting to exploit them jointly, we propose to use an advanced hybrid analog/digital beamforming architecture to efficiently process the signals at reasonable costs and complexity. The proposed system can overcome the low rank property caused by the limited number of propagation paths.

List of Original Articles

Parts of this thesis have been published in the following peer reviewed articles, which are referred to in the text by their Roman numerals (I-VIII):

Journal Publications

I X. Song, W. Rave, N. Babu, S. Majhi, and G. Fettweis, "Two-Level Spatial Multiplexing Using Hybrid Beamforming for Millimeter-Wave Backhaul", in *IEEE Transactions on Wireless Communications*, vol.17, no. 7, pp. 4830-4844, 2018. DOI: 10.1109/TWC.2018.2832084.[1]

II X. Song, T. Hälsig, D. Cvetkovski, W. Rave, B. Lankl, E. Grass, and G. Fettweis, "Design and Experimental Evaluation of Equalization Algorithms for Line-of-Sight Spatial Multiplexing at 60 GHz", in *IEEE Journal on Selected Areas in Communications*, vol. 36, no. 11, pp. 2570-2580, 2018. DOI: 10.1109/JSAC.2018.2872286.[1]

III X. Song, D. Cvetkovski, W. Rave, E. Grass, and G. Fettweis, "Sequential Channel Equalization in Strong Line-of-Sight MIMO Communication", in *IEEE Transactions on Wireless Communications*, accepted, 2018. DOI: 10.1109/TWC.2018.2879661.[1]

IV X. Song and G. Fettweis, "On Spatial Multiplexing of Strong Line-of-Sight MIMO with 3D Antenna Arrangements", in *IEEE Wireless Communications Letters*, vol.4, no. 4, pp. 393-396, 2015. DOI: 10.1109/LWC.2015.2424952.[2]

Conference Publications

V X. Song, T. Hälsig, W. Rave, B. Lankl, and G. Fettweis, "Analog Equalization and Low Resolution Quantization in Strong Line-of-Sight MIMO Communication", in *Proceedings of the IEEE International Conference on Communications (ICC)*, pages 1-7, Kuala Lumpur, Malaysia, 2016. DOI: 10.1109/ICC.2016.7511627.[3]

VI X. Song, W. Rave, and G. Fettweis, "Analog and Successive Channel Equalization in Strong Line-of-Sight MIMO Communication", in *Proceedings of the IEEE International Conference on Communications (ICC)*, pages 1-7, Kuala Lumpur, Malaysia, 2016. DOI: 10.1109/ICC.2016.7511058.[3]

[1] © 2018 IEEE
[2] © 2015 IEEE
[3] © 2016 IEEE

VII X. Song, C. Jans, L. Landau, D. Cvetkovski, and G. Fettweis, ”A 60GHz LOS MIMO Backhaul Design Combining Spatial Multiplexing and Beamforming for a 100Gbps Throughput”, in *Proceedings of the IEEE Global Communications Conference (GLOBECOM)*, pages 1-6, San Diego, USA, 2015. DOI: 10.1109/GLOCOM.2015.7417737.[4]

VIII X. Song, L. Landau, J. Israel, and G. Fettweis, ”Strong LOS MIMO for Short Range mmWave Communication - Towards 1 Tbps Wireless Data Bus”, in *Proceedings of the IEEE International Conference on Ubiquitous Wireless Broadband (ICUWB)*, pages 1-5, Montreal, Canada, 2015. DOI: 10.1109/ICUWB.2015.7324516.[4]

Personal use of this material is permitted. Permission from IEEE must be obtained for all other uses, in any current or future media, including reprinting/republishing this material for advertising or promotional purposes, creating new collective works, for resale or redistribution to servers or lists, or reuse of any copyrighted component of this work in other works.

In addition to the above listed publications, until December 2018, the author published the following publications [SI12, ANHT+13, AANS+13, SSF16, SCH+17] with details presented in the bibliography of this thesis.

[4] © 2015 IEEE

Contents

List of Abbreviations

1D	One Dimension
1G	First Generation
2D	Two Dimension
3D	Three Dimension
4G	Fourth Generation
ADC	Analog-to-Digital Converter
AFE	Analog Front-Ends
AoA	Angle of Arrival
AoD	Angle of Departure
AWG	Arbitrary Waveform Generator
AWGN	Additive White Gaussian Noise
BPCU	Bits Per Channel Use
CBBU	Central Baseband Unit
CEPT	European Conference of Postal and Telecommunications Administrations
CFO	Carrier Frequency Offset
CIR	Channel Impulse Response
CSI	Channel State Information
DAC	Digital-to-Analog Converter
DD	Decision-Directed
DD-LMS	Decision-Directed Least Mean Square
DFT	Discrete Fourier Transform

DoF	Degrees of Freedom
ECC	Electronic Communications Committee
EIRP	Equivalent Isotropically Radiated Power
EVM	Error Vector Magnitude
FCC	Federal Communications Commission
FFT	Fast Fourier Transform
FIR	Finite Impulse Response
IAI	Interantenna Interference
IDFT	Inverse Discrete Fourier Transform
i.i.d.	Independent and Identical Distributed
I/Q	In-/Quadrature-phase
LMS	Least Mean Square
LoS	Line-of-Sight
LTE	Long-Term Evolution
IEC	International Electrotechnical Commission
IEEE	Institute of Electrical and Electronics Engineers
ISI	Intersymbol Interference
ISO	International Organization for Standardization
MIMO	Multiple-Input-Multiple-Output
MMSE	Minimum Mean Squared Error
MMSE-FIR	Minimum Mean Squared Error Finite Impulse Response
mmWave	Millimeter Wave
MVU	Minimum-Variance Unbiased
non-LoS	Non Line-of-Sight
NOPS	Number of Operations
PAPR	Peak to Average Power Ratio
PSD	Power Spectral Density

QAM	Quadrature Amplitude Modulation
RF	Radio Frequency
RRC	Root-Raised-Cosine
RTO	Real-Time Oscilloscope
Rx	Receiver
SCE	Sequential Channel Equalization
SFO	Sampling Frequency Offset
SINR	Signal-to-Interference-Plus-Noise Ratio
SISO	Single-Input-Single-Output
SNR	Signal-to-Noise Ratio
STIAI+PISIE	Single-Tap Interantenna Interference and Parallel Intersymbol Interference Equalization
Tx	Transmitter
ULA	Uniform Linear Array
URA	Uniform Rectangular Array
UPA	Uniform Planar Array
VGA	Variable Gain Amplifier
VPS	Variable Phase Shifter
WDFT	Winograd Discrete Fourier Transform
WL	Widely Linear
ZF	Zero-Forcing
ZFE	Zero-Forcing Equalization

Mathematical Notations

Operators and Functions

$\approx$	Approximately equal
$\neq$	Not equal
$\triangleq$	Definition
$\ll$	Much less
$\gg$	Much greater
$\lessapprox$	Less than about
$\in$	Element of a set
$\succeq \mathbf{0}$	Positive semi-definite
$(\cdot)^H$	Conjugate transpose operation
$(\cdot)^T$	Transpose operation
$(\cdot)^*$	Conjugate complex operation
$(\cdot)^{-1}$	Inverse operation
$(\cdot)^\dagger$	Pseudo-inverse operation
$\|\| \cdot \|\|_F$	Frobenius norm
$[\cdot]^+$	Taking non-negative value, $\max(\cdot, 0)$
$(\cdot\|\cdot)$	Condition event
$\{\mathbf{A}\}_{bc}$	Taking (b, c)-th element of a matrix $\mathbf{A}$
$\|\mathcal{A}\|$	Cardinality of a set $\mathcal{A}$
$\forall$	For all
$\otimes$	Kronecker product
$\odot$	Hadamard product
$\sum$	Summation of values
$\measuredangle$	Taking the arguments (phases) of complex numbers/vectors
$\arg\max_x(\cdot)$	Argument of the maximum of $(\cdot)$ over the set of x
$\arg\min_x(\cdot)$	Argument of the minimum of $(\cdot)$ over the set of x
$\det(\cdot)$	Determinant of a matrix
$\mathrm{diag}(\cdot)$	Create a diagonal matrix or get diagonal elements of a matrix
$\mathbb{E}[\cdot]$	Expectation operator

$\exp(\cdot)$	Natural exponential function (i.e., with base e)
$\log_2(\cdot)$	Logarithm of $(\cdot)$ to base 2
$\max_x(\cdot)$	Maximum of $(\cdot)$ over the set of x
$\min_x(\cdot)$	Minimum of $(\cdot)$ over the set of x
$\mathcal{O}(\cdot)$	Big O notation (i.e., the order of a parameter $(\cdot)$)
$\Pr(\cdot)$	Probability function of an event $(\cdot)$
$\mathrm{sinc}(\cdot)$	Sinc-function
$\mathrm{tr}(\cdot)$	Trace (i.e., the sum of the diagonal elements of a matrix $(\cdot)$)
$\mathrm{vec}(\cdot)$	Vectorization operator

Mathematical Symbols

$\hat{(\cdot)}$	Estimates on $(\cdot)$
$\mathbf{1}_{B\times C}$	An all one matrix of size B by C
$\mathbf{0}_{B\times C}$	An all zero matrix of size B by C
$\mathbf{a}_{\mathrm{t}}(\theta_{\mathrm{t}},\phi_{\mathrm{t}})$, $\mathbf{a}_{\mathrm{r}}(\theta_{\mathrm{r}},\phi_{\mathrm{r}})$	Planar-wave array response vectors in 3D
$\mathbf{a}_{\mathrm{t}}(\theta)$, $\mathbf{a}_{\mathrm{r}}(\theta)$	Planar-wave array response vectors in 2D
$\mathcal{B}_{\mathrm{RF}}$	Beamforming vector set
b	A local integer parameter, e.g., number of bits at the output of ADCs or the index for the analog beams
$\mathbb{C}^{B\times C}$	Set of complex value matrices of size B by C
$\mathcal{CN}(\cdot,\cdot)$	Complex Gaussian distribution
C	Channel capacity
C_{opt}	Channel capacity under optimal arrangements
$C_{\mathrm{SISO}}^{\mathrm{LoS}}$	Channel capacity of a LoS SISO system
$C_{\mathrm{MIMO}}^{\mathrm{LoS}}$	System capacity of a LoS MIMO system with equal power location
$C_{\{N,P\}}$	Channel capacity for systems having N subarrays and P significant paths
c	Speed of light
$c_{\text{SP-ZFE}}^{[\mathrm{M}]}$, $c_{\text{SP-ZFE}}^{[\mathrm{A}]}$	Computational complexity for multiplications and additions of STIAI+PISIE with ZFE for IAI suppression
$c_{\text{SP-SCE}}^{[\mathrm{M}]}$, $c_{\text{SP-SCE}}^{[\mathrm{A}]}$	Computational complexity for multiplications and additions of STIAI+PISIE with SCE for IAI suppression
$c_{\text{WDFT}}^{[\mathrm{M}]}$, $c_{\text{WDFT}}^{[\mathrm{A}]}$	Computational complexity for multiplications and additions needed by a Winograd discrete Fourier transform
$c_{\text{LMS}}^{[\mathrm{M}]}$, $c_{\text{LMS}}^{[\mathrm{A}]}$	Computational complexity for multiplications and additions needed by the DD-LMS algorithm
$c_{\text{LMS,WL}}^{[\mathrm{M}]}$, $c_{\text{LMS,WL}}^{[\mathrm{A}]}$	Computational complexity for multiplications and additions needed by the widely linear DD-LMS algorithm
$\mathbf{D}_{\parallel,\mathrm{t}}$, $\mathbf{D}_{\parallel,\mathrm{r}}$	Diagonal matrices collecting the phase shifts caused by offsets along the transmit direction at Tx, Rx

$\tilde{\mathbf{D}}_{\parallel,\mathrm{t}}$, $\tilde{\mathbf{D}}_{\parallel,\mathrm{r}}$	Diagonal matrices at outer positions of the refined channel factorization, i.e., $\tilde{\mathbf{D}}_{\parallel,\mathrm{t}} \triangleq \mathbf{D}_{\text{R-}N}\mathbf{D}_{\parallel,\mathrm{t}}$, $\tilde{\mathbf{D}}_{\parallel,\mathrm{r}} \triangleq \mathbf{D}_{\parallel,\mathrm{r}}\mathbf{D}_{\text{L-}N}$
$\mathbf{D}_{\text{L-}N}$, $\mathbf{D}_{\text{R-}N}$	Two diagonal matrices in relation $\mathbf{H}_{\mathrm{o}} = \mathbf{D}_{\text{L-}N}\,\mathbf{W}_{\text{IDFT-}N}\,\mathbf{D}_{\text{R-}N}$
$\mathbf{D}_1$, $\mathbf{D}_2$	Two diagonal matrices in SEC, i.e., $\mathbf{W}_{\text{sce}} \triangleq \mathbf{D}_2 \cdot \mathbf{W}_{\text{fix}} \cdot \mathbf{D}_1$
$\mathbf{D}_{\phi,\text{Tx}}[k]$, $\mathbf{D}_{\phi,\text{Rx}}[k]$	Diagonal matrices collecting the CFOs at Tx, Rx
$\mathbf{D}_{\phi,\text{Tx},L}[k]$	Matrix collecting Tx CFOs of L symbols, i.e., $\mathbf{D}_{\phi,\text{Tx},L}[k] \triangleq \mathrm{diag}\left(\mathbf{D}_{\phi,\text{Tx}}[k],\ldots,\mathbf{D}_{\phi,\text{Tx}}[k-L+1]\right)$
$\mathbf{D}_{\psi,\text{Tx}}[q]$, $\mathbf{D}_{\psi,\text{Rx}}[q]$	Phase rotations at Tx and Rx from sub-frame q to sub-frame $q+1$, i.e., $\mathbf{D}_{\psi,\text{Tx}}[q] \triangleq \mathrm{diag}(e^{j\boldsymbol{\psi}_{\text{Tx}}[q]})$, $\mathbf{D}_{\psi,\text{Rx}}[q] \triangleq \mathrm{diag}(e^{-j\boldsymbol{\psi}_{\text{Rx}}[q]})$
$\hat{\mathbf{D}}_{\phi,\text{Tx}}[q_{\mathrm{s}}\vert q]$,$\hat{\mathbf{D}}_{\phi,\text{Rx}}[q_{\mathrm{s}}\vert q]$	Prediction on the accumulated Tx and Rx CFO rotation during the transmission of the q_{s}-th symbol of the sub-frame q
$D_{n_{\mathrm{r}}n_{\mathrm{t}}}$	Distance between Tx-n_{t} and Rx-n_{r}
D_p	Propagation distance of the p-th significant path in the single subarray system.
$D_p^{(n_{\mathrm{r}}n_{\mathrm{t}})}$	Distance between the n_{r}-th receive subarray and the n_{t}-th transmit subarray via the p-th path
$\mathbf{d}_1$, $\mathbf{d}_2$	Vectors containing the diagonal entries of $\mathbf{D}_1$, $\mathbf{D}_2$
d_{t}, d_{r}	Antenna (subarray) spacings at Tx, Rx
$d_{\mathrm{t,h}}$, $d_{\mathrm{t,v}}$	Horizontal and vertical antenna (subarray) spacings at Tx
$d_{\mathrm{r,h}}$, $d_{\mathrm{r,v}}$	Horizontal and vertical antenna (subarray) spacings at Rx
d_{LoS}	Optimal symmetric antenna spacing in LoS MIMO systems of ULAs
d_{v}, d_{h}	Optimal symmetric antenna spacing in LoS MIMO systems of URAs
$d_{\max}$	$d_{\max} \triangleq d_{\mathrm{v}} \cdot (N_{\mathrm{v}}-1)$
d_{s}	General antenna spacing
d_{sub}	Subarray spacing
d_{e}	Spacing of antenna elements within a subarray
$\mathrm{EVM}_{n_{\mathrm{t}}}$	EVM of the n_{t}-th stream
$\mathbf{e}[k]$	Error signal, i.e., $\mathbf{e}[k] = \hat{\mathbf{s}}[k] - \bar{\mathbf{s}}[k]$
$\mathbf{F}_{\mathrm{BB}}$	Baseband precoder
$\mathbf{F}_{\mathrm{RF}}$	RF precoder at a single subarray
$\mathbf{F}_{\mathrm{RF},N}$	RF precoder at N subarrays
$\widetilde{\mathbf{F}}$	Equivalent baseband precoder
$\mathcal{F}_{\mathrm{RF}}$	RF precoder codebook
F	Noise figure
$\mathbf{f}_b$	The b-th analog beamforming vector (column vector) of $\mathbf{F}_{\mathrm{RF}}$
f_{c}	Carrier frequency
$f_h(h)$	Spatial oscillation frequency as a function of h
f_{s}	Symbol rate
$\mathbf{G}_{\mathrm{ZFE}}[q_{\mathrm{s}}\vert q]$	IAI suppression matrix with ZFE
$\mathbf{G}_{\mathrm{SCE}}[q_{\mathrm{s}}\vert q]$	IAI suppression matrix with SCE
$\mathbf{G}_L[k]$	Time varying adaptive filter of L taps
$\mathbf{G}_{\text{LMS}}[k]$	DD-LMS filter
$\mathbf{G}_{\text{LMS,WL}}[k]$	Widely linear DD-LMS filter

$g_{\mathrm{Tx}}(M)$, g_{Tx}	Subarray beamforming gain at Tx
$g_{\mathrm{Rx}}(M)$, g_{Rx}	Subarray beamforming gain at Rx
$\mathbf{H}$	MIMO channel matrix
$\mathbf{H}_{\mathrm{LoS}}$	LoS MIMO channel matrix (phase couplings)
$\mathbf{H}_{\mathrm{LoS,h}}$, $\mathbf{H}_{\mathrm{LoS,v}}$	LoS MIMO phase couplings for horizontal and vertical arrays
$\mathbf{H}_{\mathrm{o}}$	Optimal phase coupling matrix in symmetric LoS MIMO setups
$\mathbf{H}_{\mathrm{oh}}$, $\mathbf{H}_{\mathrm{ov}}$	Optimal phase coupling matrices of the horizontal and vertical arrays
$\mathbf{H}_{\perp}$	Phase coupling matrix resulted from the broadside arrangement w.r.t. the transmit direction, $\mathbf{H}_{\mathrm{LoS}} = \mathbf{D}_{\parallel,\mathrm{r}}\mathbf{H}_{\perp}\mathbf{D}_{\parallel,\mathrm{t}}$
$\tilde{\mathbf{H}}_{\perp}$	Matrix at the middle position of the refined channel factorization, i.e., $\mathbf{H}_{\mathrm{LoS}} = \tilde{\mathbf{D}}_{\parallel,\mathrm{r}}\tilde{\mathbf{H}}_{\perp}\tilde{\mathbf{D}}_{\parallel,\mathrm{t}}$
$\mathbf{H}_{\Delta}$	Difference between $\mathbf{H}_{\perp}$ and $\mathbf{H}_{\mathrm{o}}$, i.e., $\mathbf{H}_{\Delta} \triangleq \mathbf{H}_{\perp} - \mathbf{H}_{\mathrm{o}}$
$\tilde{\mathbf{H}}_{\Delta}$	Difference between $\tilde{\mathbf{H}}_{\perp}$ and an IDFT matrix, e.g., $\tilde{\mathbf{H}}_{\Delta} \triangleq \tilde{\mathbf{H}}_{\perp} - \mathbf{W}_{\text{IDFT-}N}$
$\mathbf{H}_{n_{\mathrm{r}}n_{\mathrm{t}}}$	Channel between the n_{t}-th transmit subarray and the n_{r}-th receive subarray
$\mathbf{H}_{\phi}[q]$	Initial channel state of the q-th sub-frame
$\hat{\mathbf{H}}_{\phi}[q_{\mathrm{s}}\|q]$	Prediction on the effective channel during the transmission of the q_{s}-th symbol of the sub-frame q
$\mathbf{H}[l]$	The l-th tap of the effective channel including AFEs
$\mathbf{H}_{L}$	Channel matrix collecting L taps, i.e., $\mathbf{H}_{L} \triangleq \big[\mathbf{H}[1], \mathbf{H}[2], \cdots, \mathbf{H}[L]\big]$
$\mathbf{H}_{\phi,L}[k]$	The time varying effective matrix of L taps, i.e., $\mathbf{H}_{\phi,L}[k] \triangleq \mathbf{D}_{\phi,\mathrm{Rx}}[k] \cdot \mathbf{H}_{L} \cdot \mathbf{D}_{\phi,\mathrm{Tx},L}[k]$
$\mathbf{H}_{\mathrm{eff}}$	Effective channel including RF precoders and RF equalizers
$\mathbf{H}_{p}$	Phase couplings via the p-th path
$H(\cdot)$	Entropy of the parameter $(\cdot)$
$\mathbf{h}_{n_{\mathrm{t}}}$ $\mathbf{h}_{n'_{\mathrm{t}}}$	Column vectors of $\mathbf{H}_{\mathrm{LoS}}$
$h_{n_{\mathrm{r}}n_{\mathrm{t}}}$, $h_{n_{\mathrm{r}}n_{\mathrm{t}}}[l]$	Channel coefficients
h	Height
$\mathbf{I}_{N}$	An identity matrix of a size N by N
I, $\tilde{I}$	Mutual information
$I_{\{N,P\}}$, $\tilde{I}_{\{N,P\}}$	Mutual information for systems having N subarrays and P significant paths
i	Local index, e.g., index for Tx or Rx side, $i \in \{\mathrm{t}, \mathrm{r}\}$
K_{c}	Number of subcarriers
K_{o}	Oversampling factor
K_{w}	Window of the DFT operation
k	Discrete time domain index
k_{B}	Boltzmann constant
k_{λ}	$k_{\lambda} \triangleq 2\pi/\lambda$
k_{q}	Sampling index at the beginning of the q-th sub-frame
L	Length of significant channel taps being considered
L_{P}	Preamble length
L_{M}	Midamble length

L_{D}	Data section length
L_{T}	Training sequence length, $L_{\mathrm{T}} \in \{L_{\mathrm{P}}, L_{\mathrm{M}}\}$
L_{SF}	Sub-frame length, i.e., $L_{\mathrm{SF}} \triangleq L_{\mathrm{T}} + L_{\mathrm{D}}$
l	Channel tap index
M, M^2	Number of antennas within a subarray
M_{s}	Number of constellation points in QAM
m, $\{m_{\mathrm{y}}, m_{\mathrm{z}}\}$	Index of an antenna within a subarray
$\mathbf{N}_{\mathrm{T}}[q]$	The noise of the received training sequences of the q-th sub-frame
$\mathcal{N}(\cdot,\cdot)$	Normal (Gaussian) distribution
N	Number of antennas (subarrays) at Tx and at Rx when $N_{\mathrm{t}} = N_{\mathrm{r}}$
N_{t}	Number of transmit antennas (subarrays)
N_{r}	Number of receive antennas (subarrays)
N_{h}	Number of horizontal antennas (subarrays)
N_{v}	Number of vertical antennas (subarrays)
$N_{\max}$	$\max\{N_{\mathrm{r}}, N_{\mathrm{t}}\}$
$N_{\min}$	$\min\{N_{\mathrm{r}}, N_{\mathrm{t}}\}$
N_{SF}	Number of sub-frames in one burst of transmission
N_{s}	Number of spatial data streams
N_{RF}	Number of RF chains (per subarray)
$\mathbf{n}$, $\mathbf{n}[k]$, $n_{n_{\mathrm{r}}}[k]$	Noise symbol, noise vector
$\mathbf{n}_{\text{eff}}$	Effective noise vector in digital baseband
$\tilde{\mathbf{n}}$	The equivalent noise vector in the water-filling algorithm
n_{t}, n'_{t}	Index of transmit antennas (subarrays)
n_{r}	Index of receive antennas (subarrays)
$\{n_{\mathrm{h}}, n_{\mathrm{v}}\}$	Index of antennas in a uniform planar array
P	Number of significant paths
P_{T}	Transmit power
P_{eirp}	EIRP limit
P_{C}	Power constraint
$\mathrm{P}(u^i_{\mathrm{x}}, u^i_{\mathrm{y}}, u^i_{\mathrm{z}})$	Plane with normal vector $[u^i_{\mathrm{x}}, u^i_{\mathrm{y}}, u^i_{\mathrm{z}}]^T$
p	Index of significant paths (path directions)
$\mathbf{Q}_{y'_i}(\vartheta_i)$, $\mathbf{Q}_{z'_i}(\varphi_i)$, $\mathbf{Q}_i(\varphi_i, \vartheta_i)$	Rotation matrices around the y'_i-axis and z'_i-axis Coordinate transformation matrix, i.e., $\mathbf{Q}_i(\varphi_i, \vartheta_i) \triangleq \mathbf{Q}_{z'_i}(\varphi_i)\mathbf{Q}_{y'_i}(\vartheta_i)$
$\mathcal{Q}_b(\cdot)$	Quantization function with b bits for in-phase components and b bits for quadrature-phase components
q	Index for sub-frames
q_{s}	Index for symbols within a sub-frame, $0 \le q_{\mathrm{s}} \le L_{\mathrm{SF}} - 1$
$\mathbf{R}_{\mathbf{s}}$, $\mathbf{R}_{\tilde{\mathbf{s}}}$	Covariance matrices of $\mathbf{s}$ and $\tilde{\mathbf{s}}$
$\mathbf{R}_{\mathbf{y}_L\mathbf{y}_L}[k]$	Auto-correlation matrix of $\mathbf{y}_L$, i.e., $\mathbf{R}_{\mathbf{y}_L\mathbf{y}_L}[k] = \mathbb{E}\left[\mathbf{y}_L[k]\mathbf{y}_L^H[k]\right]$
$\mathbf{R}_{\mathbf{n}_{\text{eff}}}$	Covariance matrix of the effective noise $\mathbf{n}_{\text{eff}}$
$\mathbf{R}_{\mathbf{n}}$	Covariance matrix of the noise after baseband processing, i.e., $\mathbf{R}_{\mathrm{n}} \triangleq \sigma^2_{\mathrm{n}}\mathbf{W}^H_{\mathrm{BB}}\mathbf{W}^H_{\mathrm{RF},N}\mathbf{W}_{\mathrm{RF},N}\mathbf{W}_{\mathrm{BB}}$
R	Rates

$R(\mathbf{W})$	The achievable rate with a linear equalizer $\mathbf{W}$
r	Number of butterfly points
$\mathcal{S}$	A finite set containing all possible modulated transmit vectors
$\mathbf{s}$, $\mathbf{s}[k]$	Transmit signal (time-domain)
$\mathbf{s}_L[k]$	A vector collecting L transmit symbols, i.e., $\mathbf{s}_L[k] \triangleq \left[\mathbf{s}^T[k], \mathbf{s}^T[k-1], \cdots, \mathbf{s}^T[k-L+1]\right]^T$
$\tilde{\mathbf{s}}$	Equivalent transmit signal, $\tilde{\mathbf{s}} \triangleq \mathbf{D}_{\|,\mathrm{t}} \cdot \mathbf{s}$
$\bar{\mathbf{s}}[k]$	Decided symbol (decisions)
s_{n_t}, $s_{n_\mathrm{t}}[k]$	The n_t-th entry of $\mathbf{s}$, $\mathbf{s}[k]$
T_c	Coherence time
T_d	Delay spread
T_K	Absolute temperature in Kelvin
T_s	Symbol duration
$\mathbf{U}$, $\mathbf{V}$, $\mathbf{U}_\perp$, $\mathbf{V}_\perp$	Unitary matrices in SVD
$\mathbf{u}_i$, $\mathbf{v}_i$	Singular vectors
$\mathbf{W}$	A linear equalizer
$\mathbf{W}_{\text{IDFT-}N}$	IDFT matrix of N points
$\mathbf{W}_{\text{DFT-}N}$	DFT matrix of N points
$\mathbf{W}_\mathrm{MMSE}$	MMSE equalizer
$\mathbf{W}_\mathrm{ZF}$	Zero-forcing equalizer
$\mathbf{W}_\mathrm{BL}$	Baseline equalizer
$\mathbf{W}_\mathrm{sce}$	SCE equalizer
$\mathbf{W}_\mathrm{fix}$	A fixed equalizer
$\mathbf{W}_{\text{BM-}N}$	N-point Butler matrix
$\mathbf{W}_\mathrm{BB}^H$	Baseband equalizer
$\mathbf{W}_\mathrm{RF}^H$	RF equalizer at a single subarray
$\mathbf{W}_{\mathrm{RF},N}^H$	RF equalizer at N subarrays
$\widetilde{\mathbf{W}}^H$	Equivalent baseband equalizer
$\mathcal{W}_\mathrm{RF}$	RF equalizer codebook
W	Bandwidth
W_co	Coherence bandwidth
W_s	Signal bandwidth of a sub-carrier
$\mathbf{w}_{n_\mathrm{t}}^T$	The n_t-th row vector of $\mathbf{W}$
$\mathbf{w}_b$	The b-th analog beamforming vector (column vector) of $\mathbf{W}_\mathrm{RF}$
$\mathbf{X}_\mathrm{T}[q]$	The training sequences of the q-th sub-frame
$(x_{n_\mathrm{t}}, y_{n_\mathrm{t}}, z_{n_\mathrm{t}})$	Coordinates of Tx-n_t w.r.t. the Tx phase center
$(x_{n_\mathrm{r}}, y_{n_\mathrm{r}}, z_{n_\mathrm{r}})$	Coordinates of Rx-n_r w.r.t. the Rx phase center
(x_i, y_i, z_i), (x_i', y_i', z_i')	Cartesian coordinate systems
$x_{\mathrm{T},n_\mathrm{t}}[k]$	Samples of the oversampled training sequences at Tx-n_t
$\mathbf{Y}_\mathrm{T}[q]$	Received training sequences of the q-th sub-frame
$\mathcal{Y}_\mathrm{Q}$, $\widetilde{\mathcal{Y}}_\mathrm{Q}$	Finite sets containing all possible $\mathbf{y}_\mathrm{Q}$, $\tilde{\mathbf{y}}_\mathrm{Q}$
$\mathbf{y}$, $\mathbf{y}[k]$, $y_{n_\mathrm{r}}[k]$, $y_{n_\mathrm{r}}'[k]$	Receive signal (time-domain)
$\tilde{\mathbf{y}}$	Equalized symbol vector with an equalizer $\mathbf{W}$, i.e., $\tilde{\mathbf{y}} \triangleq \mathbf{W} \cdot \mathbf{y}$

$\mathbf{y}_{\mathrm{Q}}$, $\tilde{\mathbf{y}}_{\mathrm{Q}}$	Quantized signal of $\mathbf{y}$, $\tilde{\mathbf{y}}$
$\mathbf{y}_L[k]$	A vector collecting L received symbols, i.e., $\mathbf{y}_L[k] \triangleq \left[\mathbf{y}^T[k], \mathbf{y}^T[k-1], \cdots, \mathbf{y}^T[k-L+1]\right]^T$
$\tilde{y}_{n_{\mathrm{t}}}$	The n_{t}-th entry of $\tilde{\mathbf{y}}$
$\mathbf{z}$, $\mathbf{z}_{n_{\mathrm{t}}}$	Precoded baseband signals
α, $\alpha(D)$	Common path gains
$\alpha_p^{(n_{\mathrm{r}}n_{\mathrm{t}})}$, $\alpha_{\mathrm{LoS}}^{(n_{\mathrm{r}}n_{\mathrm{t}})}$	Path gains between Tx-n_{t} and Rx-n_{r}
α_p	The channel gain of the p-th significant path
Γ_p	Reflection coefficient of the p-th path
γ	Signal-to-noise ratio (SNR)
γ_η	SNR of the η-th sub-channel
$\tan\delta$	loss tangent
ϵ	Normalized matrix approximation error
ϵ_{r}	Relative dielectric constant
$\varepsilon[k]$	Sampling frequency offset
$\varepsilon_\Delta[k]$	Sampling frequency offset difference
$\bar{\varepsilon}_\Delta$	The mean value of $\varepsilon_\Delta[k]$
η	Subchannel index
Θ_{s}	Angular spread
Θ_{3dB}	Half power beamwidth
Θ_{null}	First-null beamwidth
θ_{t}, ϕ_{t}	Azimuth and elevation angles of departure
θ_{r}, ϕ_{r}	Azimuth and elevation angles of arrival
θ_p^{t}, ϕ_p^{t}	Azimuth and elevation angles of departure of the p-th significant path
θ_p^{r}, ϕ_p^{r}	Azimuth and elevation angles of arrival of the p-th significant path
$\tilde{\theta}_b^{\mathrm{t}}$, $\tilde{\phi}_b^{\mathrm{t}}$	Steering angles of $\mathbf{f}_b$
$\tilde{\theta}_b^{\mathrm{r}}$, $\tilde{\phi}_b^{\mathrm{r}}$	Steering angles of $\mathbf{w}_b$
$\tilde{\theta}_b$	Steering direction of a symmetric setup with symmetric b-th beams at transceivers, i.e., having $\tilde{\theta}_b \triangleq \tilde{\theta}_b^{\mathrm{t}} = -\tilde{\theta}_b^{\mathrm{r}}$
κ	Water level in the water-filling algorithm
$\Lambda_{n_{\mathrm{r}}n_{\mathrm{t}}}[k]$	The correlation between the oversampled received training sequence and the corresponding transmit training sequence
λ	Wavelength
μ	Step size in DD-LMS estimation
ν	Index (an integer) for antenna arrangement solutions
ξ_η	Allocated power to the η-th subchannel
$\mathbf{\Sigma}$, $\mathbf{\Sigma}_\perp$	Singular value matrices in SVD
σ_{n}^2	Variance of the noise (noise power)
σ_η	The η-th singular value
$\sigma^2_{\phi_{\Delta,\text{Tx-}n_{\mathrm{t}}}}$, $\sigma^2_{\phi_{\Delta,\text{Rx-}n_{\mathrm{r}}}}$	Variances of $\phi_{\Delta,\text{Tx-}n_{\mathrm{t}}}[k]$, $\phi_{\Delta,\text{Rx-}n_{\mathrm{r}}}[k]$
$\sigma^2_{\varepsilon_\Delta}$	Variance of $\varepsilon_\Delta[k]$

$\sigma_{\{N,P\}}$	Singular values of the effective channel of a system having N subarrays and P significant paths
τ_p	Relative delay
$\boldsymbol{\phi}_{\mathrm{Tx}}[q]$, $\boldsymbol{\phi}_{\mathrm{Rx}}[q]$	The phase terms of the diagonal elements of $\mathbf{D}_{\phi,\mathrm{Tx}}[k_q]$ and $\mathbf{D}_{\phi,\mathrm{Rx}}[k_q]$
φ_{t}, φ_{r}, ϑ_{t}, ϑ_{r}	Rotation angles
ϕ	Phase difference between two paths
$\tilde{\phi}_1$, $\tilde{\phi}_2$	First and second order approximation of ϕ
$\phi_{\mathrm{e},1}$, $\phi_{\mathrm{e},2}$	Approximation errors, i.e., $\phi_{\mathrm{e},1} \triangleq \phi - \tilde{\phi}_1$, $\phi_{\mathrm{e},2} \triangleq \phi - \tilde{\phi}_2$
$\phi_{\mathrm{e,max}}$	Maximum allowed phase error
$\phi_{\text{Tx-}n_{\mathrm{t}}}[k]$, $\phi_{\text{Rx-}n_{\mathrm{r}}}[k]$	The accumulated phase variations of oscillators at Tx-n_{t} and Rx-n_{r} over time
$\phi_{\Delta,\text{Tx-}n_{\mathrm{t}}}[k]$	Random phase variations of the oscillators at Tx-n_{t} for each sample
$\phi_{\Delta,\text{Rx-}n_{\mathrm{r}}}[k]$	Random phase variations of the oscillators at Rx-n_{r} for each sample
$\bar{\phi}_{\Delta,\text{Tx-}n_{\mathrm{t}}}$, $\bar{\phi}_{\Delta,\text{Rx-}n_{\mathrm{r}}}$	Mean values of the $\phi_{\Delta,\text{Tx-}n_{\mathrm{t}}}[k]$, $\phi_{\Delta,\text{Rx-}n_{\mathrm{r}}}[k]$
$\boldsymbol{\Psi}$	Diagonal matrix containing the gain coefficients of the sub-channels in the water-filling algorithm
ψ_η	The η-th diagonal element of $\boldsymbol{\Psi}$
$\boldsymbol{\psi}_{\mathrm{Tx}}[q]$, $\boldsymbol{\psi}_{\mathrm{Rx}}[q]$	Phase increments at Tx and Rx from sub-frame q to sub-frame $q+1$, i.e., $\boldsymbol{\psi}_{\mathrm{Tx}}[q] \triangleq \boldsymbol{\phi}_{\mathrm{Tx}}[q+1] - \boldsymbol{\phi}_{\mathrm{Tx}}[q]$, $\boldsymbol{\psi}_{\mathrm{Rx}}[q] \triangleq \boldsymbol{\phi}_{\mathrm{Rx}}[q+1] - \boldsymbol{\phi}_{\mathrm{Rx}}[q]$

List of Figures

List of Tables

Chapter 1

Introduction

The way of communication shapes our society and daily life. From 1G to 4G, from analog to digital, from voice calls to data roaming, mobile telecommunications has been providing people with higher and higher throughput and serving more and more demands. With data-rate hungry applications like augmented and virtual reality, with massive numbers of connected devices, the rapid growth in mobile traffic keeps creating unprecedented challenges to cellular networks.

According to the wireless roadmap made in year 2014 [Fet14a], peak user data rates in cellular networks are expected to reach multi-Gbit/s. In order to achieve this, denser networks with highly interconnected base stations and access points are widely considered [BLM+14]. In addition, densification of the network can fulfill the low latency requirements by future time-critical applications [Fet14b]. Connecting massive numbers of nodes via wired front-/backhaul links is economically infeasible and very time consuming, especially considering the variety of deployment scenarios.

Flexible high-throughput wireless solutions are an important alternative to fiber-optic links. According to the statistics from Ericsson [ERI17], about 70 percent of cell sites are connected via wireless backhaul nowadays. This number will still be larger than 65 percent in 2022 (excluding China, Japan, and Korea). In addition, millimeter wave (mmWave) bands have become popular for the evolution of the wireless backhaul network beyond 2020 with their large new spectrum for enhancing the symbol rates. According to the prediction in [ERI17], more than 20 percent of new backhaul deployments in 2025 will be using V-band (60 GHz) and E-band (70/80 GHz), and this number will keep growing afterward.

In this thesis, we will focus on a technology called Line-of-Sight (LoS) Multiple-Input-Multiple-Output (MIMO) communication. In general, MIMO technologies can transmit parallel streams at the same time-frequency resource using multiple transmit and receive antennas. In contrast to the single-input-single-output (SISO) wireless backhaul links, LoS MIMO based systems allow the throughput to scale linearly with the number of deployed antennas. In year 2017, the European Electronic Communications Committee (ECC) started to consider the usage of LoS MIMO technologies in fixed service links [ECC17]. Furthermore, with large bandwidth, LoS MIMO communication at mmWave frequencies is a promising candidate for solving this last mile problem.

We formulate the conventional general maximum throughput of the frequency-flat MIMO

channel [Tel99, Fos96] as[1]

$$R = W \cdot \log_2 \det(\mathbf{I} + \gamma \cdot \mathbf{H}\mathbf{H}^H), \tag{1.1}$$

where W, γ, and $\mathbf{H}$ denote the bandwidth, signal-to-noise ratio (SNR), and the MIMO channel matrix, respectively. In this thesis, we show that the LoS MIMO communication at mmWave frequencies can simultaneously provide large values to these parameters for ultra high throughputs at a relatively low complexity level.

In this chapter, we first introduce the state-of-the-art works on SISO and cross-polarized wireless backhaul links in Sec 1.1. Then a brief overlook on the contributions as well as the outline of the thesis are specified in Sec. 1.2. Finally, the notation conventions of the thesis are provided in Sec. 1.3.

1.1 SISO and Cross-Polarized Backhaul Technologies

To support multiple users with cellular peak data rates of multi-Gbit/s, the requirements on the throughput of small-cell front-/backhaul should be at least one order of magnitude higher, e.g., tens-Gbit/s or even 100 Gbit/s. However, even using the carrier aggregation technologies and differently polarized signals, microwave systems currently available on the market can provide only up to 4 Gbit/s for the LoS backhaul links [Dra16]. Lack of bandwidth is a key reason that limits the throughput of those conventional microwave backhaul systems.

MmWave band is a suitable candidate for enhancing the throughput due to its large available bandwidth. Around 60 GHz, IEEE 802.11ay [GSCK17] regulates six channels of 2.16 GHz bandwidth each for outdoor wireless backhaul and allows channel bonding mechanisms for four of those channels. By bonding four channels at 60 GHz and using 16-QAM (quadrature amplitude modulation), the single stream transmission can achieve 28.16 Gbit/s at a distance of 0.8 meter [WMT+17].

High pathloss is one limitation of utilizing mmWave [Fri46]. With directive antennas or beamforming technologies, the short range limitation due to the high pathloss can be overcome. With the help of highly directive antennas of 55.1dBi, the authors of [ABM+15] demonstrated a single stream mmWave transmission over an 850 m distance at a 240 GHz carrier frequency. Under the LoS dominant scenario, an error vector magnitude (EVM) value of -11.9dB is achieved with a 32 Gbaud 4-QAM modulation, yielding 64 Gbit/s.

In order to transmit more streams using the same time-frequency resource, cross-polarized antennas with strong polarization selectivity are also considered in backhaul applications, e.g., supported by IEEE 802.11ay. Experimental results [MMS+09] have shown that 60 GHz antennas can have a cross polarization discrimination factor of approximately 20dB under the LoS conditions. Being considered as polarization separation of two SISO channels in this work, the parallel stream number is limited by a maximum value of two.

[1] The mathematical notation $\mathbf{I}$ denotes an identity matrix. The operators $\det(\cdot)$ and $(\cdot)^H$ denote the determinant and conjugate transpose of a matrix, respectively, while operator $\log_2$ denotes the binary logarithm operation.

1.2 Contributions and Outline of This Work

In contrast to the prevailing interpretation of LoS channels[2], parallel streams with approximately equal sub-channel quality can be transmitted theoretically within the LoS path. This is independent of the polarization diversity and can be used in addition to it. Instead of exploiting the spatial multiplexing between different LoS/reflected paths, the existence of spatial multiplexing gains is reported for strong LoS fixed radio in [DF98, CLS04]. Under the spherical wave model, orthogonal channel matrices with condition numbers (the ratio of the maximum singular value to the minimum singular value of a matrix) as low as one can be obtained with the widely spaced antennas [GBGP02, HK03, Lar05]. Considering LoS applications like front-/backhaul, our works in Chapter 3 show that data rates 100 Gbit/s or more are feasible, even in the case of using just a single 2.16 GHz channel, if tens of parallel streams are transmitted.

Besides the feasibility, another important aspect of building such systems is the complexity. MIMO processing for multiple parallel streams and high data rates per stream can be very computationally intensive [MZ08], e.g., the computational complexity of a general matrix multiplication grows quadratically with the number of spatial streams. One important aspect for implementing these systems is thus to find processing architectures that have suitable complexity and scale well during the system expansion with more streams.

In this thesis, we investigate mmWave MIMO systems for transmitting multiple streams under the LoS condition. The focus is the system design allowing high throughput with reliable signal estimation at a relatively low complexity level. Specifically, we first study the antenna topology solutions that provide mmWave backhaul links with flexibility, sufficient receive power and high spatial multiplexing gain at reasonable array sizes. Then, LoS MIMO signal processing algorithms that keep the complexity increasing approximately linearly during system expansion are proposed. With possible imperfect arrangements and imperfect hardware in practical systems, the proposed algorithms are evaluated in terms of throughput, robustness, estimation error, and complexity. As a benchmark, those results are compared with the state-of-the-art channel equalization algorithms like zero-forcing. Finally, the antenna arrangement dependent spatial multiplexing within a single LoS path is introduced to other reflected paths for further throughput enhancement.

The proposed methods in this thesis can be used in general for all LoS MIMO systems, e.g., Tera-bit-per-second short range board-to-board wireless communication proposed in our earlier work [SLIF15]. However, in order to understand the importance of the contribution more intuitively and to have a consistent discussion, we only consider systems in backhaul scenarios.

The subsequent chapters of this thesis are organized as follows:

- ▷ **Chapter 2** provides fundamental information on the LoS MIMO communication. First, a generic MIMO model with multipath propagation is described with a discussion on different scattering conditions. Subsequently, under a strong LoS condition, the antenna topology dependent LoS MIMO communication is introduced with its orthogonality and antenna arrangements. Finally, based on the simulation results, we show that this antenna topology dependent LoS spatial multiplexing is only weakly sensitive to deviations in-

[2] For transceivers at large separations, the LoS path with planar wave propagation between two locations is considered as a spatial keyhole. The LoS channel is predicted to have a rank one channel matrix [CFV00, TV05].

duced by small tilts or translations. The discussions on the spatial multiplexing gains and their examples have been presented in part in [SRB+18, SCR+18].

- ▷ **Chapter 3** focuses on antenna topologies in LoS MIMO communication. First, a general channel factorization model is presented. The LoS MIMO channel can always be factorized into a product of three matrices. Since the two outer matrices are diagonal matrices and do not influence the capacity, after interpreting their physical meaning, a general solution on optimal antenna topology is presented. Besides summarizing all discovered linear and planar arrangements, this general solution also suggests undiscovered 2D solutions under any rotation direction and 3D solutions. By checking the validation conditions of different wave propagation models at different antenna spacings, we derive the array response vector with mixed antenna spacings. Finally, in this chapter, a widely spaced multi-subarray system is proposed for the mmWave LoS MIMO backhaul communication with realistic link budget calculations. The major results of this chapter have been presented in part in [SF15, SJL+15, SRB+18].

- ▷ **Chapter 4** shows a novel algorithm, namely sequential channel equalization, for the strong LoS MIMO channel equalization. The equalization is applied in a reverse order w.r.t. the channel factorization model in Chapter 3. Being a good tradeoff between complexity and robustness against displacement errors, the proposed algorithm can be applied to the LoS MIMO systems with uniform linear or rectangular arrays using digital or analog equalization. By considering the usage of the Winograd butterfly and Butler DFT-matrices, the number of multiplications in both digital and analog implementations of the proposed solution is increasing approximately linearly w.r.t. the number of antennas, while the complexity of the state-of-the-art designs, like zero-forcing, exhibits quadratic growth. The major results of this chapter have been presented in part in [SCR+18, SRF16, SHR+16].

- ▷ **Chapter 5** investigates the issues that arise from the imperfect hardware of practical mmWave LoS MIMO systems and how to effectively handle them using signal processing techniques. At first, we formulate a signal model of LoS MIMO communication with oscillator variations. Considering the channel and hardware properties, a novel frame structure with high temporal efficiency is then proposed together with a corresponding channel estimation method. Based on the channel estimation results, we show that the required MIMO processing can be decoupled into two steps. The first one suppresses the interantenna interference including the carrier frequency offsets. In the second step, the intersymbol interference caused by the frequency-selective components is suppressed via a parallel structure. As a comparison, a Decision-Directed Least Mean Square approach (DD-LMS) for joint processing of all effects is also introduced. As verified experimentally, only the widely linear version of the DD-LMS approach achieves performance of about 0.2dB$\sim$0.8dB better than the proposed architecture, but requires significantly higher complexity, especially during system expansion. The major results of this chapter have been presented in part in [SCR+18, SHC+18].

- ▷ **Chapter 6** shows that using the same widely spaced multi-subarray antenna topology

as in Chapter 3 and under the appearance of other reflected paths, the spatial multiplexing within each path direction can be expected simultaneously in several directions. The spatial multiplexing between different path directions and within an individual path direction are found at two different levels and can be jointly exploited. Merging the two kinds of spatial multiplexing into a combined channel model and connecting it with a hybrid beamforming architecture, a novel mmWave system is proposed which achieves spatial multiplexing of a higher order than conventional ones. The major results of this chapter have been presented in part in [SRB+18].

▷ **Chapter 7** summarizes the key achievements of this work and gives an outlook on important remaining challenges.

1.3 Notations

In this thesis, the following notations are used.

- a or A in normal font refers to a complex number. Upper- and lowercase variables written in boldface, $\mathbf{A}$ and $\mathbf{a}$, denote matrices and column vectors, respectively.
- Variables with hats, e.g., $\hat{a}$, $\hat{\mathbf{a}}$ and $\hat{\mathbf{A}}$, denote the estimates on the corresponding a, $\mathbf{a}$ and $\mathbf{A}$, respectively.
- We denote sets by calligraphic letters $\mathcal{A}$ and their cardinalities with $|\mathcal{A}|$.
- $\{\mathbf{A}\}_{bc}$ denotes the (b, c)-th element of $\mathbf{A}$, while a_i denotes the i-th element of vector $\mathbf{a}$.
- $\mathbf{A}^T$, $\mathbf{A}^*$, $\mathbf{A}^H$, $\mathbf{A}^{-1}$, $\mathbf{A}^\dagger$ and $||\mathbf{A}||_F$ denote the transpose, conjugate complex, conjugate transpose, inverse, pseudo-inverse and Frobenius norm of $\mathbf{A}$, respectively.
- $\mathbf{A} \otimes \mathbf{B}$ is the Kronecker product of $\mathbf{A}$ and $\mathbf{B}$.
- $\mathbf{A} \odot \mathbf{B}$ is the Hadamard product of $\mathbf{A}$ and $\mathbf{B}$;
- $\mathcal{CN}(\mathbf{a}, \mathbf{A})$ is the multivariate complex Gaussian distribution with a mean vector $\mathbf{a}$ and a covariance matrix $\mathbf{A}$. While $\mathcal{N}(a, b)$ denotes a normal Gaussian distribution with a mean value a and a covariance value b.
- $\mathrm{diag}(\mathbf{A})$ gives a vector collecting the diagonal elements of $\mathbf{A}$, while $\mathrm{diag}(\mathbf{a})$ gives a diagonal matrix with the vector $\mathbf{a}$ collecting its diagonal elements. Furthermore, $\mathrm{diag}([\mathbf{A}_1, \ldots, \mathbf{A}_b])$ gives a block diagonal matrix with matrices $\mathbf{A}_1, \ldots, \mathbf{A}_b$ on its diagonal.
- $\mathbf{A} \succeq \mathbf{0}$ means that the matrix $\mathbf{A}$ is positive semi-definite.
- $\measuredangle a$ is the phase of the complex number a, while $\measuredangle \mathbf{a}$ refers the vector collecting the phase terms of $\mathbf{a}$.

- $\mathbf{I}_N$ is the $N \times N$ identity matrix, $\mathbf{1}_{B\times C}$ and $\mathbf{0}_{B\times C}$ denote the all one matrix and the all zero matrix of size $B \times C$, respectively.
- $\mathbb{C}^{B\times C}$ denotes the set of complex matrices of size $B \times C$.
- Expectation is denoted by $\mathbb{E}[\cdot]$, and $\mathbf{a} * \mathbf{b}$ indicates the convolution operation between two vectors $\mathbf{a}$ and $\mathbf{b}$.
- $\mathrm{tr}(\mathbf{A})$ and $\det(\mathbf{A})$ denote the trace and the determinant of $\mathbf{A}$, respectively;
- $\mathrm{sinc}(\cdot)$ is the sinc function of a parameter;
- vec$(\cdot)$ is the vectorization operator.
- The notation $[a]^+$ is used for taking a non-negative value as $\max(a, 0)$.
- $\mathcal{O}(\cdot)$ is the big O notation describing the order of a parameter.

Chapter 2

Fundamentals of Spatial Multiplexing

Before starting detailed studies on parallel stream transmission in backhaul scenarios, we briefly present the state-of-the-art works in MIMO communication with a focus on LoS spatial multiplexing in this chapter. We first make a brief review of the advantages of multiple antenna systems. In particular, bearing the stationarity of fixed wireless communication in mind, we introduce the general time-invariant transmission model for MIMO wireless communications and briefly discuss the channel model under different scattering environments. Subsequently, we specify the considered LoS MIMO channel which will be used through this thesis with a discussion on its antenna arrangement dependent spatial multiplexing. Eventually, via simulation, we study the sensitivity of this antenna topology dependent LoS spatial multiplexing w.r.t. deviations induced by tilts or translations.

2.1 Multi-Antenna Techniques

Multi-antenna technologies are widely used by modern wireless communication systems for harvesting spatial multiplexing gain, array gain, and diversity gain, which improve spectral efficiency, coverage, and reliability, respectively [TV05]. Considering their significant benefits in improving the service of wireless communication, we briefly summarize them as follows:

Spatial Multiplexing Gain: In contrast to the *logarithmic* increase of data rate w.r.t. SNR over a classical single additive white Gaussian noise (AWGN) channel [Sha48], Telatar [Tel99] and Foschini [FG98] provided the crucial insight that increasing the number of antennas is capable of increasing the spectral efficiency *linearly*. Multiple data streams, i.e., spatial multiplexing, can be transmitted over the same time-frequency resource under the provision that the environment offers *independent* propagation paths. Therefore, in practice, the scattering environments and antenna arrangements influence the spectral efficiency of a MIMO system. More detailed discussions on this relation will be presented later in Sec. 2.1.2.

Array Gain: Applying beamforming on antenna arrays has been proved to provide high directivity and power gain [Bal05]. By knowing the channel information, appropriate signal processing algorithms, e.g., maximal-ratio combining, can combine signals at multiple antennas for power enhancement. For example, if the angles of departure/arrival (AoD/AoA) of planar electromagnetic waves are known, beamforming algorithms can enhance the transmit/receive signal power at the AoD/AoA directions. The resulting power gain thus enhances the coverage,

especially in mmWave frequencies with high pathloss [BBS13]. Due to the directivity of the beam patterns, beamforming technologies are also widely used for multi-user communication scenarios with spatial separation.

Diversity Gain: Diversity is obtained by adding redundancy to the same information over different time, frequency, and/or space. Temporal and frequency diversity can be used in single-/multi-antenna systems and can combat fading due to movement and multipath propagation. Since deep fading is less likely to happen all the time and at all the frequencies, the reliability of transmitting the information is improved. With the help of multiple antennas at different locations, the transmitter and/or receiver can provide more copies and/or observations to the same signal, e.g., using space-time coding [TSC98, Ala98]. With independent propagation paths, multi-antenna systems thus provide an additional degree of diversity in comparison to single antenna systems.

Considering scenarios like backhaul communication, the physical channel is stationary over long time periods. Therefore, backhaul links are generally expected to be reliable. As introduced earlier in Chapter 1, this work focuses on combining the array gain and the spatial multiplexing gain for mmWave LoS MIMO communication.

2.1.1 Wireless MIMO Channel as a Linear Time-Invariant System

In this section, we consider a communication system with N_t antennas at the transmitter (Tx) and N_r antennas at the receiver (Rx). Due to the mobility of the users and/or of the reflectors, the physical channel of wireless communication is in general time-varying. However, the channel can be assumed stationary over a coherence time window T_c. The coherence time T_c is determined by the maximum Doppler shifts, i.e., Doppler spread. More detailed discussions can be found in [TV05]. This work focuses on backhaul scenarios where mobility rarely takes place. Instead, the stationary time of the channel is more influenced by weather changes, i.e., the channel is quasi-stationary over much longer time periods than in usual mobile communication.

In general, multipath propagation may exist in each transmit-receive antenna pair due to reflection, scattering, and diffraction. In this case, the radiated signal from the transmit antenna Tx-n_t arrives at the receive antenna Rx-n_r with different attenuation values and delays, see Fig. 2.1. Thus, the receive signal is the superimposition of several transmit signals and their weighted time-delayed copies.

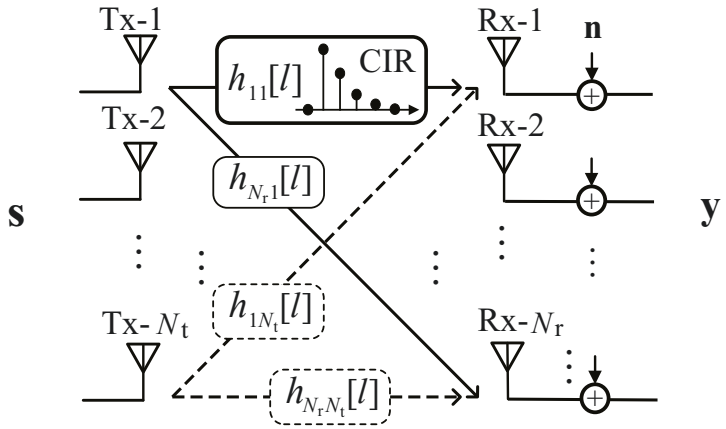

Figure 2.1: MIMO channel with multi-path propagation.

The multipath propagation is widely modeled with the channel impulse responses (CIRs) in the power delay profile, which collects the path gains and delays of different paths. To simplify the discussion and considering quasi-stationary scenarios, we assume the gains and the delays of paths do not depend on the time. Further assuming them to be frequency independent, at time instant k, the relation between the discrete (sampled) output signal $y_{n_\mathrm{r}}[k]$ at Rx-n_r and the discrete baseband input signal $s_{n_\mathrm{t}}[k]$ at Tx-n_t can be modeled as [TV05]

$$y_{n_\mathrm{r}}[k] = \sum_{n_\mathrm{t}} \sum_{l} h_{n_\mathrm{r} n_\mathrm{t}}[l] s_{n_\mathrm{t}}[k-l] + n_{n_\mathrm{r}}[k], \tag{2.1}$$

where $h_{n_\mathrm{r} n_\mathrm{t}}[l]$ is the l-th complex channel tap between Tx-n_t and Rx-n_r. $n_{n_\mathrm{r}}[k]$ denotes the noise of the received signal $y_{n_\mathrm{r}}[k]$ at the time instant k. Here, $h_{n_\mathrm{r} n_\mathrm{t}}[l]$ is the complex channel coefficient that is resolvable in time and is the sum over all non-time-resolvable paths with relative delays τ_p that fall in a delay bin $[l/W - 1/(2W), l/W + 1/(2W))$, where W is the bandwidth of the continuous time signal. The term relative delay means the arrival time difference between the earliest significant path (often the LoS component) and the corresponding path p. Considering the argument above, $h_{n_\mathrm{r} n_\mathrm{t}}[l]$ can be written as

$$h_{n_\mathrm{r} n_\mathrm{t}}[l] = \sum_{p} \alpha_p^{(n_\mathrm{r} n_\mathrm{t})} e^{j 2\pi f_\mathrm{c} \tau_p}, \;\; \text{s.t.} \;\; \frac{l}{W} - \frac{1}{2W} \leq \tau_p < \frac{l}{W} + \frac{1}{2W}, \tag{2.2}$$

where f_c denotes the carrier frequency and $j = \sqrt{-1}$. $\alpha_p^{(n_\mathrm{r} n_\mathrm{t})}$ denotes the complex path gain. In the case that the signal bandwidth W is much smaller than the coherence bandwidth W_co, i.e., $W \ll W_\mathrm{co}$, the channel in (2.1) is considered to have a single tap (flat fading). In terms of time domain representation, the symbol duration $T_\mathrm{s} \propto 1/W$ is much larger than the delay spread $T_\mathrm{d} = \max_p \tau_p \propto 1/W_\mathrm{co}$, i.e., $T_\mathrm{s} \gg T_\mathrm{d}$. If the condition is violated, the channel is considered as a multi-tap channel and is considered as frequency selective containing intersymbol interference (ISI) in time domain.

Considering scenarios like backhaul communication at mmWave frequencies, typically high gain and high directive antennas are used. The LoS path has the absolute dominance and other paths can be much weaker. Therefore, a single path (tap) channel is assumed, namely strong LoS communication. The channel response between Tx-n_t and Rx-n_r can be written as

$$h_{n_\mathrm{r} n_\mathrm{t}} = \alpha_\mathrm{LoS}^{(n_\mathrm{r} n_\mathrm{t})}, \tag{2.3}$$

where the complex path gain $\alpha_\mathrm{LoS}^{(n_\mathrm{r} n_\mathrm{t})}$ is introduced to replace $\alpha_1^{(n_\mathrm{r} n_\mathrm{t})}$ for clarifying the situation in the strong LoS scenario. Under a flat-fading assumption, the general linear system model for a LoS MIMO system can be written as

$$\mathbf{y} = \mathbf{H}\,\mathbf{s} + \mathbf{n}\,, \tag{2.4}$$

where $\mathbf{s} \in \mathbb{C}^{N_\mathrm{t} \times 1}$ and $\mathbf{y} \in \mathbb{C}^{N_\mathrm{r} \times 1}$ are the input and output of the linear discrete-time channel. Furthermore, $\mathbf{n} \sim \mathcal{CN}(\mathbf{0}, \sigma_\mathrm{n}^2 \mathbf{I}_{N_\mathrm{r}})$ is the complex white Gaussian noise vector with independent and identical distributed (i.i.d.) entries that are circularly symmetric, while σ_n^2 is the variance of the noise.

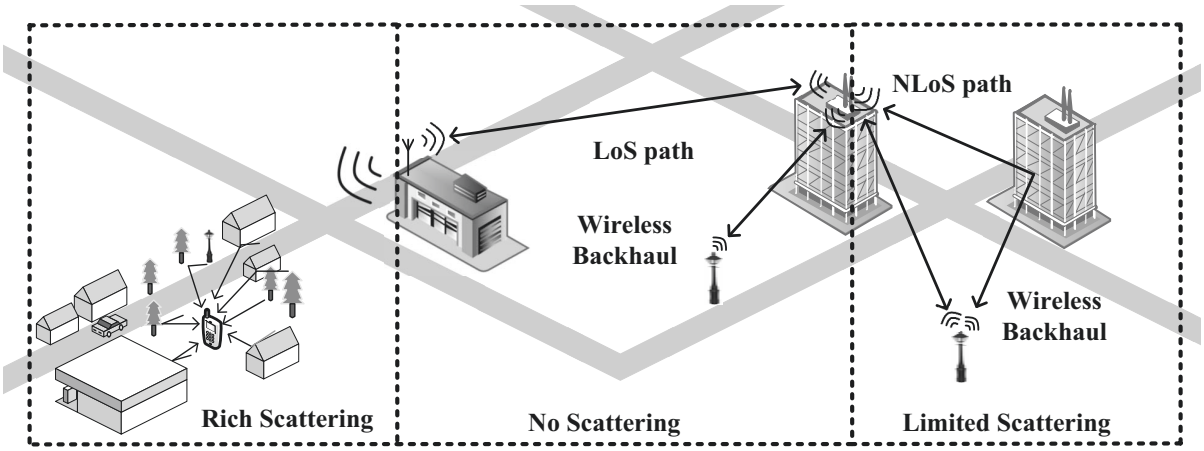

Figure 2.2: Scattering Scenarios.

2.1.2 Spatial Multiplexing and Environments

As discussed earlier, the spectral efficiency of a MIMO system depends on the scattering environments and antenna arrangements. To put our proposed approach into perspective, we briefly summarize several scenarios, namely rich scattering, limited scattering, and no scattering, see Fig. 2.2. The spatial multiplexing under those scenarios is frequently considered as follows:

Rich Scattering: Spatial multiplexing gains with rich scattering environments were initially studied in the seminal works of MIMO in [Tel99, Fos96]. Under the assumption of a large number of reflecting/scattering paths and considering paths to be independent of each other, the sum of many random path gains in (2.2) follows a complex Gaussian distribution by the central limit theorem. The magnitude of the channel response will follow the so-called Rayleigh distribution. In this non line-of-sight (non-LoS) MIMO case, all entries of the channel matrix in the commonly used linear transmission model are assumed to follow a complex Gaussian distribution. Furthermore, those entries can be modeled as *independent* for sufficiently wide antenna spacings, i.e., wider than the coherence distance that is in the order of the carrier wavelength [Lee72]. Eventually, under the appearance of a significant path like a LoS path, the so-called Rician distribution is considered in the literature [TV05]. But due to the complicated form of Rician distribution, the Rayleigh distribution is the more popular model for sub-6 GHz access network channels.

Limited Scattering: In mmWave communication, only limited resolvable paths are found in outdoor environments, e.g., a path number of 2$\sim$7 [RSM$^+$13, GDM$^+$15, ZVM10]. Therefore, in the so-called limited scattering environments, mmWave systems encounter sparsity in both the angular and delay domains. The channel coefficients between different transmit-receive antenna pairs are correlated with each other, while the channel matrices are commonly modeled with planar waves [Say02]. The planar wave model simplifies the mathematical expression with enough accuracy in the far-field of densely packed antenna arrays, although it is only the first-order *approximation* of spherically propagating electromagnetic waves. However, even with large numbers of antennas, the achievable spatial multiplexing of the densely packed arrays is upper-bounded by the number of resolvable paths [GDM$^+$15, AMGPH14]. To cope with the low rank property and the complexity required by full digital beamforming at large arrays, hybrid analog/digital beamforming algorithms in [ZMK05, VvdV10, AHAS$^+$12] are widely

considered for mmWave communication. The discussion on the relation between wave models and antenna spacings will be made later in Chapter 3. Meanwhile, spatial multiplexing under limited scattering will be presented in more detail in Chapter 6, where we will further combine it with the spatial multiplexing within a single path direction.

No Scattering: Within a single LoS path direction, we can *still* achieve spatial multiplexing through special antenna arrangements, namely LoS spatial multiplexing. In order to do this, the original spherical waves emitted by point sources must be considered. This spatial multiplexing gain cannot be derived mathematically if one only uses the simpler planar wave model. By arranging antennas with wide spacings, the curvature of the spherical wave fronts becomes important and can be exploited. With smart antenna arrangements, e.g., as in the works of [GBGP02, HK03, Lar05], *structured phase* couplings can be introduced to the MIMO channels under LoS conditions. Orthogonal channel matrices can be obtained in this case and provide spatial multiplexing already over a single path direction. For mmWave backhaul communication in scenarios with transceivers that are located above rooftops, very high gain and high directive antennas are used. This case leads to the dominance of the LoS path, and the other paths, e.g., reflections from side buildings, are much weaker. The physical channel, in this case, is expected to have a single tap without clustering, if the Fresnel zones are not partially blocked [M$^+$17].

Due to the more or less stationary situation in fixed wireless access applications and high gain antennas with high directivity, we will use a *deterministic* MIMO channel model with links using the spherical-wave model in the following that only takes geometrical properties of the antenna arrays at transmitter and receiver side into account. In the next section, we will introduce the antenna arrangement dependent LoS MIMO communication with its classic solution on the antenna topology.

2.2 Line-of-Sight Spatial Multiplexing

Instead of exploiting spatial multiplexing based on different LoS/NLoS paths, LoS MIMO approaches have shown the existence of spatial multiplexing gains within a single path direction [DF98, CLS04]. By remodeling the channel with spherical waves, particular antenna spacings not only restore the full rank of $\mathbf{H}$ but also provide a *condition number* being one in the ideal case [GBGP02, HK03, Lar05]. Using the same time-frequency resource and co-polarized antennas, parallel streams with approximately equal sub-channel quality can then be transmitted theoretically within the LoS path direction.

2.2.1 Parallel Antenna Topologies

In this part, we introduce the state-of-the-art works on antenna topology with a focus on the arrays that are arranged in parallel. Here, we modify the classic symmetric LoS MIMO system with equal antenna numbers and spacings at Tx and Rx in [Lar05] to a more general asymmetric setup, which would generalize the parallel solutions.

Physical Channel Model: Let us assume that Tx and Rx are two uniform linear arrays (ULA) parallel to the y-axis at $x = 0$ and $x = D$, respectively, see Fig. 2.3. Here, the variable D denotes the transmit distance. The antennas Tx-1 and Rx-1 at bottom ends of the two arrays are

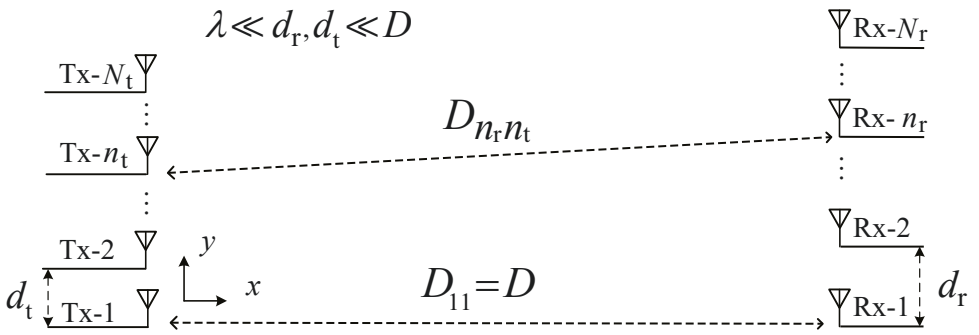

Figure 2.3: A LoS MIMO system with parallel uniform linear arrays.

both located on the x-axis with $y = 0$. A carrier frequency f_c with a corresponding wavelength $\lambda = c/f_\mathrm{c}$ is used by the transceiver arrays. Furthermore, the Tx and Rx consist of N_t and N_r isotropic antenna elements with spacings d_t and d_r, respectively, and $\lambda \ll d_\mathrm{t}, d_\mathrm{r} \ll D$. Moreover, let us use $D_{n_\mathrm{r}n_\mathrm{t}}$ to denote the distance between the n_r-th receive element and the n_t-th transmit element. The associated channel matrix is written as

$$\mathbf{H} = \alpha \underbrace{\mathbf{H}_\mathrm{LoS}}_{\substack{\text{Phase} \\ \text{Couplings}}}, \tag{2.5}$$

where α indicates the common channel gain between all transmit-receive antenna pairs[1]. $\mathbf{H}_\mathrm{LoS} \in \mathbb{C}^{N_\mathrm{r} \times N_\mathrm{t}}$ describes the relative phase shifts between all antenna pairs with unit magnitude entries. The works in [BOO09, PSDT15] show that spherical wave model is more accurate and has even positive consequences than the conventional approach using a plane-wave model for widely spaced antennas. Describing the propagation with the spherical wave model, this phase coupling between Rx-n_r and Tx-n_t can be expressed as

$$\{\mathbf{H}_\mathrm{LoS}\}_{n_\mathrm{r}n_\mathrm{t}} = e^{-j\frac{2\pi}{\lambda}\cdot(D_{n_\mathrm{r}n_\mathrm{t}} - D)}. \tag{2.6}$$

where the common phase term $2\pi D/\lambda$ is deducted for simplification of the discussion later.

In this work, we assume the channel matrix $\mathbf{H}$ to be deterministic due to the quasi-deterministic scenarios like wireless backhaul. For practical systems, $\mathbf{H}$ may have variations, e.g., due to different displacement errors during mass deployment. In this work, we consider $\mathbf{H}$ as a fixed value after having one realization on antenna geometry. In the rest of this section, we focus on the parallel ideal arrangements which lead to orthogonal $\mathbf{H}_\mathrm{LoS}$ without any displacements.

Uniform Linear Antenna Arrangements: As can be seen from (2.6), if $D_{n_\mathrm{r}n_\mathrm{t}}$ values differ from each other by certain fractions of λ, the phase shifts of different antenna pairs will differ by certain fractions of 2π. This motivates the antenna topology design that leads to spatial multiplexing in strong LoS conditions.

Let us first examine the geometry property of $D_{n_\mathrm{r}n_\mathrm{t}}$. Without loss of generality, we assume $N_\mathrm{t} \leq N_\mathrm{r}$ first. Describing the location of Tx-n_t and Rx-n_r in a Cartesian coordinate system as

[1] As shown later, under the assumptions that $\lambda \ll d_\mathrm{t}, d_\mathrm{r} \ll D$, the $D_{n_\mathrm{r}n_\mathrm{t}}$ values will differ from each other by certain fractions of λ, which are negligible for calculating the channel gain.

$(0,(n_\mathrm{t}-1)d_\mathrm{t})$ and $(D,(n_\mathrm{r}-1)d_\mathrm{r})$, respectively, it leads that

$$\begin{aligned} D_{n_\mathrm{r}n_\mathrm{t}} &= \sqrt{D^2+[(n_\mathrm{r}-1)d_\mathrm{r}-(n_\mathrm{t}-1)d_\mathrm{t}]^2} \\ &\approx D+\frac{[(n_\mathrm{r}-1)d_\mathrm{r}-(n_\mathrm{t}-1)d_\mathrm{t}]^2}{2D} \\ &= D+\frac{(n_\mathrm{r}-1)^2d_\mathrm{r}^2-2(n_\mathrm{r}-1)(n_\mathrm{t}-1)d_\mathrm{r}d_\mathrm{t}+(n_\mathrm{t}-1)^2d_\mathrm{t}^2}{2D}, \end{aligned} \tag{2.7}$$

where the approximation follows from the first order Taylor expansion of the square root using $d_\mathrm{t},d_\mathrm{r}\ll D$, e.g., $(1+a)^{1/2}\approx 1+a/2$ s.t., $a\ll 1$. Moreover, the n_t-th column of the matrix $\mathbf{H}_\mathrm{LoS}$ can be found as

$$\mathbf{h}_{n_\mathrm{t}}=\exp\Big(j\frac{2\pi}{\lambda}D\Big)\cdot\Big[\exp\Big(-j\frac{2\pi}{\lambda}D_{1n_\mathrm{t}}\Big),\ \ldots,\ \exp\Big(-j\frac{2\pi}{\lambda}D_{N_\mathrm{r}n_\mathrm{t}}\Big)\Big]^T. \tag{2.8}$$

In order to have $\mathbf{H}_\mathrm{LoS}$ orthogonal, the inner product of any two different columns $\mathbf{h}_{n_\mathrm{t}}$ and $\mathbf{h}_{n_\mathrm{t}'}$ is equal to zero, i.e.,

$$\begin{aligned} \mathbf{h}_{n_\mathrm{t}'}^H\mathbf{h}_{n_\mathrm{t}} &= \sum_{n_\mathrm{r}=1}^{N_\mathrm{r}}\exp\Big[j\frac{2\pi}{\lambda}(D_{n_\mathrm{r}n_\mathrm{t}'}-D_{n_\mathrm{r}n_\mathrm{t}})\Big] \\ &= \underbrace{\exp\Big\{j\frac{2\pi}{\lambda}\cdot\frac{[(n_\mathrm{t}'-1)^2-(n_\mathrm{t}-1)^2]d_\mathrm{t}^2}{2D}\Big\}}_{\triangleq A}\cdot\sum_{n_\mathrm{r}=1}^{N_\mathrm{r}}\exp\Big[j\frac{2\pi d_\mathrm{r}d_\mathrm{t}}{\lambda D}(n_\mathrm{t}-n_\mathrm{t}')(n_\mathrm{r}-1)\Big] \\ &= A\cdot\frac{1-\exp\Big[j\frac{2\pi d_\mathrm{r}d_\mathrm{t}}{\lambda D}N_\mathrm{r}(n_\mathrm{t}-n_\mathrm{t}')\Big]}{1-\exp\Big[j\frac{2\pi d_\mathrm{r}d_\mathrm{t}}{\lambda D}(n_\mathrm{t}-n_\mathrm{t}')\Big]} \\ &= A\cdot\exp\Big[j\frac{\pi d_\mathrm{r}d_\mathrm{t}(N_\mathrm{r}-1)(n_\mathrm{t}-n_\mathrm{t}')}{\lambda D}\Big]\cdot\frac{\sin(\frac{\pi d_\mathrm{r}d_\mathrm{t}}{\lambda D}N_\mathrm{r}(n_\mathrm{t}-n_\mathrm{t}'))}{\sin(\frac{\pi d_\mathrm{r}d_\mathrm{t}}{\lambda D}(n_\mathrm{t}-n_\mathrm{t}'))}=0, \end{aligned} \tag{2.9}$$

where A is defined for simplifying the derivation. One solution to (2.9) can be found as

$$d_\mathrm{r}d_\mathrm{t}=\lambda D/N_\mathrm{r}. \tag{2.10}$$

which is also a joint condition on the antenna spacings at Tx and Rx. Similarly, if $N_\mathrm{t}>N_\mathrm{r}$, the rows of $\mathbf{H}_\mathrm{LoS}$ are orthogonal to each other when $d_\mathrm{r}d_\mathrm{t}=\lambda D/N_\mathrm{t}$. In addition, we would like to note that other solutions to (2.9) exist and the one in (2.10) always provides the shortest antenna spacing. Other solutions for a given N_r should also have the numerator in (2.9) being zero, while avoiding the denominator being zero for all n_t, n_t' that $n_\mathrm{t}\neq n_\mathrm{t}'$.[2] For example, when $N_\mathrm{t}=N_\mathrm{r}=2$, more solutions are found with

$$d_\mathrm{r}d_\mathrm{t}=\nu\lambda D/N_\mathrm{r},\quad \nu\in\{1,3,5,7,...\}. \tag{2.11}$$

Next, let us consider a symmetric setup. In this work, we define a symmetric LoS MIMO system as a system with an equal number of antennas at Rx and Tx, i.e., $N\triangleq N_\mathrm{t}=N_\mathrm{r}$ and an equal antenna spacing, i.e., $d_\mathrm{LoS}\triangleq d_\mathrm{r}=d_\mathrm{t}$. For symmetric systems, this antenna spacing,

[2] Otherwise, the L'Hospital's rule would apply, and it gives a non-zero inter product between $\mathbf{h}_{n_\mathrm{t}'}$ and $\mathbf{h}_{n_\mathrm{t}}$.

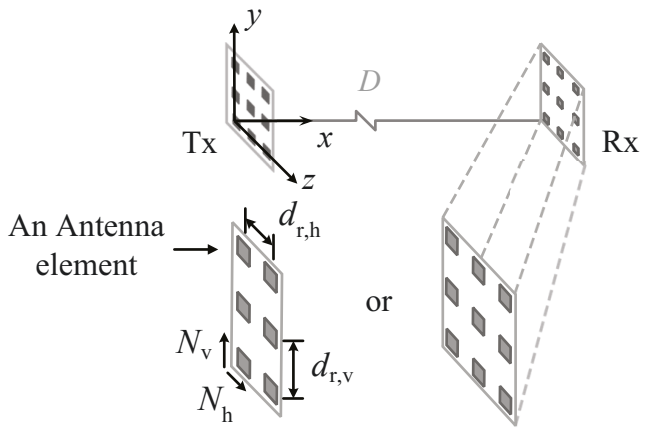

Figure 2.4: A LoS MIMO system with parallel uniform rectangular arrays of $N = N_{\mathrm{v}} \cdot N_{\mathrm{h}}$ elements each side.

which will be intensively used in this thesis, becomes a function of the wavelength, the transmit distance, and the number of antennas as

$$d_{\mathrm{LoS}} = \sqrt{\frac{\lambda D}{N}}. \tag{2.12}$$

Furthermore, the phase coupling matrix $\mathbf{H}_{\mathrm{o}}$ from this optimal arrangement has the property

$$\mathbf{H}_{\mathrm{o}}^{H} \cdot \mathbf{H}_{\mathrm{o}} = N \cdot \mathbf{I}_N, \tag{2.13}$$

which was our design goal. Meanwhile, the entries of $\mathbf{H}_{\mathrm{o}}$ in an optimally arranged symmetric system with parallel ULAs satisfy $\{\mathbf{H}_{\mathrm{o}}\}_{n_{\mathrm{r}} n_{\mathrm{t}}} \approx e^{-j\pi(n_{\mathrm{r}}-n_{\mathrm{t}})^2/N}$, considering (2.7).

As an example, when $N = 3$, $\mathbf{H}_{\mathrm{o}}$ becomes

$$\mathbf{H}_{\mathrm{o}} = \begin{bmatrix} 1 & e^{-j\frac{\pi}{3}} & e^{-j\frac{4\pi}{3}} \\ e^{-j\frac{\pi}{3}} & 1 & e^{-j\frac{\pi}{3}} \\ e^{-j\frac{4\pi}{3}} & e^{-j\frac{\pi}{3}} & 1 \end{bmatrix}. \tag{2.14}$$

Uniform Rectangular Antenna Arrangements: As shown in [Lar05], the orthogonality of LoS MIMO channel can also be achieved with uniform rectangular arrays (URAs), see Fig. 2.4. Assuming that each row has N_{h} antennas along the z-axis and each column of the array has N_{v} antennas along the y-axis, the transceiver arrays consist of $N = N_{\mathrm{h}} \cdot N_{\mathrm{v}}$ elements each. The phase coupling matrix $\mathbf{H}_{\mathrm{LoS}}$ can then be factorized into a Kronecker product of two phase coupling matrices of ULAs along two orthogonal directions as

$$\mathbf{H}_{\mathrm{LoS}} = \mathbf{H}_{\mathrm{LoS,h}} \otimes \mathbf{H}_{\mathrm{LoS,v}}\,, \tag{2.15}$$

where $\mathbf{H}_{\mathrm{LoS,h}}$ and $\mathbf{H}_{\mathrm{LoS,v}}$ denote two phase coupling matrices of ULAs with N_{h} and N_{v} elements, respectively. Therefore, the horizontal and vertical antenna spacings can be independently designed. In case that both the horizontal and vertical arrays satisfy the optimal ULA arrangements in (2.10), $\mathbf{H}_{\mathrm{LoS,h}}$ and $\mathbf{H}_{\mathrm{LoS,v}}$ are then obviously orthogonal matrices and can be denoted as $\mathbf{H}_{\mathrm{oh}}$ and $\mathbf{H}_{\mathrm{ov}}$, respectively. Therefore, the optimal antenna spacing $d_{\mathrm{t,h}},\ d_{\mathrm{r,h}},\ d_{\mathrm{t,v}}$ and

$d_{\mathrm{r,v}}$ of URAs in the horizontal and vertical directions of the parallel planes given by [BOO06] satisfy

$$d_{\mathrm{t,h}} \cdot d_{\mathrm{r,h}} = \frac{\lambda D}{N_{\mathrm{h}}}, \;\; d_{\mathrm{t,v}} \cdot d_{\mathrm{r,v}} = \frac{\lambda D}{N_{\mathrm{v}}}. \tag{2.16}$$

Considering that the Hermitian operation is distributive over the Kronecker product $(\mathbf{A} \otimes \mathbf{B})^H = \mathbf{A}^H \otimes \mathbf{B}^H$ and the mixed-product property of the Kronecker product $(\mathbf{A} \otimes \mathbf{B})(\mathbf{C} \otimes \mathbf{D}) = (\mathbf{AC}) \otimes (\mathbf{BD})$ in [Loa00], the orthogonality still holds for $\mathbf{H}_{\mathrm{o}} = \mathbf{H}_{\mathrm{oh}} \otimes \mathbf{H}_{\mathrm{ov}}$ as

$$\mathbf{H}_{\mathrm{o}}^H \cdot \mathbf{H}_{\mathrm{o}} = (\mathbf{H}_{\mathrm{oh}} \otimes \mathbf{H}_{\mathrm{oh}})^H \cdot (\mathbf{H}_{\mathrm{ov}} \otimes \mathbf{H}_{\mathrm{ov}}) = N_{\mathrm{h}} N_{\mathrm{v}} \cdot \mathbf{I}_{N_{\mathrm{h}} N_{\mathrm{v}}}. \tag{2.17}$$

Non-parallel Arrangements: Above, we have discussed the antenna arrangements on two parallel lines or planes. However, the orthogonality can also be achieved with arrangements on tilted non-parallel lines/planes. In [BOO06], the authors present non-parallel linear and planar solutions. Specifically, the planar array solutions were only known for limited planar rotation directions and the arrays are restricted to URA. In the next chapter, we provide a universal antenna topology solution to LoS MIMO systems. The above discussed arrangement solutions are all found as special cases and the planar antenna topology solutions under any rotation direction are provided, and solutions with 3D structures are also enabled.

MmWave LoS communication: LoS MIMO point-to-point communication at millimeter waves is promising for wireless backhaul systems. Considering the achievable ranks and the associated good condition numbers in (2.13), the LoS spatial multiplexing can multiply the data rates of SISO backhaul links. In addition, due to the small wavelength in (2.12), mmWave wireless communication systems also have reasonable antenna sizes. This may help to utilize such spatial multiplexing gains in practical systems, beyond the power gains achievable with beamforming. As an example, for 60 GHz systems ($\lambda \simeq 5$ mm), (2.12) shows that two linear arrays of a length about 1 m each allow 4 parallel streams for 100 m front-/backhaul communication. The concept of using mmWave frequencies is checked by the channel measurements provided in [HCGL17], which shows a good agreement between theory and practice. In Chapter 5 later, we will present experimental data transmission using LoS MIMO technologies at mmWave frequencies.

2.2.2 The Capacity of Line-of-Sight MIMO Systems

In this part, we discuss the channel capacity with/without channel state information (CSI) at Tx. Here, we always assume the Rx knows the CSI perfectly. Let us use $\mathbf{R}_{\mathbf{s}} \triangleq \mathbb{E}[\mathbf{s}\mathbf{s}^H]$ to denote the covariance matrix of $\mathbf{s}$. Considering a practical system with an average transmit power constraint P_{T}, the relation $\mathrm{tr}(\mathbf{R}_{\mathbf{s}}) \leq P_{\mathrm{T}}$ must hold and $\mathbf{R}_{\mathbf{s}}$ is positive semi-definite.

1) CSI Available at the Tx

The channel capacity with a deterministic $\mathbf{H}$ in (2.4) can be formulated as [Tel99]

$$C = \max_{\substack{\mathbf{R}_{\mathbf{s}}:\, \mathbf{R}_{\mathbf{s}} \succeq \mathbf{0}, \\ \mathrm{tr}(\mathbf{R}_{\mathbf{s}}) \leq P_{\mathrm{T}}}} \log_2 \det(\mathbf{I}_{N_{\mathrm{r}}} + \frac{1}{\sigma_{\mathrm{n}}^2} \cdot \mathbf{H} \cdot \mathbf{R}_{\mathbf{s}} \cdot \mathbf{H}^H), \tag{2.18}$$

where Gaussian signaling with $\mathbf{s}$ following circularly symmetric complex Gaussian distributions is considered here since it is capacity achieving. As proved in [Tel99], Gaussian signaling is the entropy maximizer of $\mathbf{s}$ given $\mathbf{R_s}$. In the case of LoS MIMO communication, we write the channel as $\alpha \cdot \mathbf{H}_{\mathrm{LoS}}$ instead of $\mathbf{H}$. Having the $\mathbf{H}$ perfectly known at Tx, the optimal solution to $\mathbf{R_s}$ can be found by the well known water-filling algorithm [Tel99, CT06]. By doing a singular value decomposition (SVD) to $\mathbf{H} = \mathbf{U}\mathbf{\Sigma}\mathbf{V}^H$, (2.18) can be written as

$$C = \sum_{\eta=1}^{N_{\min}} \log_2 \left(1 + \frac{\sigma_\eta^2}{\sigma_{\mathrm{n}}^2} \cdot \xi_\eta\right), \tag{2.19}$$

where σ_η is the η-th singular value of $\mathbf{H}$, $1 \leq \eta \leq N_{\min}$ and $N_{\min} = \min\{N_{\mathrm{r}}, N_{\mathrm{t}}\}$. Here, ξ_η is the non-negative power allocated to the η-th subchannel. Considering a 'water level' of κ, the ξ_η is found as

$$\xi_\eta = \left[\kappa - \frac{\sigma_{\mathrm{n}}^2}{\sigma_\eta^2}\right]^+ \text{ s.t. } \sum_\eta \xi_\eta = P_{\mathrm{T}}. \tag{2.20}$$

Here, the notation $[\cdot]^+$ denotes $\max(\cdot, 0)$. Then, the solution to $\mathbf{R_s}$ can be found as

$$\mathbf{R_s} = \mathbf{V} \cdot \mathrm{diag}\{\underbrace{[\xi_1, \xi_2, \ldots, \xi_{N_{\min}}, 0, \ldots, 0]^T}_{\in \mathbb{C}^{N_{\mathrm{t}} \times 1}}\} \cdot \mathbf{V}^H. \tag{2.21}$$

With Optimal Arrangements: In the LoS MIMO communication, if the columns or rows of $\mathbf{H}_{\mathrm{LoS}}$ in (2.5) are orthogonal to each other, the $N_{\min}$ parallel subchannels are found of equal quality. This is resulted from the fact that the first $N_{\min}$ non-zero singular values of $\mathbf{H}_{\mathrm{LoS}}$ are of an equal value of $\sqrt{N_{\max}}$, where $N_{\max} = \max\{N_{\mathrm{r}}, N_{\mathrm{t}}\}$. The transmit power is then equally allocated at $N_{\min}$ streams. The channel capacity with optimal arrangements is thus found with an equal power allocation scheme as

$$C_{\mathrm{opt}} = \underbrace{N_{\min}}_{\substack{\text{Spatial} \\ \text{Multiplexing}}} \cdot \log_2 \left(1 + \frac{\alpha^2}{\sigma_{\mathrm{n}}^2} \cdot \underbrace{\frac{N_{\max}}{N_{\min}}}_{\text{Array Gain}} \cdot P_{\mathrm{T}}\right), \tag{2.22}$$

For comparison, the channel capacity of LoS SISO communication, which is an AWGN channel, is given by [Sha48] as

$$C_{\mathrm{SISO}}^{\mathrm{LoS}} = \log_2 \left(1 + \frac{\alpha^2}{\sigma_{\mathrm{n}}^2} \cdot P_{\mathrm{T}}\right) = \log_2 (1 + \gamma), \tag{2.23}$$

where γ denotes the SNR as $\gamma = \alpha^2 P_{\mathrm{T}}/\sigma_{\mathrm{n}}^2$. For the LoS MIMO systems with an equal number of antennas at Tx and Rx, $N_{\mathrm{t}} = N_{\mathrm{r}} = N$ and in the ideal case with full orthogonality, we have $C_{\mathrm{opt}} = N \cdot C_{\mathrm{SISO}}^{\mathrm{LoS}}$.

2) CSI Not Available at the Tx

In the case that $\mathbf{H}_{\mathrm{LoS}}$ is unknown at the Tx, the matrix $\mathbf{R_s}$ that maximizes (2.18) is in general unknown. However, for the case $N_{\mathrm{r}} \geq N_{\mathrm{t}}$, the Tx should expect the subchannels are of equal/nearly equal quality. In high SNR regions, this leads equal power allocation

$\mathbf{R_s} = (P_\mathrm{T}/N_\mathrm{t})\mathbf{I}_{N_\mathrm{t}}$ having similar performance as the optimal one in (2.21). For $N_\mathrm{r} < N_\mathrm{t}$, the setup is not very meaningful. This is because the array gain in (2.22) requires precoding with CSI. In this work, we assume $N_\mathrm{r} \geq N_\mathrm{t}$ with a focus on the case with $N_\mathrm{r} = N_\mathrm{t}$. In the following, we denote $C_\mathrm{MIMO}^\mathrm{LoS}$ as the capacity in the case of equal power uncorrelated transmit signals at different Tx antennas. We refer to $C_\mathrm{MIMO}^\mathrm{LoS}$ as *system capacity*, since we assume that no CSI is available at Tx and in the case uncorrelated Gaussian input signals with equal power are capacity-achieving.

With Equal Power Allocation: Using equal power uncorrelated sources, the channel capacity in (2.18) collapses to the famous equation [FG98, Tel99]

$$C_\mathrm{MIMO}^\mathrm{LoS} = \log_2 \det(\mathbf{I}_{N_\mathrm{r}} + \frac{\gamma}{N_\mathrm{t}} \cdot \mathbf{H}_\mathrm{LoS}\mathbf{H}_\mathrm{LoS}^H), \tag{2.24}$$

where the SNR at each received antenna $\gamma = \alpha^2 P_\mathrm{T}/\sigma_\mathrm{n}^2$ is the same defined as in (2.23). For the LoS MIMO systems with an equal number of antennas at Tx and Rx, $N_\mathrm{t} = N_\mathrm{r} = N$ and in the ideal case with full orthogonality $\mathbf{H}_\mathrm{LoS} = \mathbf{H}_\mathrm{o}$, we have $C_\mathrm{MIMO}^\mathrm{LoS} = C_\mathrm{opt} = N \cdot C_\mathrm{SISO}^\mathrm{LoS}$. Since (2.24) is considerably more amenable to analysis, if one replaces $\mathbf{H}_\mathrm{LoS}$ by a general channel matrix $\mathbf{H}$, this formulation with equal power entries of $\mathbf{s}$ is known in the literature as 'convenient general capacity expression' [FG98]. The formulation in (2.24) is also very widely used as the 'capacity' in LoS MIMO communication works [Lar05, BOO06, BOO05]. In the next section and chapter 4, we will look at the scenario with $\mathbf{H}_\mathrm{LoS}$ unknown at Tx and the uncorrelated signal sources are considered with equal power, i.e., $\mathbf{R_s} = (P_\mathrm{T}/N_\mathrm{t})\mathbf{I}_{N_\mathrm{t}}$. In those cases, to simplify the discussion, the system capacity in (2.24) is used for evaluating the potential spectral efficiency gain.

Besides, we would like to note that the equal power allocation is widely considered for other scenarios like the so-called 'quasi-static' multi-antenna fading channels [FG98] with random fading coefficients and with no CSI at Tx. For example, the entries of the channel matrix are i.i.d Gaussian distributed and stay constant during one burst transmission. Even knowing the distribution of the channel realizations, without CSI at the Tx, the corresponding covariance matrix $\mathbf{R_s}$ is also in general unknown [YDKP14]. For simplification, the equal power allocation to Tx antennas is often assumed, e.g., in [FG98, Tel99, GSS$^+$03, YDKP14].

As described above, LoS MIMO systems rely on the array geometry and the corresponding orthogonality of the phase relationships between antennas. This may cause problems influencing the performance in practice and therefore shall be considered. If the optimal spacing criterion is not fulfilled, e.g., due to implementation tolerances, the orthogonality of the channel is degraded. In spite of that in practical scenarios it is difficult to exactly achieve orthogonality, it has been shown that the system is robust in terms of system capacity against moderate translation and rotation changes [Lar05, SHR$^+$16], when one uses moderate numbers of antennas. This robustness property of the LoS spatial multiplexing will be presented at the mmWave frequencies via numerical evaluations in the next section and can be explained via a mathematical model proposed in Sec. 3.1.

2.3 Robustness Against Displacement Errors

Considering practical systems for mass deployment, such systems should operate with only minor adjustment efforts and displacements are expected to result in limited error ranges. To study

the robustness w.r.t. displacement errors, the author of [Lar05] provided a numerical evaluation based analysis on systems operating at a carrier frequency of 38 GHz. The antenna spacing in that work is optimized for a targeting distance of 1000 m. In order to stay consistent with 60 GHz backhaul systems that are considered through the rest of this thesis, our analysis in this part follows the approach in [Lar05] with different parameter settings.

Antenna Setup and Evaluation Criteria: To simplify the discussion, we consider an equal number of antennas at Tx and Rx, i.e., $N_{\mathrm{t}} = N_{\mathrm{r}} = N$, with an equal spacing in (2.12). Further considering high throughput backhaul systems, we evaluate systems built of URAs which are capable of providing larger numbers of parallel streams, i.e., $N = \{4,\, 9,\, 16,\, 25\}$, in limited spaces than ones built of ULAs. Furthermore, in later evaluation, we assume a carrier frequency of 60 GHz with $\lambda = 5$ mm and a targeting transmit distance of 100 m, to which the antenna spacings are set accordingly. Considering the possible high SNR values of backhaul communication, a SNR value of $\gamma = 20$dB is assumed. To evaluate the relative spatial multiplexing loss, the normalized system capacity $C^{\mathrm{LoS}}_{\mathrm{MIMO}}/C^{\mathrm{LoS}}_{\mathrm{SISO}}/N$ is considered as the evaluation criterion.[3]

Displacement Error Types: The displacement errors of the Rx arrays have 6 degrees of freedom (DoF) as shown in Fig. 2.5. Considering symmetric setups with an equal number of vertical and horizontal antennas $N_{\mathrm{v}} = N_{\mathrm{h}}$, the displacement error types can be further reduced to the following four types for the numerical evaluation:

- Translation errors in the transmit direction (x-axis), annotated as forward and back;
- Translation errors in the y'-(or z'-)axis, annotated as up and down(or left and right);
- Rotation errors around the y'-(or z'-)axis, annotated as yaw (or pitch);
- Rotation errors around the transmit direction (x-axis), annotated as roll.

Fig. 2.6 illustrates the normalized system capacity versus the four different types of displacement errors. It shows that the system capacity of a deterministic LoS MIMO system under optimal/suboptimal antenna arrangements is only weakly sensitive to deviations induced by small tilts or translations, but the LoS MIMO system gets more sensitive with more antenna elements. Taking 90% of the largest normalized system capacity as a reference for analyzing the tolerated displacement errors, a translation error range of $[-13,\, 23]$ m in the transmit direction is allowed, see Fig. 2.6 (a). Meanwhile, the spatial multiplexing is more robust against the translation error in the y'-(or z'-)axis, the rotation error around the y'-(or z'-)axis, and the rotation error around the transmit direction (x-axis) with error ranges of $[-47, 47]$ m, $[-44^\circ, 44^\circ]$, and $[-28^\circ, 28^\circ]$, respectively. Based on the above discussions, we see that, although the exact values of entries $\{\mathbf{H}_{\mathrm{LoS}}\}_{n_{\mathrm{r}}n_{\mathrm{t}}}$ in (2.6) are quite sensitive w.r.t. displacement errors, the spatial multiplexing gain in LoS MIMO communication is nevertheless robust, in the sense that the required antenna arrangements may not need to be achieved with high accuracy.

We must mention here that, the above results are obtained via modeling the antennas with isotropic antenna patterns. In mmWave communication, directive antennas are normally used to overcome the short range limit, but cause troubles with their narrow beamwidth. For example, a minimum V-band antenna gain of 30dBi is recommended by ECC [ECC09] with a half power beamwidth of about 6° [Hil76, Bal05]. Power differences up to several decibels between the different MIMO paths can be observed [HCGL17, HCGL18], when displacement errors, due

[3] The definitions of $C^{\mathrm{LoS}}_{\mathrm{MIMO}}$ and $C^{\mathrm{LoS}}_{\mathrm{SISO}}$ are given in (2.24) and (2.23), respectively.

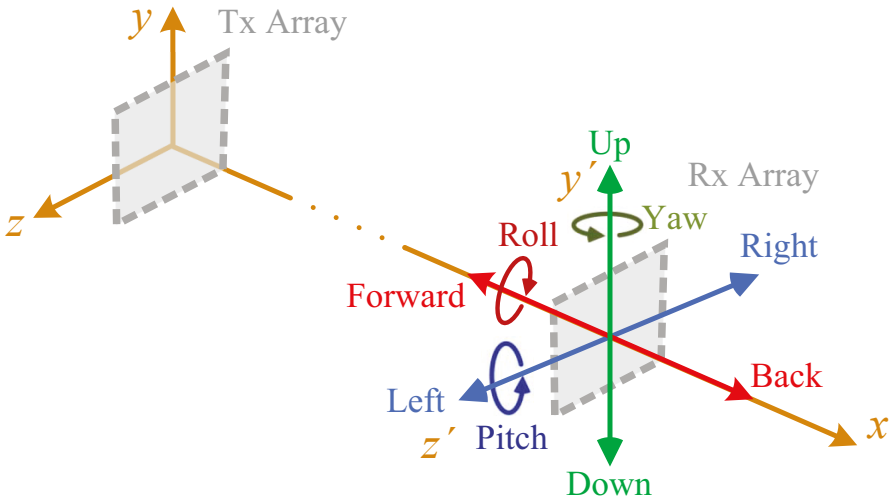

Figure 2.5: The 6 degrees of freedom of displacement errors. (Source: [SCR+18] © 2018 IEEE).

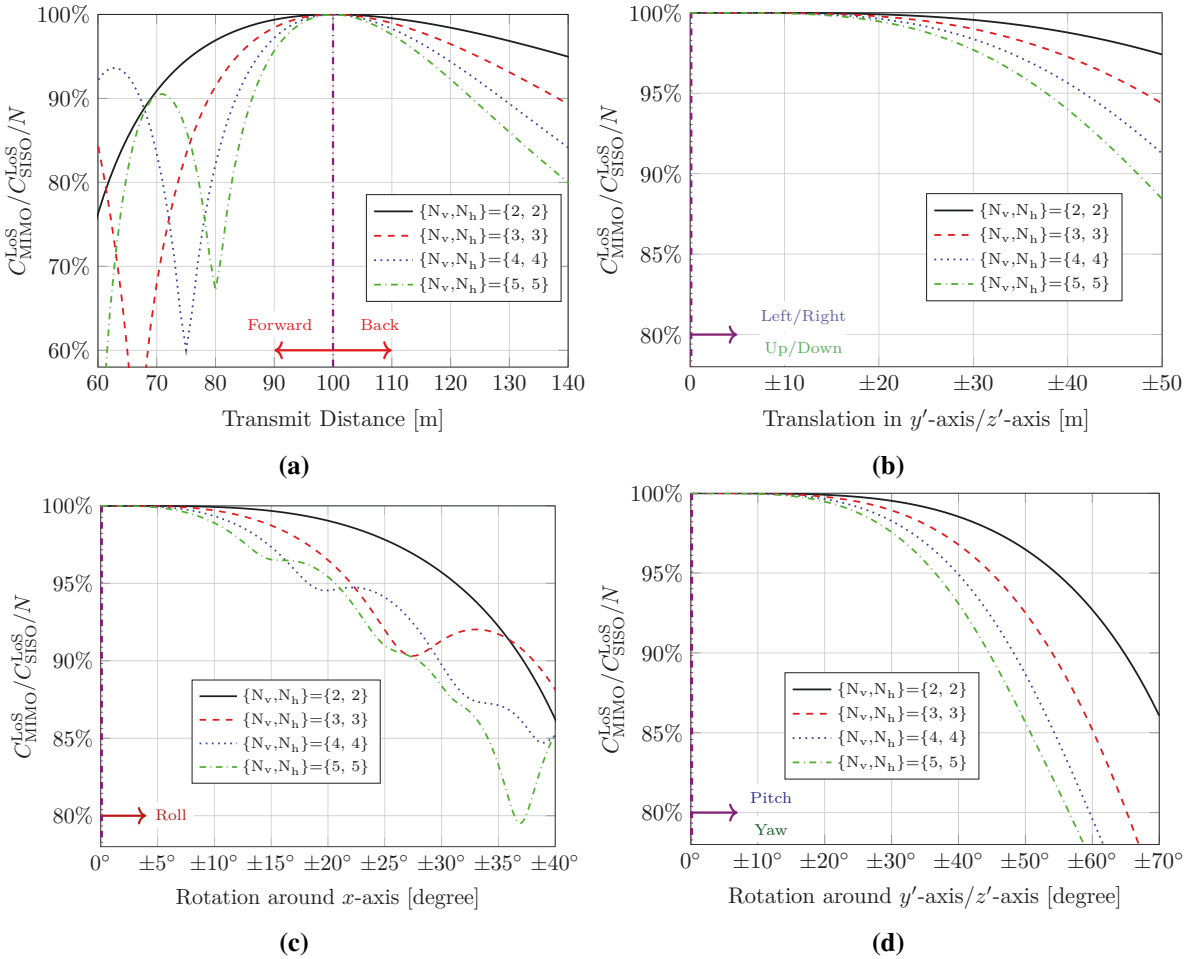

Figure 2.6: The normalized system capacity vs. different displacement error types.

to misalignment or wind, change the radiation pattern significantly. Therefore, considering the efforts needed for beam alignments during deployment, three types of displacement errors including the translation error in the y'-(or z'-)axis, the rotation error around the y'-(or z'-)axis, and the rotation error around the transmit direction (x-axis) would not exceed the tolerable error ranges.

For different deployment scenarios with very different distances, the antenna spacing must be chosen accordingly. Besides using arrays that are resizable/reconfigurable according to (2.12), one can use several fixed arrays for different communication ranges. Furthermore, the works in [TSMR09, ZO13] have proposed non-uniform designs, which achieve better average performance over a wider range of distances, at the cost of reduced maximum throughput, i.e., the channel matrix is not orthogonal. The idea in those works is that one can apply exhaustive search algorithms for finding the antenna arrangements with better average performance at different distances. In the rest of this thesis, we only consider uniform designs, since the translation error range of $[-13,\ 23]$ m in the transmit direction is quite large for the resizable/reconfigurable arrays with an estimated transmit distance of 100 m.

2.4 Summary

This chapter has laid the fundamentals for the LoS spatial multiplexing. In particular, the antenna arrangement dependent LoS MIMO communication relies on the spherical wave propagation, and orthogonal channels can be obtained via the phase couplings between arrays as

$$\mathbf{H}_{\mathrm{o}}^{H} \cdot \mathbf{H}_{\mathrm{o}} = N \cdot \mathbf{I}_{N},$$

which is the most important property of the LoS MIMO channel. In addition, when placing two parallel and symmetric linear/planar arrays at two fixed locations, the antenna spacing is chosen according to the communication distance D, the wavelength λ, and the number of antennas N as

$$d_{\mathrm{LoS}} = \sqrt{\frac{\lambda D}{N}}.$$

Moreover, displacement errors may weaken the LoS spatial multiplexing, but this loss is relatively low with moderate displacement errors during simulation, which indicates relatively strong robustness of this LoS spatial multiplexing. These findings motivate utilizing LoS MIMO technologies at mmWave and even higher frequencies for the data rate critical applications, like wireless front-/backhaul. To build such systems with ultra large bandwidth, we will focus on the antenna topology and low complexity signal processing technologies in the upcoming chapters. In particular, with the mathematical model developed in the next chapter, namely the LoS MIMO channel factorization, we provide a general solution for the antenna topology. In Chapter 4 and 5, we will use this orthogonal property for reducing the complexity in signal processing.

In this chapter, we summarize the key learning points for engineers as:

- LoS MIMO technology offers another degree to increase the spectral efficiency of fixed wireless communication.
- Antennas need to be arranged according to the transmit distance, the carrier frequency and the number of streams.
- In ideal cases, orthogonal channel matrices are obtained, i.e., parallel sub-channels of equal channel quality.

Chapter 3

Line-of-Sight MIMO Evolution

In the last chapter, we have demonstrated that specifically arranged antennas can achieve spatial multiplexing gains under deterministic LoS conditions. We have seen that the system capacity of a deterministic LoS MIMO system under the optimal antenna arrangement is only weakly sensitive to deviations introduced by small tilts or translations. However, for fixed wireless communication with possiblely many different deployment scenarios, alternative antenna topologies on rotated lines and planes [BOO06, ZCZ+12] have not led to a general solution.

In this chapter, we focus on the antenna topology under LoS scenarios including the following contributions:

1. We derive a channel factorization model for LoS MIMO communication in 3D space. The model is a product of three matrices. The two outer factors are diagonal matrices, while the matrix in the middle determines the channel capacity and singular values.

2. Based on the channel factorization model, we show a general geometrical solution from a projection point of view. This solution summarizes the arrangement solutions on non-parallel lines and provides undiscovered planar antenna topology solutions under any rotation direction and 3D solutions. Specifically, the planar array solutions were only known for limited planar rotation directions in the literature.

3. The array response vector with two different antenna spacing orders is investigated. The purpose of this investigation is to study arrays with two different spacings and to keep the math simple with small enough approximation errors.

4. By using two different antenna spacings, a two-level hierarchical MIMO system that combines the spatial multiplexing gain and the beamforming gain is proposed for the mmWave wireless backhaul. Link budgets based on a realistic channel model show that the proposed multi-subarray LoS MIMO system offers the potential of achieving 100 Gbit/s under LoS conditions.

3.1 LoS MIMO Channel Factorization

In this section, the influence of shifting antennas in the transmit direction is investigated. The system under investigation consists of two opposing antenna arrays separated by a distance of

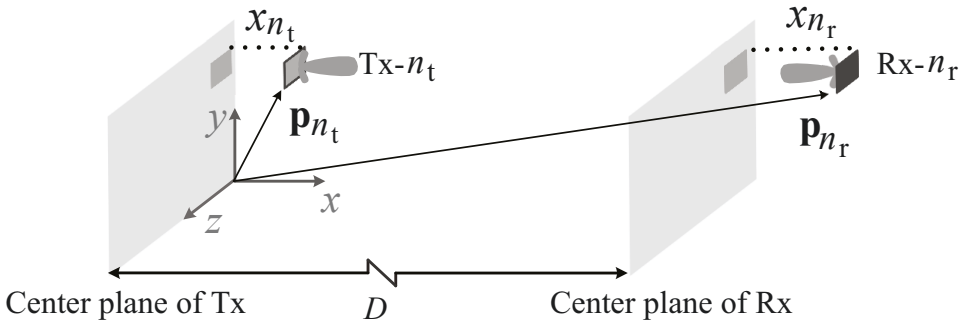

Figure 3.1: 3D Antenna Arrangement Model. (Source: [SF15] © 2015 IEEE).

D. For simplicity, we consider one antenna Tx-n_t of the transmit antenna array and one antenna Rx-n_r of the receive antenna array, as indicated in Fig. 3.1. Additionally, we assume that the phase center of the transmitter antenna array is located at (0, 0, 0) and the transmit direction is along the x-axis. Therefore, the phase center of the receive antenna is located at (D, 0, 0). The positions of the antenna Tx-n_t and Rx-n_r can be described by the vectors

$$\mathbf{p}_{n_\mathrm{t}} = [x_{n_\mathrm{t}}, y_{n_\mathrm{t}}, z_{n_\mathrm{t}}]^T, \;\; \mathbf{p}_{n_\mathrm{r}} = [D + x_{n_\mathrm{r}}, y_{n_\mathrm{r}}, z_{n_\mathrm{r}}]^T, \tag{3.1}$$

where we assume that the additional displacements along transmit direction and the antenna aperture, the area of the projection of the array in the yz-plane, are much smaller than the transmit distance, i.e., $x_{n_\mathrm{t}}, x_{n_\mathrm{r}}, y_{n_\mathrm{t}}, y_{n_\mathrm{r}}, z_{n_\mathrm{t}}, z_{n_\mathrm{r}} \ll D$. The antenna distance $D_{n_\mathrm{r}n_\mathrm{t}}$ between antenna Tx-n_t and Rx-n_r, which determines the entries of the channel matrix and ultimately determines the link performance according to (2.6), may be written as

$$\begin{aligned} D_{n_\mathrm{r}n_\mathrm{t}} &= ||\mathbf{p}_{n_\mathrm{t}} - \mathbf{p}_{n_\mathrm{r}}||_F = \sqrt{(D + x_{n_\mathrm{r}} - x_{n_\mathrm{t}})^2 + (y_{n_\mathrm{r}} - y_{n_\mathrm{t}})^2 + (z_{n_\mathrm{r}} - z_{n_\mathrm{t}})^2} \\ &= (D + x_{n_\mathrm{r}} - x_{n_\mathrm{t}}) \cdot \left[1 + \Big(\frac{y_{n_\mathrm{r}} - y_{n_\mathrm{t}}}{D + x_{n_\mathrm{r}} - x_{n_\mathrm{t}}}\Big)^2 + \Big(\frac{z_{n_\mathrm{r}} - z_{n_\mathrm{t}}}{D + x_{n_\mathrm{r}} - x_{n_\mathrm{t}}}\Big)^2\right]^{\frac{1}{2}}. \end{aligned} \tag{3.2}$$

Applying the first order Taylor expansion to the square root, i.e., $(1+a)^{1/2} \approx 1 + a/2$ if $a \ll 1$, and considering $x_{n_\mathrm{t}}, x_{n_\mathrm{r}}, y_{n_\mathrm{t}}, y_{n_\mathrm{r}}, z_{n_\mathrm{t}}, z_{n_\mathrm{r}} \ll D$, the antenna distance $D_{n_\mathrm{r}n_\mathrm{t}}$ becomes

$$\begin{aligned} D_{n_\mathrm{r}n_\mathrm{t}} &\approx D + x_{n_\mathrm{r}} - x_{n_\mathrm{t}} + \frac{(y_{n_\mathrm{r}} - y_{n_\mathrm{t}})^2}{2(D + x_{n_\mathrm{r}} - x_{n_\mathrm{t}})} + \frac{(z_{n_\mathrm{r}} - z_{n_\mathrm{t}})^2}{2(D + x_{n_\mathrm{r}} - x_{n_\mathrm{t}})} \\ &\approx D + x_{n_\mathrm{r}} - x_{n_\mathrm{t}} + \frac{(y_{n_\mathrm{r}} - y_{n_\mathrm{t}})^2}{2D} + \frac{(z_{n_\mathrm{r}} - z_{n_\mathrm{t}})^2}{2D}. \end{aligned} \tag{3.3}$$

Then, one may write (2.6) as

$$\{\mathbf{H}_\mathrm{LoS}\}_{n_\mathrm{r}n_\mathrm{t}} = e^{-j\frac{2\pi}{\lambda}x_{n_\mathrm{r}}} \cdot e^{-j\frac{2\pi}{\lambda}\frac{(y_{n_\mathrm{r}} - y_{n_\mathrm{t}})^2 + (z_{n_\mathrm{r}} - z_{n_\mathrm{t}})^2}{2D}} \cdot e^{j\frac{2\pi}{\lambda}x_{n_\mathrm{t}}}. \tag{3.4}$$

The channel gain consists of three independent parts including two linear channel gains $e^{j\frac{2\pi}{\lambda}x_{n_\mathrm{t}}}$ and $e^{-j\frac{2\pi}{\lambda}x_{n_\mathrm{r}}}$ caused by the offsets in the transmit direction at Tx and Rx, respectively, and the planar channel gain $e^{-j\frac{2\pi}{\lambda}\frac{(y_{n_\mathrm{r}} - y_{n_\mathrm{t}})^2 + (z_{n_\mathrm{r}} - z_{n_\mathrm{t}})^2}{2D}}$ caused by the antenna arrangement on the plane that is perpendicular to the transmit direction (broadside relative to the transmit direction).

Consequently, when there are offsets along the x-axis (transmit direction), the channel matrix $\mathbf{H}_\mathrm{LoS}$ can directly be decomposed into

$$\mathbf{H}_\mathrm{LoS} = \mathbf{D}_{\parallel,\mathrm{r}} \cdot \mathbf{H}_\perp \cdot \mathbf{D}_{\parallel,\mathrm{t}}, \tag{3.5}$$

where $\mathbf{D}_{\parallel,\mathrm{t}}$, $\mathbf{D}_{\parallel,\mathrm{r}}$ are the diagonal matrices that collect the phase shifts caused by the offsets along the transmit direction at Tx and Rx, respectively, i.e., $\{\mathbf{D}_{\parallel,\mathrm{t}}\}_{n_\mathrm{t}n_\mathrm{t}} \triangleq e^{j\frac{2\pi x_{n_\mathrm{t}}}{\lambda}}$, $n_\mathrm{t} \in [1, N_\mathrm{t}]$, $\{\mathbf{D}_{\parallel,\mathrm{r}}\}_{n_\mathrm{r}n_\mathrm{r}} \triangleq e^{-j\frac{2\pi x_{n_\mathrm{r}}}{\lambda}}$, $n_\mathrm{r} \in [1, N_\mathrm{r}]$. $\mathbf{H}_\perp$ is the channel matrix contributed by the spatial multiplexing on the broadside relative to the transmit direction with $\{\mathbf{H}_\perp\}_{n_\mathrm{r}n_\mathrm{t}} \triangleq e^{-j\frac{2\pi}{\lambda}\frac{(y_{n_\mathrm{r}}-y_{n_\mathrm{t}})^2+(z_{n_\mathrm{r}}-z_{n_\mathrm{t}})^2}{2D}}$.

The role of the x-values is therefore different from the roles of the y- and z-values for capacity calculation. The phase variations caused by the offsets along the transmit direction occur at outer positions. In this case, the channel capacity in LoS MIMO communication in (2.18) is given as

$$\begin{aligned}
C &= \max_{\substack{\mathbf{R}_\mathbf{s}\colon \mathbf{R}_\mathbf{s}\succeq\mathbf{0},\\ \mathrm{tr}(\mathbf{R}_\mathbf{s})\le P_\mathrm{T}}} \log_2\det(\mathbf{I}_{N_\mathrm{r}} + \frac{\alpha^2}{\sigma_\mathrm{n}^2}\cdot\mathbf{D}_{\parallel,\mathrm{r}}\cdot\mathbf{H}_\perp\cdot\underbrace{\mathbf{D}_{\parallel,\mathrm{t}}\cdot\mathbf{R}_\mathbf{s}\cdot\mathbf{D}_{\parallel,\mathrm{t}}^H}_{\triangleq\mathbf{R}_{\tilde{\mathbf{s}}}}\cdot\mathbf{H}_\perp^H\cdot\mathbf{D}_{\parallel,\mathrm{r}}^H)\\
&= \max_{\substack{\mathbf{R}_{\tilde{\mathbf{s}}}\colon \mathbf{R}_{\tilde{\mathbf{s}}}\succeq\mathbf{0},\\ \mathrm{tr}(\mathbf{R}_{\tilde{\mathbf{s}}})\le P_\mathrm{T}}} \log_2\det(\mathbf{I}_{N_\mathrm{r}} + \frac{\alpha^2}{\sigma_\mathrm{n}^2}\cdot\mathbf{D}_{\parallel,\mathrm{r}}\cdot\mathbf{H}_\perp\cdot\mathbf{R}_{\tilde{\mathbf{s}}}\cdot\mathbf{H}_\perp^H\cdot\mathbf{D}_{\parallel,\mathrm{r}}^H)\\
&= \max_{\substack{\mathbf{R}_{\tilde{\mathbf{s}}}\colon \mathbf{R}_{\tilde{\mathbf{s}}}\succeq\mathbf{0},\\ \mathrm{tr}(\mathbf{R}_{\tilde{\mathbf{s}}})\le P_\mathrm{T}}} \log_2\det(\mathbf{I}_{N_\mathrm{r}} + \frac{\alpha^2}{\sigma_\mathrm{n}^2}\cdot\mathbf{H}_\perp\cdot\mathbf{R}_{\tilde{\mathbf{s}}}\cdot\mathbf{H}_\perp^H\cdot\mathbf{D}_{\parallel,\mathrm{r}}^H\cdot\mathbf{D}_{\parallel,\mathrm{r}})\\
&= \max_{\substack{\mathbf{R}_{\tilde{\mathbf{s}}}\colon \mathbf{R}_{\tilde{\mathbf{s}}}\succeq\mathbf{0},\\ \mathrm{tr}(\mathbf{R}_{\tilde{\mathbf{s}}})\le P_\mathrm{T}}} \log_2\det(\mathbf{I}_{N_\mathrm{r}} + \frac{\alpha^2}{\sigma_\mathrm{n}^2}\cdot\mathbf{H}_\perp\cdot\mathbf{R}_{\tilde{\mathbf{s}}}\cdot\mathbf{H}_\perp^H),
\end{aligned} \tag{3.6}$$

where the second equivalent considers that the $\tilde{\mathbf{s}} \triangleq \mathbf{D}_{\parallel,\mathrm{t}}\cdot\mathbf{s}$ has the same power/distribution as $\mathbf{s}$, i.e., $\mathrm{tr}(\mathbf{R}_{\tilde{\mathbf{s}}}) = \mathbb{E}[\tilde{\mathbf{s}}^H\tilde{\mathbf{s}}] = \mathbb{E}[\mathbf{s}^H\mathbf{s}] = \mathrm{tr}(\mathbf{R}_\mathbf{s})$. In addition, the third equivalent follows from determinant identity $\det(\mathbf{I}+\mathbf{AB}) = \det(\mathbf{I}+\mathbf{BA})$. Thus, the capacity of the LoS MIMO channel with CSI at both Tx and Rx is invariant with respect to the offsets in the transmit direction. This is also hold for the system capacity in (2.24) having uncorrelated equal power sources as

$$C_{\mathrm{MIMO}}^{\mathrm{LoS}} = \log_2\det(\mathbf{I}_{N_\mathrm{r}} + \frac{\gamma}{N_\mathrm{t}}\mathbf{H}_\perp\cdot\mathbf{H}_\perp^H). \tag{3.7}$$

Furthermore, the singular value matrix $\mathbf{\Sigma}$ of $\mathbf{H}_{\mathrm{LoS}}$ is equivalent to the singular value matrix $\mathbf{\Sigma}_\perp$ of $\mathbf{H}_\perp$ as

$$\mathbf{H}_{\mathrm{LoS}} = \mathbf{D}_{\parallel,\mathrm{r}}\cdot\underbrace{\mathbf{H}_\perp}_{\text{SVD}}\cdot\mathbf{D}_{\parallel,\mathrm{t}} = \underbrace{\mathbf{D}_{\parallel,\mathrm{r}}\cdot\mathbf{U}_\perp}_{\triangleq\mathbf{U}}\mathbf{\Sigma}_\perp\underbrace{\mathbf{V}_\perp^H\cdot\mathbf{D}_{\parallel,\mathrm{t}}}_{\triangleq\mathbf{V}^H} = \mathbf{U}\mathbf{\Sigma}_\perp\mathbf{V}^H, \tag{3.8}$$

where $\mathbf{H}_\perp = \mathbf{U}_\perp\mathbf{\Sigma}_\perp\mathbf{V}_\perp^H$. $\mathbf{U}$ and $\mathbf{V}$ are still unitary matrices as $\mathbf{U}\mathbf{U}^H = \mathbf{U}^H\mathbf{U} = \mathbf{I}_{N_\mathrm{r}}$ and $\mathbf{V}\mathbf{V}^H = \mathbf{V}^H\mathbf{V} = \mathbf{I}_{N_\mathrm{t}}$.

Projection View: From (3.6), it follows that the capacity of the LoS MIMO channel is invariant with respect to the offsets in the transmit direction, as the singular values of $\mathbf{H}$ are only affected by $\mathbf{H}_\perp$ under the approximation in (3.3). Therefore, only the projection of the antenna topology on the plane that is perpendicular to the transmit direction matters. The optimized solution for point-to-point 2D LoS MIMO transceivers in (2.16) is the best solution for point-to-point LoS MIMO array with possible 3D structures, if one wishes to achieve the highest capacity with a given antenna number.

However, if one considers the projection of the antenna arrangements into multiple directions, 3D antenna structures are promising to provide better solutions. In network based MIMO system with point-to-multipoint LoS communication, e.g. multiple access wireless backhaul, and point-to-point communication with reflection components in limited scattering environments, the projection has to be considered jointly for several directions simultaneously.

Robustness w.r.t. Displacement Errors: As discussed earlier in Sec. 2.3, although the exact values of entries $\{\mathbf{H}_{\mathrm{LoS}}\}_{n_{\mathrm{r}}n_{\mathrm{t}}}$ are quite sensitive w.r.t. displacement errors, the spatial multiplexing gain in LoS MIMO communication is nevertheless robust, in the sense that the required antenna arrangement does not need to be achieved with high accuracy. This can be explained via our channel factorization model in (3.5). The role of x-values is again different from the roles of y- and z-values. In case there are displacements relative to the optimal arrangement, the phase coupling matrix $\mathbf{H}_{\mathrm{LoS}}$ then have mismatches w.r.t. the ideal parallel case $\mathbf{H}_{\mathrm{o}}$ in (2.13), $\mathbf{H}_{\mathrm{LoS}} \neq \mathbf{H}_{\mathrm{o}}$. The dominant phase shifts of $\mathbf{H}_{\mathrm{LoS}}$ are contributed by $\mathbf{D}_{\parallel,\mathrm{r}}$ and $\mathbf{D}_{\parallel,\mathrm{t}}$, which do not influence the orthogonality. For the displacements in the yz-plane, the errors are measured in units of $\sqrt{\lambda D}$ instead of λ. It turns $\mathbf{H}_{\perp}$ into a less sensitive term. Therefore, the LoS spatial multiplexing with spacings like $\sqrt{\lambda D/N}$ in deterministic scenarios has a high robustness. This property, as will be shown with more details in the next chapter, results in possible large complexity reduction when equalizing the LoS MIMO channel.

3.2 3D Optimal Antenna Arrangements

It is obvious from (3.6) and (3.8) that the channel capacity of two 1D or 2D MIMO oblique arrays can be easily obtained via projecting onto the broadside relative to the transmit direction. Thus, the optimal solutions of the antenna spacings under different out-of-plane rotations can also be obtained via mapping the broadside solution for transmit direction back to the plane where the arrays are located.

3.2.1 Uniform Linear Array

In this part, we derive the optimal arrangements for two virtual arrays at arbitrarily rotations, as indicated in Fig. 3.2. Two parallel Cartesian coordinate systems are located at Tx and Rx with origins at the lower ends of the ULAs. The x-axes are both on the line connecting Tx and Rx and are in the direction from Tx to Rx. The Tx array is located in the xy-plane, without loss of generality. Furthermore, the arrays at the Tx and Rx have angles φ_{t} and φ_{r} w.r.t. the y-axes in their local spherical coordinate systems, respectively. Considering (2.10) and mapping

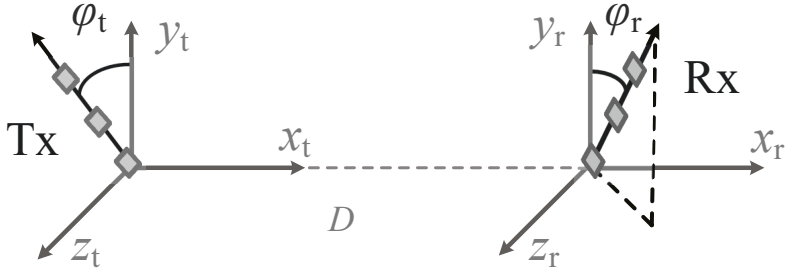

Figure 3.2: ULA solutions on oblique lines. (Source: [SF15] © 2015 IEEE).

the arrangement of the parallel solutions back to the rotated lines, the two arrays are found as ULAs again with spacings d_{t} and d_{r} satisfying

$$d_{\mathrm{t}} \cdot d_{\mathrm{r}} = \frac{\lambda D}{\cos\varphi_{\mathrm{t}} \cos\varphi_{\mathrm{r}} N_{\max}}, \tag{3.9}$$

where $N_{\max} = \max\{N_{\mathrm{r}}, N_{\mathrm{t}}\}$. This solution for linear arrays at arbitrary rotations was first derived differently in [BOO05]. In that work, the derivation is carried out similar to Sec. 2.2. In particular, the positions of antennas on rotated lines are described with an assumption that they are uniformly spaced. Then the condition leading to zero inner products between columns of $\mathbf{H}_{\mathrm{LoS}}$ is derived. For completeness, we present this solution from a projection point of view by using our channel factorization model.

3.2.2 Uniform Planar Array

In this part, the optimal antenna arrangements on the arbitrarily rotated planes that do not contain the transmission direction vector are investigated.

Problem Description: Considering a 2D MIMO system as illustrated in Fig. 3.3, two parallel Cartesian coordinate systems $(x_{\mathrm{t}}, y_{\mathrm{t}}, z_{\mathrm{t}})$ and $(x_{\mathrm{r}}, y_{\mathrm{r}}, z_{\mathrm{r}})$ are constructed at Tx and Rx with origins at the bottom left of the Tx array and the bottom right of the Rx array, respectively. The x-axes are both in direction from Tx to Rx. The y-axes can be chosen freely, for instance, perpendicular to the ground. In the oblique MIMO systems, transceivers are intended to be placed on the targeting planes $\mathrm{P}(u_{\mathrm{x}}^i, u_{\mathrm{y}}^i, u_{\mathrm{z}}^i) \triangleq \{(x_i, y_i, z_i) | \, u_{\mathrm{x}}^i \, x_i + u_{\mathrm{y}}^i \, y_i + u_{\mathrm{z}}^i \, z_i = 0\}$, $u_{\mathrm{x}}^i \neq 0$, $i \in \{\mathrm{t}, \mathrm{r}\}$ and achieving the optimal spatial multiplexing gain. The parameters u_{x}^i, u_{y}^i, u_{z}^i are the x, y and

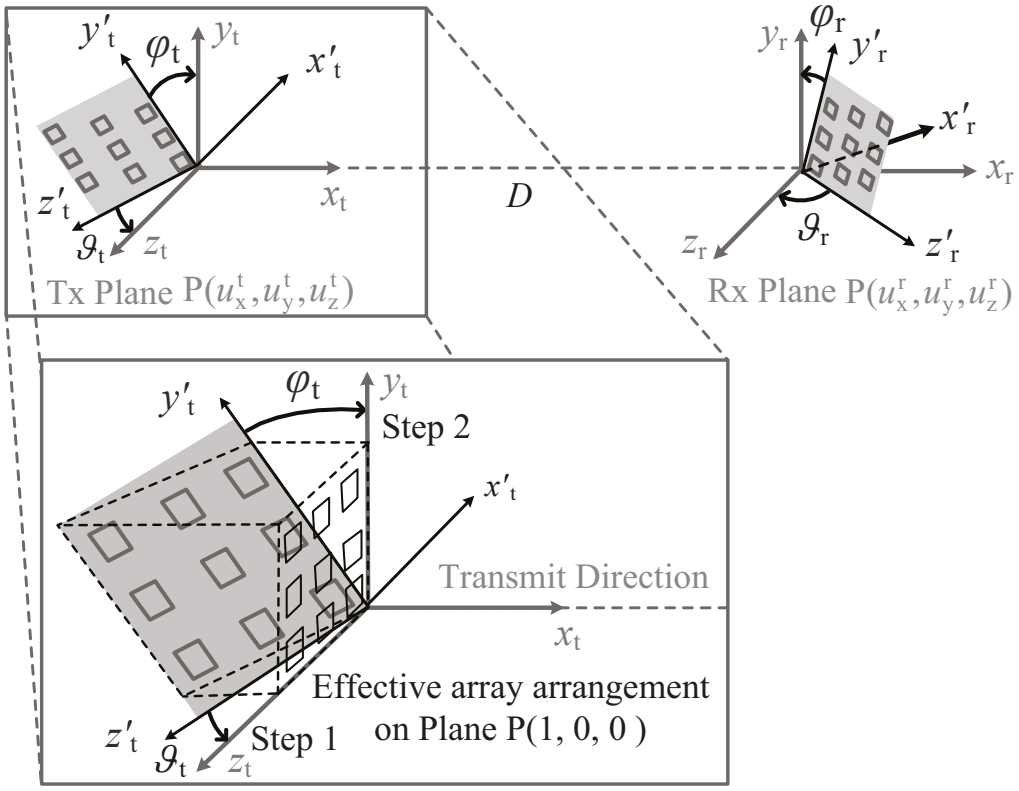

Figure 3.3: Uniform planar array solutions on oblique planes. (Source: [SF15] © 2015 IEEE).

z components of the plane's normal vector in the Cartesian coordinate system (x_i, y_i, z_i), respectively. In this part, besides knowing the equal antenna number $N = N_{\rm h} \cdot N_{\rm v}$ of the Tx and Rx arrays, the transmit distance D, and the wavelength λ, we assume the normal vectors $[u_{\rm x}^i, u_{\rm y}^i, u_{\rm z}^i]^T$ of the Tx and Rx arrays are also known. In the following, the positions of antennas on the targeting plane are derived.

Local Cartesian Coordinate Systems: Two local Cartesian coordinate systems (x_i', y_i', z_i'), $i \in \{{\rm t}, {\rm r}\}$ are defined accordingly with the same origins of the systems (x_i, y_i, z_i). The x_i'-axis is set to be perpendicular to the plane ${\rm P}(u_{\rm x}^i, u_{\rm y}^i, u_{\rm z}^i)$. In the following derivation, we set y_i'-axes as the line where the plane ${\rm P}(u_{\rm x}^i, u_{\rm y}^i, u_{\rm z}^i)$ crosses the $x_i y_i$-plane, while the z_i'-axis is set accordingly. This would simplify the transformations between Cartesian coordinate systems since y_i'-axis is orthogonal to both z_i'-axis and z_i-axis. The transformation from coordinate systems (x_i', y_i', z_i') to (x_i, y_i, z_i) is then found of only two steps, i.e., the rotation around the y_i'-axis and the rotation around z_i'-axis. The overall transformation matrix is modeled as [Kui99]

$$\mathbf{Q}_i(\varphi_i, \vartheta_i) = \mathbf{Q}_{z_i'}(\varphi_i)\mathbf{Q}_{y_i'}(\vartheta_i) = \begin{bmatrix} \cos\varphi_i & \sin\varphi_i & 0 \\ -\sin\varphi_i & \cos\varphi_i & 0 \\ 0 & 0 & 1 \end{bmatrix} \begin{bmatrix} \cos\vartheta_i & 0 & -\sin\vartheta_i \\ 0 & 1 & 0 \\ \sin\vartheta_i & 0 & \cos\vartheta_i \end{bmatrix} \tag{3.10}$$

where $\mathbf{Q}_{y_i'}(\cdot)$ and $\mathbf{Q}_{z_i'}(\cdot)$ are the rotation matrices around the y_i'-axis and z_i'-axis, respectively. Their parameters ϑ_i and φ_i are yaw and pitch angles, respectively, and $-\pi \le \vartheta_i, \varphi_i < \pi$. For the sketch in Fig. 3.3, it is found that $\vartheta_{\rm t}, \varphi_{\rm r} > 0$ and $\varphi_{\rm t}, \vartheta_{\rm r} < 0$.

Rotation Angles: During the deployment, ϑ_i and φ_i can be measured as the angle between z_i'-axis and z_i-axis, and the angle between y_i'-axis and y_i-axis, respectively. In this part, we derive their values in terms of the $y_i'z_i'$-plane's normal vector $\mathbf{u}_{y_i'z_i'} \triangleq [u_{\rm x}^i, u_{\rm y}^i, u_{\rm z}^i]^T$ which satisfies the coordinate transform $\mathbf{u}_{y_i'z_i'} = \mathbf{Q}_i(\varphi_i, \vartheta_i) \cdot [1, 0, 0]^T = [\cos\vartheta_i \cdot \cos\varphi_i, \, -\cos\vartheta_i \cdot \sin\varphi_i, \, \sin\vartheta_i]^T$. Thus, the ϑ_i and φ_i can be obtained via

$$\vartheta_i = \arcsin u_{\rm z}^i, \;\; \varphi_i = -\arctan\frac{u_{\rm y}^i}{u_{\rm x}^i}, \;\; u_{\rm x}^i \neq 0. \tag{3.11}$$

Antenna Locations in the Cartesian Coordinate System (x_i, y_i, z_i): The plane ${\rm P}(u_{\rm x}^i, u_{\rm y}^i, u_{\rm z}^i)$ can be formulated considering that its point (x_i, y_i, z_i) satisfy $[x_i, y_i, z_i] \cdot \mathbf{u}_{y_i'z_i'} = 0$, i.e.,

$$\cos\vartheta_i \cdot \cos\varphi_i \cdot x_i - \cos\vartheta_i \cdot \sin\varphi_i \cdot y_i + \sin\vartheta_i \cdot z_i = 0. \tag{3.12}$$

The parallel URA solutions with equal transceiver antennas, as indicated in (2.16), are located on the $y_i z_i$-plane ${\rm P}(1, 0, 0)$ with normal vector $[1, \, 0, \, 0]^T$. The coordinate of its antenna element $(n_{\rm v}, n_{\rm h})$, $n_{\rm v} \in \{1, \cdots, N_{\rm v}\}$, $n_{\rm h} \in \{1, \cdots, N_{\rm h}\}$ on ${\rm P}(1, 0, 0)$ is

$$[y_i, z_i]_{n_{\rm v} n_{\rm h}}^T = [(n_{\rm v} - 1)d_{i,{\rm v}}, \, (n_{\rm h} - 1)d_{i,{\rm h}}]^T, \; i \in \{{\rm t}, {\rm r}\}, \tag{3.13}$$

where $d_{\rm t,h}$, $d_{\rm r,h}$, $d_{\rm t,v}$ and $d_{\rm r,v}$ should satisfy the relation in (2.16).

By mapping the parallel solution from ${\rm P}(1, 0, 0)$ to ${\rm P}(u_{\rm x}^i, u_{\rm y}^i, u_{\rm z}^i)$ according to (3.12) and see Fig. 3.3, the transceiver coordinates in the Cartesian coordinate system (x_i, y_i, z_i) become

$$\begin{bmatrix} x_i \\ y_i \\ z_i \end{bmatrix}_{n_{\rm v} n_{\rm h}} = \begin{bmatrix} \frac{\cos\vartheta_i \cdot \sin\varphi_i \cdot (n_{\rm v}-1)d_{i,{\rm v}} - \sin\vartheta_i \cdot (n_{\rm h}-1)d_{i,{\rm h}}}{\cos\vartheta_i \cdot \cos\varphi_i} \\ (n_{\rm v} - 1)d_{i,{\rm v}} \\ (n_{\rm h} - 1)d_{i,{\rm h}} \end{bmatrix}. \tag{3.14}$$

Antenna Locations in the Cartesian Coordinate System (x_i', y_i', z_i'): The coordinate of the $(n_{\mathrm{v}}, n_{\mathrm{h}})$-th antenna element on the targeting $y_i'z_i'$-plane are thus found as

$$\begin{bmatrix} x_i' \\ y_i' \\ z_i' \end{bmatrix}_{n_{\mathrm{v}}n_{\mathrm{h}}} = \mathbf{Q}_i^{-1}(\varphi_i, \vartheta_i) \cdot \begin{bmatrix} x_i \\ y_i \\ z_i \end{bmatrix}_{n_{\mathrm{v}}n_{\mathrm{h}}} = \begin{bmatrix} 0 \\ \frac{\cos\vartheta_i \cdot (n_{\mathrm{v}}-1)d_{i,\mathrm{v}} - \sin\vartheta_i \sin\varphi_i \cdot (n_{\mathrm{h}}-1)d_{i,\mathrm{h}}}{\cos\vartheta_i \cdot \cos\varphi_i} \\ (n_{\mathrm{h}}-1)d_{i,\mathrm{h}} / \cos\vartheta_i \end{bmatrix}. \quad (3.15)$$

As shown in [BOO06], self-orthogonal LoS channel matrices are feasible with arrangements on tilted non-parallel lines/planes with limited rotation directions. In particular, when a URA is assumed during the derivation of the orthogonality, it leads to solutions with only limited planar rotation directions, i.e., the rotation around z_i-axis or y_i-axis, but not both. We generalize these results by showing that the second principal direction[1] of the uniform planar array (UPA) is not necessarily orthogonal to the first one as for a URA, because the projection of the optimal orthogonal design onto a tilted plane leads to parallelograms. As can be seen from (3.15), the antenna arrangement should not always be rectangular to achieve the optimal multiplexing gain in a strong LoS MIMO channel. Therefore, (3.15) includes all 2D antenna topology solutions for any 'oblique angle' or 'angular tilt'. Eventually, (2.16) and (3.5) jointly suggest alternative antenna topologies on any arbitrarily curved surface and topologies with even more complicated 3D structures, since only the projection on the plane that is perpendicular to the transmit direction determines the channel capacity in the strong LoS MIMO communication.

3.3 Array Responses at a Given Distance

In this part, we first examine the dependence of array response models on antenna spacing with a general 1×2 single-input-multiple-output system at a given distance. In particular, we will derive the condition for which it can be modeled with the planar wave propagation. Furthermore, considering the approximation applied in (2.7) and (3.3), the applicable region of wave propagation models in terms of antenna spacings is provided here for rigorous analysis. This analysis provides the fundamentals for merging the usage of two different array response models in Sec. 3.4 and Chapter 6.

3.3.1 Wave Models and Antenna Spacings

Since antennas in far-field region act as point sources, we consider spherically propagating electromagnetic waves for individual antenna elements. The transmitter Tx with one antenna is communicating with two isotropic receive antennas as shown in Fig. 3.4 (a). A carrier frequency with a wavelength of λ is used, and the transmitter is D and D' meters away from the two receive antennas Rx-1 and Rx-2, respectively. The spacing between Rx-2 and Rx-1 is denoted by d_{s}. Meanwhile, we assume that λ is much smaller than D and D', i.e., $\lambda \ll \{D, D'\}$. For simplifying later calculations, we introduce the oblique angle θ of the source point w.r.t. the Rx array and also the distance a between Tx and the line connecting the receive antennas. The first receive antenna Rx-1 is b meters away from the projected point so that $D = \sqrt{a^2 + b^2}$. Here, we assume the transceiver arrays do not communicate via their near fire-end directions i.e., $\theta \neq \pi/2$.

[1] The principal direction is defined as the direction along which the antennas are aligned accordingly.

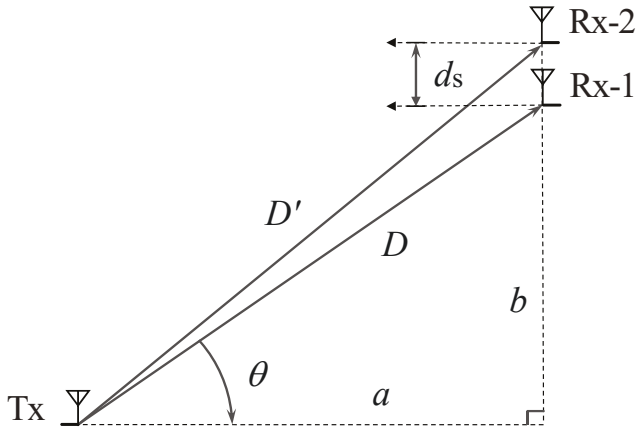

(a) Scenario sketch

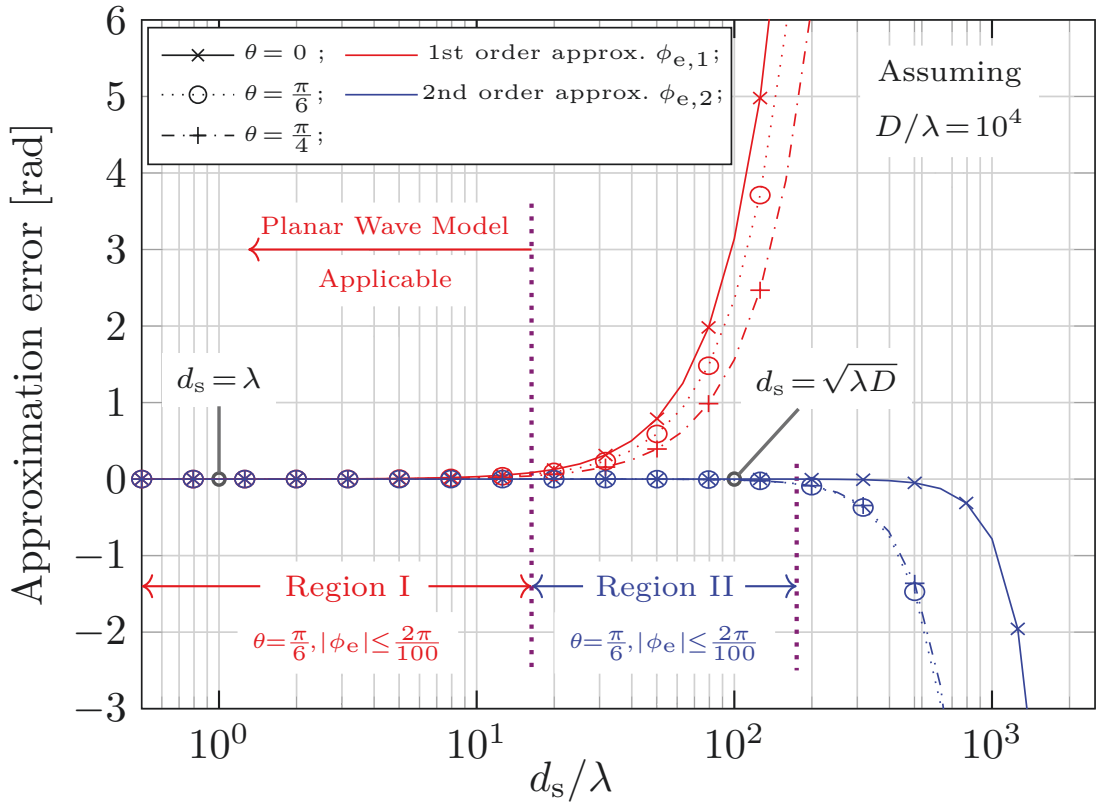

(b) Errors of different approximations

Figure 3.4: Wave Models and Antenna Spacings. For antenna spacings in the order of $\mathcal{O}(\sqrt{\lambda D})$, the planar wave model would be improper and may lose the nice property of possible structured phase couplings. (Source: [SRB+18] © 2018 IEEE).

The phase difference ϕ of the wavefronts arriving at Rx-1 and Rx-2 can be expressed as

$$\begin{aligned}
\phi &= -\frac{2\pi}{\lambda}(D' - D) = -\frac{2\pi}{\lambda}\left[\sqrt{a^2 + (b + d_s)^2} - \sqrt{a^2 + b^2}\right] \\
&= -\frac{2\pi\sqrt{a^2 + b^2}}{\lambda}\left[\left(1 + \frac{2bd_s}{a^2 + b^2} + \frac{d_s^2}{a^2 + b^2}\right)^{1/2} - 1\right] \\
&= -\frac{2\pi\sqrt{a^2 + b^2}}{\lambda}\left[\sqrt{1 + 2\sin\theta\frac{d_s}{\sqrt{a^2 + b^2}} + (\frac{d_s}{\sqrt{a^2 + b^2}})^2} - 1\right].
\end{aligned} \tag{3.16}$$

Applying the Taylor expansion to the square root, ϕ can be written by

$$\phi = -\frac{2\pi\sqrt{a^2+b^2}}{\lambda}\Big[\sin\theta\frac{d_\mathrm{s}}{\sqrt{a^2+b^2}}+\big(\frac{1-\sin^2\theta}{2}\big)\big(\frac{d_\mathrm{s}}{\sqrt{a^2+b^2}}\big)^2-\frac{\sin\theta\cos^2\theta}{2}\big(\frac{d_\mathrm{s}}{\sqrt{a^2+b^2}}\big)^3+\dots\Big]$$
$$\overset{(1)}{=} -\frac{2\pi D}{\lambda}\Big[\sin\theta\big(\frac{d_\mathrm{s}}{D}\big) \;+\; \frac{\cos^2\theta}{2}\big(\frac{d_\mathrm{s}}{D}\big)^2 \;-\; \frac{\sin\theta\cos^2\theta}{2}\big(\frac{d_\mathrm{s}}{D}\big)^3 \;+\; \dots\Big], \tag{3.17}$$

where $\overset{(1)}{=}$ denotes an equality based on the fact that $D=\sqrt{a^2+b^2}$, and we show the expansion up to the third order of d_s/D.

The phase difference ϕ can be approximated differently with different orders of d_s/D. We denote the first order and the second order approximations as

$$\tilde{\phi}_1 = -2\pi\cdot\frac{\sin\theta\, d_\mathrm{s}}{\lambda} \quad \text{and} \quad \tilde{\phi}_2 = -2\pi\big(\frac{\sin\theta\, d_\mathrm{s}}{\lambda}+\frac{\cos^2\theta}{2}\cdot\frac{d_\mathrm{s}^2}{\lambda D}\big), \tag{3.18}$$

respectively. It is noticed that the first-order approximation is the propagation model used by array response vectors under planar wave propagation. Their approximation errors are defined as $\phi_{\mathrm{e},1}\triangleq\phi-\tilde{\phi}_1$ and $\phi_{\mathrm{e},2}\triangleq\phi-\tilde{\phi}_2$. In order to limit the approximation error, we define a term $\phi_{\mathrm{e,max}}$ indicating the maximum allowed phase error, e.g., $\phi_{\mathrm{e,max}}=2\pi/100$, and $|\phi_{\mathrm{e},1}|$, $|\phi_{\mathrm{e},2}|\le\phi_{\mathrm{e,max}}$. This leads to two regions I and II, see Fig. 3.4 (b). In region I, the antenna spacing is less than about 10λ, $d_\mathrm{s}\lessapprox 10\lambda$, and the approximation should contain the first order term in (3.17). While, in region II with $d_\mathrm{s}\lessapprox 100\lambda\in\mathcal{O}(\sqrt{\lambda D})$, the approximation should contain at least the first two order terms in (3.17). For example, the first-order approximation is large in Region II due to the lack of the second-order term $-\pi\cos^2\theta\cdot d_\mathrm{s}^2/(\lambda D)$, which is non-negligible for $d_\mathrm{s}\in\mathcal{O}(\sqrt{\lambda D})$. Motivated by this, the two regions can be quantitatively derived by having the higher order terms of d_s/D equal to $\phi_{\mathrm{e,max}}$ as

$$\text{Region I where } \phi\approx\tilde{\phi}_1 : d_\mathrm{s}\le\sqrt{\frac{\phi_{\mathrm{e,max}}\lambda D}{\pi\cos^2\theta}}. \tag{3.19}$$

$$\text{Region II where } \phi\approx\tilde{\phi}_2 : \sqrt{\frac{\phi_{\mathrm{e,max}}\lambda D}{\pi\cos^2\theta}}<d_\mathrm{s}\le\min\{\sqrt[3]{\frac{\phi_{\mathrm{e,max}}\lambda D^2}{\pi\sin\theta\cos^2\theta}},\sqrt[4]{\frac{4\phi_{\mathrm{e,max}}\lambda D^3}{\pi}}\}. \tag{3.20}$$

Here, we would like to note that the numerical evaluation in Fig. 3.4 (b) also shows that the approximations that keep the second order terms $(d_\mathrm{s}/D)^2$ in (2.7) and (3.3) have enough accuracy in approximating spherical wave propagation for arrays with sizes in Region II. In Sec. 3.4 and Chapter 6, antenna spacings in two different orders are considered, $d_\mathrm{s}\in\mathcal{O}(\lambda)$ and $d_\mathrm{s}\in\mathcal{O}(\sqrt{\lambda D})$. Their applicable wave models are summarized in Proposition 1.

Proposition 1. (Wave Models and Antenna Spacings): If the antenna arrays are separated by D and are communicating at a carrier frequency with a wavelength of λ that is much smaller than D, i.e., $\lambda\ll D$, the first-order approximation of the spherical wave by the planar wave model can be applied if the inter-antenna spacing d_s is in the order of $\mathcal{O}(\lambda)$. For larger antenna spacings $d_\mathrm{s}\in\mathcal{O}(\sqrt{\lambda D})$, the approximation of the spherical wave should be kept up to at least the second order terms in (3.17).

3.3.2 Array Response Vector of an Array of Subarrays

The description of the array response vector following the planar wave model is widely used for simplifying the descriptions of the spatial signature for densely packed antennas. Meanwhile,

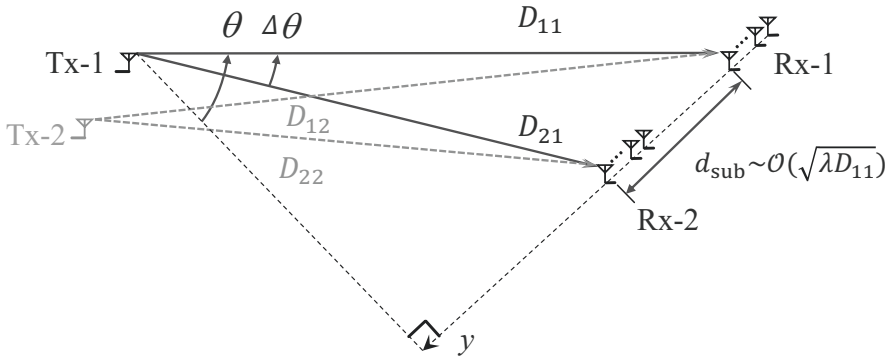

Figure 3.5: Schematic illustration for deriving the array response vector of an array of 2 subarrays. (Source: [SRB+18] © 2018 IEEE).

the specially arranged and widely spaced elements offer LoS spatial multiplexing and can only be considered under the spherical wave model. To combine their benefits together, let us first examine the array response vector of an array having two widely spaced subarrays, where each individual subarray contains densely packed antennas.

An array of subarrays: Here we consider the array response vector of an array of subarrays at Rx, as shown in Fig. 3.5. Two subarrays Rx-1 and Rx-2 have the same antenna structure with M antenna elements being $\lambda/2$ spaced, $d_{\mathrm{e}} = \lambda/2$. Furthermore, we assume that the phase center[2] of the n_{r}-th subarray is separated from the point source Tx-n_{t} by the distance $D_{n_{\mathrm{r}}n_{\mathrm{t}}}$ and $D_{n_{\mathrm{r}}n_{\mathrm{t}}} \gg \lambda$. The two subarrays are aligned along the y-axis and separated by the inter-subarray distance d_{sub} in order of $\mathcal{O}(\sqrt{\lambda D_{11}})$. For simplification, we limit the discussion on the xy-plane of subarrays. Tx-1 is oblique w.r.t. the normal directions of Rx-1 and Rx-2 by azimuth angles θ and $\theta - \Delta\theta$, respectively.

Array response vector: Considering Proposition 1, the subarray response vectors can be approximated by a planar wave model. However, since the subarrays are widely spaced, the spherical wave model should be used to model the relative phase differences of the wave fronts from one direction. Due to the assumptions $D_{11} \gg \lambda$ and $d_{\mathrm{sub}} \in \mathcal{O}(\sqrt{\lambda D_{11}})$, it is found that $D_{11} \gg d_{\mathrm{sub}} \gg \lambda$. This leads to a negligible difference between AoAs at different subarrays, i.e., $\Delta\theta \approx 0$. Therefore, by collecting array response vectors at the subarray level, the array response vector $\mathbf{a}_1$ of an array of subarrays w.r.t. Tx-1 can be written as

$$\mathbf{a}_1 = [e^{-j\frac{2\pi}{\lambda}\cdot D_{11}} \cdot \mathbf{a}_{\mathrm{r}}^T(\theta),\, e^{-j\frac{2\pi}{\lambda}\cdot D_{21}} \cdot \mathbf{a}_{\mathrm{r}}^T(\theta)]^T = [e^{-j\frac{2\pi}{\lambda}\cdot D_{11}},\, e^{-j\frac{2\pi}{\lambda}\cdot D_{21}}]^T \otimes \mathbf{a}_{\mathrm{r}}(\theta). \tag{3.21}$$

The vector $\mathbf{a}_{\mathrm{r}}(\theta) \in \mathbb{C}^{M\times 1}$ denotes the array response vector under planar wave assumption as [Bal05]

$$\mathbf{a}_{\mathrm{r}}(\theta) = \left[1,\, \ldots,\, e^{-jk_\lambda d_{\mathrm{e}}(m-1)\sin\theta},\, \ldots,\, e^{-jk_\lambda d_{\mathrm{e}}(M-1)\sin\theta}\right]^T, \tag{3.22}$$

where $k_\lambda \triangleq 2\pi/\lambda$. The parameter m, $1 \le m \le M$, is the index of an antenna within the subarray.

Similarly, considering a scenario with two transmitters Tx-1 and Tx-2, which are separated by a distance in the order of $\mathcal{O}(\sqrt{\lambda D_{11}})$, we have the phase coupling matrix as

$$\mathbf{H} = \begin{bmatrix} e^{-j\frac{2\pi}{\lambda}\cdot D_{11}} & e^{-j\frac{2\pi}{\lambda}\cdot D_{12}} \\ e^{-j\frac{2\pi}{\lambda}\cdot D_{21}} & e^{-j\frac{2\pi}{\lambda}\cdot D_{22}} \end{bmatrix} \otimes \mathbf{a}_{\mathrm{r}}(\theta), \tag{3.23}$$

which can be seen as a generalization of (2.6).

[2] The subarray's phase center is set at its lower end.

3.4 Multi-Subarray LoS MIMO System

In this section, the parameters for designing a mmWave LoS MIMO system are evaluated.[3] The array response vector of an array of subarrays, as being derived above, will be used to model the channel. The transmission rate is evaluated accordingly to the Equivalent Isotropically Radiated Power (EIRP) regulations that can be used in a practical system. Furthermore, due to the ultra-high link budgets, LoS MIMO spatial multiplexing becomes a promising technology in enhancing the throughput of the fixed wireless communication. In this section, the computations are carried out based on a realistic channel model taking into account: free space path loss, oxygen absorption, rain attenuation, front-end loss, antenna gains of identical antenna elements, array gain, thermal noise, noise figure, etc.

3.4.1 Antenna Array Design

As discussed above, mmWave band is a suitable candidate for enhancing the throughput due to its large available bandwidth. However, high pathloss is one critical limitation of utilizing the mmWave band [Fri46]. Having directive antennas and/or applying beamforming for array power gains are widely considered in overcoming the short range limitation [HGPR$^+$16]. In this part, we investigate the potential of systems deploying the aforementioned LoS spatial multiplexing on top of the array power gain.

We are considering a two-level hierarchical MIMO system with a strong LoS channel model as illustrated in Fig. 3.6 (a). On the higher level, this is a MIMO system that contains N_t and N_r subarrays at Tx and Rx, respectively, to exploit the spatial multiplexing gain in deterministic channels. In this work, the array of several widely spaced subarrays is named 'super-array'. The lower level refers to the architecture of the subarrays. As an example, all subarrays are modeled as uniform square arrays that consist of $M \times M$ $\lambda/2$-spaced antenna elements each. The function of the subarrays is to provide a certain antenna gain and directivity of the transmission which makes the assumption of strong LoS channel more realistic in practical applications like wireless backhaul. In order to use the subarray response vector under planar wave modeling, we assume $M \cdot d_\mathrm{e} \ll \sqrt{\lambda D}$, where $d_\mathrm{e} = \lambda/2$ is the spacing between antenna elements within a subarray.

Under the assumption that the subarray spacings are much smaller than the transmit distance D, the channel between equally polarized n_t-th transmit subarray and n_r-th receive subarray is modeled as

$$\mathbf{H}_{n_\mathrm{r} n_\mathrm{t}} = \mathbf{a}_\mathrm{r}(\theta_\mathrm{r}, \phi_\mathrm{r}) \cdot \alpha(D) e^{-j\frac{2\pi}{\lambda}(D_{n_\mathrm{r} n_\mathrm{t}} - D)} \cdot \mathbf{a}_\mathrm{t}^H(\theta_\mathrm{t}, \phi_\mathrm{t}), \tag{3.24}$$

where $\alpha(D)$ is the common channel gain of the LoS path, θ_r (ϕ_r) and θ_t (ϕ_t) are its azimuth (elevation) angles of arrival and departure, respectively. $D_{n_\mathrm{r} n_\mathrm{t}}$ denotes the propagation link distances between the phase centers of the corresponding subarrays. $\mathbf{a}_\mathrm{t}(\theta_\mathrm{t}, \phi_\mathrm{t}) \in \mathbb{C}^{M^2 \times 1}$ and $\mathbf{a}_\mathrm{r}(\theta_\mathrm{r}, \phi_\mathrm{r}) \in \mathbb{C}^{M^2 \times 1}$ denote the array response vectors at Tx and Rx, respectively. In the case that the normal vector of the array is along x'-axis with M elements on both y'-axis and z'-axis, as shown in Fig. 3.6 (b), the array response vector $\mathbf{a}_\mathrm{t}(\theta_\mathrm{t}, \phi_\mathrm{t})$ at Tx under the planar wave model

[3] In this part, 100 m is considered as an exemplary transmit distance for the small-cell backhaul communication.

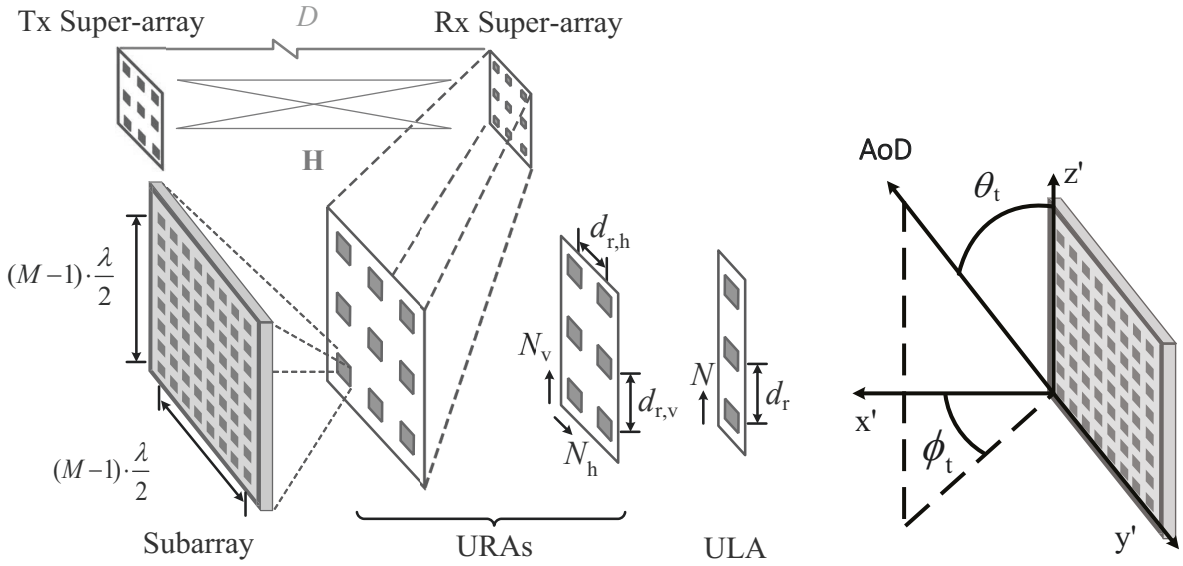

(a) Super-arrays and Subarrays **(b)** Steering Vector Model

Figure 3.6: A Multi-Subarray LoS MIMO System. (Source: [SJL+15] © 2015 IEEE).

is given by

$$\mathbf{a}_{\mathrm{t}}(\theta_{\mathrm{t}},\phi_{\mathrm{t}}) = \left[1,\ \ldots,\ e^{-jk_\lambda d_{\mathrm{e}}((M-1)\sin\theta_{\mathrm{t}}\sin\phi_{\mathrm{t}}+(M-1)\cos\phi_{\mathrm{t}})}\right]^T, \tag{3.25}$$

where $k_\lambda \triangleq 2\pi/\lambda$, and $d_{\mathrm{e}} = \lambda/2$ denotes the antenna spacing at subarrays. The $\mathbf{a}_{\mathrm{r}}(\theta_{\mathrm{r}},\phi_{\mathrm{r}})$ at Rx is formulated in a similar fashion.

Therefore, the channel matrix between different subarrays is found as

$$\mathbf{H} = \begin{bmatrix} \mathbf{H}_{11} & \cdots & \mathbf{H}_{1N_{\mathrm{t}}} \\ \vdots & \ddots & \vdots \\ \mathbf{H}_{N_{\mathrm{r}}1} & \cdots & \mathbf{H}_{N_{\mathrm{r}}N_{\mathrm{t}}} \end{bmatrix} = \left[\alpha(D)\cdot\mathbf{H}_{\mathrm{LoS}}\right] \otimes \left[\mathbf{a}_{\mathrm{r}}(\theta_{\mathrm{r}},\phi_{\mathrm{r}})\cdot\mathbf{a}_{\mathrm{t}}^H(\theta_{\mathrm{t}},\phi_{\mathrm{t}})\right], \tag{3.26}$$

where $\mathbf{H}_{\mathrm{LoS}}$ is the same matrix as in (2.6). Since the matrix to the right of the Kronecker product in (3.26) is of a rank one, achieving maximum spatial multiplexing given a certain number of subarrays turns into the same problem as maximizing the determinant of $\mathbf{H}_{\mathrm{LoS}}$ as in Sec. 2.2. Therefore, the solution is to arrange the subarrays according to the rule of LoS MIMO antenna arrangements. In addition, we would like to note that putting subarrays close to each other would limit the achievable spatial multiplexing gain. Furthermore, another important benefit of replacing highly directive antennas in conventional LoS MIMO systems with subarrays is that the narrow beams can be better aligned due to the beam steering capability at the lower level.

3.4.2 A Link Budget Model

In this part, we assume that the Tx array and the Rx array are facing each other and are arranged symmetrically with $N = N_{\mathrm{t}} = N_{\mathrm{r}} = N_{\mathrm{h}} \cdot N_{\mathrm{v}}$. The subarray spacings satisfy the requirements for optimally arranging the LoS MIMO systems in (2.12) and (2.16). Considering analog beamsteering towards the transmit direction at each subarray, the system allows an acceptable computational complexity on the higher level to fully exploit the spatial multiplexing gain.

Parameters	W	T_{K}	$\alpha(D)^2$		
	Bandwidth 802.11ay	Absolute Temperature	Free Space Path Loss [Fri46]	Oxygen Absorption [SC97]	Rain Absorption [SC97]
Value	2.16 GHz	293 K	$(4\pi D/\lambda)^2$	15dB/km	18dB/km
Parameters	σ_{n}^2		$g_{\mathrm{Tx}}^2(M)$, $g_{\mathrm{Rx}}^2(M)$		
	Thermal Noise	Noise Figure	Array Gain	Antenna Gain [KLN+11]	Front End Loss [KLN+11]
Value	$k_{\mathrm{B}}T_{\mathrm{K}}W$	5dB	M^2	6dBi	2dB

Table 3.1: Link Budget Parameters

One may write the received signal on the higher level as

$$\mathbf{y} \;=\; g_{\mathrm{Rx}}(M)\cdot g_{\mathrm{Tx}}(M)\cdot \alpha(D)\cdot \mathbf{H}_{\mathrm{LoS}}\cdot \mathbf{s}+\mathbf{n}, \tag{3.27}$$

where $g_{\mathrm{Tx}}(M)$, $g_{\mathrm{Rx}}(M)$ are the subarray beamforming gains at the Tx and Rx, respectively. Here, we recall that $\mathbf{n}$ is complex white Gaussian noise vector with $\mathbf{n}\sim\mathcal{CN}^{N\times 1}(0,\sigma_{\mathrm{n}}^2\mathbf{I}_N)$. Further assuming that i.i.d. Gaussian symbols are transmitted, i.e., $\mathbf{s}\sim\mathcal{CN}^{N\times 1}(0,\sigma_{\mathrm{s}}^2\mathbf{I}_N)$, the maximum data rate of such a system can be found as

$$\begin{aligned} R &= W\cdot\log_2\det\left[\mathbf{I}_N+\frac{[g_{\mathrm{Rx}}(M)\cdot g_{\mathrm{Tx}}(M)\cdot\alpha(D)]^2\cdot\sigma_{\mathrm{s}}^2}{\sigma_{\mathrm{n}}^2}\mathbf{H}_{\mathrm{LoS}}\mathbf{H}_{\mathrm{LoS}}^H\right] \\ &= N\cdot W\cdot\log_2\left[1+\frac{[g_{\mathrm{Rx}}(M)\cdot g_{\mathrm{Tx}}(M)\cdot\alpha(D)]^2\cdot N\sigma_{\mathrm{s}}^2}{\sigma_{\mathrm{n}}^2}\right], \end{aligned} \tag{3.28}$$

where W denotes the bandwidth. To simplify later discussions, the effective SNR γ of the parallel streams is defined as $\gamma\triangleq[g_{\mathrm{Rx}}(M)\cdot g_{\mathrm{Tx}}(M)\cdot\alpha(D)]^2\cdot N\sigma_{\mathrm{s}}^2/\sigma_{\mathrm{n}}^2$. In addition, the transmit power is found as $P_{\mathrm{T}}=N\cdot\sigma_{\mathrm{s}}^2$.

Link Budget Parameters: In this work, we consider the mmWave communication at 60 GHz. The unlicensed 60 GHz band is a suitable candidate for fully exploiting the spatial multiplexing gains in LoS MIMO channels due to its large available bandwidth, channel sparsity, and reasonable array sizes. Communication in the 60 GHz region suffers from high atmospheric attenuation (e.g., oxygen absorption) and rain attenuation which must be taken into account for the link budget calculation. Further considering the possible front-end loss and the antenna gain at individual antennas, the parameters[4] in Tab. 3.1 are used for estimating $g_{\mathrm{Rx}}(M), g_{\mathrm{Tx}}(M), \alpha(D)$ and σ_{n}^2 at 60 GHz, where $k_{\mathrm{B}}=1.380649\cdot10^{-23}\mathrm{J/K}$ is the Boltzmann constant, and T_{K} is the absolute temperature in Kelvin.

EIRP Constraints: The EIRP limit regulates the emission to avoid harmful interference to authorized radio services in the band. The EIRP limit for 60 GHz devices located outdoors has been amended to the following: 'The average EIRP limit from $40\mathrm{dBm}$ to $82\mathrm{dBm}$ minus $2\mathrm{dB}$ for every dB that the antenna gain is below $51\mathrm{dBi}$' [FCC13][5]. That means the EIRP limit P_{eirp}

[4] The rain absorption value is taken at the rainfall rate of $50\,\mathrm{mm/hour}$.

[5] The peak EIRP limit is also amended with $3\ \mathrm{dBm}$ addition to the average EIRP limit. For modulated signals with peak-to-average power ratios higher that $3\ \mathrm{dB}$, the maximal transmit power should be further restricted. In this work, we neglect the possible degradation of the radiated power due to the high PAPR caused by the modulation schemes to provide an upper bound to the data rates.

Index	$N = N_{\mathrm{v}} \cdot N_{\mathrm{h}}$	M^2	$R\,[\mathrm{Gbit/s}]$	$\gamma[\mathrm{dB}]$	BPCU	$P_{\mathrm{T}}[\mathrm{dBm}]$	Height×Width
1	1	4^2	13.2	18.3	6.1	26	$7.5\mathrm{mm} \times 7.5\mathrm{mm}$
2	$4 = 2 \cdot 2$	4^2	52.8	18.3	24.4	26	$0.50\mathrm{m} \times 0.50\mathrm{m}$
3	$9 = 3 \cdot 3$	4^2	118.8	18.3	54.9	26	$0.82\mathrm{m} \times 0.82\mathrm{m}$
4	$16 = 4 \cdot 4$	4^2	211.2	18.3	87.6	26	$1.06\mathrm{m} \times 1.06\mathrm{m}$
5	$4 = 2 \cdot 2$	8^2	69.9	24.3	32.3	19.9	$0.50\mathrm{m} \times 0.50\mathrm{m}$
6	$16 = 4 \cdot 4$	8^2	279.3	24.3	129.3	19.9	$1.06\mathrm{m} \times 1.06\mathrm{m}$
7	$4 = 2 \cdot 2$	16^2	87.0	30.4	40.3	13.9	$0.50\mathrm{m} \times 0.50\mathrm{m}$
8	$16 = 4 \cdot 4$	16^2	347.3	30.4	160.8	13.9	$1.06\mathrm{m} \times 1.06\mathrm{m}$

Table 3.2: Example Parameters of Wireless Backhaul Systems under EIRP limit at a transmit Distance of 100 m.

in terms of dBm for 60 GHz devices located outdoors can be formulated as

$$P_{\mathrm{eirp}}[\mathrm{dBm}] \triangleq \max\Big[\min\big[82 - 2(51 - g_{\mathrm{Tx}}^2[\mathrm{dBi}]), 82\big], 40\Big]\ \mathrm{dBm}. \tag{3.29}$$

The maximum transmit power P_{T} that can be used is therefore constrained by the EIRP limit and can be calculated as:

$$P_{\mathrm{T}}[\mathrm{dBm}] = P_{\mathrm{eirp}}[\mathrm{dBm}] - g_{\mathrm{Tx}}^2[\mathrm{dBi}]. \tag{3.30}$$

In the following discussion, we set $P_{\mathrm{eirp}} = 40$dBm, since no super directive subarray is used.

Link Budget Results: Several link budgets at 100 m based on the model described above are exemplified in Tab. 3.2 with several typical and moderate parameter settings on N and M^2. It is worth to note that with LoS spatial multiplexing, the spectral efficiency has the potential of reaching one hundred bits per channel use (BPCU). Considering the degradation of the system due to effects like RF impairments and possible high peak-to-average power ratio (PAPR) values, the system should be designed in a reasonable size with high throughput including some redundancy. Further considering that high SNR values require hardware impairments to be low, which may leads high costs, system setups with indices from 2 to 6 in Tab. 3.2 are then the most interesting ones at 100 meters in setting up connections in the order of 100 Gbit/s. The maximum width and height of the arrays are not larger/much larger than 1 meter. Meanwhile, they are operating at SNR values without ultra-high quality requirements on the hardware, which may potentially reduce the cost. Most importantly, these setups can reach link budgets in the order of 100 Gbit/s, i.e., at least about 52.8 Gbit/s using one 2.16 GHz channel at 60 GHz, which can be further scaled by using other resources. For example, the maximum data rates in the table can be doubled by expanding the system with cross-polarized antennas, but a signal-to-interference-plus-noise ratio (SINR) ceiling should be expected due to the non-ideal polarization separation. Furthermore, IEEE 802.11ay [GSCK17] allows channel bonding mechanisms for four of those 2.16 GHz channels around 60 GHz, which can scale the throughput as well.

Beam Pattern and Angular Spread of Subarrays: In earlier parts of this section, an approximation is considered via assuming the subarray beamforming gains $g_{\mathrm{Tx}}(M)$ and $g_{\mathrm{Rx}}(M)$ are the same for different subarray pairs. Here, we would like to provide a brief examination on the beampattern of the subarrays with different antenna numbers. Let us consider a symmetric uniform linear multi-subarray system with N_{v}-subarrays being vertically arranged. Under an optimal arrangement, the subarray spacing is found as $d_{\mathrm{v}} = \sqrt{\lambda D / N_{\mathrm{v}}}$, see Fig. 3.7. Meanwhile,

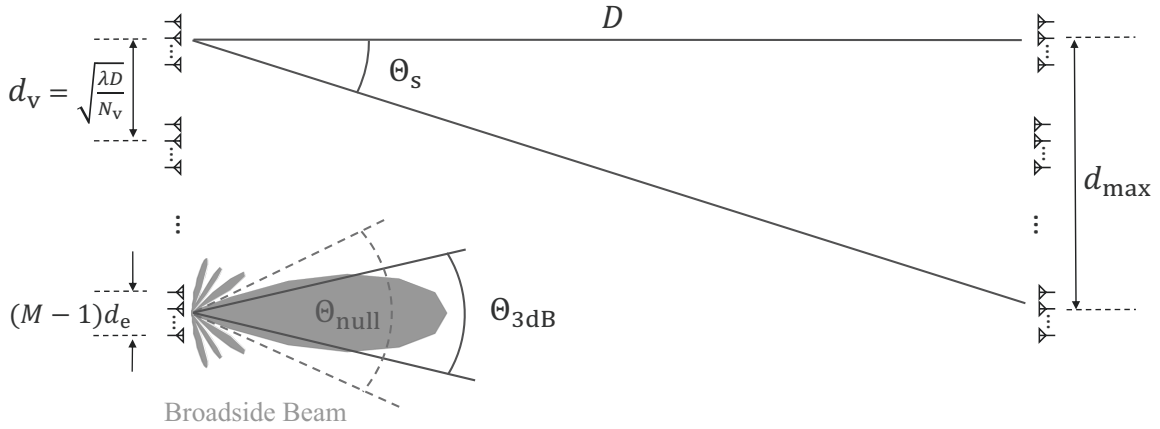

Figure 3.7: Beam pattern and angular spread of subarrays.

M isotropic antenna elements are assumed for each subarray and are also arranged vertically. In this thesis, we consider only a small number of subarrays in one dimension, e.g., $N_\mathrm{v} \leq 5$. To simplify the discussion later and with a small N_v, we rewrite the assumption $Md_\mathrm{e} \ll \sqrt{\lambda D}$ as $Md_\mathrm{e} \ll \sqrt{\lambda D/N_\mathrm{v}}$ without loss of generality.

Let us first exam the angular spread of the subarrays in the LoS direction. The largest dimension of the super-array is about $d_\mathrm{max} \triangleq d_\mathrm{v} \cdot (N_\mathrm{v} - 1) < \sqrt{\lambda D N_\mathrm{v}}$. Considering the subarray at the edge of the super-array and that $d_\mathrm{v} \ll D$, the angular spread $\Theta_\mathrm{s} > 0$ of subarrays on the other side of the link would satisfy $\sin\Theta_\mathrm{s} \approx \tan\Theta_\mathrm{s} = d_\mathrm{max}/D < \sqrt{\lambda N_\mathrm{v}/D}$. In addition, according to the characteristics of the broadside beam pattern presented in [Bal05, Hil76], its half power beamwidth Θ_3dB is found with a relation $\sin(\Theta_\mathrm{3dB}/2) \approx 0.44\lambda/(Md_\mathrm{e}) \gg \sqrt{\lambda N_\mathrm{v}/D} > \sin\Theta_\mathrm{s}$. Then, since $\Theta_\mathrm{3dB} \gg \Theta_\mathrm{s}$, we can ignore the subarray power gain differences under the condition that $Md_\mathrm{e} \ll \sqrt{\lambda D/N_\mathrm{v}}$. When one increases M and keeps d_e constant (this would increases the aperture of the subarray as a single radiation source), the approximation error of using planar wave modeling gets larger and Θ_3dB gets smaller. In the extreme case when two subarrays connect to each other, i.e., $Md_\mathrm{e} = \sqrt{\lambda D/N_\mathrm{v}}$, the channel should be modeled with spherical waves between different antenna pairs in the first place. Meanwhile, the first-null beamwidth in the far-field (at distances further than D) would satisfy $\sin(\Theta_\mathrm{null}/2) \approx \lambda/(Md_\mathrm{e}) = \sqrt{\lambda N_\mathrm{v}/D} > \sin\Theta_\mathrm{s}$ [Bal05]. Therefore, for systems with ultra-large subarrays, all subarrays are still working within the main lobe of the broadside beam.

3.5 Summary

In this chapter, we have first derived the channel factorization model for LoS MIMO communication in (3.5) as

$$\mathbf{H}_\mathrm{LoS} = \mathbf{D}_{\parallel,\mathrm{r}} \cdot \mathbf{H}_\perp \cdot \mathbf{D}_{\parallel,\mathrm{t}}.$$

The two outer diagonal matrices, respectively on the right and left hand side, do not influence the channel capacity and singular values. Subsequently, from a projection point of view, we prove that the capacity of a strong point-to-point LoS MIMO channel is invariant with respect to the third dimension of the array structure. In particular, the aperture of the array in broadside relative to transmit direction determines the performance. This proof leads to two other interest-

ing conclusions. Firstly, the optimized solutions for the 2D LoS MIMO array are also the best solutions for point-to-point 3D LoS MIMO systems. Secondly, the optimal antenna arrangements on any curved surface can be easily obtained via mapping the corresponding broadside arrangement to the surface. As an example, 1D or 2D antenna arrangements that compensate the degradation from the tilt angles are discussed and presented.

In the latter part of this chapter, we proposed a two-level hierarchical MIMO system that combines the LoS spatial multiplexing gain with the beamforming gain intended for applications such as wireless backhaul. In addition to the system architecture, a channel model for calculating the link budget is introduced. The realistic parameters for the proposed channel were used for computations. The applied computations following IEEE 802.11ay and EIRP limit at 57$\sim$64 GHz band regulations showed that the system is capable of achieving more than 100 Gbit/s at a transmission distance of 100 m with reasonable antenna sizes, especially for operating in the 60 GHz band which exhibits high power attenuation.

In this chapter, we summarize the key learning points for engineers as:

- Optimal antenna arrangements on any curved surface can be obtained via mapping the corresponding broadside arrangement to the surface during deployments.
- LoS spatial multiplexing is quite robust against moderate displacement errors.
- By deploying spatial multiplexing on top of the directive antennas and/or array gains, LoS MIMO systems offer a great potential in supporting data rates well above 100 Gbit/s.

Chapter 4

Sequential Channel Equalization in Strong LoS MIMO communication

In this chapter, we show a novel algorithm for LoS MIMO channel equalization. Antenna displacement errors are inevitable in practice. Therefore, the channel matrices can be very different at different antenna topology realizations. Straightforward implementations like the zero-forcing algorithm without exploiting the special properties of the LoS MIMO channel can result in high complexity. As shown earlier in Sec. 3.1, the LoS MIMO channel can be factorized into a product of three matrices with two outer matrices contributing the most varying terms. This motivates an idea to equalize the channel in the reverse order of the factorization. During the discussion in this chapter, we show that such an equalization method is a good trade-off between complexity and robustness.

Within this chapter, we develop the concept in the following steps:

1. We show the relation between the LoS spatial multiplexing with displacements and Discrete Fourier Transform (DFT) matrices. In particular, the middle matrix of the channel factorization can be ideally an inverse DFT (IDFT) matrix that is perturbed by certain displacement errors.

2. With the help of Winograd butterflies [Win78], a novel equalization with lower complexity, denoted as *Sequential Channel Equalization* (SCE), becomes feasible and can be applied in the reverse order of the channel factorization. Additionally, the settings for the variable parameters are specified based on the channel estimate without the knowledge about the accurate geometric relations over long distances.

3. Motivated by the energy efficiency improvement, a sequential channel equalization based design for analog equalization is proposed with standard Butler matrices. The complexities of both digital and analog solutions increase almost linearly w.r.t. the number of antennas, compared to the quadratic increments observed in the conventional approaches. Furthermore, the analog network wiring can be significantly simplified.

4. As found numerically, the proposed method performs nearly as good as the zero-forcing based algorithms, while having significantly lower complexity.

4.1 Channel Factorization With Displacements

In this section, we examine the relation between the channel factorization model, displacement errors, and DFT matrices. We start the discussion first with uniform linear arrays (ULAs) and then extend the result to uniform rectangular arrays (URAs).

Uniform Linear Arrays: Let us first study the transceiver arrays that are parallel as in Sec. 2.2. For simplicity, we consider the number of antennas to be equal at Rx and Tx, $N_{\mathrm{t}} = N_{\mathrm{r}} = N$. By putting (2.7) into (2.6), the phase coupling between Rx-n_{r} and Tx-n_{t} is found as

$$\{\mathbf{H}_{\mathrm{LoS}}\}_{n_{\mathrm{r}}n_{\mathrm{t}}} = e^{-j\pi(n_{\mathrm{r}}-1)^2 d_{\mathrm{r}}^2/(\lambda D)} \cdot e^{j2\pi(n_{\mathrm{r}}-1)(n_{\mathrm{t}}-1)d_{\mathrm{r}}d_{\mathrm{t}}/(\lambda D)} \cdot e^{-j\pi(n_{\mathrm{t}}-1)^2 d_{\mathrm{t}}^2/(\lambda D)}. \tag{4.1}$$

Then, it is not hard to find that the middle of the channel factorization is a Vandermonde matrix. Under optimal arrangements $d_{\mathrm{r}}d_{\mathrm{t}} = \lambda D/N$, it is even an IDFT matrix $\mathbf{W}_{\text{IDFT-}N}$ of N points, i.e., $\{\mathbf{W}_{\text{IDFT-}N}\}_{n_{\mathrm{r}}n_{\mathrm{t}}} = e^{j2\pi(n_{\mathrm{r}}-1)(n_{\mathrm{t}}-1)/N}$. This relation can be formulated by multiplying two diagonal matrices $\mathbf{D}_{\text{L-}N}$ and $\mathbf{D}_{\text{R-}N}$ to the left and right of $\mathbf{W}_{\text{IDFT-}N}$, respectively, as

$$\mathbf{H}_{\mathrm{o}} = \mathbf{D}_{\text{L-}N}\, \mathbf{W}_{\text{IDFT-}N}\, \mathbf{D}_{\text{R-}N}, \tag{4.2}$$

where the diagonal elements of $\mathbf{D}_{\text{L-}N}$ and $\mathbf{D}_{\text{R-}N}$ are found as $\{\mathbf{D}_{\text{L-}N}\}_{n_{\mathrm{r}}n_{\mathrm{r}}} \triangleq e^{-j\pi(n_{\mathrm{r}}-1)^2 d_{\mathrm{r}}^2/(\lambda D)}$ and $\{\mathbf{D}_{\text{R-}N}\}_{n_{\mathrm{t}}n_{\mathrm{r}}} \triangleq e^{-j\pi(n_{\mathrm{t}}-1)^2 d_{\mathrm{t}}^2/(\lambda D)}$, respectively. For instance, the $\mathbf{H}_{\mathrm{o}}$ in (2.14) with $N = 3$ and $d_{\mathrm{r}} = d_{\mathrm{t}} = \sqrt{\lambda D/N}$ is found as

$$\mathbf{H}_{\mathrm{o}} = \begin{bmatrix} 1 & & \\ & e^{-j\frac{\pi}{3}} & \\ & & e^{-j\frac{4\pi}{3}} \end{bmatrix} \begin{bmatrix} 1 & 1 & 1 \\ 1 & e^{j\frac{2\pi}{3}} & e^{j\frac{4\pi}{3}} \\ 1 & e^{j\frac{4\pi}{3}} & e^{j\frac{8\pi}{3}} \end{bmatrix} \begin{bmatrix} 1 & & \\ & e^{-j\frac{\pi}{3}} & \\ & & e^{-j\frac{4\pi}{3}} \end{bmatrix}. \tag{4.3}$$

By separating phase shifts contributed by position displacements along the transmit direction, we recall the channel factorization in (3.5). The matrix $\mathbf{H}_{\mathrm{LoS}}$ can be directly decomposed into

$$\mathbf{H}_{\mathrm{LoS}} = \mathbf{D}_{\parallel,\mathrm{r}} \cdot \mathbf{H}_{\perp} \cdot \mathbf{D}_{\parallel,\mathrm{t}}.$$

Following the discussion on robustness in Sec. 3.1, the spatial multiplexing gain in LoS MIMO communication is quite robust against displacement errors, because the displacement errors on $\mathbf{H}_{\perp}$ are small, since they are measured in a larger unit of $\sqrt{\lambda D}$. Considering displacements of the optimal arrays involving translations and rotations, the matrix $\mathbf{H}_{\perp}$ differs from $\mathbf{H}_{\mathrm{o}}$ by $\mathbf{H}_{\Delta}$. The channel matrix $\mathbf{H}_{\mathrm{LoS}}$ in (3.5) then can be written as

$$\mathbf{H}_{\mathrm{LoS}} = \mathbf{D}_{\parallel,\mathrm{r}} \cdot \underbrace{(\mathbf{H}_{\mathrm{o}} + \mathbf{H}_{\Delta})}_{\mathbf{H}_{\perp}} \cdot \mathbf{D}_{\parallel,\mathrm{t}}. \tag{4.4}$$

Further considering (4.2), the channel can also be factored in terms of the IDFT matrix. For simplification, we restrict the discussions to ULAs of N elements. Combining (4.2) and (4.4), the matrix $\mathbf{H}_{\mathrm{LoS}}$ can be factored as a product of matrices $\tilde{\mathbf{D}}_{\parallel,\mathrm{t}}$, $\tilde{\mathbf{D}}_{\parallel,\mathrm{r}}$, and $\tilde{\mathbf{H}}_{\perp}$ as

$$\mathbf{H}_{\mathrm{LoS}} = \underbrace{\mathbf{D}_{\parallel,\mathrm{r}}\mathbf{D}_{\text{L-}N}}_{\triangleq\tilde{\mathbf{D}}_{\parallel,\mathrm{r}}} \cdot \underbrace{(\mathbf{W}_{\text{IDFT-}N} + \mathbf{D}^{*}_{\text{L-}N}\mathbf{H}_{\Delta}\mathbf{D}^{*}_{\text{R-}N})}_{\triangleq\tilde{\mathbf{H}}_{\perp}} \cdot \underbrace{\mathbf{D}_{\text{R-}N}\mathbf{D}_{\parallel,\mathrm{t}}}_{\triangleq\tilde{\mathbf{D}}_{\parallel,\mathrm{t}}}, \tag{4.5}$$

where $\tilde{\mathbf{H}}_\perp$ has a small difference $\tilde{\mathbf{H}}_\Delta \triangleq \tilde{\mathbf{H}}_\perp - \mathbf{W}_{\text{IDFT-}N} = \mathbf{D}^*_{\text{L-}N}\mathbf{H}_\Delta\mathbf{D}^*_{\text{R-}N}$ to $\mathbf{W}_{\text{IDFT-}N}$ within certain displacement error ranges. It is noticeable that the two factorizations in (4.4) and (4.5) have the same structure with outer factors being the sensitive terms. The usage of the tilde marker ($\tilde{}$) denotes the factorization with $\mathbf{W}_{\text{IDFT-}N}$ dominating the middle term.

Uniform Rectangular Arrays: Considering two N-element parallel URAs, the channel can be seen as a combination of channels resulting from linear arrays that are vertically and horizontally arranged. The optimal antenna spacings $d_{\text{t,v}},\ d_{\text{r,v}},\ d_{\text{t,h}}$, and $d_{\text{r,h}}$ of URAs mainly depend on the transmit distance D, wavelength λ, and the number of antennas $N_{\text{v}}(N_{\text{h}})$ in the vertical (horizontal) direction as (2.16). Here, we recall that the optimal arrangement of URAs makes $\mathbf{H}_{\text{LoS}}$ a spatially orthogonal matrix $\mathbf{H}_{\text{o}}$ with $\mathbf{H}_{\text{o}}^H \cdot \mathbf{H}_{\text{o}} = N \cdot \mathbf{I}_N$. The matrix $\mathbf{H}_{\text{o}}$ is found as the Kronecker product between the coupling matrices $\mathbf{H}_{\text{oh}}$, $\mathbf{H}_{\text{ov}}$ of the vertical and horizontal arrays in (2.17) as

$$\mathbf{H}_{\text{o}} = \mathbf{H}_{\text{oh}} \otimes \mathbf{H}_{\text{ov}},$$

where $\mathbf{H}_{\text{oh}}$ and $\mathbf{H}_{\text{ov}}$ are orthogonal matrices of sizes $N_{\text{h}} \times N_{\text{h}}$ and $N_{\text{v}} \times N_{\text{v}}$, respectively. $\mathbf{H}_{\text{oh}}$ and $\mathbf{H}_{\text{ov}}$ have similar relations with IDFT matrices as in (4.2) by replacing N with N_{h} and N_{v}, respectively.

Considering the mixed-product property [Loa00] of the Kronecker product $(\mathbf{A} \otimes \mathbf{B})(\mathbf{C} \otimes \mathbf{D}) = (\mathbf{AC}) \otimes (\mathbf{BD})$, a similar property as (4.2) can be found for $\mathbf{H}_{\text{o}}$ w.r.t. a 2D IDFT as

$$\mathbf{H}_{\text{o}} = (\mathbf{D}_{\text{L-}N_{\text{h}}} \otimes \mathbf{D}_{\text{L-}N_{\text{v}}})\,(\mathbf{W}_{\text{IDFT-}N_{\text{h}}} \otimes \mathbf{W}_{\text{IDFT-}N_{\text{v}}})\,(\mathbf{D}_{\text{R-}N_{\text{h}}} \otimes \mathbf{D}_{\text{R-}N_{\text{v}}}), \tag{4.6}$$

where $\mathbf{D}_{\text{L-}N_{\text{h}}}$ ($\mathbf{D}_{\text{L-}N_{\text{v}}}$), $\mathbf{D}_{\text{R-}N_{\text{h}}}$ ($\mathbf{D}_{\text{R-}N_{\text{v}}}$) and $\mathbf{W}_{\text{IDFT-}N_{\text{h}}}$ ($\mathbf{W}_{\text{IDFT-}N_{\text{v}}}$) are similarly defined as $\mathbf{D}_{\text{L-}N}$, $\mathbf{D}_{\text{R-}N}$, and $\mathbf{W}_{\text{IDFT-}N}$ in (4.2), respectively, by replacing N with N_{h} (N_{v}).

Following the same discussion from (4.2) to (4.4), the relation in (4.4) can be also found for URAs as

$$\mathbf{H}_{\text{LoS}} = \tilde{\mathbf{D}}_{\|,\text{r}} \cdot \underbrace{(\mathbf{W}_{\text{IDFT-}N_{\text{h}}} \otimes \mathbf{W}_{\text{IDFT-}N_{\text{v}}} + \tilde{\mathbf{H}}_\Delta)}_{\triangleq \tilde{\mathbf{H}}_\perp} \cdot \tilde{\mathbf{D}}_{\|,\text{t}}, \tag{4.7}$$

where $\tilde{\mathbf{D}}_{\|,\text{r}} \triangleq \mathbf{D}_{\|,\text{r}}(\mathbf{D}_{\text{L-}N_{\text{h}}} \otimes \mathbf{D}_{\text{L-}N_{\text{v}}})$, $\tilde{\mathbf{D}}_{\|,\text{t}} \triangleq (\mathbf{D}_{\text{R-}N_{\text{h}}} \otimes \mathbf{D}_{\text{R-}N_{\text{v}}})\mathbf{D}_{\|,\text{t}}$, and $\tilde{\mathbf{H}}_\Delta \triangleq (\mathbf{D}^*_{\text{L-}N_{\text{h}}} \otimes \mathbf{D}^*_{\text{L-}N_{\text{v}}})\mathbf{H}_\Delta(\mathbf{D}^*_{\text{R-}N_{\text{h}}} \otimes \mathbf{D}^*_{\text{R-}N_{\text{v}}})$.

It is observed from (4.5) and (4.7) that the 1D or 2D IDFT matrices are the dominating terms. Since the computation complexity is crucial for the systems operating at high symbol rates like wireless backhaul during system expansion, this observation leads to the idea for the complexity reduction in the next section.

4.2 Description of Sequential Channel Equalization (SCE)

For practical backhaul systems with massive deployments, the displacement errors of LoS MIMO antenna arrangements should be taken into consideration. Although the coherence time of the channel is expected to be very long due to the quasi-deterministic scenarios, the variability of the deployment requires flexible algorithms. As discussed previously, the conventional methods, i.e., straightforward implementations of ZF and minimum mean square error (MMSE) algorithms, do not consider the special property of LoS MIMO channels and require N^2 complex

number multiplications per received symbol. We denote their complexity[1] as $\mathcal{O}(N^2)$. In this work, we propose to use SCE with three steps considering the property of the LoS MIMO matrix $\mathbf{H}_{\mathrm{LoS}}$ specified in (4.5) and (4.7). The number of multiplications required by the proposed method is only increasing almost linearly w.r.t. small values of N in full digital implementation. We summarize our ideas on SCE as follows:

- Equalization can be performed in the reverse order w.r.t. the channel factorization in (4.5) or (4.7), yielding an equalizer structure equivalent to ZF equalization.
- Since the matrix in the middle can be approximated by an IDFT matrix, Fast Fourier Transform (FFT) can be used for channel equalization with reduced complexity.
- The complexity for the outer diagonal matrices is only of a linear order $\mathcal{O}(N)$.

4.2.1 Signal Estimation with Linear Algorithms

Let us assume that the Tx and the Rx of a LoS MIMO system are separated by a transmit distance D and consist of N uniformly arranged isotropic antennas each. A carrier frequency f_{c} with a corresponding wavelength $\lambda = c/f_{\mathrm{c}}$ is used by the transceiver arrays. To simplify the later discussions, we assume the common channel gain α in the LoS MIMO channel model (2.5) to be one. Therefore, the general linear system model in (2.4) can be presented with the matrix $\mathbf{H}_{\mathrm{LoS}}$ as

$$\mathbf{y} = \mathbf{H}_{\mathrm{LoS}} \cdot \mathbf{s} + \mathbf{n}, \tag{4.8}$$

where $\mathbf{s} \in \mathbb{C}^{N\times 1}$ and $\mathbf{y} \in \mathbb{C}^{N\times 1}$ are the transmitted signal vector and the received signal vector, respectively. The noise vector $\mathbf{n}$ is modeled with i.i.d. complex white Gaussian random entries that are circularly symmetric, $\mathbf{n} \sim \mathcal{CN}(\mathbf{0}, \sigma_{\mathrm{n}}^2 \cdot \mathbf{I}_N)$. The physical channel/coupling matrix between $\mathbf{s}$ and $\mathbf{y}$ is denoted by $\mathbf{H}_{\mathrm{LoS}} \in \mathbb{C}^{N\times N}$ as before. Furthermore, it is assumed that the power is allocated uniformly at streams with i.i.d. Gaussian signaling $\mathbf{s} \sim \mathcal{CN}(\mathbf{0}, \sigma_{\mathrm{s}}^2 \cdot \mathbf{I}_N)$. Considering that $\alpha = 1$, the SNR value γ in (2.24) satisfies $\gamma = N\sigma_{\mathrm{s}}^2/\sigma_{\mathrm{n}}^2$ in this chapter.

In this section, we restrict the discussion on signal estimation to linear algorithms due to their low complexity, which is a crucial aspect for ultra wideband systems like wireless backhaul systems. Exhaustive search algorithms, like the maximum likelihood estimation [Say10], may require higher complexity (exponential complexity in N) than necessary especially for systems operating at high SNR regions. We formulate the the maximum likelihood estimation with a random quantity $\mathbf{s}$ as

$$\hat{\mathbf{s}} = \arg\max_{\mathbf{s}} \, p_{\mathbf{y},\mathbf{s}}(\mathbf{y}, \mathbf{s}) = \arg\min_{\mathbf{s}} \, ||\mathbf{y} - \mathbf{H}_{\mathrm{LoS}} \cdot \mathbf{s}||_F^2, \tag{4.9}$$

where $p_{\mathbf{y},\mathbf{s}}(\mathbf{y}, \mathbf{s})$ is the joint likelihood function of $\mathbf{y}$ and $\mathbf{s}$ with $\mathbf{y}$ fixed for each realization. This complexity argument also holds for interference cancellation algorithms, like the successive interference cancellation using sorted QR decomposition [WBKK03], due to their multi-layer structures. Linear estimation is therefore a straightforward, low complexity strategy to find the estimates.

[1] To obtain the equalizer matrix, the complexity is of a cubic order $\mathcal{O}(N^3)$. This initial complexity is neglected in this work since it approaches zero after averaging over long transmission time.

We assume that the Rx has perfect channel knowledge on $\mathbf{H}_{\mathrm{LoS}} \in \mathbb{C}^{N\times N}$ and Rx, Tx have been synchronized. Knowing the CSI, different equalization algorithms can be applied. We express the equalized symbol vector $\tilde{\mathbf{y}}$ with an equalizer $\mathbf{W}$ as

$$\tilde{\mathbf{y}} \triangleq \hat{\mathbf{s}} = \mathbf{W}\cdot\mathbf{y} = \mathbf{W}\cdot\mathbf{H}_{\mathrm{LoS}}\cdot\mathbf{s} + \mathbf{W}\cdot\mathbf{n}. \tag{4.10}$$

Examining the n_{t}-th entry $\tilde{y}_{n_{\mathrm{t}}}$ of $\tilde{\mathbf{y}}$, we have

$$\tilde{y}_{n_{\mathrm{t}}} = \mathbf{w}_{n_{\mathrm{t}}}^T\mathbf{h}_{n_{\mathrm{t}}}s_{n_{\mathrm{t}}} + \sum_{n_{\mathrm{r}}=1,n_{\mathrm{r}}\neq n_{\mathrm{t}}}^{N} \mathbf{w}_{n_{\mathrm{t}}}^T\mathbf{h}_{n_{\mathrm{r}}}s_{n_{\mathrm{r}}} + \mathbf{w}_{n_{\mathrm{t}}}^T\mathbf{n}, \tag{4.11}$$

where $s_{n_{\mathrm{t}}}$ is the n_{t}-th entry of $\mathbf{s}$. The vector $\mathbf{w}_{n_{\mathrm{t}}}^T$ is the n_{t}-th row vector of $\mathbf{W}$, while the vector $\mathbf{h}_{n_{\mathrm{t}}}$ is the n_{t}-th column vector of $\mathbf{H}_{\mathrm{LoS}}$. The term $\sum_{n_{\mathrm{r}}=1,n_{\mathrm{r}}\neq n_{\mathrm{t}}}^{N}\mathbf{w}_{n_{\mathrm{t}}}^T\mathbf{h}_{n_{\mathrm{r}}}s_{n_{\mathrm{r}}}$ models the interference from other streams. Assuming equal power uncorrelated sources and the symbols are circularly symmetric Gaussian distributed with $\mathbf{s}\sim\mathcal{CN}(\mathbf{0},\sigma_{\mathrm{s}}^2\cdot\mathbf{I}_N)$, the interference is also Gaussian distributed. In this case, the achievable rate $R(\mathbf{W})$ with linear receiver processing can be formulated as

$$R(\mathbf{W}) = \sum_{n_{\mathrm{t}}=1}^{N}\log_2\left(1+\frac{|\mathbf{w}_{n_{\mathrm{t}}}^T\mathbf{h}_{n_{\mathrm{t}}}|^2\sigma_{\mathrm{s}}^2}{\sum_{n_{\mathrm{r}}=1,n_{\mathrm{r}}\neq n_{\mathrm{t}}}^{N}|\mathbf{w}_{n_{\mathrm{t}}}^T\mathbf{h}_{n_{\mathrm{r}}}|^2\sigma_{\mathrm{s}}^2 + \mathbf{w}_{n_{\mathrm{t}}}^T(\mathbf{w}_{n_{\mathrm{t}}}^T)^H\sigma_{\mathrm{n}}^2}\right). \tag{4.12}$$

In the following, we will discuss two state-of-the-art linear estimation algorithms and link them with the proposed SCE algorithm.

1) Minimum Mean Square Error (MMSE) Estimation

The channel equalizer $\mathbf{W}_{\mathrm{MMSE}}$ is determined by minimizing the mean squared error between the transmitted signal and the estimated signal $\mathbf{W}_{\mathrm{MMSE}} = \arg\min_{\mathbf{W}}\mathbb{E}[||\tilde{\mathbf{y}}-\mathbf{s}||_F^2]$, and is formulated as

$$\mathbf{W}_{\mathrm{MMSE}} \triangleq (\mathbf{H}_{\mathrm{LoS}}^H\mathbf{H}_{\mathrm{LoS}} + \frac{\sigma_{\mathrm{n}}^2}{\sigma_{\mathrm{s}}^2}\mathbf{I}_N)^{-1}\mathbf{H}_{\mathrm{LoS}}^H. \tag{4.13}$$

This solution is the optimal linear estimator with the mean square error as its cost criteria [Say10].

2) Zero-Forcing (ZF) Estimation

The ZF algorithm defines an equalizer with the pseudo-inverse of the channel matrix as

$$\mathbf{W}_{\mathrm{ZF}} \triangleq (\mathbf{H}_{\mathrm{LoS}}^H\mathbf{H}_{\mathrm{LoS}})^{-1}\mathbf{H}_{\mathrm{LoS}}^H. \tag{4.14}$$

One of the main drawbacks in implementing ZF based equalization is that, if the channel matrix is ill-conditioned, the algorithm suffers from noise enhancement. However, for optimal and even near-optimal arrangements, the channel in LoS MIMO communication is expected to be well-conditioned. Given that the $||\mathbf{y}-\mathbf{H}_{\mathrm{LoS}}\cdot\mathbf{s}||_F^2$ in (4.9) is convex, this solution is also the least squares estimator for $\mathbf{s}$ as $\frac{\partial||\mathbf{y}-\mathbf{H}_{\mathrm{LoS}}\cdot\mathbf{s}||_F^2}{\partial\mathbf{s}}\big|_{\mathbf{s}=\mathbf{W}_{\mathrm{ZF}}\mathbf{y}} = 0$.

In the rest of this chapter, we consider ZF as our baseline algorithm based on the following arguments. Firstly, for communication systems with high SNR values like in backhaul scenarios,

i.e., $\sigma_{\mathrm{s}}^2 \gg \sigma_{\mathrm{n}}^2$, the MMSE estimation can be well approximated by the ZF estimation. Secondly, in the low SNR region, the effective SNR values in (4.11) under optimal arrangements, i.e., $(\mathbf{w}_{n_{\mathrm{t}}}^T \mathbf{h}_{n_{\mathrm{t}}} s_{n_{\mathrm{t}}})^2/(\mathbf{w}_{n_{\mathrm{t}}}^T \mathbf{n})^2$, are also the same for both algorithms, since $\mathbf{H}_{\mathrm{LoS}}$ is orthogonal. This makes both ZF estimation and MMSE estimation being system capacity achieving solutions as $R(\mathbf{W}_{\mathrm{ZF}}) = R(\mathbf{W}_{\mathrm{MMSE}}) = C_{\mathrm{MIMO}}^{\mathrm{LoS}}$, although the biased MMSE estimation provides less estimation errors than the unbiased ZF estimation in general. Eventually, ZF requires no information on the SNR value, which makes the implementation simpler. As a conclusion, ZF represents a minimum-variance unbiased (MVU) estimator to the transmitted data under optimal arrangements. Considering it as the baseline comparison algorithm for near optimal arrangements, we define the baseline algorithm as

$$\mathbf{W}_{\mathrm{BL}} \triangleq \mathbf{W}_{\mathrm{ZF}}. \tag{4.15}$$

For the LoS MIMO system with optimal and sub-optimal arrangements, the channel is expected to be full rank. Therefore, considering the channel factorization in (4.5), the baseline algorithm is also equivalent to

$$\mathbf{W}_{\mathrm{BL}} = \tilde{\mathbf{D}}_{\parallel,\mathrm{t}}^{-1}(\mathbf{W}_{\text{IDFT-}N} + \tilde{\mathbf{H}}_{\Delta})^{-1}\tilde{\mathbf{D}}_{\parallel,\mathrm{r}}^{-1}. \tag{4.16}$$

3) Sequential Channel Equalization (SCE)

Motivated by the factorization in (4.5), a novel three-step equalization method is proposed in a reverse order. Three matrix multiplications are performed sequentially with the outer ones being diagonal matrices. Therefore, the design of SCE follows the ZF criterion, but can be considered as a low-complexity approximation to the ZF based algorithm in (4.16). The SCE matrix $\mathbf{W}_{\mathrm{sce}}$ is modeled as

$$\mathbf{W}_{\mathrm{sce}} \triangleq \mathbf{D}_2 \cdot \mathbf{W}_{\mathrm{fix}} \cdot \mathbf{D}_1, \tag{4.17}$$

where $\mathbf{D}_1$ and $\mathbf{D}_2$ are two diagonal matrices. For different antenna topology realizations, the two matrices $\mathbf{D}_1$ and $\mathbf{D}_2$ are chosen accordingly to the resulted $\mathbf{H}_{\mathrm{LoS}}$. Considering ULAs at Tx and Rx with N elements each, $\mathbf{W}_{\mathrm{fix}}$ can be implemented with a fixed N-point DFT matrix

$$\mathbf{W}_{\mathrm{fix}} = \mathbf{W}_{\text{DFT-}N}, \tag{4.18}$$

where $\{\mathbf{W}_{\text{DFT-}N}\}_{n_{\mathrm{r}}n_{\mathrm{t}}} \triangleq e^{-j2\pi(n_{\mathrm{r}}-1)(n_{\mathrm{t}}-1)/N}$. Furthermore, considering URAs at Tx and Rx with $N = N_{\mathrm{v}} \cdot N_{\mathrm{h}}$ elements each, the $\mathbf{W}_{\mathrm{fix}}$ can be implemented with $\mathbf{W}_{\mathrm{fix}} = \mathbf{W}_{\text{DFT-}N_{\mathrm{h}}} \otimes \mathbf{W}_{\text{DFT-}N_{\mathrm{v}}}$, if one considers the channel factorization model for URA systems in (4.7).

In practice, those DFT operations can be implemented with the FFT based structures of reduced complexity. Thus, the usage of $\mathbf{W}_{\mathrm{fix}}$ for equalizing $\tilde{\mathbf{H}}_{\perp}$ brings the benefit of saving computational complexity at the cost of slightly lower SINR caused by $\tilde{\mathbf{H}}_{\Delta}$. This comes from the fact that, within certain displacement error ranges, the entries of $\tilde{\mathbf{H}}_{\Delta}$ are of small values $|\{\tilde{\mathbf{H}}_{\Delta}\}_{n_{\mathrm{r}}n_{\mathrm{t}}}| \ll 1$. With optimal arrangements ($\tilde{\mathbf{H}}_{\Delta} = \mathbf{0}$), such an estimator following (4.17) is also expected to achieve the system capacity.

In this work, the design of SCE follows the ZF criterion, but its performance is impaired by the interference caused by $\tilde{\mathbf{H}}_{\Delta}$. Since the zero-forcing based algorithm is capable of offering an interference-free solution, the objective function of setting $\{\mathbf{D}_1, \mathbf{D}_2\}$ in this work is stated as the 'distance' between $\mathbf{W}_{\mathrm{sce}}$ and the ZF baseline algorithm $\mathbf{W}_{\mathrm{BL}}$ (the targeting operation) in

terms of least squares as

$$\{\mathbf{D}_1, \mathbf{D}_2\} = \arg\min_{\mathbf{D}_1,\mathbf{D}_2} ||\mathbf{D}_2 \cdot \mathbf{W}_{\text{fix}} \cdot \mathbf{D}_1 - \mathbf{W}_{\text{BL}}||_F^2, \tag{4.19}$$

where $\mathbf{D}_1$ and $\mathbf{D}_2$ can be seen as estimates on $\tilde{\mathbf{D}}_{\|,\text{r}}^{-1}$ and $\tilde{\mathbf{D}}_{\|,\text{t}}^{-1}$ in (4.16), respectively, under the perturbation of $\tilde{\mathbf{H}}_{\Delta}$.

4.2.2 Solution to Parameter Settings

For any LoS MIMO array pair with out-of-plane rotations, the $\mathbf{D}_{\|,\text{t}}$, $\mathbf{D}_{\|,\text{r}}$ terms are introduced by the offsets. In order to eliminate their effects on the resulting channel, the diagonal matrices $\mathbf{D}_1$ and $\mathbf{D}_2$ in (4.17) should be set as variable parameters for different antenna geometric realizations. However, due to the quasi-deterministic scenarios like wireless backhaul, $\mathbf{D}_1$ and $\mathbf{D}_2$ can be considered as fixed equalizers for each realization with a computational complexity of $\mathcal{O}(N)$ each. In this part, we seek to design matrices $\{\mathbf{D}_1, \mathbf{D}_2\}$ that minimize the distance w.r.t. the zero forcing algorithm as stated in (4.19).

Since $\mathbf{D}_1$ and $\mathbf{D}_2$ are diagonal matrices, we introduce two vectors $\mathbf{d}_1$ and $\mathbf{d}_2$ containing the diagonal entries of $\mathbf{D}_1$ and $\mathbf{D}_2$, respectively, as

$$\mathbf{d}_1 \triangleq \text{diag}\{\mathbf{D}_1\} \quad \text{and} \quad \mathbf{d}_2 \triangleq \text{diag}\{\mathbf{D}_2\}. \tag{4.20}$$

Then the least squares problem statedin (4.19) can be reformulated as

$$\begin{aligned}\{\mathbf{d}_1, \mathbf{d}_2\} &= \arg\min_{\mathbf{d}_1,\mathbf{d}_2} ||\underbrace{\mathbf{W}_{\text{fix}}}_{(4.18)} \odot [\mathbf{d}_2 \cdot \mathbf{d}_1^T] - \underbrace{\mathbf{W}_{\text{BL}}}_{(4.14)}||_F^2 \\ &= \arg\min_{\mathbf{d}_1,\mathbf{d}_2} ||\mathbf{W}_{\text{DFT-}N} \odot [\mathbf{d}_2 \cdot \mathbf{d}_1^T] - (\mathbf{H}_{\text{LoS}}^H \mathbf{H}_{\text{LoS}})^{-1} \mathbf{H}_{\text{LoS}}^H||_F^2.\end{aligned} \tag{4.21}$$

Here, we recall that the operator $\odot$ represents the Hadamard product. Considering that $\mathbf{W}_{\text{DFT-}N} \odot \mathbf{W}_{\text{DFT-}N}^* = \mathbf{1}_{N\times N}$, the problem becomes

$$\begin{aligned}\{\mathbf{d}_1, \mathbf{d}_2\} &= \arg\min_{\mathbf{d}_1,\mathbf{d}_2} ||\mathbf{W}_{\text{fix}} \odot [\mathbf{d}_2 \cdot \mathbf{d}_1^T] - [\mathbf{W}_{\text{fix}} \odot \mathbf{W}_{\text{fix}}^*] \odot \mathbf{W}_{\text{BL}}||_F^2, \\ &= \arg\min_{\mathbf{d}_1,\mathbf{d}_2} ||\mathbf{W}_{\text{fix}} \odot [\mathbf{d}_2 \cdot \mathbf{d}_1^T - \mathbf{W}_{\text{fix}}^* \odot \mathbf{W}_{\text{BL}}]||_F^2,\end{aligned} \tag{4.22}$$

where the second equality is obtained via the associative and distributive properties of the Hadamard product. Considering that $||\mathbf{A}||_F^2 = \sum_{b=1}^{N}\sum_{c=1}^{N} |\{\mathbf{A}\}_{bc}|^2$, $\mathbf{A} \in \mathbb{C}^{N\times N}$ and the entries of $\mathbf{W}_{\text{fix}}$ are of a unit magnitude, the least squares problem becomes

$$\{\mathbf{d}_1, \mathbf{d}_2\} = \arg\min_{\mathbf{d}_1,\mathbf{d}_2} ||[\mathbf{d}_2 \cdot \mathbf{d}_1^T] - \mathbf{W}_{\text{fix}}^* \odot \mathbf{W}_{\text{BL}}||_F^2. \tag{4.23}$$

The problem stated in (4.23) is a low-rank (rank one) matrix approximation problem for the outer product $\widetilde{\mathbf{A}} \triangleq \mathbf{d}_2 \cdot \mathbf{d}_1^T$. The analytical solution can be provided by applying the singular value decomposition (SVD). Arranging the singular values in descending order, we have

$$\mathbf{W}_{\text{fix}}^* \odot \mathbf{W}_{\text{BL}} = [\mathbf{u}_1 \ \dots \ \mathbf{u}_N] \begin{bmatrix} \sigma_1 & & \\ & \ddots & \\ & & \sigma_N \end{bmatrix} \begin{bmatrix} \mathbf{v}_1^H \\ \vdots \\ \mathbf{v}_N^H \end{bmatrix} = \sigma_1 \mathbf{u}_1 \mathbf{v}_1^H + \underbrace{\sum_{i=2}^{N} \sigma_i \mathbf{u}_i \mathbf{v}_i^H}_{\text{Approximation errors}}. \tag{4.24}$$

According to the matrix approximation lemma or the so-called Eckart-Young theorem [KS17], the solution to the approximation $\widetilde{\mathbf{A}}$ would be $\sigma_1 \mathbf{u}_1 \mathbf{v}_1^H$. Without loss of generality, we get the solution for $\{\mathbf{d}_1, \mathbf{d}_2\}$ as the dominant singular vectors of $\mathbf{W}_{\text{fix}}^* \odot \mathbf{W}_{\text{BL}}$. That is

$$\mathbf{d}_1 = \sqrt{\sigma_1}(\mathbf{v}_1^H)^T, \quad \mathbf{d}_2 = \sqrt{\sigma_1}\mathbf{u}_1. \tag{4.25}$$

This would conclude the steps for setting the matrices $\{\mathbf{D}_1, \mathbf{D}_2\}$ for LoS MIMO systems. Then the resulted approximation error in (4.23), also according to the Eckart-Young theorem [KS17], satisfies

$$||[\mathbf{d}_2 \cdot \mathbf{d}_1^T] - \mathbf{W}_{\text{fix}}^* \odot \mathbf{W}_{\text{BL}}||_F^2 = \sum_{i=2}^{N} \sigma_i^2. \tag{4.26}$$

In order to evaluate the accuracy of the approximation from the SCE to the ZF based algorithm quantitatively in later numerical evaluations, a ratio ϵ denoting the normalized matrix approximation error is defined in this work as

$$\epsilon \triangleq \sum_{i=2}^{N} \sigma_i^2 / \sigma_1^2. \tag{4.27}$$

Since the proposed algorithm equalizes LoS channels with $\mathbf{H}_\Delta = 0$ in (4.4) perfectly, ϵ is found to be zero. Therefore, ϵ is also considered as a relative indicator for 'how well the $\mathbf{H}_\perp$ is approximated by $\mathbf{H}_{\text{o}}$'. Before comparing the performance difference between ZF algorithm and its low complexity approximation SCE in Sec. 4.5, we will present the possible complexity reduction using SCE next.

4.3 Complexity Reduction in Digital Processing

In this part, we show the complexity reduction of the proposed SCE w.r.t. the baseline algorithm. As discussed earlier, the weight matrix $\mathbf{W}_{\text{fix}}$ can be chosen as a DFT matrix. This DFT multiplication can exploit the benefits of the butterfly designs in FFT. For uniform rectangular LoS MIMO arrays, the operation $\mathbf{W}_{\text{fix}} = \mathbf{W}_{\text{DFT-}N_{\text{h}}} \otimes \mathbf{W}_{\text{DFT-}N_{\text{v}}}$ can be realized by cascading multiple butterflies in two stages, as shown in Fig. 4.1. Butterfly based FFT is capable of reducing the complexity $\mathcal{O}(N^2)$ of a DFT operation to a value of $\mathcal{O}(N \log N)$ for very large N. Considering that the size of symmetric URA systems should be moderate, e.g., assuming the one-dimensional size $(N_{\text{v}} - 1)\sqrt{\lambda D / N_{\text{v}}}$ is not much larger than 1 meter, we limit our discussion to arrays having maximum 5 antennas in one direction. i.e., $N_{\text{v}},\ N_{\text{h}} \leq 5$. Specifically, for a backhaul system operating at a distance of 100 meters with a carrier frequency $f_{\text{c}} = 60$ GHz, the maximum array size of $1.26\text{m} \cdot 1.26\text{m}$ is assumed. With the help of the Winograd butterfly [Win78], it is shown below that the computational complexity is approximately linear w.r.t. N.

The butterfly structure is the basic unit for FFT calculation. For units with r-point butterfly structure, a number of $\frac{N}{r} \log_r N$ units is needed for an FFT of $N = r^\zeta$ points with ζ stages. Apart from the standard radix-2 butterfly structure, Winograd Discrete Fourier Transform (WDFT) gives the theoretical basis for designing butterflies with general prime numbers such as radices $r = 3,\ 5,\ 7, \ldots$. Considering that the complexity of complex multiplications is higher than

that of complex additions[2], a WDFT based butterfly structure is preferred. It has the minimum number of multiplications at the expense of introducing addition operations. In [LN11], the butterfly structures for 3 and 5-point DFTs are proposed and have been widely used in LTE systems.

We would like to note here that an addition operation between two complex numbers weighted by 1, -1, j, $-j$ is only two real addition operations between different real/imaginary parts and requires no multiplication. Meanwhile, the trivial multiplication with $1/2$ is also not counted for complexity due to the fact that it is implemented via one bit right shift in the register. In the example of a radix-3 Winograd butterfly in Fig. 4.1, a single unit requires only one complex multiplication with $\chi = -\sin(2\pi/3)$ and 6 addition operations. The complexity of butterflies with radix-2, 3, 5 can be found in Table 4.1 which is calculated according to [LN11]. We also would like to note here that the 4-point FFT can be implemented via the Cooley-Tukey algorithm [CT65] with four radix-2 butterflies. As discussed earlier, the involved twiddle factors 1 and j require no additional multiplication.

Based on the required number of butterflies for $\mathbf{W}_{\text{fix}}$ and multiplications at the first stage $\mathbf{D}_1$ and the last stage $\mathbf{D}_2$, the complexity for SCE in terms of the number of operations for equalizing a receive vector $\mathbf{y} \in \mathbb{C}^{N\times 1}$ can be found in Table 4.1. In the example with $N = N_{\text{v}} \cdot N_{\text{h}} = 3 \cdot 3$ in Fig. 4.1, six radix-3 Winograd butterfly units are needed with overall 6 complex multiplications and 36 complex additions. Considering the complexity of $\mathbf{D}_1$, $\mathbf{D}_2$ with 18 complex multiplications, the overall operations for sequentially equalizing a $\mathbf{y} \in \mathbb{C}^{9\times 1}$, i.e., $\mathbf{D}_2 \cdot \mathbf{W}_{\text{fix}} \cdot \mathbf{D}_1 \cdot \mathbf{y}$ are 24 complex multiplications and 36 complex additions. As a comparison, Table 4.1 also includes the complexity of multiplying a ZF based matrix $\mathbf{W}_{\text{BL}} \in \mathbb{C}^{N\times N}$, which requires N^2 complex multiplications and $N(N-1)$ complex additions.

For the values of N in the range of interest, the complexity of SCE is dominated by the

[2] A multiplication of two complex numbers requires four real multiplications and two real additions, while the complex addition requires two real additions. Plus and minus operations are all counted as addition operations.

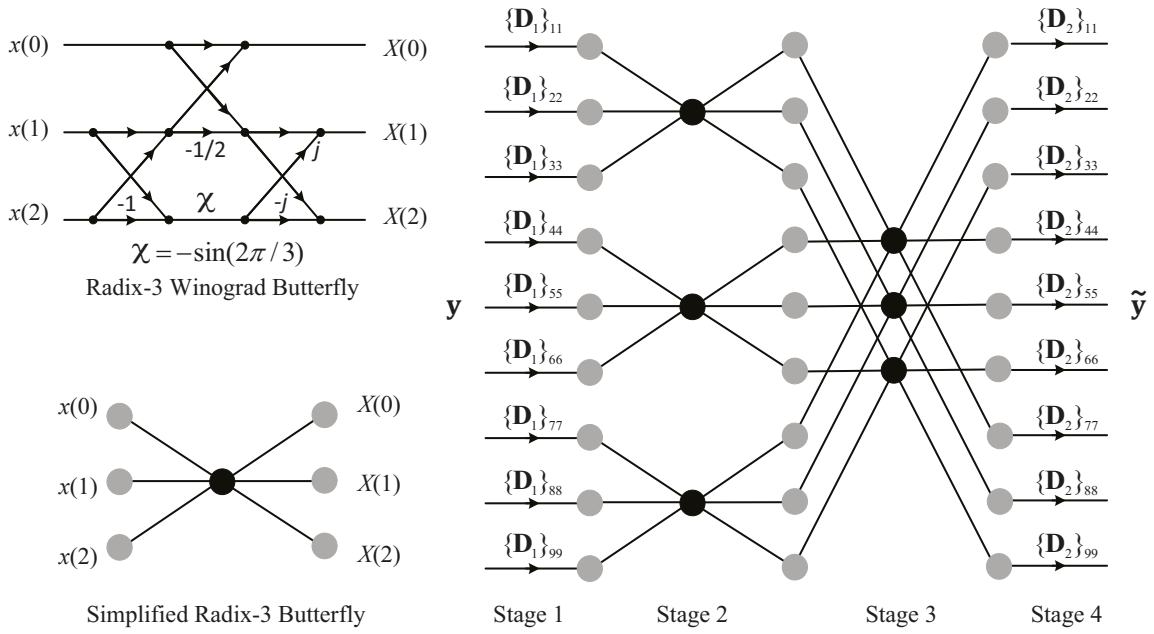

Figure 4.1: Radix-3 Winograd butterfly structure and the four stages in equalization of a LoS MIMO system with $N_{\text{v}} = N_{\text{h}} = 3$ elements on each side. (Source: [SCR+18] © 2018 IEEE).

# of Multiplications (# of Additions)		r-point Butterfly	$N = N_{\mathrm{v}} \cdot N_{\mathrm{h}}$: Antenna number with N-stream transmission						
			$2 \cdot 1$	$3 \cdot 1$	$4 \cdot 1$	$\underline{3 \cdot 3}$	$4 \cdot 3$	$4 \cdot 4$	$5 \cdot 5$
Array Size at 100m			0.5m	0.82m	1.06 m	0.82m·0.82m	1.06m·0.82m	1.06m·1.06m	1.26m·1.26m
Radix	$r = 2$	0 (2)	0 (2)		0 (8)		0 (24)	0 (64)	
	$r = 3$	1 (6)		1 (6)		$\underline{6}$ (36)	4 (24)		
	$r = 5$	4 (18)							40 (180)
$\mathbf{D}_1$ and $\mathbf{D}_2$			4 (0)	6 (0)	8 (0)	$\underline{18}$ (0)	24 (0)	32 (0)	50 (0)
NOPS - SCE			**4 (2)**	**7 (6)**	**8 (8)**	**$\underline{24}$ ($\underline{36}$)**	**28 (48)**	**32 (64)**	**90 (180)**
NOPS - ZFE			**4 (2)**	**9 (6)**	**16 (12)**	**$\underline{81}$ ($\underline{72}$)**	**144 (132)**	**256 (240)**	**625 (600)**

Table 4.1: The Number of Operations (NOPS) in Sequential Channel Equalization (SCE) and Zero Forcing based Equalization (ZFE). (Source: [SCR+18] © 2018 IEEE).

$2N$ multiplications at $\mathbf{D}_1$ and $\mathbf{D}_2$, since the Winograd butterflies introduce mainly addition operations. Based on the values in Table 4.1, the required number of complex multiplications is reduced from N^2 to approximately $2N$, while the number of complex additions is reduced to $\mathcal{O}(N \log N)$. Since the complexity of complex multiplications is higher than that of additions, we conclude that the complexity grows almost linearly w.r.t. N.

Furthermore, we must note that the computational complexity required by multiplying $\mathbf{D}_1$ and $\mathbf{D}_2$ may not be even necessary. It is influenced by the possible synchronization setup. If there is a common carrier frequency offset between Tx antennas and Rx antennas, one needs to multiply $\mathbf{D}_1$ and $\mathbf{D}_2$ at the beginning and at end of the channel equalization setups, respectively. For systems having independent oscillators at different antennas, which will be discussed in the next chapter with a hardware-in-the-loop LoS MIMO demonstrator, these ideally static phase compensation $\mathbf{D}_1$ and $\mathbf{D}_2$ can be applied jointly with synchronization. As a consequence, the factorization into 3 matrices is only necessary at the beginning of a burst transmission for establishing the link. During data transmission, the channel equalization collapses to an FFT operation.

4.4 Analog Equalizing Network Design

Previously, we discussed the potential of computational complexity reduction of using SCE with digital implementations. Another topic being widely considered in LoS MIMO communication is analog equalization. In this section, we discuss the complexity reduction of using SCE with analog implementation. This section is organized as follows: We first introduce the concept of analog equalization in strong LoS MIMO communication with its potential benefits. Then, two state-of-the-art designs are presented. These two designs are considered as two extreme cases: one design has low complexity with ultra-high sensitivity while the other is quite robust to the displacement errors with high system complexity. Being considered as a good trade-off between complexity and robustness, a new SCE based design is proposed. The proposed design

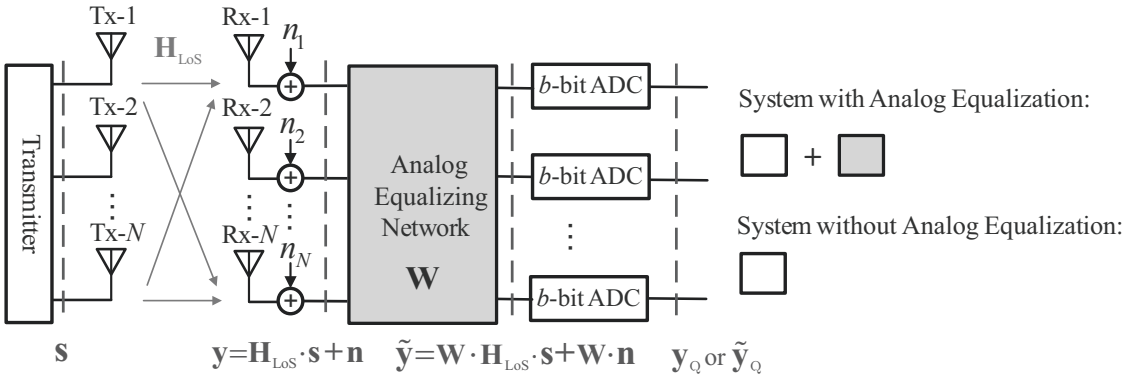

Figure 4.2: The LoS MIMO system block diagram with/without analog equalization. (Source: [SCR+18] © 2018 IEEE).

is specified first for ULAs and then for URAs using Butler matrices.

4.4.1 Low Resolution Quantization with Analog Equalization

Energy efficiency is another key performance indicator for the practical feasibility of wireless backhaul solutions. Due to the wide bandwidths at mmWave frequencies, the sampling rates of the *analog-to-digital converters* (ADCs) reach to several or tens giga-samples-per-second. Unfortunately, high speed, high resolution (e.g., 8-12 bits) ADCs are costly and power-hungry [MH14]. The amplitude resolutions (later referred as resolutions) of the ADCs should thus be kept as low as possible, as the power consumption scales exponentially with the number of quantization bits and represents a major factor in the system's energy efficiency. Correspondingly, our work in this section considers LoS MIMO communication with low precision ADCs, e.g., 1$\sim$3 bits, which reduce the power consumption and the cost.

Considering the signal at a single receive antenna, the MIMO superposition of the transmitted data streams imposes challenges to the quantization due to the high signal dynamic range. Low resolution ADCs are likely to lose more information bits in MIMO communication than in parallel single-stream communication. To allow the use of low resolution ADCs, a possible solution is to use analog components for channel equalization such that the quantization is applied after separating the streams as shown in Fig. 4.2 with an equal number of antennas at Tx and Rx. The linear signal estimator $\mathbf{W}$ is implemented in the analog domain. The analog estimator $\mathbf{W}$ can be implemented in many ways. Their block diagrams will be shown later in Fig. 4.4, Fig. 4.5 and Fig. 4.6 with detailed discussions. In the next part, we will first discuss the potential of using analog equalizing networks for reducing the required resolution of quantizers in LoS MIMO systems.

Mutual Information with Quantization: For simplification, in this section, we assume the entries of $\mathbf{s}$ are rectangular QAM signals with M_{s} constellation points, e.g., $M_{\text{s}} = 16$. Meanwhile, signals at different transmit antennas are uncorrelated with equal power and their constellations are of an equal probability. Considering Fig. 4.2, let us denote $\mathbf{y}_{\text{Q}} \triangleq \mathcal{Q}_b(\mathbf{y})$ and $\tilde{\mathbf{y}}_{\text{Q}} \triangleq \mathcal{Q}_b(\tilde{\mathbf{y}})$ as the quantized signals of $\mathbf{y}$ and $\tilde{\mathbf{y}}$, which are analog signals without and with analog equalizing network, respectively. Here, the notation $\mathcal{Q}_b(\cdot)$ denotes the quantization function which is a non-linear mapping from continuous input signals to discrete output signals. The parameter b denotes the number of bits representing the in-phase components and the quadrature-

phase components. Now let us compare the mutual information of $I(\mathbf{s};\mathbf{y}_{\mathrm{Q}})$ with $I(\mathbf{s};\tilde{\mathbf{y}}_{\mathrm{Q}})$ when the channel matrix $\mathbf{H}_{\mathrm{LoS}}$ is assumed to be perfectly known. The mutual information $I(\mathbf{s};\mathbf{y}_{\mathrm{Q}})$ between the transmit and the receive vectors is defined in the standard way by a difference of unconditional and conditional entropy as

$$I(\mathbf{s};\mathbf{y}_{\mathrm{Q}}) = H(\mathbf{y}_{\mathrm{Q}}) - H(\mathbf{y}_{\mathrm{Q}}|\mathbf{s}) = I(\mathbf{s};\mathcal{Q}_b(\mathbf{H}_{\mathrm{LoS}}\cdot\mathbf{s}+\mathbf{n})). \tag{4.28}$$

Similarly, the mutual information $I(\mathbf{s};\tilde{\mathbf{y}}_{\mathrm{Q}})$ is defined as

$$I(\mathbf{s};\tilde{\mathbf{y}}_{\mathrm{Q}}) = H(\tilde{\mathbf{y}}_{\mathrm{Q}}) - H(\tilde{\mathbf{y}}_{\mathrm{Q}}|\mathbf{s}) = I\big(\mathbf{s};\mathcal{Q}_b(\mathbf{W}\cdot\mathbf{H}_{\mathrm{LoS}}\cdot\mathbf{s}+\mathbf{W}\cdot\mathbf{n})\big). \tag{4.29}$$

Since the received signal $\mathbf{y}$ is a composite of structurally interfered signals, the analog equalizing network constructs new weighted vectors $\tilde{\mathbf{y}}$ by combining the received signals from different receive antennas. The analog equalizing network may reshape the distribution of the constellations on the complex constellation plane of every data stream before the quantization. As can be seen from (4.29), a joint design on the quantizer $\mathcal{Q}_b(\cdot)$ and the analog equalizing network $\mathbf{W}$ can provide mutual information higher than the design without analog equalizing network, since

$$\max_{\mathcal{Q}_b(\cdot)} I(\mathbf{s};\mathcal{Q}_b(\mathbf{H}_{\mathrm{LoS}}\cdot\mathbf{s}+\mathbf{n})) \leq \max_{\mathcal{Q}_b(\cdot),\mathbf{W}} I\big(\mathbf{s};\mathcal{Q}_b(\mathbf{W}\cdot\mathbf{H}_{\mathrm{LoS}}\cdot\mathbf{s}+\mathbf{W}\cdot\mathbf{n})\big). \tag{4.30}$$

Considering that the quantization function is a non-linear function which is hard to analyze, this section only considers a simple scenario with a given complex number quantizer, i.e., uniform b-bits ADCs for in-phase and quadrature components of each stream, and a given $\mathbf{W}$ being either $\mathbf{W}_{\mathrm{ZF}}$ or $\mathbf{W}_{\mathrm{sce}}$. In the rest of this part, we show that using $\mathbf{W}$ can lead to $I(\mathbf{s};\tilde{\mathbf{y}}_{\mathrm{Q}}) \geq I(\mathbf{s};\mathbf{y}_{\mathrm{Q}})$ in both cases with and without noise, which motives the usage of analog equalization.

1) Mutual Information without Noise

As we are focusing on the effects caused by using analog equalizing network and quantizers, we can first limit the discussion to the noise-free case (high SNR limit). If one uses $\mathbf{W}_{\mathrm{ZF}}$ for analog equalization, $\tilde{\mathbf{y}}$ has the same probability distribution as $\mathbf{s}$, since $\tilde{\mathbf{y}} = \mathbf{W}_{\mathrm{ZF}}\mathbf{H}_{\mathrm{LoS}}\mathbf{s} = \mathbf{s}$. Having the number of quantization outputs greater than or equal to the number of amplitude levels of the M_{s}-QAM signaling, i.e., $2^b \geq \sqrt{M_{\mathrm{s}}}$, the quantization will have no information loss meaning $H(\tilde{\mathbf{y}}_{\mathrm{Q}}) = H(\mathbf{s})$.

As an example, let us consider a ULA LoS MIMO system with i.i.d. 16-QAM signaling transmitted on each of the three streams $N = 3$. The antenna spacing d_{LoS} is optimized for an estimated distance of 100 m with a carrier frequency of $f_{\mathrm{c}} = 60$ GHz. A displacement error is also introduced with a true transmit distance of 105 m and a rotation error (pitch) around z'-axis of 5°, see Fig. 2.5. The noise free constellation points of $\mathbf{y}$ and $\tilde{\mathbf{y}}$ can be found in Fig. 4.3 (a). y_1, y_2 and y_3 denote the entries of the vector $\mathbf{y} = [y_1,\, y_2,\, y_3]^T$, while $\tilde{y}_1$, $\tilde{y}_2$, and $\tilde{y}_3$ are similarly found as $\tilde{\mathbf{y}} = [\tilde{y}_1,\, \tilde{y}_2,\, \tilde{y}_3]^T$. The SCE based analog equalizing network, which will be introduced later in Sec. 4.4.3, is considered here for this evaluation. Considering that the equalized symbols $\tilde{\mathbf{y}}$ are separated before the low resolution quantization, the quantizer can set its thresholds between the clusters of equalized symbols. With $b \geq 2$ in the noise free case, non-coarse

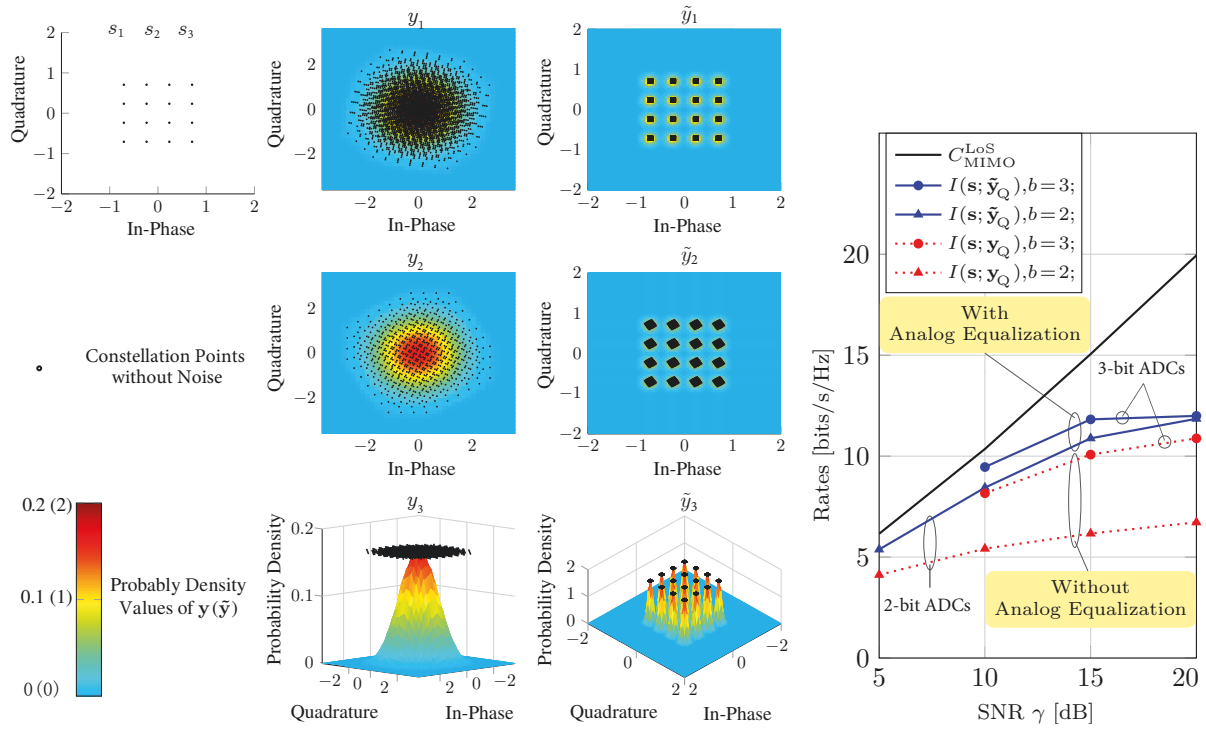

(a) Scatter plots and distribution density of constellations at different stages, $\gamma = 20$ dB;

(b) Numerically evaluated mutual information;

Figure 4.3: The signals before and after analog equalization with $N = 3$. (Source: [SCR+18] © 2018 IEEE).

quantization can be easily made. The definitions of coarse and non-coarse quantization can be found in [NI06]. We adopt it for our scenario for the sake of completeness.

Definition 1. *Considering a finite set $\mathcal{S}$ containing all possible modulated transmit vectors, $|\mathcal{S}| = M_{\text{s}}^N$, a quantization scheme is called* **coarse** *iff*

$$\exists(\mathbf{s}_1, \mathbf{s}_2 \neq \mathbf{s}_1) \in \mathcal{S} \;\; : \;\; \mathcal{Q}_b(\mathbf{y}_1) = \mathcal{Q}_b(\mathbf{y}_2), \tag{4.31}$$

where $\mathbf{y}_1$ and $\mathbf{y}_2$ are the noise-free receive vectors corresponding to the transmit vector $\mathbf{s}_1$ and $\mathbf{s}_2$, respectively. Otherwise, it is said to be **non-coarse**.

With the non-coarse quantization schemes which are feasible for systems with analog equalization, it holds that $H(\mathbf{s}) = H(\tilde{\mathbf{y}}_{\text{Q}})$. Coarse quantization may lead to ambiguity of the transmit vectors. Here, we would like to note that, if the channel is not equalized and low resolution ADCs are used, the quantization schemes on $\mathbf{y}$ can be coarse. Such quantization schemes may lose information due to the possible ambiguity as $H(\mathbf{y}_{\text{Q}}) \leq H(\mathbf{s})$, and the conditional entropy $H(\mathbf{s}|\mathbf{y}_{\text{Q}})$ is greater than or equal to zero as

$$H(\mathbf{s}|\mathbf{y}_{\text{Q}}) = H(\mathbf{s}) - H(\mathbf{y}_{\text{Q}}) + \underbrace{H(\mathbf{y}_{\text{Q}}|\mathbf{s})}_{=0} \geq 0, \tag{4.32}$$

where it holds that $H(\mathbf{y}_{\text{Q}}|\mathbf{s}) = H(\mathcal{Q}_b(\mathbf{H}_{\text{LoS}} \cdot \mathbf{s})|\mathbf{s}) = 0$ as $\mathcal{Q}_b(\cdot)$ and $\mathbf{H}_{\text{LoS}}$ are known to the Rx. Similar property is also found for $H(\tilde{\mathbf{y}}_{\text{Q}}|\mathbf{s})$ as $H(\tilde{\mathbf{y}}_{\text{Q}}|\mathbf{s}) = 0$. Considering the non-coarse

quantization and coarse quantization for systems with and without analog equalizing network, respectively, the following relation is found between $I(\mathbf{s};\tilde{\mathbf{y}}_{\mathrm{Q}})$ and $I(\mathbf{s};\mathbf{y}_{\mathrm{Q}})$ as

$$I(\mathbf{s};\tilde{\mathbf{y}}_{\mathrm{Q}}) = H(\tilde{\mathbf{y}}_{\mathrm{Q}}) - \underbrace{H(\tilde{\mathbf{y}}_{\mathrm{Q}}|\mathbf{s})}_{=0} = H(\mathbf{s}) \geq H(\mathbf{s}) - \underbrace{H(\mathbf{s}|\mathbf{y}_{\mathrm{Q}})}_{\geq 0} = I(\mathbf{s};\mathbf{y}_{\mathrm{Q}}). \tag{4.33}$$

With the arguments above, we show that in the noise-free case (high SNR limit), analog equalizing network reduces the information loss of using low resolution ADCs in LoS MIMO scenarios as $I(\mathbf{s};\tilde{\mathbf{y}}_{\mathrm{Q}}) \geq I(\mathbf{s};\mathbf{y}_{\mathrm{Q}})$.

2) Mutual Information with Noise

For the cases with intermediate and low SNR values, we apply a numerical evaluation for comparing $I(\mathbf{s};\mathbf{y}_{\mathrm{Q}})$ with $I(\mathbf{s};\tilde{\mathbf{y}}_{\mathrm{Q}})$. Here, the same system setup and the same displacement errors are considered as the earlier part. In addition, i.i.d. white Gaussian noise is considered for each stream. As can be seen in Fig. 4.3 (a) with SNR being 20dB, the analog equalizing network can reshape the distribution of the receive signal in the complex constellation plane of every data stream before quantization. In addition, the received constellations of $\mathbf{y}$ are found Gaussian-like at each stream. This leads to larger variances and larger dynamic ranges at an individual stream. Therefore, to have less information loss, higher resolutions might be expected for quantization of the systems without analog equalization.

In this part, the mutual information $I(\mathbf{s};\mathbf{y}_{\mathrm{Q}})$ between the input signal $\mathbf{s}$ and the output signal $\mathbf{y}_{\mathrm{Q}}$ is evaluated via [Sha48]

$$I(\mathbf{s};\mathbf{y}_{\mathrm{Q}}) = \sum_{\mathbf{y}_{\mathrm{Q}}\in\mathcal{Y}_{\mathrm{Q}}} \sum_{\mathbf{s}\in\mathcal{S}} \Pr(\mathbf{s},\mathbf{y}_{\mathrm{Q}}) \log_2 \frac{\Pr(\mathbf{s},\mathbf{y}_{\mathrm{Q}})}{\Pr(\mathbf{s})\Pr(\mathbf{y}_{\mathrm{Q}})}, \tag{4.34}$$

where $\mathcal{Y}_{\mathrm{Q}}$ is a finite set containing all possible output vectors at the quantizer $\mathcal{Q}_b(\mathbf{y}_{\mathrm{Q}})$. $\Pr(\mathbf{s},\mathbf{y}_{\mathrm{Q}})$ is the joint probability function of $\mathbf{s}$ and $\mathbf{y}_{\mathrm{Q}}$, while $\Pr(\mathbf{s})$ and $\Pr(\mathbf{y}_{\mathrm{Q}})$ are the probability mass functions of $\mathbf{s} \in \mathcal{S}$ and $\mathbf{y}_{\mathrm{Q}} \in \mathcal{Y}_{\mathrm{Q}}$, respectively. $I(\mathbf{s};\tilde{\mathbf{y}}_{\mathrm{Q}})$ is similarly defined as $I(\mathbf{s};\mathbf{y}_{\mathrm{Q}})$ by replacing $\mathbf{y}_{\mathrm{Q}}$ and $\mathcal{Y}_{\mathrm{Q}}$ with $\tilde{\mathbf{y}}_{\mathrm{Q}}$ and $\widetilde{\mathcal{Y}}_{\mathrm{Q}}$, respectively. $\widetilde{\mathcal{Y}}_{\mathrm{Q}}$ is a finite set containing all possible output vectors at the quantizer $\mathcal{Q}_b(\tilde{\mathbf{y}}_{\mathrm{Q}})$.

In Fig. 4.3 (b), we show the mutual information of a 3×3 MIMO system with and without the analog equalizing network and for different quantization resolutions. Their quantization ranges are set to the maximum input magnitude in the noise-free case. The results reveal a couple of interesting facts. Without the analog network, the mutual information is lower and a higher resolution will be required in order to achieve a similar performance. At high SNR ranges, the maximum possible transmission rate of three streams using 16-QAM with an equal probability, which is 12 bits/s/Hz, can be approximately achieved when using the analog equalizer with low resolution ADCs. In addition, a relatively large mutual information can be found at intermediate and low SNR values. Therefore, for systems with analog equalizers and low resolution ADCs, the required SNR is not necessarily high. Eventually, we would like to note that since the channel can be equalized in the analog domain, the computational complexity reduction during post-processing is also expected.

4.4.2 The State-of-the-Art Works on Analog Equalizing Network

The state-of-the-art works on the analog equalization focus on two different approaches, a fixed network design for optimal arrangements [HSS+13, HSS+14] and a ZF based design for systems with displacement errors [STS+08a, STS+08b, SST+09]. Both designs share the same analog equalizing network block diagram as shown in Fig. 4.4 (a) with two different designs on the stream separation components. The signal from each receive antenna is split into N copies by a signal splitter. Then, every stream separation component combines the copies from all received signals and reconstructs the signal of the corresponding transmit antenna. As can be seen from the block diagram, the conventional approaches implement naive matrix multiplications with large overheads in wiring (many crossovers of wires) and large control efforts during the system expansion with more streams. After introducing those conventional approaches in this part, in Sec. 4.4.3, we will show that the SCE based equalizing network simplifies the wiring and control efforts by exploiting the aforementioned channel property of LoS MIMO communication.

The works in [HSS+13, HSS+14] use fixed analog equalizing networks with

$$\mathbf{W} = \mathbf{H}_{\mathrm{o}}^{H}, \tag{4.35}$$

as sketched in Fig. 4.4 (b) assuming optimal LoS MIMO arrangements. As mentioned above, optimal arrangements lead to orthogonal phase coupling matrices with entries having unit modulus, $\mathbf{H}_{\mathrm{o}}^{H} \cdot \mathbf{H}_{\mathrm{o}} = N \cdot \mathbf{I}_N$. Therefore, such a weight matrix is capable of equalizing the channel under an optimal antenna arrangement. However, such a system is more widely considered in short range communication due to its high requirements on arrangement precision. If displacement errors occur, the phase coupling matrix $\mathbf{H}_{\mathrm{LoS}}$ will have mismatches with $\mathbf{H}_{\mathrm{o}}$, $\mathbf{H}_{\mathrm{LoS}} \neq \mathbf{H}_{\mathrm{o}}$. All the N^2 entries within $\mathbf{H}_{\mathrm{LoS}}$ change rapidly w.r.t. offset differences along x-directions, see (3.5) where $x_{n_{\mathrm{t}}}$ and $x_{n_{\mathrm{r}}}$ are normalized w.r.t. an ultra-small distance λ. As shown by our earlier work in [SRF16], a fixed analog equalizing network without variable components is very sensitive to displacements introduced by deployment, especially for rotation errors around y-axis or z-axis, e.g., very strong interference is observed with rotation errors in order of 0.1°.

To cope with different displacement errors during massive deployments, although the channel of each deployment has high temporal stability, variable channel equalization methods need to be developed for different realizations. The channel could only be fully equalized using analog components allowing arbitrary magnitude scaling and phase shifting operations. ZF based analog equalization methods are then proposed and realized. Works in [STS+08a, STS+08b] demonstrate an analog equalizing network for a 2×2 LoS MIMO system with phase shifters operating at intermediate frequencies. The suggested analog equalizing network can provide communication at distances of 6 meters in an indoor environment and 41 meters in an outdoor environment. This work is extended to a 4×4 MIMO system with variable gain amplifiers (VGA) allowing magnitude scaling and variable phase shifters (VPS) [SST+09]. For completeness, their design on stream separation components is depicted in Fig. 4.4 (c). The function of such a ZF based analog equalizing network can be recognized corresponding to the earlier mentioned solution in (4.14) as

$$\mathbf{W} = \mathbf{W}_{\mathrm{ZF}}. \tag{4.36}$$

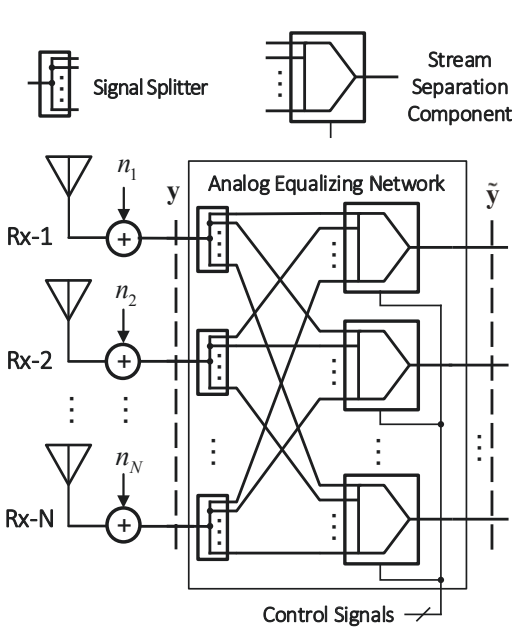

(a) Analog Equalizing network block diagram;

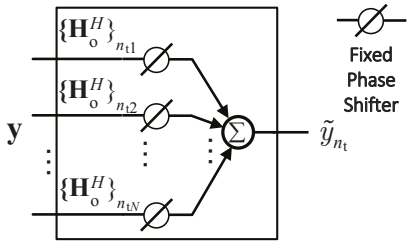

(b) Design of stream separation components using fixed phase shifters;

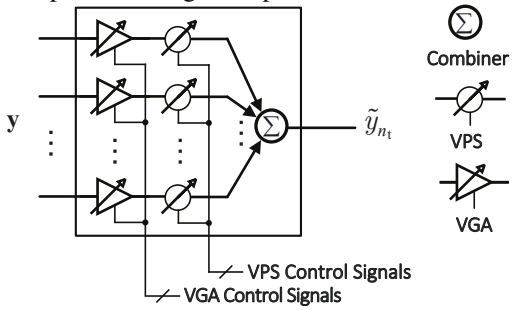

(c) Design of stream separation components using fully configurable components;

Figure 4.4: Conventional analog equalization designs with a naive matrix multiplication. (Source: [SCR+18] © 2018 IEEE).

However, the ZF based analog equalizing network requires ultra-high complexity on network wiring, e.g., many crossovers, many splitters, many combiners and high control complexity. In addition, it can be seen in Fig. 4.4 (a) and (c) that N^2 VGA-VPS pairs are required for equalizing the almost deterministic channel. Considering their power consumption, an example of a CMOS based VPS for 60GHz is presented in [LLWC09] with 10 mW in their test. Although the power consumption is, in general, less than that of the ADCs, the number of linear phase shifters should also be limited. In the next part of this section, we show that the sequential channel equalizing network requires only $2N$ VGA-VPS pairs with a well-known fixed network including wiring, i.e., Butler matrices.

4.4.3 Sequential Channel Equalization with Butler Matrices

With perfect equalization, the spatial multiplexing gain is quite robust w.r.t displacements as shown in Sec. 2.3. Only for rather large displacements, the undesired interferences become large and spatial multiplexing gains decrease. However, in practical implementations with low resolution ADCs, the systems suffer from high quantization errors. Having the channel perfectly equalized requires very complicated hardware design, high control complexity, and high power consumption. On the other hard, the performance of simple fixed implementations is quite sensitive and becomes practically infeasible. Seeking for a good compromise between complexity and performance, in this section, we propose a novel design on the analog equalizing network following the SCE steps specified in Sec. 4.2.1. The proposed network achieves high robustness with a complexity that is increasing almost linearly w.r.t. the number of streams.

Following the discussions in Sec. 4.2.1, the analog equalizing network can be applied in three steps corresponding to the matrices $\mathbf{D}_1$, $\mathbf{W}_{\text{fix}}$, and $\mathbf{D}_2$ in (4.17). The fixed equalizing

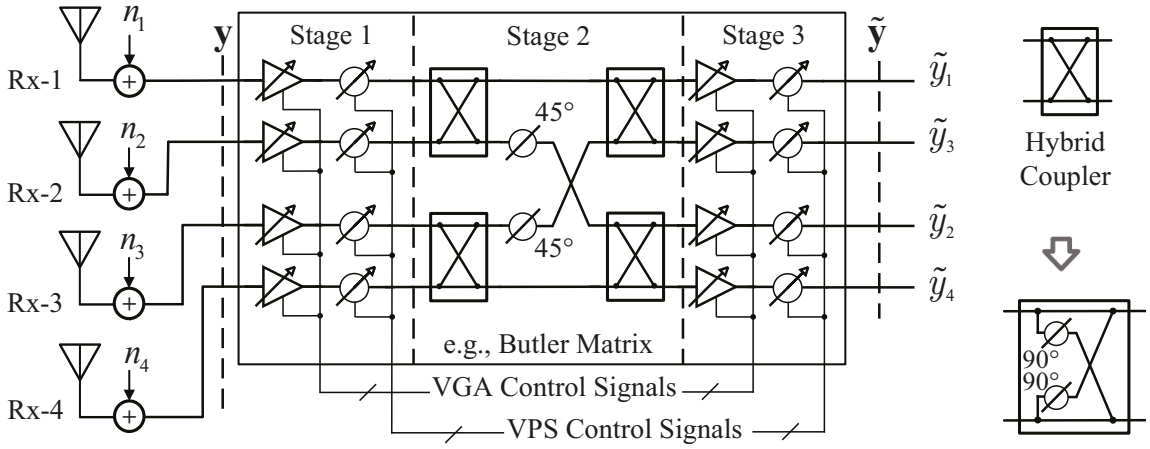

Figure 4.5: Schematic illustration of a sequential analog equalizing network. A LoS MIMO system with ULAs of $N = 4$ is assumed here. (Source: [SCR+18] © 2018 IEEE).

network $\mathbf{W}_{\text{fix}}$ in the middle can be designed in multiple ways, e.g., $\mathbf{W}_{\text{fix}} = \mathbf{H}_{\text{o}}^H$ or $\mathbf{W}_{\text{fix}} = \mathbf{W}_{\text{DFT-}N}$ with the same structure as Fig. 4.4 (b). However, such layouts require a large number of fixed phase shifters and a large amount of efforts in wiring. Instead of having an exact N-point DFT matrix in the second stage, the design for the fixed analog equalizing network can be further simplified using an N-point Butler matrix $\mathbf{W}_{\text{fix}} = \mathbf{W}_{\text{BM-}N}$, which is an analog circuit equivalent to FFT [Han09], see Fig. 4.5 with an example of $N = 4$. Butler matrices of other values are also available, e.g., an implementation with $N = 3$ can be found in [ZSS+14].

Originally, Butler matrices are typically found in RF network designs for analog beamforming purposes. The FFT based[3] Butler matrix is widely considered for orthogonal beamforming since multiple ports can be used simultaneously. The Butler matrix approach does not require the usage of VPSs or VGAs. It operates in an efficient way with the minimum number of components and minimum path length of all uniform excitation beamforming networks [Han09]. The number of required fixed phase shifters is reduced from N^2 to an order of $\mathcal{O}(N \log N)$.

Since the effective matrix $\mathbf{W}_{\text{BM-}N}$ of a Butler matrix design is a DFT based matrix, the performance is equivalent to a complete fixed analog network that produces $\mathbf{W}_{\text{fix}} = \mathbf{W}_{\text{DFT-}N}$ or $\mathbf{W}_{\text{fix}} = \mathbf{H}_{\text{o}}^H$. The steps for finding the parameters of $\mathbf{D}_1$ and $\mathbf{D}_2$ are the same as the algorithm specified in Sec. 4.2.2. The suggested design uses fewer controllable elements. The number of fully configurable VGA-VPS pairs is reduced from N^2 to $2N$. Therefore, we conclude that the proposed analog equalizing network design reduces the system complexity significantly and overcomes the complicated wiring challenges via using standard Butler matrix designs of fewer fixed phase shifters. The hybrid couplers used in Butler matrices have no crossover, and a cascade of two hybrid couplers would work as a crossover (the signals at two inputs are switched at the outputs). This would make the complete Butler matrix design having only one layer on the substrate.

In the rest of this section, we examine the design of analog SCE with URAs. Considering the similarity between (4.5) and (4.7), the crucial parts are the DFT matrix and the Kronecker

[3] The effective matrix $\mathbf{W}_{\text{BM-}N}$ can always be transformed into a DFT matrix by multiplying two diagonal matrices $\mathbf{D}_L$, $\mathbf{D}_R$ to the left and right, respectively, as $\mathbf{W}_{\text{DFT-}N} = \mathbf{D}_L \mathbf{W}_{\text{BM-}N} \mathbf{D}_R$. Since, the diagonals of $\mathbf{D}_L$ and $\mathbf{D}_R$ are of a unit magnitude and present phase shifts, $\mathbf{H}_{\text{o}}$ in (4.2) can also be written as $\mathbf{H}_{\text{o}} = (\mathbf{D}_{\text{L-}N}\mathbf{D}_R^*)\, \mathbf{W}_{\text{BM-}N}^* \, (\mathbf{D}_L^* \mathbf{D}_{\text{R-}N})$.

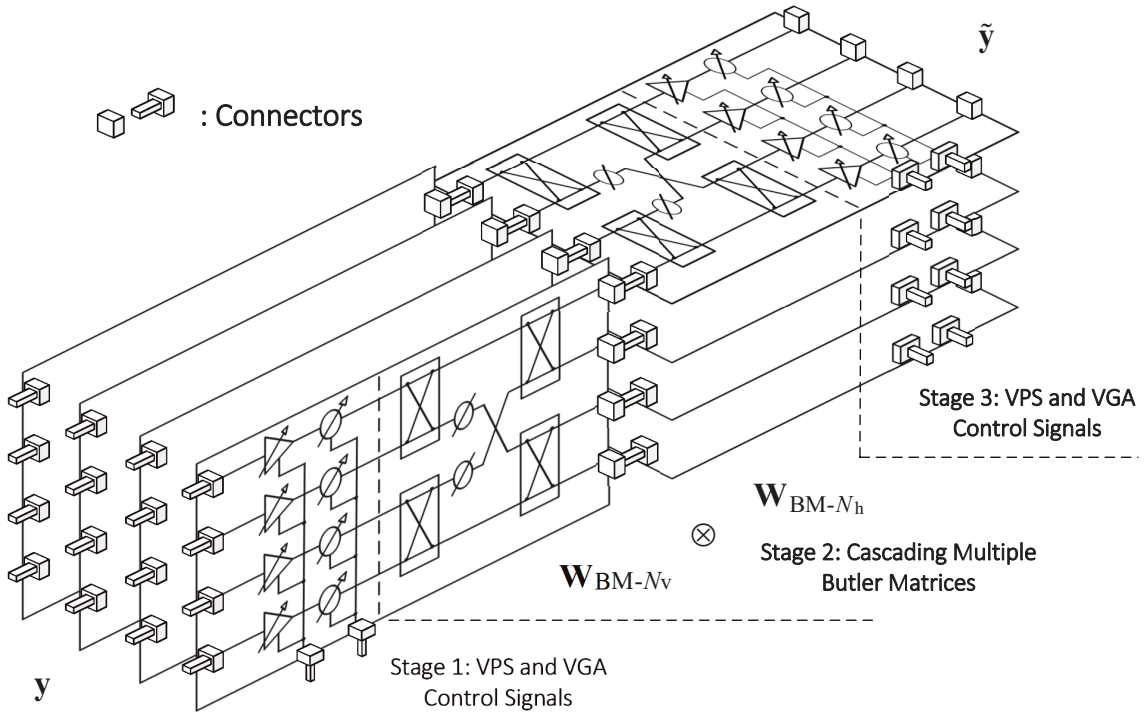

Figure 4.6: Schematic illustration of an analog equalizing network with cascading multiple Butler matrices in 3D. (Source: [SCR+18] © 2018 IEEE).

product of two DFT matrices. Therefore, equalizing $\mathbf{H}_{\mathrm{o}}$ of an URA with $N_{\mathrm{v}} \cdot N_{\mathrm{h}}$ antennas can be related to the Kronecker product between two Butler matrices. We propose to use a fixed analog equalizing network that reduces the complexity of the fixed analog equalization design for URAs in (4.35) as

$$\mathbf{W}_{\mathrm{fix}} = \mathbf{W}_{\text{BM-}N_{\mathrm{h}}} \otimes \mathbf{W}_{\text{BM-}N_{\mathrm{v}}}. \tag{4.37}$$

The Kronecker product operation in the hardware design for a fixed network is implemented as a two-stage repetitive operation. The signals of each stage can be split into multiple subsets and each subset is applied with the same operation at this stage. Therefore, the design complexity reduces significantly. One way of realizing the Kronecker product in RF designs is cascading two decks of boards with Butler matrices [Han09, CHT+12], also known as 2D Butler matrices. Instead of designing a fixed network with N^2 different paths between each input and output, the complexity is reduced to two fixed Butler matrices with N_{v}-points and N_{h}-points, respectively. An example of connecting two sets of Butler matrices, i.e., two decks of boards with $N_{\mathrm{v}} = 4$, $N_{\mathrm{h}} = 4$, is shown in Fig. 4.6. A LoS MIMO system with URAs of $N_{\mathrm{v}} = N_{\mathrm{h}} = 4$ is assumed here. The signal $\mathbf{y}$ is the input through the connectors on the left side of the diagram. The output $\tilde{\mathbf{y}}$ of the analog equalizing network on the right connects to the ADCs.

We would like to note that our earlier works in [SHR+16, SRF16] showed the feasibility of equalizing the channel in three steps, where the fixed network is chosen as $\mathbf{H}_{\mathrm{o}}^{-1}$. The same approach with $\mathbf{W}_{\mathrm{fix}} = \mathbf{H}_{\mathrm{o}}^{-1}$ is also considered independently in [MSAM15, SMMA16]. However, in those works [SHR+16, MSAM15, SRF16, SMMA16], the methods for setting the parameters of $\mathbf{D}_1$ and $\mathbf{D}_2$ are based on awareness of the channel factorization in (4.4). With the proposed SCE parameter setting method in Sec. 4.2, a more realistic assumption is made on the requirements, where only the channel matrix $\mathbf{H}_{\mathrm{LoS}}$ needs to be known (i.e., estimated) rather than its

factored form. The work in [MSAM15] also showed that the three-step equalization can be combined with a space-time equalization method. With an ultra-large bandwidth, e.g., 20 GHz at a carrier frequency of 130 GHz, displacements may introduce time-delay of several symbol durations. By introducing symbol-level delays at $\mathbf{D}_1$, $\mathbf{D}_2$, the performance floor of the conventional space-time linear processing with finite-impulse-response filters can be eliminated.

4.5 Performance Evaluation

As previously discussed, the SCE can potentially offer lower equalization complexity compared to the direct matrix inversion methods. However, this comes at the cost of having uncompensated inter-stream interference. The performance of the systems with SCE is not expected to be better than that of the ZF based solution, but rather to provide a robust performance within certain displacement error ranges. To evaluate the performance loss, the achievable rate $R(\mathbf{W})$ with linear receiver processing in (4.12) provides a good evaluation criterion.

As discussed above, the inter-stream interference is introduced by imperfect interference

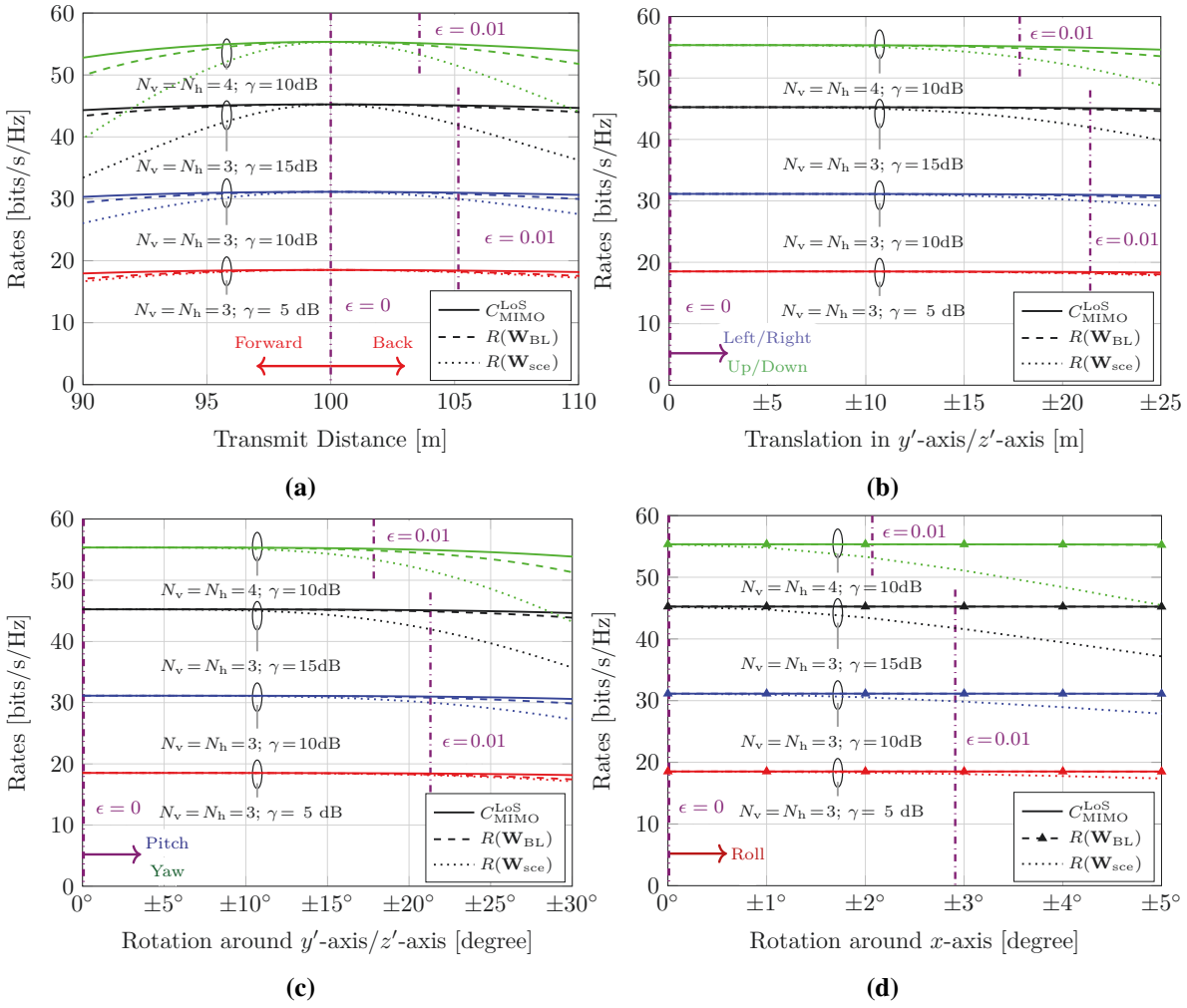

Figure 4.7: The system capacity and the achievable rates of different equalization algorithms w.r.t. different displacement errors. URAs are assumed with $N_v = N_h$ and are examined at different SNRs γ. (Source: [SCR+18] © 2018 IEEE).

suppression, since the term $\tilde{\mathbf{H}}_{\Delta}$ is ignored. In order to emulate the $\tilde{\mathbf{H}}_{\Delta}$ caused by displacement errors, the displacement error model in Sec. 2.3 is again considered with Rx arrays having 6 DoF in space, as shown in Fig. 2.5. For reducing the DoF to four, we again evaluate systems of URAs with $N = 3{\cdot}3$ and $N = 4{\cdot}4$ at different SNR values $\gamma = N\sigma_{\mathrm{s}}^2/\sigma_{\mathrm{n}}^2$. Furthermore, the inter-antenna spacings $\{d_{\mathrm{v}}, d_{\mathrm{h}}\}$ are optimized for parallel symmetric Tx and Rx at a target/estimated distance of $100\ \mathrm{m}$ with a carrier frequency of $f_{\mathrm{c}} = 60\ \mathrm{GHz}$.

Fig. 4.7 illustrates the system capacity $C_{\mathrm{MIMO}}^{\mathrm{LoS}}$ in (2.24) with equal power uncorrelated sources, the achievable rates of the SCE algorithm $R(\mathbf{W}_{\mathrm{sce}})$ and the ZF based algorithm $R(\mathbf{W}_{\mathrm{BL}})$ in (4.12). Here, we recall that ϵ is an indicator for the accuracy of the approximation from $\mathbf{W}_{\mathrm{sce}}$ to $\mathbf{W}_{\mathrm{BL}}$. Within the error ranges being considered, it can be found that displacement errors decrease the system capacity and the achievable rates of different equalization algorithms. The performance of the proposed algorithm is more sensitive to displacement errors[4]. With higher SNR values and more antenna elements, the performance loss gets larger with more displacement errors, but only slightly if one measures the performance loss in percentage. In addition, for intermediate and low SNR values, the performance loss is relatively low, since the error is more dominated by the power of the noise. Furthermore, if one considers the application scenarios with analog equalization and low resolution ADCs in Fig. 4.3 (b), the system has less performance loss in comparison with the system capacity at the low and intermediate SNR regions. This is also the region where SCE is quite robust against displacement errors. Therefore, we conclude that the proposed SCE algorithm with lower complexity is approximately as good as the ZF based algorithm for LoS MIMO systems in low and moderate SNR ranges within the displacement errors ranges being considered. For systems with high deployment accuracy, SCE works approximately as good as the ZF algorithm in high SNR regions also, with its great potential in reducing the complexity.

Fig. 4.7 (d) also suggests that more calibration efforts should be spent in reducing the roll errors since it is the most sensitive term, e.g., using a laser pointer with a cross pattern. This is because the proposed algorithm is not designed for calibrating with the in-plane displacement errors (the plane that is perpendicular to the transmit direction). Furthermore, the rotation errors of the arrays with directive antennas are expected to be relatively low during deployments. As discussed in Sec. 2.3, the beam alignment of antennas with 30dBi requires the rotation errors to be controlled within the range of $[-3^{\circ}, 3^{\circ}]$. In addition, based on our further simulations, the performance of ULAs is less sensitive to displacement errors than URAs, especially the sensitivity to roll errors is reduced to that of pitch/yaw errors. In other words, less effort is required for positioning the systems with ULAs.

Here, we also would like to make a brief discussion on the achievable positioning accuracy during deployment. The roll errors together with pitch errors can be limited to small values easily. In practice, the 6 DoF alignment control over long distances can be applied using high precision GNSS receivers and optical alignment, e.g., laser, camera. By using a camera, the work in [KKK15] achieves position errors of several millimeters and rotation errors less than one degree, e.g., the roll errors are less than 0.5°. These achieved error values are much smaller than the displacement error ranges being considered in this work.

[4] Here, we would like to note that the values of N being considered in this evaluation are already quite large for practical systems. This gives very challenging/sensitive scenarios during the robustness test.

4.6 Summary

In this chapter, an algorithm named sequential channel equalization has been proposed for strong LoS MIMO communication. Under optimal LoS MIMO antenna arrangements, IDFT like channel matrices can be obtained. Within certain displacement error ranges, the channel can be factored into a product of three matrices with the middle one dominated by an inverse DFT matrix, while the two diagonal matrices at outer positions represent the most variable terms and should be compensated adaptively. Therefore, three steps are applied sequentially in the reverse order of the channel factorization in (4.17) as

$$\mathbf{W}_{\text{sce}} \triangleq \mathbf{D}_2 \cdot \mathbf{W}_{\text{fix}} \cdot \mathbf{D}_1.$$

Adapting the sequential channel equalization to digital equalization and with the help of butterfly structures, the computational complexity is only increasing approximately linearly w.r.t. the number of streams, while the complexity of straightforward ZF implementation increases quadratically. By adapting the algorithm to analog equalization, the control complexity is also reduced to the order of $\mathcal{O}(N)$. With the help of standard Butler matrices, the complexity, e.g., wiring and the design of a DFT based equalizing network, can be further reduced. We also showed that the proposed algorithm is applicable to equalize the LoS MIMO channels with both linear and rectangular antenna arrangements. The numerical results show that, within certain displacement error ranges that are bigger than the typical errors during deployments, the proposed algorithm performs nearly as good as the zero-forcing based algorithm.

In this chapter, we summarize the key learning points for engineers as:

- Applying channel equalization in the reverse order w.r.t. the channel factorization, only the channel matrix needs to be known (i.e., estimated) rather than its factored form.
- The strong LoS MIMO channel can be equalized with an approximately linear complexity during the system expansion with more streams.
- Analog equalization can reduce the possible information loss due to the usage of low resolution ADCs in LoS MIMO communication.

Chapter 5

Hardware Imperfections and Compensation

In this chapter, with a hardware-in-the-loop demonstrator, we show that a parallel signal processing architecture can be used to handle the RF impairments in mmWave LoS MIMO systems. Practical mmWave systems may suffer from several different hardware impairments, including carrier frequency offsets (CFO), frequency-selective components, in-/quadrature-phase (I/Q) imbalances, and others [WMT+17, AK15, DOA+17], mainly due to their large bandwidths. Leaving the impairments uncompensated causes an error floor and reduces the maximum throughput [ZMB+14]. This becomes even more critical for systems with multiple spatial streams, where these effects occur in multiple different transceivers. Compensating the described effects and jointly processing the multiple streams at Gbit/s backhaul data rates are computationally intensive. One crucial aspect for these high-performance systems is thus to find processing architectures that can cope with the above mentioned impairments at implementable complexities and that scale well with the number of parallel streams.

The contents of this chapter are presented in the following order:

1. We introduce a general signal model according to the hardware-in-the-loop LoS MIMO demonstrator, where each transmit-receive antenna pair has its own CFO value.

2. An efficient frame structure for the system is then proposed and takes two effects into account: one due to the stationary channel, and the other due to the time-varying behavior of the oscillators. Based on the frame structure, a method for efficiently estimating the LoS MIMO channel and the CFOs is specified.

3. After describing several RF impairment effects that require special attention for mmWave LoS MIMO front-/backhaul systems, we propose a parallel signal processing architecture for frame based single carrier transmission. The proposed architecture divides the MIMO processing into a LoS MIMO equalization step and an RF impairment compensation step. The processing sub-steps for synchronization, frequency-selectivity compensation, and I/Q Imbalance compensation are applied in parallel, which has a good scalability to systems with even more streams. Furthermore, a decision-directed least mean square (DD-LMS) adaptive filtering approach that handles all effects simultaneously, but is of higher complexity, is introduced for baseline comparison.

4. With the hardware-in-the-loop demonstrator, the proposed frame design and signal processing architecture are validated. The architecture with high temporal efficiency and low complexity shows approximately equal sub-channel quality as the baseline high complexity DD-LMS scheme.

5.1 Signal Model and Experimental Setup

So far, we have considered the channel to be frequency-flat and time-invariant. However, several imperfections of the hardware can affect the overall transmission characteristic. Namely, the works [WMT+17, DOA+17, HCGL18] have shown that frequency-selectivity and time-varying behavior, e.g., due to the front-ends, should be expected because of the large bandwidth of mmWave systems. Furthermore, variations in the transmission channel, e.g., due to weather changes, can affect both frequency-selectivity and time-varying behavior, as well as attenuation and phase relations [ABM+15, KAM+15, XRBS00, ZWG15]. For example, rain rates of 40 mm/h can increase attenuation by up to 15dB and lower the Rician factor by 2dB for link distances of hundreds of meters.

In this section, considering the usage of widely spaced analog front-ends (AFEs) with independent oscillators, a signal model that includes frequency offsets is studied. Then, a demonstrator using off-the-shelf mmWave AFEs is specified for identifying the involved RF impairments and evaluating the performance of the proposed transmission architectures in a practical system.

5.1.1 General Signal Model for LoS MIMO Systems

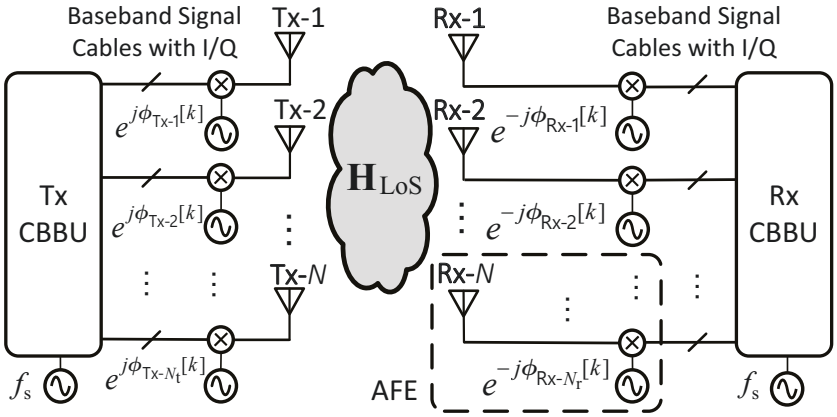

Figure 5.1: MIMO system synchronization setup, where single sampling clock references and multiple independent carrier frequency references are used. (Source: [SHC+18] © 2018 IEEE).

In a multiple antenna system with multiple front-ends, there are a wide variation of synchronization setups that can be used depending on the complexity and size constraints [PTL+16]. Due to widely spaced antennas in LoS MIMO backhaul and the need for highly integrated mmWave AFEs, the following system setup will be considered. The carrier frequency for each front-end will be generated from an independent oscillator, see Fig. 5.1. Taking the receiver side as an example, the signals are first downconverted to baseband at the antennas, and then collected by a central baseband unit (CBBU) for signal processing. The sampling frequency

f_s can then be shared from a reference clock between the different streams for the complete receiver setup.

For the present system, the two commonly encountered synchronization parameters can, thus, be summarized as follows

1. Carrier frequency offset (CFO) denotes the progressive phase variations caused by the oscillators at different Tx and Rx front-ends. It includes a fixed contribution from the carrier frequency difference and a varying part, e.g., due to phase noise.

2. Sampling frequency offset (SFO) is the common sampling clock difference between sampling clocks f_s at the Tx and the Rx.

Considering the system model illustrated in Fig. 5.1, the impact of both effects on the discrete baseband signal at time instant k can be modeled as

$$y'_{n_\mathrm{r}}[k] = \sum_{l=-\infty}^{\infty} \left(\sum_{n_\mathrm{t}=1}^{N_\mathrm{t}} e^{-j\phi_{\text{Rx-}n_\mathrm{r}}[l]} \cdot \{\mathbf{H}_\mathrm{LoS}\}_{n_\mathrm{r}n_\mathrm{t}} \cdot e^{j\phi_{\text{Tx-}n_\mathrm{t}}[l]} \cdot s_{n_\mathrm{t}}[l] \right) \cdot \mathrm{sinc}\left(\pi(k - \varepsilon[k] - l)\right) + n_{n_\mathrm{r}}[k], \tag{5.1}$$

where $y'_{n_\mathrm{r}}[k]$ and $s_{n_\mathrm{t}}[k]$ are the n_r-th receive signal and the n_t-th transmit signal, respectively. $n_{n_\mathrm{r}}[k]$ is a Gaussian noise process at the n_r-th receive front-end with $n_{n_\mathrm{r}}[k] \sim \mathcal{CN}(0, \sigma_\mathrm{n}^2)$. For simplification, we present the sampling model of a continuous-time signal with a sinc-function $\mathrm{sinc}(\cdot)$, although the root-raised-cosine (RRC) filters are more often used in practical systems (also in the experimental setup later). The phase processes $\phi_{\text{Rx-}n_\mathrm{r}}[k]$ and $\phi_{\text{Tx-}n_\mathrm{t}}[k]$ encapsulate the phase variations due to the oscillators of receive front-end Rx-n_r and transmit front-end Tx-n_t over time, respectively, with

$$\phi_{\text{Rx-}n_\mathrm{r}}[k] = \phi_{\text{Rx-}n_\mathrm{r}}[k-1] + \phi_{\Delta,\text{Rx-}n_\mathrm{r}}[k], \tag{5.2}$$

$$\phi_{\text{Tx-}n_\mathrm{t}}[k] = \phi_{\text{Tx-}n_\mathrm{t}}[k-1] + \phi_{\Delta,\text{Tx-}n_\mathrm{t}}[k], \tag{5.3}$$

where $\phi_{\text{Rx-}n_\mathrm{r}}[1]$, $\phi_{\text{Tx-}n_\mathrm{t}}[1]$ specify the initial phases of the corresponding oscillators. The terms $\phi_{\Delta,\text{Rx-}n_\mathrm{r}}[k]$ and $\phi_{\Delta,\text{Tx-}n_\mathrm{t}}[k]$ are the random phase variations of the oscillators at each sample, and are assumed to follow $\phi_{\Delta,\text{Rx-}n_\mathrm{r}}[k] \sim \mathcal{N}(\bar{\phi}_{\Delta,\text{Rx-}n_\mathrm{r}}, \sigma^2_{\phi_{\Delta,\text{Rx-}n_\mathrm{r}}})$ and $\phi_{\Delta,\text{Tx-}n_\mathrm{t}}[k] \sim \mathcal{N}(\bar{\phi}_{\Delta,\text{Tx-}n_\mathrm{t}}, \sigma^2_{\phi_{\Delta,\text{Tx-}n_\mathrm{t}}})$, respectively. The means $\bar{\phi}_{\Delta,\text{Rx-}n_\mathrm{r}}$ and $\bar{\phi}_{\Delta,\text{Tx-}n_\mathrm{t}}$ of the Gaussian processes stand for the mean CFO contributions. With $\bar{\phi}_{\Delta,\text{Rx-}n_\mathrm{r}}$ and $\bar{\phi}_{\Delta,\text{Tx-}n_\mathrm{t}}$ being zero, this kind of phase variation process is popular known as Wiener process. However, we must mention that, for the experimental system specified later, the first moments $\bar{\phi}_{\Delta,\text{Rx-}n_\mathrm{r}}$ and $\bar{\phi}_{\Delta,\text{Tx-}n_\mathrm{t}}$ of the phase variation processes are dependent on time and are gradually changing. Therefore, in the following analysis, the first moments are only considered to be stationary within certain relatively short time periods.

The SFO, expressed through the convolution with a sinc-function, acts as a common intersymbol interference generating filter. Similar to the CFO it can be modeled as

$$\varepsilon[k] = \varepsilon[k-1] + \varepsilon_\Delta[k], \tag{5.4}$$

where $\varepsilon_\Delta[k] \sim \mathcal{N}(\bar{\varepsilon}_\Delta, \sigma^2_{\varepsilon_\Delta})$ is the sampling time difference between Tx and Rx, e.g., due to SFO and timing jitter. Note that in continuous transmission modes the rate differences also need to

eventually be matched by, e.g., adding guard times, or removing samples, and adding floating buffers. This will not be treated further in this work.

As will be shown later, the sampling frequency synchronization is always performed first. Thus, with $\varepsilon[k] \approx 0$ and under Nyquist Sampling, a model only including CFO for the LoS MIMO system can be written in matrix notation as

$$\mathbf{y}[k] = \mathbf{D}_{\phi,\mathrm{Rx}}[k]\mathbf{H}_{\mathrm{LoS}}\mathbf{D}_{\phi,\mathrm{Tx}}[k]\mathbf{s}[k] + \mathbf{n}[k], \tag{5.5}$$

where

- $\mathbf{s}[k] \triangleq \left[s_1[k], \ \cdots, \ s_{N_\mathrm{t}}[k]\right]^\mathrm{T}$ collects the transmit symbols at the Nyquist Sampling;
- $\mathbf{y}[k] \triangleq \left[y_1[k], \ \cdots, \ y_{N_\mathrm{r}}[k]\right]^\mathrm{T}$ collects the receive symbols at the Nyquist Sampling;
- $\mathbf{n}[k] \triangleq \left[n_1[k], \ \cdots, \ n_{N_\mathrm{r}}[k]\right]^\mathrm{T}$ collects the corresponding noise symbols;
- $\mathbf{D}_{\phi,\mathrm{Rx}}[k] \triangleq \mathrm{diag}\left(-e^{j\phi_{\text{Rx-}1}[k]}, \ldots, e^{-j\phi_{\text{Rx-}N_\mathrm{r}}[k]}\right)$ is a $N_\mathrm{r} \times N_\mathrm{r}$ diagonal matrix collecting the CFOs at the receiver;
- $\mathbf{D}_{\phi,\mathrm{Tx}}[k] \triangleq \mathrm{diag}\left(e^{j\phi_{\text{Tx-}1}[k]}, \ldots, e^{j\phi_{\text{Tx-}N_\mathrm{t}}[k]}\right)$ is a $N_\mathrm{t} \times N_\mathrm{t}$ diagonal matrix collecting the CFOs at the transmitter.

5.1.2 Experimental Setup

In order to evaluate the performance of a practical system with the proposed algorithms and to demonstrate the LoS spatial multiplexing, a hardware-in-the-loop 2×2 LoS MIMO system was set up in an anechoic chamber with a shorter distance than what would typically be used in a backhaul deployment[1]. The purpose of carrying out the experiments in such a controlled

[1] The author would like to thank Darko Cvetkovski from Humboldt-Universität zu Berlin and Tim Hälsig from Universität der Bundeswehr München for providing the experimental data and the benchmark results. More details on the measurement procedure and channel properties can be found in [HCGL18, CGHL17]. The data is shared to the author for verifying the baseband algorithms in this chapter based on our long-term cooperation in the framework of priority program SPP 1655 "Wireless Ultra High Data Rate Communication for Mobile Internet Access" supported by the German Research Foundation (DFG).

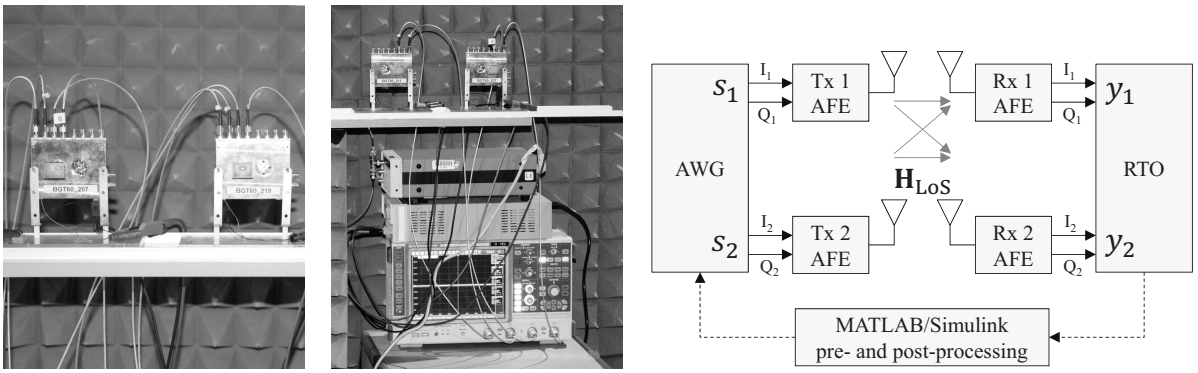

(a) mmWave AFE at Tx; **(b)** Rx setup including RTO; **(c)** Block-diagram of the demonstrator;

Figure 5.2: A 2×2 mmWave LoS MIMO demonstrator. (Source: [SCR+18, SHC+18] © 2018 IEEE).

environment is to focus on the hardware challenges in the pure LoS MIMO channel, and their corresponding signal processing algorithms. The transmit and receive arrays were set up at a transmit distance of $D = 5.5$ m with an optimal antenna spacing of $d_{\mathrm{LoS}} = 202$ mm, according to (2.11). With a 60.48 GHz carrier frequency, i.e., $\lambda \approx 5$ mm, the condition $D \gg d_{\mathrm{LoS}} \gg \lambda$ is approximately fulfilled. It should be noted that due to the manual arrangement of the setup, position and rotation tolerances of approximately ± 2 mm and $\pm 5^{\circ}$ respectively, can be expected.

The wireless transmission was performed using off-the-shelf mmWave AFEs and a complex double-sided transmission bandwidth of 1.25 GHz. The transmitted waveforms were precompiled and generated by a multi-channel arbitrary waveform generator (AWG) connected to the baseband inputs of the Tx AFEs. The signals at the baseband outputs of the Rx AFEs were captured by a real-time oscilloscope (RTO) for further offline post-processing, see Figure 5.2.

5.2 Frame Based Channel State Information Acquisition

In order to account for the stationary environment and the gradually varying oscillators, we first specify a frame structure that provides high temporal efficiency, highly reliable channel estimation, and good tracking performance on phase variations. Then, SFO estimation, LoS MIMO tap estimation, and CFO estimation are specified based on the proposed frame structure. To simplify the discussion in the rest of this work, we focus on systems with equal antenna numbers, i.e., $N_{\mathrm{r}} = N_{\mathrm{t}} = N$.

5.2.1 Frame Structure Design

A specific frame structure is proposed for mmWave LoS MIMO communication, see Fig. 5.3. Single carrier waveforms are considered here due to their better PAPR values, which potentially increase the transmit power in backhaul links with a peak EIRP constraint. Orthogonal/quasi-orthogonal training sequences of length L_{P}, denoted as $\mathbf{X}_{\mathrm{T}}[1] = [\mathbf{p}_1, \ldots, \mathbf{p}_N]^T \in \mathbb{C}^{N \times L_{\mathrm{P}}}$, are sent at the beginning as preambles and provide a reliable estimation of the channel with a large L_{P} value. Although the physical transmission channel can be considered as deterministic, the effective channel that includes the independent oscillators of the setup still vary due to carrier frequency offsets. Therefore, orthogonal/quasi-orthogonal midambles of a shorter length L_{M} are introduced periodically for estimating this variation. Together with the preambles at the start of the burst, N_{SF} sub-frames are formed which consist of a training sequence of length

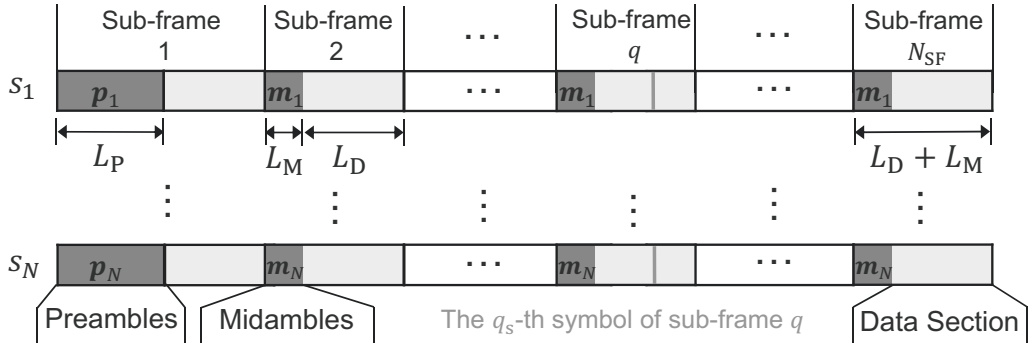

Figure 5.3: Structure of one frame. (Source: [SHC+18] © 2018 IEEE).

Structure Name	Type-A	Type-B	DD-LMS
Preamble Length (L_{P})	1023		
Midamble Length (L_{M})	127		-
Data Section Length (L_{D})	896	1919	231K
$L_{\mathrm{D}} + L_{\mathrm{M}}$	1023	2046	-
Number of Sub-Frames (N_{SF})	230	115	-
Temporal Efficiency	0.872	0.934	0.996
Modulation Scheme	QPSK		
Symbol Rate	1.25 GBd		
Transmission Rate [Gbit/s]	4.36	4.67	4.98

Table 5.1: Frame Structure Properties. The parameters are chosen in a way that balances the temporal efficiency and the reliability of the channel estimates. (Source: [SHC+18] © 2018 IEEE).

$L_{\mathrm{T}} \in \{L_{\mathrm{P}}, L_{\mathrm{M}}\}$ and a data section of length L_{D} each. In this work, we denote the midambles of the q-th sub-frame as $\mathbf{X}_{\mathrm{T}}[q] = [\mathbf{m}_1, \ldots, \mathbf{m}_N]^T \in \mathbb{C}^{N \times L_{\mathrm{M}}}$, $2 \leq q \leq N_{\mathrm{SF}}$. Furthermore, we denote the length of the sub-frame as $L_{\mathrm{SF}} \triangleq L_{\mathrm{T}} + L_{\mathrm{D}}$.

It is typically assumed that the SFO and CFOs are rather constant, i.e., they do not arbitrarily change in a short period of time. In this work, for updating the estimation, we omit the variations of SFO and CFOs within one training period but consider its variation on the frame level. In order to evaluate the impact of the non-stationarity of the effective channel, two different structures with the same timescale, annotated as Type-A and Type-B in Tab. 5.1, are investigated. The two frame structures use preambles of the same length for the initial channel estimation. Considering that the physical channel is essentially static over a long time period, the LoS MIMO equalization matrix during transmission of the complete frame of N_{SF} data sections is calculated based on this initial estimate. In addition, the usage of midambles can provide tracking of phase variations at a smaller cost than repetitively using the longer preambles. The main difference between the frame types is that Type-A spends more resources on estimating the phase variations than Type-B, yielding lower temporal efficiency. Temporal efficiency is defined as the ratio of the length of all N_{SF} data sections to the length of the complete frame. The data aided decision directed least-mean-square (DD-LMS), to be introduced later, just makes use of one preamble for initialization, and does not require midambles. For completeness, its frame structure is also specified in Tab. 5.1. The involved parameters should be carefully set according to the phase process of the AFEs. In particular, for the present setup with $\hat{\sigma}^2_{\phi_{\Delta,\mathrm{Tx}\text{-}n_{\mathrm{t}}}} = \hat{\sigma}^2_{\phi_{\Delta,\mathrm{Rx}\text{-}n_{\mathrm{r}}}} \approx 3.5 \cdot 10^{-6}\,\mathrm{rad}^2$, a phase deviation of $\pm\sqrt{L_{\mathrm{D}} + L_{\mathrm{T}}} \cdot 0.45^\circ$ per sub-frame can be expected. Therefore, for 4-QAM symbol alphabets, settings with $L_{\mathrm{D}} + L_{\mathrm{M}} < 3000$ are suitable choices. The used values in Tab. 5.1 obey the above discussion and are chosen based on experimental evaluations of multiple parameter settings.

5.2.2 Channel State Information Estimation

In this section, we focus on the LoS MIMO tap estimation and the CFO estimation based on the proposed frame structure at the Nyquist sampling rate during baseband signal processing.

SFO Estimation: In this section, the SFO is estimated at first based on the pre- and midambles with a correlation based method proposed in [GHLS02, WCS05]. The sampling index k_q at the beginning of the q-th sub-frame are found with the highest correlation peak and an esti-

mate $\hat{\varepsilon}[k_q]$ is made for $\varepsilon[k]$ in (5.1) of samples within the q-th sub-frame. Since SFO estimation is not the focus of our work, we repeat several key steps that are used during the post-processing in the Appendix A.1. For data processing and channel estimation after SFO compensation, down-sampling to symbol rate is performed and the Nyquist sampling rate is considered in the rest of this work[2].

Joint Channel and CFO Estimation Methods: From (5.5), the physical channel and CFO require a joint estimation in general. This MIMO CSI estimation problem was considered previously in the literature, under different assumptions. The work in [GS06] reported an algorithm that estimates the CSI in frequency-selective channels under the assumption that the CFO is equal for all transmit-receive antenna pairs. Considering flat channels, [HL16] studied synchronization with the shared carrier frequency for LoS MIMO systems. The work in [BS03] proposes the use of maximum likelihood principles for the joint estimation of multiple CFOs and channel gains, in flat channels. By modeling independent phase noise processes at individual antennas, [MNB$^+$12] proposes a decision-directed least squares method for tracking the phase variation at the cost of high complexity for flat fading channels, e.g., $\mathcal{O}(N^6)$.

For the experimental system, the CFO values are relatively small w.r.t. the symbol rate, e.g., the estimated normalized angular CFOs have mean values in the order of $10^{-4}\,\mathrm{rad/symbol}$ [HCGL18]. Additionally, the variance of phase noise is small with $\hat{\sigma}^2_{\phi_{\Delta,\text{Tx-}n_\text{t}}} = \sigma^2_{\phi_{\Delta,\text{Rx-}n_\text{r}}} \approx 3.5 \cdot 10^{-6}\,\mathrm{rad}^2$. Estimating those small CFOs using a single training sequence set requires fairly long training sequences leading to a low temporal efficiency. The above properties and statements hold similarly for a practical multi-stream backhaul system. Therefore, we decouple the joint estimation problem into two steps having relatively low complexity. First, we estimate the channel at the start of each sub-frame and then the CFO estimation is carried out using the estimates of the two neighboring sub-frames.

LoS MIMO Tap Estimation: Considering (5.5), the initial channel state of the q-th sub-frame can be defined as

$$\mathbf{H}_\phi[q] \triangleq \mathbf{D}_{\phi,\text{Rx}}[k_q]\mathbf{H}_\text{LoS}\mathbf{D}_{\phi,\text{Tx}}[k_q]. \tag{5.6}$$

Here, we recall that k_q is the the sampling index at the beginning of the q-th sub-frame. To simplify the discussion later, the accumulated phase shifts of oscillators at the q-th sub-frame, which collect the phase terms of $\mathbf{D}_{\phi,\text{Tx}}[k_q]$ and $\mathbf{D}_{\phi,\text{Rx}}[k_q]$, are defined as $\boldsymbol{\phi}_\text{Tx}[q] \triangleq [\phi_{\text{Tx-}1}[k_q], ..., \phi_{\text{Tx-}N}[k_q]]^T$ and $\boldsymbol{\phi}_\text{Rx}[q] \triangleq [\phi_{\text{Rx-}1}[k_q], ..., \phi_{\text{Rx-}N}[k_q]]^T$, respectively, i.e., $\mathbf{D}_{\phi,\text{Tx}}[k_q] = \mathrm{diag}(e^{j\boldsymbol{\phi}_\text{Tx}[q]})$ and $\mathbf{D}_{\phi,\text{Rx}}[k_q] = \mathrm{diag}(e^{-j\boldsymbol{\phi}_\text{Rx}[q]})$.

In the proposed frame based transmission scheme, N training sequences with length L_T are radiated by N transmit antennas at the beginning of each sub-frame. As defined in Sec. 5.2.1, the matrix $\mathbf{X}_\text{T}[q] \in \mathbb{C}^{N\times L_\text{T}}$ collects the training sequences of the q-th sub-frame. Then, by assuming that the channel is stationary during training sequence transmission, the received preambles $\mathbf{Y}_\text{T}[q] \in \mathbb{C}^{N\times L_\text{T}}$ of the q-th sub-frame are found according to (5.5) as

$$\mathbf{Y}_\text{T}[q] = \mathbf{H}_\phi[q]\mathbf{X}_\text{T}[q] + \mathbf{N}_\text{T}[q], \tag{5.7}$$

where $\mathbf{N}_\text{T}[q] \in \mathbb{C}^{N\times L_\text{T}}$ contains the noise. With orthogonal/quasi-orthogonal training se-

[2] For having a fair performance comparison with the DD-LMS algorithm, the same symbol set after SFO compensation is also used for analyzing DD-LMS.

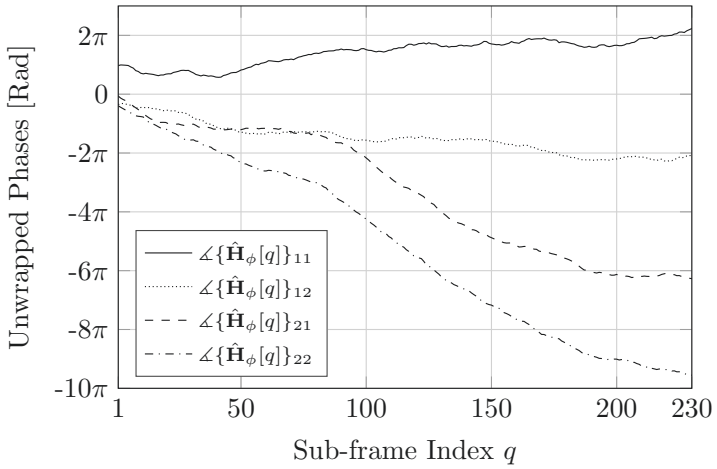

Figure 5.4: Phase variations of the effective channel on the time scale of multiple sub-frames.

quences, and using the least squares algorithm, we estimate the initial channel state as

$$\begin{aligned}\hat{\mathbf{H}}_{\phi}[q] &= \mathbf{Y}_{\mathrm{T}}[q]\mathbf{X}_{\mathrm{T}}^{\mathrm{H}}[q](\mathbf{X}_{\mathrm{T}}[q]\mathbf{X}_{\mathrm{T}}^{\mathrm{H}}[q])^{-1} \\ &= \mathbf{H}_{\phi}[q] + \underbrace{\mathbf{N}_{\mathrm{T}}[q]\mathbf{X}_{\mathrm{T}}^{\mathrm{H}}[q](\mathbf{X}_{\mathrm{T}}[q]\mathbf{X}_{\mathrm{T}}^{\mathrm{H}}[q])^{-1}}_{\text{Estimation Errors}} \end{aligned} \tag{5.8}$$

CFO Estimation: In this part, we use channel estimation results of two neighboring sub-frames for an estimate of the CFO. As mentioned above, for the experimental system, the CFO values are relatively small w.r.t. the symbol rate. However, on the time scale of one or multiple sub-frames, the accumulated phase changes are non-negligible as shown in Fig. 5.4. Frame structure type-A is used here for visualizing the variation. Furthermore, the CFO values are found to be also gradually changing and their estimates need updates.

In order to have good performance with large frame/sub-frame sizes, the accumulated phase changes need to be compensated. According to (5.6), the following relation is found for the neighboring baseband coupling matrices $\mathbf{H}_{\phi}[q]$

$$\mathbf{H}_{\phi}[q+1] = \mathbf{D}_{\psi,\mathrm{Rx}}[q]\mathbf{H}_{\phi}[q]\mathbf{D}_{\psi,\mathrm{Tx}}[q], \tag{5.9}$$

where $\mathbf{D}_{\psi,\mathrm{Tx}}[q] \triangleq \mathrm{diag}(e^{j\boldsymbol{\psi}_{\mathrm{Tx}}[q]})$ and $\mathbf{D}_{\psi,\mathrm{Rx}}[q] \triangleq \mathrm{diag}(e^{-j\boldsymbol{\psi}_{\mathrm{Rx}}[q]})$ are two $N\times N$ diagonal matrices. The phase terms $\boldsymbol{\psi}_{\mathrm{Tx}}[q]$ and $\boldsymbol{\psi}_{\mathrm{Rx}}[q]$ of their diagonal elements are phase increments at Tx and Rx from sub-frame q to sub-frame $q+1$, $\boldsymbol{\psi}_{\mathrm{Tx}}[q] \triangleq \boldsymbol{\phi}_{\mathrm{Tx}}[q+1] - \boldsymbol{\phi}_{\mathrm{Tx}}[q]$ and $\boldsymbol{\psi}_{\mathrm{Rx}}[q] \triangleq \boldsymbol{\phi}_{\mathrm{Rx}}[q+1] - \boldsymbol{\phi}_{\mathrm{Rx}}[q]$, respectively. Omitting the estimation errors in (5.8), we have

$$\hat{\mathbf{H}}_{\phi}[q+1] \approx \mathbf{D}_{\psi,\mathrm{Rx}}[q]\hat{\mathbf{H}}_{\phi}[q]\mathbf{D}_{\psi,\mathrm{Tx}}[q]. \tag{5.10}$$

In order to estimate the evolution of the phase coupling, (5.10) is vectorized as

$$\mathrm{vec}(\hat{\mathbf{H}}_{\phi}[q+1]) = \mathrm{vec}(\hat{\mathbf{H}}_{\phi}[q]) \odot \mathrm{vec}(e^{-j\boldsymbol{\psi}_{\mathrm{Rx}}[q]} \cdot e^{j\boldsymbol{\psi}_{\mathrm{Tx}}^{T}[q]}), \tag{5.11}$$

$$\mathrm{vec}(\hat{\mathbf{H}}_{\phi}[q+1]) \odot \mathrm{vec}(\hat{\mathbf{H}}_{\phi}^{*}[q]) = \mathrm{vec}(e^{-j\boldsymbol{\psi}_{\mathrm{Rx}}[q]} \cdot e^{j\boldsymbol{\psi}_{\mathrm{Tx}}^{T}[q]}), \tag{5.12}$$

where $e^{j-\boldsymbol{\psi}_{\mathrm{Rx}}[q]}$, $e^{j\boldsymbol{\psi}_{\mathrm{Tx}}^{T}[q]}$ are a column vector and a row vector that collect the diagonal entries of $\mathbf{D}_{\psi,\mathrm{Rx}}[q]$ and $\mathbf{D}_{\psi,\mathrm{Tx}}[q]$, respectively.

We reformulate (5.12) in terms of its phase coupling as

$$\measuredangle\mathrm{vec}(\hat{\mathbf{H}}_\phi[q+1]) - \measuredangle\mathrm{vec}(\hat{\mathbf{H}}_\phi[q]) = \underbrace{\Big[\mathbf{I}_N \otimes \mathbf{1}_{N\times 1},\ -\mathbf{1}_{N\times 1} \otimes \mathbf{I}_N\Big]}_{\triangleq\ \mathbf{C}\ \in\mathbb{C}^{N^2\times 2N}} \begin{bmatrix}\boldsymbol{\psi}_{\mathrm{Tx}}[q]\\ \boldsymbol{\psi}_{\mathrm{Rx}}[q]\end{bmatrix}. \tag{5.13}$$

The estimate of the CFOs $\boldsymbol{\psi}_{\mathrm{Rx}}[q]$ and $\boldsymbol{\psi}_{\mathrm{Tx}}[q]$ during the q-th sub-frame transmission can be obtained via[3]

$$\begin{bmatrix}\hat{\boldsymbol{\psi}}_{\mathrm{Tx}}[q]\\ \hat{\boldsymbol{\psi}}_{\mathrm{Rx}}[q]\end{bmatrix} = \mathbf{C}^\dagger \cdot \Big(\measuredangle\mathrm{vec}(\hat{\mathbf{H}}_\phi[q+1]) - \measuredangle\mathrm{vec}(\hat{\mathbf{H}}_\phi[q])\Big). \tag{5.14}$$

This information can be used for de-rotating the data symbols of the q-th sub-frame at Rx and Tx with the progressively added terms $\hat{\boldsymbol{\psi}}_{\mathrm{Rx}}[q]/L_{\mathrm{SF}}$ and $-\hat{\boldsymbol{\psi}}_{\mathrm{Tx}}[q]/L_{\mathrm{SF}}$, respectively. After equalizing the symbols of the q-th sub-frame, the accumulated phase shifts $\boldsymbol{\phi}_{\mathrm{Rx}}[q]$ and $\boldsymbol{\phi}_{\mathrm{Tx}}[q]$ at the start of the sub-frame q is found as

$$\begin{bmatrix}\hat{\boldsymbol{\phi}}_{\mathrm{Tx}}[q+1]\\ \hat{\boldsymbol{\phi}}_{\mathrm{Rx}}[q+1]\end{bmatrix} = \begin{bmatrix}\hat{\boldsymbol{\phi}}_{\mathrm{Tx}}[q]\\ \hat{\boldsymbol{\phi}}_{\mathrm{Rx}}[q]\end{bmatrix} + \begin{bmatrix}\hat{\boldsymbol{\psi}}_{\mathrm{Tx}}[q]\\ \hat{\boldsymbol{\psi}}_{\mathrm{Rx}}[q]\end{bmatrix}. \tag{5.15}$$

Next, we will present a low-complexity scalable LoS MIMO processing architecture based on the CSI obtained above.

5.3 Channel Synchronization and Equalization

This section focuses on effectively handling impairment effects that influence the LoS MIMO system during frame based data transmission. Single-tap strong LoS MIMO backhaul systems are usually considered to have flat channels. However, the effective channel including the wideband mmWave AFEs is frequency-selective. This phenomenon is noticed with a SISO setup using the same equipment and was also reported by other SISO measurement works, e.g., using CMOS transceivers [WMT+17]. In practical systems, the superimposed receive signals thus contain not only interantenna interference (IAI) from the MIMO coupling, but also intersymbol interference (ISI) within each stream due to the mentioned frequency-selectivity. MIMO signal processing methods generally require a quadratic order of complexity w.r.t. the number of streams N, e.g., general matrix multiplications require operations of $\mathcal{O}(N^2)$. Since the RF impairment effects get more complex in MIMO scenarios, the required complexity of conventional processing methods limits the system size, especially for high symbol rate mmWave transmission.

A low-complexity scalable LoS MIMO architecture, named single-tap interantenna interference and parallel intersymbol interference equalization (STIAI+PISIE), is proposed in this work. As will be shown later, after removing IAI in the same sense as interstream interference,

[3] The phase coupling matrix $\mathbf{C}$ and its Pseudo-inverse matrix $\mathbf{C}^\dagger$ have the same rank of $2N-1$. Therefore, it is not possible to estimate the true values of $\boldsymbol{\psi}_{\mathrm{Tx}}[q]$ and $\boldsymbol{\psi}_{\mathrm{Rx}}[q]$. But using this formula, we can estimate their differences, which are sufficient for compensating CFOs. Here, $\hat{\boldsymbol{\psi}}_{\mathrm{Tx}}[q]$ and $\hat{\boldsymbol{\psi}}_{\mathrm{Rx}}[q]$ would have the same unknown bias which cancels each other later in (5.18) or (5.19).

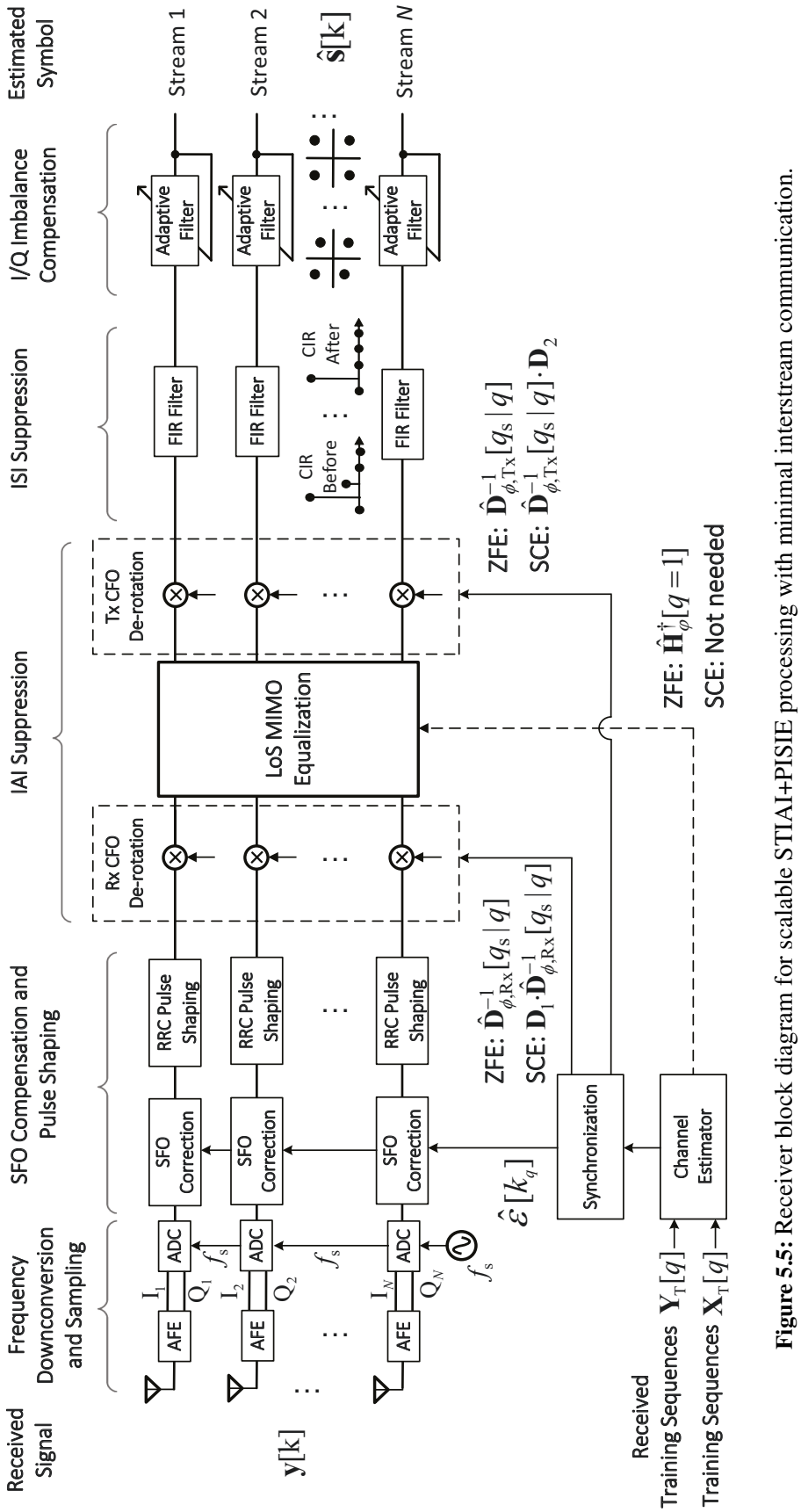

Figure 5.5: Receiver block diagram for scalable STIAI+PISIE processing with minimal interstream communication.

the remaining processing steps can be carried out independently for each stream. In this work, the complete STIAI+PISIE contains two steps. First, the LoS MIMO single-tap equalization is applied to remove the IAI. Then, the ISI introduced by frequency-selective hardware is suppressed with several parallel processing chains. The proposed architecture, therefore, includes modules for synchronization, MIMO channel equalization, ISI suppression, and I/Q imbalance compensation, see Fig. 5.5. As one method for suppressing ISI, the minimum mean square error finite impulse response (MMSE-FIR) filters are independently applied to each stream. Owing to a parallel and systolic structure, the proposed architecture is very suitable for implementation, and no clock distribution network is required for the time continuous digital operation. The proposed architecture, therefore, enables very high and scalable throughput.

5.3.1 Single-Tap Interantenna Interference and Parallel Intersymbol Interference Equalization

In this part, we specify the proposed STIAI+PISIE in terms of its modules for SFO compensation, CFO compensation, MIMO channel equalization, ISI suppression, and I/Q imbalance compensation.

SFO Compensation: Since in our system, the sampling clocks of all Tx-chains are the same and of all Rx-chains are the same (Fig. 5.1), only a single SFO value arises between Tx and Rx. The SFO is compensated using interpolation with a low pass filter based on the estimated SFO value for each receive stream in parallel. Specifically, this means

$$y_{n_\mathrm{r}}[k] = \sum_{l=-\infty}^{\infty} y'_{n_\mathrm{r}}[l] \cdot \mathrm{sinc}\left(\pi(k + \hat{\varepsilon}[k_q] - l)\right). \tag{5.16}$$

IAI Suppression: In this part, the LoS MIMO tap equalization including physical LoS MIMO channel equalization and the CFO compensation is introduced for the IAI suppression. Considering (5.6), the phase shifts caused by CFOs at Rx and Tx occur as left and right diagonal matrix multiplications to the physical channel, respectively. After gathering the accumulated phase variations $\hat{\boldsymbol{\phi}}_{\mathrm{Rx}}[q]$, $\hat{\boldsymbol{\phi}}_{\mathrm{Tx}}[q]$ and the q-th sub-frame's mean CFOs $\hat{\boldsymbol{\psi}}_{\mathrm{Rx}}[q]$, $\hat{\boldsymbol{\psi}}_{\mathrm{Tx}}[q]$, we predict the effective channel of the q_s-th baseband symbol of the sub-frame q using the interpolation algorithm as

$$\hat{\mathbf{H}}_\phi[q_\mathrm{s}|q] = \hat{\mathbf{D}}_{\phi,\mathrm{Rx}}[q_\mathrm{s}|q]\hat{\mathbf{H}}_\phi[1]\hat{\mathbf{D}}_{\phi,\mathrm{Tx}}[q_\mathrm{s}|q], \tag{5.17}$$

where $\hat{\mathbf{D}}_{\phi,\mathrm{Rx}}[q_\mathrm{s}|q] \triangleq \mathrm{diag}(e^{-j(\hat{\boldsymbol{\phi}}_{\mathrm{Rx}}[q]+\hat{\boldsymbol{\psi}}_{\mathrm{Rx}}[q]\cdot q_\mathrm{s}/L_{\mathrm{SF}})})$, $\hat{\mathbf{D}}_{\phi,\mathrm{Tx}}[q_\mathrm{s}|q] \triangleq \mathrm{diag}(e^{j(\hat{\boldsymbol{\phi}}_{\mathrm{Tx}}[q]+\hat{\boldsymbol{\psi}}_{\mathrm{Tx}}[q]\cdot q_\mathrm{s}/L_{\mathrm{SF}})})$ and we recall that L_{SF} is the sub-frame length with $L_{\mathrm{SF}} = L_{\mathrm{T}} + L_{\mathrm{D}}$. Therefore, the symbol index q_s satisfies $0 \leq q_\mathrm{s} \leq L_{\mathrm{SF}} - 1$.

As discussed in Chapter 4, this work focuses on two linear channel equalization methods, namely zero-forcing equalization (ZFE) and sequential channel equalization (SCE). Since both of the methods can be used for IAI suppression, we specify their implementations in this frame based transmission with independent CFOs in the following.

1) IAI Suppression with ZFE

The IAI Suppression with ZFE and CFO compensation are, thus, applied jointly in the reverse order w.r.t. (5.17) as

$$\mathbf{G}_{\mathrm{ZFE}}[q_{\mathrm{s}}|q] = \hat{\mathbf{D}}^{-1}_{\phi,\mathrm{Tx}}[q_{\mathrm{s}}|q]\hat{\mathbf{H}}^{\dagger}_{\phi}[1]\hat{\mathbf{D}}^{-1}_{\phi,\mathrm{Rx}}[q_{\mathrm{s}}|q], \tag{5.18}$$

where two phase de-rotation process sets $\hat{\mathbf{D}}^{-1}_{\phi,\mathrm{Rx}}[q_{\mathrm{s}}|q]$ and $\hat{\mathbf{D}}^{-1}_{\phi,\mathrm{Tx}}[q_{\mathrm{s}}|q]$ are found to compensate the CFOs at Rx and Tx, respectively. Their progressively added phase terms at the q-th sub-frame are found as $\hat{\boldsymbol{\psi}}_{\mathrm{Rx}}[q]/L_{\mathrm{SF}}$ and $-\hat{\boldsymbol{\psi}}_{\mathrm{Tx}}[q]/L_{\mathrm{SF}}$, respectively, which are estimated in (5.14). The initial phase values of two de-rotation processes are set as zeros.

2) IAI Suppression with SCE

Jointly considering the reverse order of (5.17) and the steps of SCE in (4.17), the complete equalization including SCE and CFO compensation is modeled as

$$\mathbf{G}_{\mathrm{SCE}}[q_{\mathrm{s}}|q] = \hat{\mathbf{D}}^{-1}_{\phi,\mathrm{Tx}}[q_{\mathrm{s}}|q] \cdot \mathbf{D}_2 \cdot \mathbf{W}_{\text{DFT-}N} \cdot \mathbf{D}_1 \cdot \hat{\mathbf{D}}^{-1}_{\phi,\mathrm{Rx}}[q_{\mathrm{s}}|q]. \tag{5.19}$$

where the diagonal matrices $\mathbf{D}_1$ and $\mathbf{D}_2$ are obtained by the method in Sec. 4.2.2, and we replace the $\mathbf{W}_{\mathrm{BL}}$ there with $\hat{\mathbf{H}}^{\dagger}_{\phi}[1]$. During compensating the progressively added phase rotations caused by the CFOs, the static contributions of $\mathbf{D}_1$ and $\mathbf{D}_2$ can be modeled as the initial phases of the two phase de-rotation process sets, $\mathbf{D}_1 \cdot \hat{\mathbf{D}}^{-1}_{\phi,\mathrm{Rx}}[q_{\mathrm{s}}|q]$ and $\hat{\mathbf{D}}^{-1}_{\phi,\mathrm{Tx}}[q_{\mathrm{s}}|q] \cdot \mathbf{D}_2$, respectively. Therefore, the two matrices $\mathbf{D}_1$ and $\mathbf{D}_2$ introduce no additional computational complexity after initialization.

We would like to note that certain other RF impairments like gain variations over time and gain mismatches at amplifiers can be compensated by changing the amplitudes of diagonal el-

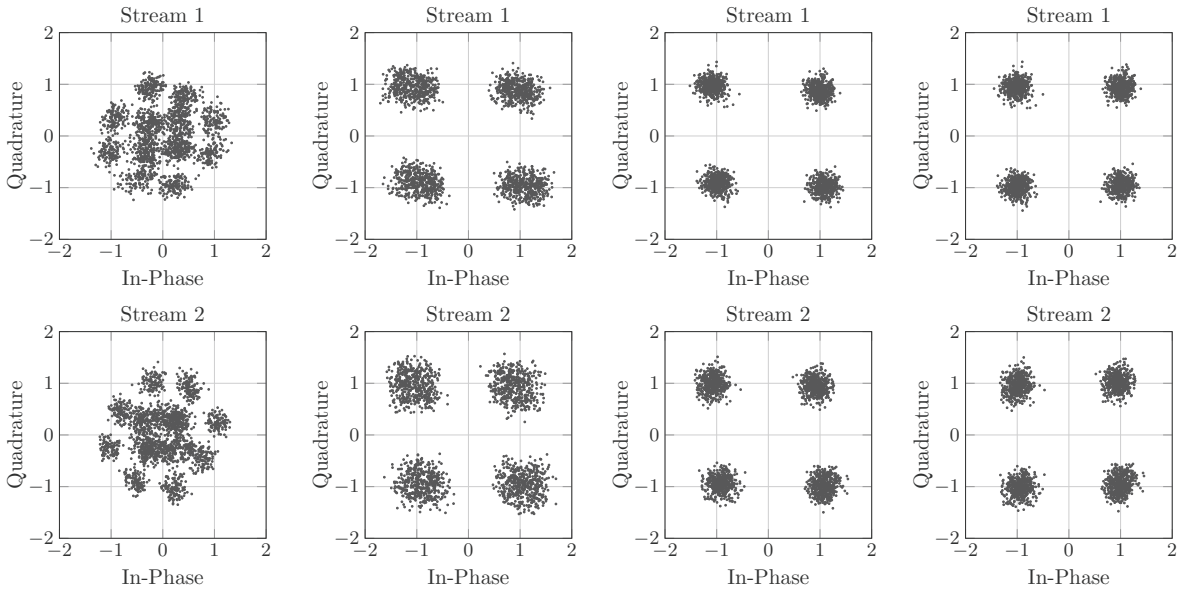

(a) Received superimposed symbols at Nyquist rate; **(b)** After IAI Suppression (e.g., $\mathrm{EVM}_1 = -12.8$dB); **(c)** After ISI Suppression (e.g., $\mathrm{EVM}_1 = -16.4$dB); **(d)** After I/Q Imbal. Comp. (e.g., $\mathrm{EVM}_1 = -17.0$dB);

Figure 5.6: Constellation diagrams of data symbols in the last sub-frame at each step of the STIAI+PISIE. (Source: [SHC+18] © 2018 IEEE).

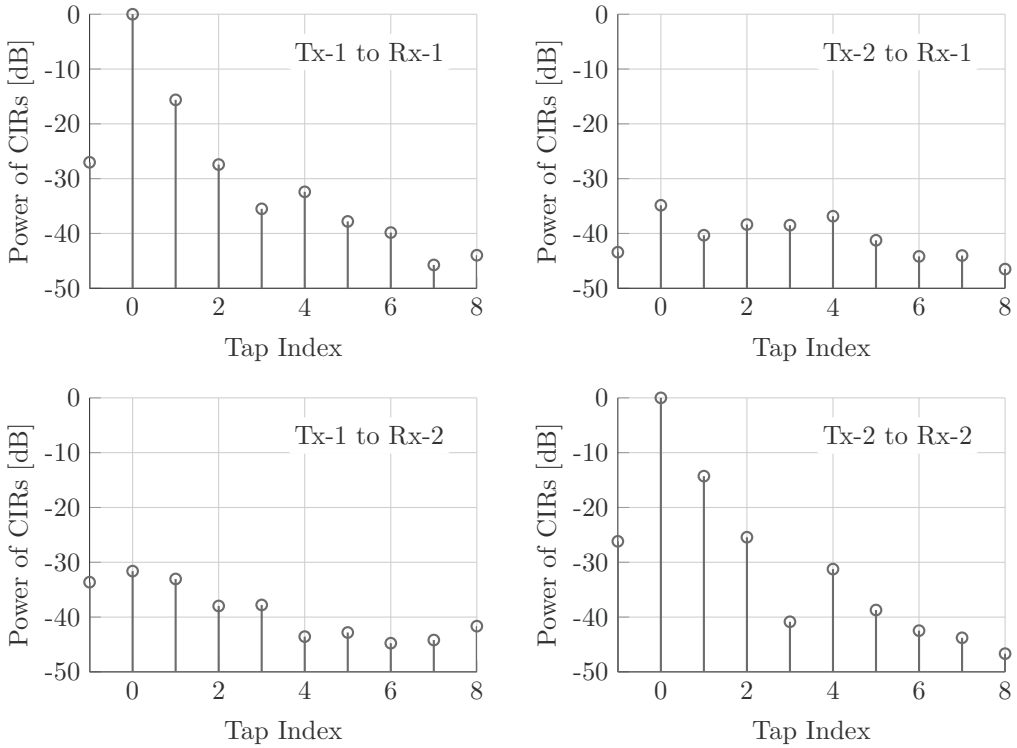

Figure 5.7: Estimated channel impulse responses of the two streams after IAI suppression at Nyquist rate. The diagonal plots show the ISI within each stream, while the off-diagonal plots show the cross-talk between streams. (Source: [SHC+18] © 2018 IEEE).

ements in $\mathbf{D}_1$ and $\mathbf{D}_2$. For simplification, we omit the discussion on those effects, since the magnitudes of the channel gains in the experiments are quite stationary. However, it should be noted that if they are strongly varying, leaving effects like amplifier gain mismatches uncompensated can limit the performance of the equalizer.

In terms of the processing architecture, an Rx CFO de-rotation unit and a Tx CFO de-rotation unit are introduced before and after the MIMO equalization module, see Fig. 5.5. Due to the fact that $\hat{\mathbf{D}}^{-1}_{\phi,\mathrm{Rx}}[q_\mathrm{s}|q]$ and $\hat{\mathbf{D}}^{-1}_{\phi,\mathrm{Tx}}[q_\mathrm{s}|q]$ are two diagonal matrices, the de-rotations can be applied independently at different streams and require only a linear complexity. We would like to note that, due to the stationary setup of backhaul links, the physical channel equalization matrix, e.g., $\hat{\mathbf{H}}^{\dagger}_{\phi}[1]$, does not need frequent updates. The MIMO equalization matrix is calculated according to the first estimation from received preambles and is used for a burst transmission.

In the evaluation later, the performance of ZFE and SCE will exhibit with approximately the same error vector magnitude (EVM) values. In this part, we stay with ZFE and it can be found in Fig. 5.6 (a) and (b) that the superimposed data symbols of the last sub-frame are well separated with the single LoS MIMO tap equalization. Each plot is based on the data symbols of the frame structure Type-B.

ISI Suppression: To independently process the ISI at different streams, possible inter-chain cross-talk must be examined first, see Fig. 5.7. It is observed that the IAI is well suppressed by the LoS MIMO equalization. However, significant ISI is found at different streams. During continuous channel measurements, these interferences are found approximately deterministic and identical between different transmit-receive antenna pairs. Therefore, a fixed MMSE-FIR

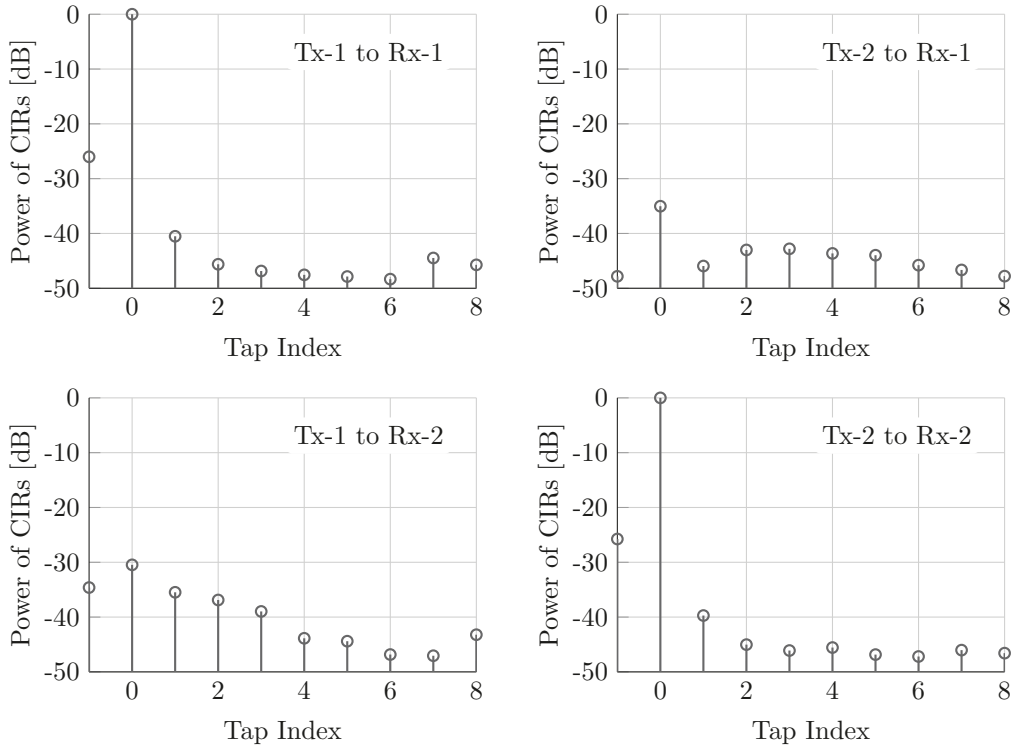

Figure 5.8: Estimated channel impulse responses of the two streams after ISI suppression at Nyquist rate. The diagonal plots show the ISI within each stream, while the off-diagonal plots show the cross-talk between streams.

filter per stream is used in order to suppress the ISI. After suppressing ISI with FIR filters having a length of $L = 7$ taps each, the inter-chain cross-talks are estimated again in Fig. 5.8. It can be observed that the channel becomes very flat. There still exists IAI in this figure of about -30dB relative to the corresponding stream. The residual IAI and also the ISI from tap index -1 are interpreted to be from the non-ideal phase compensation due to the residual estimation errors. With the experimental setup, a EVM value of -12.8dB is improved to -16.4dB by suppressing the ISI, see Fig. 5.6 (b) and (c).

I/Q Imbalance: An additional ~ 0.6dB performance gain can be obtained by compensating the I/Q imbalance of the different streams, see Fig. 5.6 (c) and (d). This is done by using a single-tap adaptive filter per stream that exploits the circularity of the data [AVR08].

As a short summary, it is noticed with the experimental system that most of the RF impairment effects of mmWave components can be suppressed in parallel at different streams, if identical or approximately identical RF components are used at different antennas. The equalization matrix does not need frequent updates due to the stationarity of the physical channel. However, using a conventional method like ZF, the computational complexity per symbol vector for the IAI suppression still scales quadratically with the antenna number. Due to the high symbol rates at mmWave frequencies, even with moderate numbers of parallel streams, the complexity increment w.r.t. stream numbers may limit further system expansion. This problem can be solved with SCE that requires almost no or an ultra-small number of multiplications during system expansion with moderate numbers of antennas.

5.3.2 Decision-Directed Adaptive Equalization

Since variations in the backhaul channel are expected to be fairly slow, even when including the effects of carrier frequency offsets [HCGL18], an adaptive filtering approach may be a viable solution for jointly compensating all involved hardware impairments. Consider the symbol-spaced baseband representation of the more general frequency-selective MIMO channel model with

$$\mathbf{y}[k] = \mathbf{D}_{\phi,\text{Rx}}[k] \cdot \sum_{l=1}^{L} \mathbf{H}[l] \cdot \left(\mathbf{D}_{\phi,\text{Tx}}[k-l+1] \cdot \mathbf{s}[k-l+1]\right) + \mathbf{n}[k], \tag{5.20}$$

$$= \underbrace{\mathbf{D}_{\phi,\text{Rx}}[k] \cdot \mathbf{H}_L \cdot \mathbf{D}_{\phi,\text{Tx},L}[k]}_{\triangleq \mathbf{H}_{\phi,L}[k]} \cdot \mathbf{s}_L[k] + \mathbf{n}[k], \tag{5.21}$$

where the subscript L means that the vector or matrix is stacked in such a way that it accounts for L channel taps, i.e., $\mathbf{s}_L[k] \triangleq \left[\mathbf{s}^T[k], \mathbf{s}^T[k-1], \cdots, \mathbf{s}^T[k-L+1]\right]^T$, and $\mathbf{D}_{\phi,\text{Tx},L}[k] \triangleq \text{diag}\left(\mathbf{D}_{\phi,\text{Tx}}[k], \ldots, \mathbf{D}_{\phi,\text{Tx}}[k-L+1]\right)$, and $\mathbf{H}_L \triangleq \left[\mathbf{H}[1], \mathbf{H}[2], \cdots, \mathbf{H}[L]\right]$, where $\mathbf{H}[l]$ is the l-th channel impulse response tap of the effective channel including AFEs. Thus, the task of CFO compensation, IAI and ISI mitigation can be summarized as equalizing the time varying matrix $\mathbf{H}_{\phi,L}[k]$.

An estimate of the data symbols using an adaptive feed-forward equalizer can be then obtained by

$$\hat{\mathbf{s}}[k] = \mathbf{G}_L[k]\mathbf{y}_L[k], \tag{5.22}$$

where subscript L accounts for L considered channel taps that influence the current observation, i.e., $\mathbf{y}_L[k] \triangleq \left[\mathbf{y}^T[k], \mathbf{y}^T[k-1], \cdots, \mathbf{y}^T[k-L+1]\right]^T$, and $\mathbf{G}_L[k]$ is a $N \times NL$ time varying adaptive filter that compensates all of the considered effects in a single step.

DD-LMS: A widely used adaptation strategy is based on the least mean square (LMS) algorithm [Say08]. In the present case, it is used in a decision-directed mode so that the error signal between the estimated data symbol $\hat{\mathbf{s}}[k]$ and the decided symbol $\bar{\mathbf{s}}[k]$ is evaluated as

$$\mathbf{e}[k] = \hat{\mathbf{s}}[k] - \bar{\mathbf{s}}[k]. \tag{5.23}$$

The update of $\mathbf{G}_L[k]$, which is denoted as $\mathbf{G}_{\text{LMS}}[k]$ in case of a DD-LMS filter, can then be computed from iteration k to $k+1$ as

$$\mathbf{G}_{\text{LMS}}[k+1] = \mathbf{G}_{\text{LMS}}[k] - \mu \cdot \mathbf{e}[k]\mathbf{y}_L^{\text{H}}[k]. \tag{5.24}$$

where the initial filter $\mathbf{G}_{\text{LMS}}[1]$ and the step size μ need to be selected appropriately in order for the filter to converge and/or track the changes [Say08, Rup98].

There are three main benefits to the adaptive approach. First, it is able to track more general time-varying characteristics in amplitude and phase, e.g., as observed in [HCGL18], if they are not too fast and erratic. Second, it is also able to compensate the more general frequency-selective behavior. Third, no additional training data is needed after initialization, given enough reliability of the symbol decisions. The main drawback is that the performance depends highly on the conditioning of the auto-correlation matrix $\mathbf{R}_{\mathbf{y}_L\mathbf{y}_L}[k] = \mathbb{E}\left[\mathbf{y}_L[k]\mathbf{y}_L^H[k]\right]$ and the step size μ. Since the LoS MIMO channel is generally well conditioned, as discussed in Sec. 3.1, this shortcoming should not be a problem.

Widely Linear DD-LMS: A simple extension of the filter, which can decrease the effect of I/Q imbalance, is achieved by using its widely linear (WL) version [PC95] $\mathbf{G}_{\text{LMS,WL}}[k]$. This is done by replacing $\mathbf{y}_L[k]$ in the previous equations with $\left[\mathbf{y}_L^T[k], \mathbf{y}_L^H[k]\right]^T$, which, however, increases size and complexity of the adaptive filter. As discussed earlier, both the DD-LMS and the widely linear DD-LMS are used in this work for baseline comparisons since they can handle effects like MIMO channel equalization, CFO compensation and ISI suppression jointly.

5.4 Performance Evaluation

In the following, we evaluate the performance of the proposed processing architecture in frame-based transmission, where the preambles and midambles are formed by Pseudo-random noise sequences. As a comparison, the previously described adaptive filter that jointly deals with all effects is considered.

For the ISI suppression in STIAI+PISIE algorithm, filter lengths of $L=3$ and $L=7$ will be intensively discussed for reasons explained later, and for I/Q imbalance compensation a single-tap filter was used. The parameters for the DD-LMS approach were similarly set. The filter length L is chosen the same as that of the FIR filters in the STIAI+PISIE algorithm. Meanwhile, the step size is $\mu=0.005$, and the initial filter is $\mathbf{G}_{\text{LMS}}[1]=\left[\hat{\mathbf{H}}_\phi^\dagger[1], \mathbf{0}_{N\times N(L-1)}\right]$. For the widely linear version, the same parameters were used, but with a bigger initial filter of $\mathbf{G}_{\text{LMS,WL}}[1]=\left[\hat{\mathbf{H}}_\phi^\dagger[1], \mathbf{0}_{N\times N(2L-1)}\right]$.

5.4.1 Complexity Comparison

The complexity is evaluated based on the number of complex multiplications and additions per received symbol vector. The terms $c_{\text{SP-ZFE}}^{[\text{M}]}$ and $c_{\text{SP-ZFE}}^{[\text{A}]}$ denote the number of complex multiplications and additions of STIAI+PISIE with ZFE for IAI suppression, respectively, as[4]

$$c_{\text{SP-ZFE}}^{[\text{M}]} = \underbrace{N^2+4N+2N/L_{\text{D}}}_{(5.18)} + \underbrace{LN}_{\substack{L\text{-Tap FIR}\\ \text{Filters}}} + \underbrace{3N}_{\substack{\text{I/Q Imbalance}\\ \text{Compensation}}} + \underbrace{L_{\text{M}}N^2/L_{\text{D}}}_{(5.8)} + \underbrace{2N^3/L_{\text{D}}}_{(5.14)}, \tag{5.25}$$

$$c_{\text{SP-ZFE}}^{[\text{A}]} = \underbrace{N(N-1)}_{(5.18)} + \underbrace{(L-1)N}_{\substack{L\text{-Tap FIR}\\ \text{Filters}}} + \underbrace{2N}_{\substack{\text{I/Q Imbalance}\\ \text{Compensation}}} + \underbrace{(L_{\text{M}}-1)N^2/L_{\text{D}}}_{(5.8)} + \underbrace{(2N(N^2-1)+N^2)/L_{\text{D}}}_{(5.14)}. \tag{5.26}$$

Similarly, the terms $c_{\text{SP-SCE}}^{[\text{M}]}$ and $c_{\text{SP-SCE}}^{[\text{A}]}$ denote the number of complex multiplications and

[4] The complexity for initializing the equalization, e.g., calculating $\hat{\mathbf{H}}_\phi^\dagger[1]$, is not counted here since it is negligible after averaging out with a large number of sub-frames.

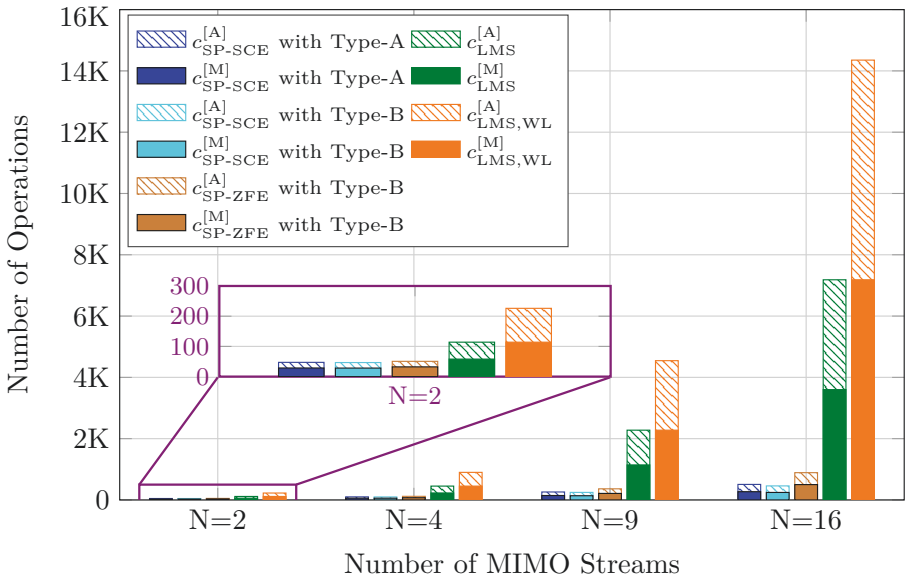

Figure 5.9: Computational complexity comparison of STIAI+PISIE and DD-LMS algorithms with $L=7$. Two different frame types are evaluated with the STIAI+PISIE algorithm. (Parts of the results are reported in [SHC+18] © 2018 IEEE).

additions of STIAI+PISIE with SCE for IAI suppression, respectively, as

$$c^{[M]}_{SP\text{-}SCE} = \underbrace{c^{[M]}_{WDFE} + 4N + 2N/L_D}_{(5.19)} + \underbrace{LN}_{\substack{L\text{-Tap FIR}\\ \text{Filters}}} + \underbrace{3N}_{\substack{\text{I/Q Imbalance}\\ \text{Compensation}}} + \underbrace{L_M N^2/L_D}_{(5.8)} + \underbrace{2N^3/L_D}_{(5.14)}, \tag{5.27}$$

$$c^{[A]}_{SP\text{-}SCE} = \underbrace{c^{[A]}_{WDFE}}_{(5.19)} + \underbrace{(L-1)N}_{\substack{L\text{-Tap FIR}\\ \text{Filters}}} + \underbrace{2N}_{\substack{\text{I/Q Imbalance}\\ \text{Compensation}}} + \underbrace{(L_M-1)N^2/L_D}_{(5.8)} + \underbrace{(2N(N^2-1)+N^2)/L_D}_{(5.14)}, \tag{5.28}$$

where $c^{[M]}_{WDFE}$ and $c^{[A]}_{WDFE}$ represent the computational complexity for multiplications and additions needed by a Winograd discrete Fourier transform with examples in Tab. 4.1, respectively.

Furthermore, the terms $c^{[M]}_{LMS}$ and $c^{[A]}_{LMS}$ denote the number of complex multiplications and additions of the LMS algorithm, respectively, as

$$c^{[M]}_{LMS} = \underbrace{LN^2}_{(5.22)} + \underbrace{LN^2 + N}_{(5.24)}, \tag{5.29}$$

$$c^{[A]}_{LMS} = \underbrace{N(LN-1)}_{(5.22)} + \underbrace{N}_{(5.23)} + \underbrace{LN^2}_{(5.24)}. \tag{5.30}$$

The multiplication and addition complexity $c^{[M]}_{LMS,WL}$, $c^{[A]}_{LMS,WL}$ in the widely linear version of LMS algorithm can be similarly calculated from the larger vector $\left[\mathbf{y}^T_L[k], \mathbf{y}^H_L[k]\right]^T$.

The complexity of the discussed algorithms can be found for some specific examples in Fig. 5.9 with $L = 7$, respectively. It can be seen that the complexity of the proposed architecture STIAI+PISIE scales better than the DD-LMS algorithms to a higher number of streams since its complexity grows slower. With a 2×2 setup, the widely linear LMS approach requires approximately 4 times more operations than the proposed algorithm. Meanwhile, for a system transmitting 16 streams, the required complexities of the STIAI+PISIE architecture using the

	Steps		$N=2$	$N=4$	$N=9$	$N=16$
STIAI+PISIE with Tybe-B	CSI Estimation		0.3	1.1	6.1	21.2
	CFO Compensation		8	16	36	64
	Channel Equalization	ZFE	4	16	81	256
		SCE	0	0	6	0
	ISI Suppression and I/Q Imba. Comp.		12	24	54	96
	Total	**ZFE**	**24.3**	**57.1**	**177**	**437**
		SCE	**20.3**	**41.1**	**102**	**181**
WL DD-LMS	Channel Equalization		24	96	486	1546
	Equalizer Updating		26	100	495	1552
	Total		**50**	**196**	**981**	**3088**

Table 5.2: The Number of Multiplications with Different Setups and Different Algorithms when $L=3$.

SCE or ZFE for IAI suppression are about 3.4%$\sim$7.0% of that of the widely linear DD-LMS[5]. In addition, the required complexities with the two different frame types are approximately equal due to the large values of L_{D}.

Here, we would like to note that, the computational complexity for compensating ISI and I/Q imbalance depends on choices of used algorithms and their parameter settings, e.g., $L=7$ in Fig. 5.9 and $L=3$ in Tab. 5.2. In Tab. 5.2, we list only the number of complex number multiplications that are needed. For those setups, the required computational complexity of the non IAI suppression parts turns to be a term that is comparable with that of the IAI suppression using the ZF algorithm during system expansion[6]. Therefore, although the channel equalization using SCE requires almost no or an ultra-small number of multiplications during system expansion, the overall computational complexity in the experimental system is not that much reduced in comparison with the analysis in Chapter 4. However, for $N=16$, $50\% \sim 60\%$ computational complexity can still be saved with L being $3 \sim 7$, if one replaces ZFE with SCE. Therefore, SCE is more interesting for the systems with analog equalization, the systems with small displacement errors, or the systems with fewer hardware imperfections, e.g., with frequency flat components and/or shared carrier oscillators at Tx and Rx. Here, we would like to note that, if one implements the analog LoS MIMO equalizer with frequency selective RF components, analog SISO ISI suppression equalizers, e.g., in [SB09, HRA10] for 60 GHz receivers, should also be added in parallel after the analog LoS MIMO equalizer. This would lead similar processing steps as the STIAI+PISIE architecture.

We would like to further note that the adaptive algorithm could also be divided into two steps or more, given that the IAI is well suppressed by a single-tap matrix. Stream separation and CFO compensation would be done first by using an adaptive filter of size $N \times N$. Then, an adaptive filter of length L can be applied at each stream independently to remove the remaining ISI and I/Q imbalance. In this case, the complexity of DD-LMS is significantly reduced. However, the adaptive algorithms used as the benchmark algorithm in this work are more robust and can handle more general matrix-valued channel impulse responses, but they can be over-designed.

[5] Since a multiplication of two complex numbers requires four real multiplications and two real additions, while the complex addition requires only two real additions, the numerical analysis is based on the number of multiplications which dominates the complexity.

[6] The IAI suppression part contains LoS MIMO channel equalization and CFO compensation.

Equalization Architecture	Equalizer Type and Frame Structure	EVM in [dB]	
		$\hat{s}_1$	$\hat{s}_2$
STIAI+PISIE	SCE with Type-A	-17.0	-16.5
	SCE with Type-B	-16.8	-16.3
	ZFE with Type-A	-17.1	-16.5
	ZFE with Type-B	-17.0	-16.3
Fully Adaptive Filter	DD-LMS	-16.4	-15.9
	widely linear DD-LMS	-17.6	-16.7

Table 5.3: EVM Values of STIAI+PISIE and LMS Algorithms when $L=7$. (Source: [SCR+18, SHC+18] © 2018 IEEE).

5.4.2 Experimental Results

The EVM is calculated as a performance metric, given by

$$\mathrm{EVM}_{n_t}\,[\mathrm{dB}] = 10\log_{10}\mathbb{E}_k[|\hat{s}_{n_t}[k]-s_{n_t}[k]|^2/|s_{n_t}[k]|^2], \tag{5.31}$$

see Tab. 5.3. Here, $L=7$ is used for the performance evaluation. Due to the sufficient SNR, an EVM of lower than -16.3dB can be achieved, whereas EVM_2 of the second stream $\hat{\mathrm{s}}_2$ yielded a slightly worse performance than EVM_1 of the first stream $\hat{\mathrm{s}}_1$. This difference can occur due to RF impairments in the respective RF-chain or due to setup displacements. With respect to the frame type selection, it can be concluded that sub-frames of shorter length (Type-A) yield slightly higher performance of 0.1 to 0.2dB relative to the longer sub-frames (Type-B) with a similar overall frame length. This shows that a high temporal efficiency transmission can be achieved with LoS MIMO based systems. Since the last sub-frame can be well equalized using the channel estimation of the first sub-frame, it is observed that the physical channel is quite stable. In addition, using SCE for IAI suppression has approximately the same performance as using ZFE for IAI suppression. With a lower complexity, the proposed architecture STIAI+PISIE outperforms the general version of the DD-LMS algorithm. Only the widely linear version of DD-LMS can achieve about 0.2dB$\sim$0.8dB better performance than the STIAI+PISIE.

As mentioned above, we use $L=7$ for the performance evaluation in Tab. 5.3. However, during performance evaluation with multiple settings on L, it is noticed that the value of EVM starts to saturate after $L=3$ of the MMSE-FIR filters and DD-LMS filters, which would consider the two delayed taps after the LoS tap in Fig. 5.7. For example, using $L=3$, a performance loss about 0.3$\sim$0.4 dB can be found on both streams. Therefore, for designing practical systems, a balancing point between the computational complexity and the performance may exist by properly choosing the value of L.

As an indicator for the equalization performance, an SNR estimation is made based on a Welch power spectral density (PSD) estimate, see Fig. 5.10. The mean signal power is estimated by taking the expectation of the in-band PSD $-\frac{f_\mathrm{s}}{2} \leq f \leq \frac{f_\mathrm{s}}{2}$, where $f_\mathrm{s}=1.25$ GBd is the symbol rate, while the noise power is estimated from the out of band PSD. With the proposed STIAI+PISIE processing architecture, we achieve an EVM value of -17.1dB, which is close to the estimated maximum SNR value of 18.5dB.

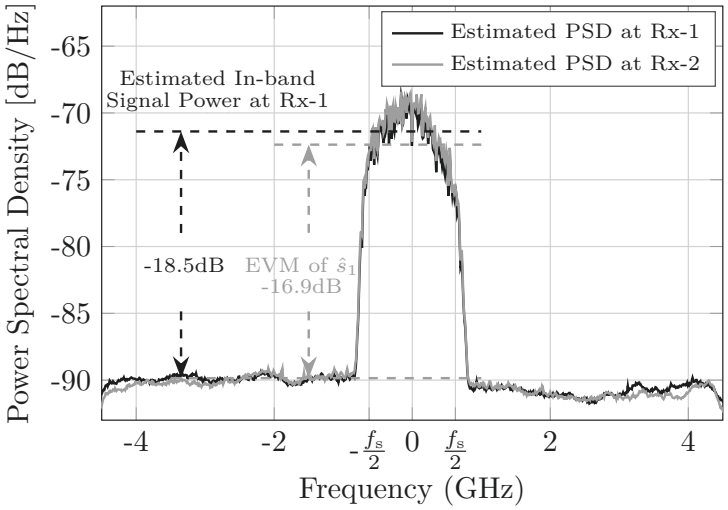

Figure 5.10: Welch power spectral density estimate.

5.5 Summary

In this chapter, we designed a processing architecture with high temporal efficiency for LoS MIMO communication. After synchronizing the sampling frequency, the channel equalization in practical LoS MIMO systems with frequency-selective and time-varying components is decomposed into two steps. First, the IAI together with CFOs are suppressed. Then, due to the usage of similar analog front-ends, the frequency-selectivity is found rather similar at different streams. Therefore, as the second step, the ISI and the I/Q imbalance introduced by the hardware are suppressed in parallel. Additionally, a DD-LMS algorithm that jointly handles all of the involved impairments is specified and used for baseline comparison. With a hardware-in-the-loop 2×2 demonstrator, the proposed signal processing chain of low complexity is shown to work nearly as good as the high complexity widely linear version of the DD-LMS algorithm. All algorithms show similar performance. However, due to the parallel structure, the required complexity of our proposed method grows very slowly with the LoS MIMO system expansion towards more spatial streams.

In this chapter, we summarize the key learning points for engineers as:

- For wideband signal processing in mmWave systems, the RF impairment issues should be considered and compensated for overcoming the possible performance floor.
- For strong LoS MIMO systems, many significant hardware impairments can be suppressed in parallel at different streams and require only an approximately linear complexity during the system expansion with more streams.
- Due to the quasi-stationary physical channel, the channel equalization matrix for the LoS MIMO tap does not need frequent updates. Meanwhile, the units for compensating hardware impairments may need frequent updates, e.g., due to the phase processes at independent oscillators.

Chapter 6

Two-Level Spatial Multiplexing

In the previous chapters, we discussed spatial multiplexing over a *single* LoS path with widely spaced antennas exploiting the phases of spherical waves. However, the most conventional strategy in mmWave MIMO communication uses densely packed antennas and exploits the spatial signature of multiple paths. In this chapter, we firstly show that those two approaches exploit two different degrees in the channel matrices, which we denote as *intra-* and *inter*-path multiplexing, respectively[1]. Then we show that the two kinds of spatial multiplexing can be jointly exploited and identify their different requirements on system design. Fulfilling all requirements simultaneously, we propose a system with multiple widely spaced subarrays. With the help of analog beamforming, the intra-path multiplexing of conventional LoS MIMO systems can be introduced to other non-LoS paths owing to its robustness and the proposed system achieves spatial multiplexing of a higher order than conventional ones.

In this chapter, we focus on combining two kinds of spatial multiplexing and harnessing them jointly with the following steps:

1. We review the conventional mmWave channel model and system model that exploit the spatial multiplexing gain by addressing the paths' spatial signature in limited scattering environments. During the discussion, it is shown that spatial multiplexing of conventional systems arises from a different source of the physical channel in comparison with LoS spatial multiplexing.

2. We propose a multi-subarray, an array of widely spaced subarrays, mmWave system design for backhaul communications, where the array sizes are moderate with high multiplexing gains in limited scattering environments. The intra-path multiplexing and inter-path multiplexing are found at two different levels. The LoS MIMO channel model and the single subarray mmWave MIMO channel model are found as specific limiting cases within this description.

3. We propose to use a hybrid analog/digital beamforming architecture to efficiently implement the proposed multi-subarray mmWave MIMO system at reasonable costs and complexity. Analog beamforming is applied at subarrays and excites the resolvable paths for

[1] Here, we would like to note that the usage of the terms inter- and intra- is not to invent new terms, but it is a good way to distinguish between the two variants of spatial multiplexing from a unified viewpoint.

signal transmission. This provides the basis for exploiting inter-path multiplexing, while the baseband digital beamforming enhances the performance via suppressing inter-path interferences of analog beams and exploiting the intra-path multiplexing.

4. We illustrate our proposed scheme by a 2-path backhaul scenario that supports this combined two-level spatial multiplexing with two subarrays at both transmitter and receiver. This example allows studying the relative increase in spectral efficiency w.r.t. the LoS MIMO system [Lar05] and the single subarray mmWave MIMO system [AHAS$^+$12].

6.1 Two Kinds of Spatial Multiplexing

In this part, we focus on conventional mmWave systems that exploit the spatial multiplexing gain by addressing the paths' spatial signature, namely 'inter-path' multiplexing. Using an array of densely packed antennas, the responses of the antennas fulfill the condition for applying the planar wave model, which is widely used by conventional mmWave systems in limited scattering environments. Then, we briefly recall the LoS multi-subarray system as an example for intra-path multiplexing.

6.1.1 Inter-path Multiplexing

Limited Scattering: Following the discussion in Sec. 2.1, the mmWave outdoor environments normally offer only limited resolvable paths, e.g., 2$\sim$7 [RSM$^+$13, GDM$^+$15, ZVM10]. Limited scattering yields sparsity in angular domain. The couplings between different transmit-receive antenna pairs are found to be mutually correlated [Say02]. Using non-LoS paths for parallel stream transmission is considered by the state-of-the-art works in backhaul communication [GDM$^+$15]. Pathloss is increasing quadratically w.r.t. carrier frequency and this leads to high power attenuation in mmWave communication. To compensate this drawback, beamforming technologies are necessary requiring densely packed antennas [BBS13]. In this way, single stream Gbit/s backhaul communication has become feasible [PCH16, HKL$^+$13].

Scattering on the surface of the reflector may strongly influence the propagation via the corresponding path. At mmWave frequencies, the reflected power is affected by the roughness of the surface [RHDM15]. For rough surfaces, the flat surface reflection coefficient needs to be multiplied by a scattering loss factor [Rap01]. In comparison with centimeter wave frequencies, for the same surface, the surface becomes rougher at mmWave frequencies after normalizing the height of protuberances w.r.t. the wavelength, enlarging the scattering loss. Therefore, objects that are 'perfectly smooth' can contribute as the sources of multipath (significant paths). Meanwhile, paths that contribute a small amount of signal power can simply be neglected. Besides very large surfaces like building facades and windows with large radar cross sections, only metallic objects like lamp posts can form non-LoS paths outdoor [RHDM15]. This explains the sparsity of the paths in mmWave frequencies.

Physical Channel Model: In this part, we assume that the Rx and Tx are equipped with a single uniform square array of M^2 densely packed antennas each. The arrays are facing each other over a transmit distance D and are communicating at a carrier frequency f_c with a wavelength of λ. Meanwhile, an antenna spacing of $d_\mathrm{e} = \lambda/2$ is assumed. To simplify the formulation

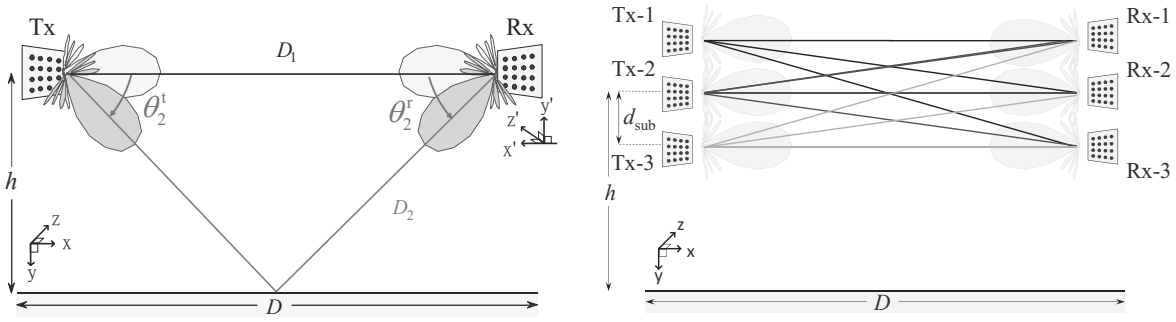

(a) mmWave Inter-path multiplexing **(b)** mmWave Intra-path multiplexing

Figure 6.1: Schematic illustration for (a) inter-path multiplexing with a single subarray pair over two paths, $\max\{N_{\mathrm{s}}\} = P = 2$; (b) a three-subarray LoS MIMO setup, $\max\{N_{\mathrm{s}}\} = N = 3$. (Sub-figure (a) is from [SRB+18] © 2018 IEEE).

of the channel and considering reflections at the ground, sides of buildings, etc., we associate each reflected path with a single reflecting object, i.e., no clusters of paths or sub-rays that would complicate the problem with angular spread are taken into account. As an example, Fig. 6.1 (a) illustrates the simplest case including the LoS path and a reflected path.

The commonly used channel model [Say02] describes the coupling between transmit and receive antennas by the superposition of the responses of all P significant paths. Under a narrow band flat fading assumption, the channel matrix $\mathbf{H} \in \mathbb{C}^{M^2 \times M^2}$ is modeled as a sum of weighted outer products of array propagation vectors

$$\mathbf{H} = \sum_{p=1}^{P} \alpha_p \, e^{-\frac{j2\pi D_p}{\lambda}} \cdot \left[\mathbf{a}_{\mathrm{r}}(\theta_p^{\mathrm{r}}, \phi_p^{\mathrm{r}}) \cdot \mathbf{a}_{\mathrm{t}}^{H}(\theta_p^{\mathrm{t}}, \phi_p^{\mathrm{t}}) \right], \tag{6.1}$$

where α_p is the channel gain of the p-th significant path, θ_p^{r} (ϕ_p^{r}) and θ_p^{t} (ϕ_p^{t}) are its azimuth (elevation) angles of arrival and departure (AoA and AoD), respectively. D_p denotes the propagation link distances between the phase centers of the transceivers via the p-th path. $\mathbf{a}_{\mathrm{t}}(\theta_p^{\mathrm{t}}, \phi_p^{\mathrm{t}}) \in \mathbb{C}^{M^2 \times 1}$ and $\mathbf{a}_{\mathrm{r}}(\theta_p^{\mathrm{r}}, \phi_p^{\mathrm{r}}) \in \mathbb{C}^{M^2 \times 1}$ denote the array response vectors of the p-th path at Tx and Rx, respectively. In the case that the normal vector of the array is along the x-axis with M elements on both the y-axis and z-axis, the array response vectors $\mathbf{a}_{\mathrm{t}}(\theta_p^{\mathrm{t}}, \phi_p^{\mathrm{t}})$ at Tx and $\mathbf{a}_{\mathrm{r}}(\theta_p^{\mathrm{r}}, \phi_p^{\mathrm{r}})$ at Rx under the planar wave model can be written in a similar fashion as (3.25). To use the planar wave model for modeling the array responses at densely packed arrays (subarrays), we assume that $M d_{\mathrm{e}} \ll \mathcal{O}(\lambda D)$.

In mmWave communication with limited scattering environments, it is typically assumed that the number of significant paths P is much smaller than the number of antennas, i.e., $P \ll M^2$ [RSM+13]. In addition, we have assumed a narrow band signal transmission in this chapter, such that the signal bandwidth $W_{\mathrm{s}} \ll f_{\mathrm{c}}$ is much smaller than the coherence bandwidth. It means, according to the discussion in Sec. 2.1, the symbol duration $T_{\mathrm{s}} \propto 1/W_{\mathrm{s}}$ is much larger than the delay spread of the significant paths. From (6.1), it is observed that, even with large numbers of antennas, the achievable spatial multiplexing of conventional mmWave communication systems is upper-bounded by the number of resolvable paths P [GDM+15, AMGPH14]. A more detailed study on the distribution of the singular values of $\mathbf{H}$ in (6.1) w.r.t. different path numbers in a backhaul scenario is provided by [GDM+15], where it is found that the first two to three paths collect most of the energy.

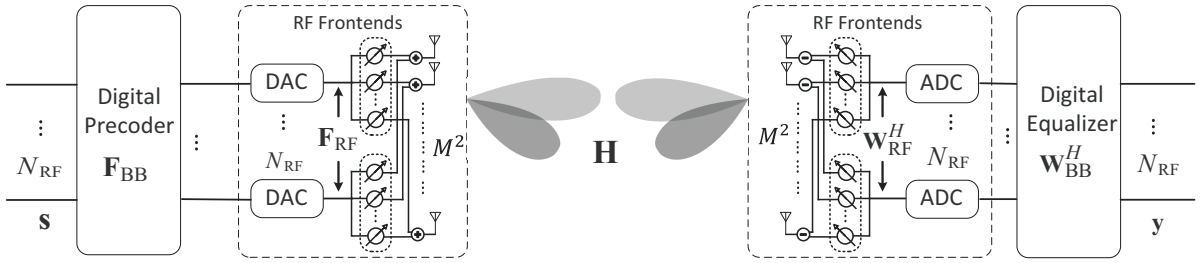

Figure 6.2: Block diagram of a mmWave single subarray system with a conventional hybrid beamforming architecture.

Hybrid Beamforming: Hybrid beamforming algorithms operate on the channel matrix $\mathbf{H}$ in two steps by concatenating *analog* beamforming and *digital* beamforming on each transceiver side. The orthogonality offered by different path directions is firstly exploited by analog beamforming. The effective channel with reduced dimensions can then be processed on digital baseband more efficiently. In sparse channel environments, a hybrid beamforming architecture is capable of achieving near optimal performances [AHAS+12] and becomes interesting for practical mmWave applications due to its reduced complexity.

In this part, we consider the same hybrid beamforming architecture as in [AHAS+12], see Fig. 6.2. N_{RF} radio frequency (RF) chains are assumed for an array of M^2 densely packed antennas, and at most N_{RF} beams can be radiated simultaneously by analog beamforming towards the P available paths. Fig. 6.1 (a) sketches a simple case with $N_{\mathrm{RF}}=2$, $P=2$. We denote the involved baseband precoder, RF precoder, baseband equalizer, and RF equalizer by matrices $\mathbf{F}_{\mathrm{BB}}\in\mathbb{C}^{N_{\mathrm{RF}}\times N_{\mathrm{RF}}}$, $\mathbf{F}_{\mathrm{RF}}\in\mathbb{C}^{M^2\times N_{\mathrm{RF}}}$, $\mathbf{W}_{\mathrm{BB}}^H\in\mathbb{C}^{N_{\mathrm{RF}}\times N_{\mathrm{RF}}}$, and $\mathbf{W}_{\mathrm{RF}}^H\in\mathbb{C}^{N_{\mathrm{RF}}\times M^2}$, respectively. The MIMO signal transmission model under such a hybrid beamforming architecture becomes

$$\mathbf{y}=\mathbf{W}_{\mathrm{BB}}^H\underbrace{\mathbf{W}_{\mathrm{RF}}^H\mathbf{H}\,\mathbf{F}_{\mathrm{RF}}}_{\triangleq\mathbf{H}_{\mathrm{eff}}}\mathbf{F}_{\mathrm{BB}}\,\mathbf{s}+\mathbf{W}_{\mathrm{BB}}^H\underbrace{\mathbf{W}_{\mathrm{RF}}^H\mathbf{n}}_{\triangleq\mathbf{n}_{\mathrm{eff}}}, \tag{6.2}$$

where $\mathbf{n}\sim\mathcal{CN}(\mathbf{0},\sigma_{\mathrm{n}}^2\,\mathbf{I}_{M^2})$ is the complex white Gaussian noise vector with i.i.d. entries that are circularly symmetric. $\mathbf{H}_{\mathrm{eff}}\in\mathbb{C}^{N_{\mathrm{RF}}\times N_{\mathrm{RF}}}$ and $\mathbf{n}_{\mathrm{eff}}\in\mathbb{C}^{N_{\mathrm{RF}}\times 1}$ are defined as the 'effective' channel matrix including analog beamforming and the effective noise vector in digital baseband, respectively. Furthermore, we denote the sets of all feasible RF precoders and RF equalizers, i.e., 'RF codebook' [HKL+13], as $\mathcal{F}_{\mathrm{RF}}$ and $\mathcal{W}_{\mathrm{RF}}$, respectively.

Effective Channel: It is seen that as a consequence of applying analog beamforming on the channel $\mathbf{H}$ described by (6.1), two groups of *inner* products between analog beamforming vectors and array response vectors occur in (6.2). $\mathbf{H}_{\mathrm{eff}}$ is generated as

$$\mathbf{H}_{\mathrm{eff}}\triangleq\mathbf{W}_{\mathrm{RF}}^H\mathbf{H}\,\mathbf{F}_{\mathrm{RF}}=\sum_{p=1}^{P}\overbrace{\alpha_p\underbrace{\left[\mathbf{W}_{\mathrm{RF}}^H\,\mathbf{a}_{\mathrm{r}}(\theta_p^{\mathrm{r}},\phi_p^{\mathrm{r}})\right]}_{\text{Array Gains at Rx}}\cdot\underbrace{\left[\mathbf{F}_{\mathrm{RF}}^H\,\mathbf{a}_{\mathrm{t}}(\theta_p^{\mathrm{t}},\phi_p^{\mathrm{t}})\right]^H}_{\text{Array Gains at Tx}}}^{\text{Effective Channel Gains}}\cdot\overbrace{e^{-\frac{j2\pi D_p}{\lambda}}}^{\text{Phase Shift}}. \tag{6.3}$$

Each path contributes one matrix in the sum. Besides the path gain α_p together its phase shift $e^{-\frac{j2\pi D_p}{\lambda}}$, such a matrix $\mathbf{H}_{\mathrm{eff}}\in\mathbb{C}^{N_{\mathrm{RF}}\times N_{\mathrm{RF}}}$ includes an outer product between array gains at Rx and Tx. Considering the limits brought by P and RF design of single subarrays N_{RF}, the number of spatial data streams N_{s} satisfies $N_{\mathrm{s}}\leq P$, $N_{\mathrm{s}}\leq N_{\mathrm{RF}}$.

6.1.2 Intra-path Multiplexing

The insights to achieve spatial multiplexing over a *single* path were developed initially for LoS MIMO communications. In contrast to the prevailing interpretation of the channel rank for LoS communication, i.e., predicting the rank of $\mathbf{H}$ to be one for $P=1$ in (6.1), spatial multiplexing can still be achieved with sufficiently wide antenna spacings[2]. This is because the used planar wave model in (6.1) is no longer applicable for widely spaced elements. By remodeling the channel with spherical waves, particular antenna spacings not only restore the full rank of $\mathbf{H}$ but also provide a condition number one in the ideal case.

Effective Channel: Let us recall the multi-Subarray LoS MIMO system as introduced earlier in Sec. 3.4.1. The Tx and Rx are identical uniform linear arrays of N-subarrays and are separated by a transmit distance D along the x-axis. Each subarray consists of $M \times M$ antenna elements with half wavelength spacing, $\lambda/2$. Meanwhile, the subarrays are widely and uniformly spaced by $d_{\mathrm{sub}} \in \mathcal{O}(\sqrt{\lambda D})$, $\lambda \ll d_{\mathrm{sub}} \ll D$. Without further scattering, the simplest LoS MIMO scenario with $N = 3$ is sketched in Fig. 6.1 (b). For multi-subarray LoS MIMO systems with N-subarrays at Rx and Tx each, the associated channel matrix is derived earlier in (3.27) as

$$\mathbf{H} = \underbrace{\alpha \cdot g_{\mathrm{Rx}}(M) \cdot g_{\mathrm{Tx}}(M)}_{\text{Effective Channel Gain}} \cdot \underbrace{\mathbf{H}_{\mathrm{LoS}}}_{\substack{\text{Phase}\\ \text{Couplings}}} . \tag{6.4}$$

Here, we recall that α indicates the common channel gain between all transmit-receive antenna pairs. $\mathbf{H}_{\mathrm{LoS}} \in \mathbb{C}^{N\times N}$ describes the relative phase shifts between all subarray pairs with unit magnitude entries. $g_{\mathrm{Tx}}(M)$, $g_{\mathrm{Rx}}(M)$ are the subarray beamforming gains at the Tx and Rx, respectively.

In earlier chapters, we have shown that the LoS spatial multiplexing with a spacing of $\sqrt{\lambda D/N}$ in deterministic scenarios has a high robustness, and a considerable gain is still expected in other path directions that are oblique w.r.t. the array's normal direction. In addition, even with a large number of antennas, the rank of single subarray systems is limited by the small number of resolvable paths under the assumption of planar wave propagation. The path directions allowing signal transmission are therefore precious. Making a good use of each direction and transmitting multiple streams with structured phase couplings offers an additional degree of freedom to further increase the throughput. Having inter-path multiplexing on one level and having intra-path multiplexing on the other, a hierarchical antenna array design will be presented next for joint exploitation, namely two-level spatial multiplexing.

6.2 Joint Exploitation of Inter- and Intra-Path Multiplexing

As discussed above in (6.3) and (6.4), conventional mmWave systems exploit the spatial multiplexing gain by addressing different sources which are complementary to each other. At the same time, the intra-path multiplexing, as shown in Sec. 3.1 from a mathematical point of view, has sufficient robustness so that its potential of adopting it to other directions is better under-

[2] For a given number of antennas, the performance also does not become monotonously better with increasing array aperture. There exists optimal antenna spacings as shown earlier.

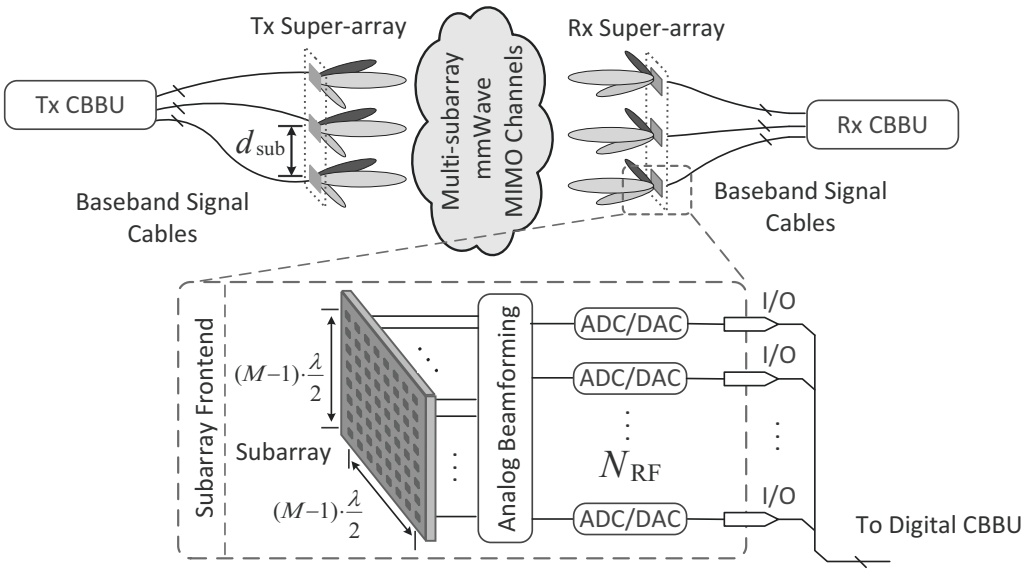

Figure 6.3: Schematic illustration for a multi-subarray system with $N = 3$ widely spaced subarrays. (Source: [SRB+18] © 2018 IEEE).

stood. Those assessments offer the theoretical basis in jointly harvesting them and establish a link between these two spatial multiplexing approaches.

In this section, we show that the above two spatial multiplexing kinds can be exploited jointly, leading to an even higher multiplexing gain in limited scattering environments. To our best knowledge, the complementary nature of the two spatial multiplexing kinds has not been reported in the literature. The combination requires (solid) understanding of 1) the array responses/wave models at different antenna spacings. 2) The conditions under which the two state-of-the-art spatial multiplexing appear or do not appear. 3) Robustness of intra-path multiplexing w.r.t. different transmit directions and displacements. Especially, understanding the robustness of intra-path multiplexing is important, while this provides the theoretical basis that the intra-path multiplexing can be adopted to other directions than LoS. They jointly form the theoretical basis of this combination.

Based on our analysis of their different requirements, robustness, and realizations in practical systems, a novel multi-subarray MIMO system with a special subarray arrangement is proposed. With two different antenna spacings in Sec. 3.3.2, the array response vector w.r.t. a source point turns into a block vector. Meanwhile, the channel matrix between two arrays of subarrays becomes a block matrix as in (3.23). As a reaction to this repetitiveness, a modified hybrid beamforming algorithm is specified which offers a solution to this two-level spatial multiplexing with its two steps, i.e., analog beamforming for addressing the spatial signatures and digital processing for resolving the structured interferences over each individual path direction. In addition, the corresponding system architecture is discussed for practical systems. At the end of this section, the spectral efficiency of the system under a total power constraint is specified for numerical evaluations.

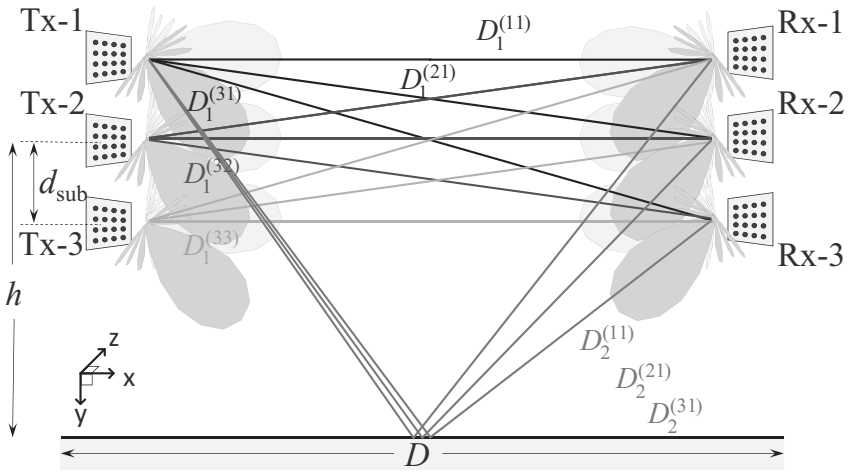

Figure 6.4: Schematic illustration for an example of two-level spatial multiplexing: over each of the two paths, three streams are multiplexed between subarrays at Tx and Rx, $\max\{N_{\text{s}}\} = N \cdot P = 6$. (Source: [SRB+18] © 2018 IEEE).

6.2.1 Two-Level Spatial Multiplexing Channel Model

In this part, based on the discussions on array response vectors in Sec. 3.3.2, a new sparse mmWave channel model is derived for systems having widely spaced multi-subarray at both sides. The proposed antenna arrangement, referred to as super-arrays, has the potential of exploiting both earlier mentioned multiplexing types simultaneously via an advanced hybrid beamforming architecture.

System Description: We again consider a multi-subarray backhaul system with the antennas arranged on two levels. The hierarchically higher level is a linear array of N uniformly spaced subarrays, while each subarray on the lower level is modeled as a uniform square array with M^2 isotropically radiating elements that are $\lambda/2$-spaced. The required area of one subarray at millimeter waves is only in the order of cm^2, see Fig 6.3. The subarray spacing d_{sub} is set following the optimal LoS MIMO spacing in (2.12), i.e., $d_{\text{sub}} \simeq \sqrt{\lambda \cdot D/N}$ and $\lambda \ll d_{\text{sub}} \ll D$, where we again assume that the Tx and Rx are facing each other and are arranged symmetrically over a distance D. Since the subarrays are widely spaced, the signals of the central baseband units (CBBUs) should be distributed/collected via baseband signal cables. Meanwhile, to reduce the required RF design efforts of the modified hybrid beamforming scheme, the analog beamforming part of each subarray uses the widely considered architecture for single subarray mmWave system designs [AHAS+12]. The ADCs and the digital-to-analog converters (DACs) can be implemented locally at the front-ends of subarrays.

We explain the potential of the proposed system in combining the intra-path multiplexing [Lar05, SF15] with the inter-path multiplexing using hybrid beamforming [AHAS+12] as follows. After applying adaptive or training based beam steering algorithms at subarrays and addressing the directions that allow energy transfer, the resolvable paths are excited, e.g., see Fig 6.4. Having widely spaced subarrays, a similar multiplexing gain as for the LoS MIMO can be expected at each individual path direction and can be exploited by the digital processing at CBBUs. It is worth noting that the intra-path multiplexing is antenna arrangement dependent. We set the value of d_{sub} following $d_{\text{sub}} \simeq \sqrt{\lambda D/N}$. On the one hand, this inter-subarray spacing is optimized for the LoS path. On the other hand, it is still a suboptimal solution for

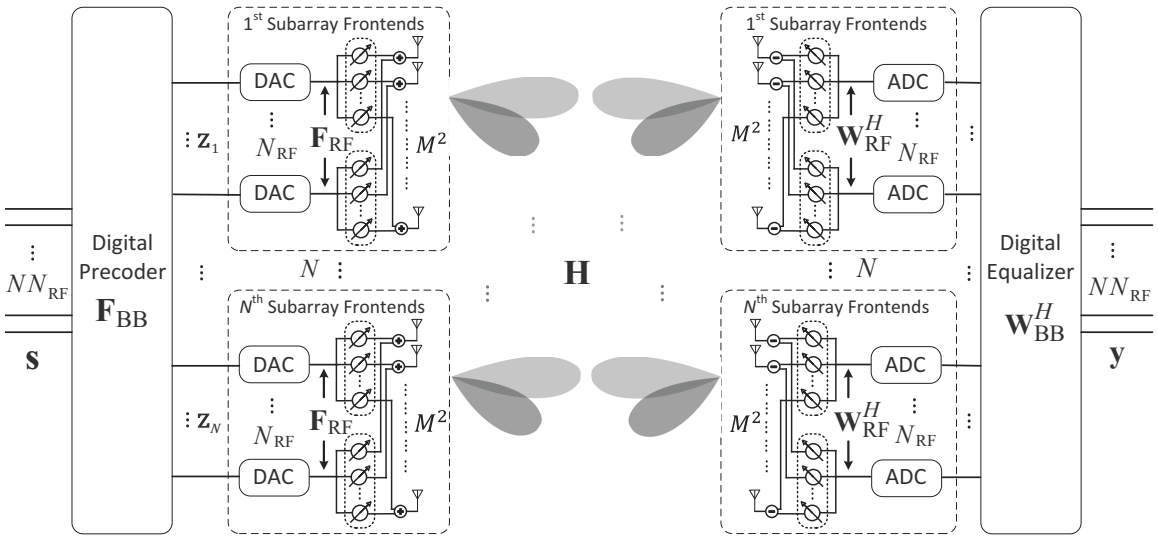

Figure 6.5: Block diagram of a mmWave multi-subarray MIMO system with an advanced hybrid beamforming architecture. (Source: [SRB+18] © 2018 IEEE).

other paths, owing to its high robustness w.r.t. relative rotations and translations as discussed in Sec. 3.1. Note that the overall spectral efficiency of the system can be further increased via antenna topology optimization using the concept in Sec. 3.1 as the projections of the arrangement can be optimized jointly for multiple directions.

Physical Channel Model: Considering the proposed N-subarray system, the channel matrix $\mathbf{H} \in \mathbb{C}^{NM^2 \times NM^2}$ in (2.4) couples $N \cdot M^2$ antenna elements on each side. Assuming $P \ll M^2$ significant paths, all subarrays on either transceiver side are facing the same set of array response vectors, $\bigcup_{p=1}^{P} \{\mathbf{a}_i(\theta_p^i, \phi_p^i)\}$, $i \in \{\mathrm{t},\, \mathrm{r}\}$, $\mathbf{a}_i(\theta_p^i, \phi_p^i) \in \mathbb{C}^{M^2 \times 1}$. This is because the assumption $D \gg d_{\mathrm{sub}}$ makes the differences on directions of the same path at different subarrays negligible. However, the relative phase differences between the phase centers of subarrays are of non-negligible values, as the subarrays are widely spaced. Guiding by the array response vector in Sec. 3.3.2, the complete channel matrix over several path directions is formulated as

$$\mathbf{H} = \sum_{p=1}^{P} \alpha_p \, \mathbf{H}_p \otimes \left[\mathbf{a}_{\mathrm{r}}(\theta_p^{\mathrm{r}}, \phi_p^{\mathrm{r}}) \cdot \mathbf{a}_{\mathrm{t}}^H(\theta_p^{\mathrm{t}}, \phi_p^{\mathrm{t}})\right]. \tag{6.5}$$

The entries of $\mathbf{H}_p$ are given again by the spherical wave model as $\{\mathbf{H}_p\}_{n_{\mathrm{r}} n_{\mathrm{t}}} = e^{-j\frac{2\pi}{\lambda} \cdot D_p^{(n_{\mathrm{r}} n_{\mathrm{t}})}}$, where $D_p^{(n_{\mathrm{r}} n_{\mathrm{t}})}$ denotes the distance between the n_{r}-th receive subarray and the n_{t}-th transmit subarray via the p-th path. The subarray response vector $\mathbf{a}_i(\theta_p^i, \phi_p^i)$, $i \in \{\mathrm{t},\, \mathrm{r}\}$ is similarly defined as (3.22).

Hybrid Beamforming: Our proposal for a two-level spatial multiplexing concept simply applies both transmission modes described in the previous section simultaneously and is illustrated schematically in Fig 6.4. As one may recognize, hybrid beamforming, more precisely the additional degrees of freedom due to pattern multiplication of an *array* of subarrays, provides the basis to connect both approaches in a two-level hierarchical multiplexing system. Analog beamforming provides the first separation of the data streams transmitted along different paths, i.e., by angular/gain differences, and reduces the required dimension for digital processing. Providing the subarrays with those anisotropic beamforming gains and owing to the robustness of

intra-path multiplexing, the intra-path multiplexing can be realized in parallel at all path directions. Meanwhile, via digital baseband processing, the parallel streams folded on each path can be resolved together with residual interference from other path directions.

To extend (6.2) and (6.3), let us firstly extend the conventional hybrid beamforming scheme of single subarray systems [AHAS+12] to the block diagram in Fig. 6.5 with N subarrays. To stay consistent with Sec. 6.1.1, we assume again that P paths and N_{RF} RF chains are available at each subarray, while all distances involved in the geometric relations of reflecting objects w.r.t. the transceivers are much larger than d_{sub}. Applying the same analog beamforming strategy to all N subarrays, we simplify the complexity of required analog beamforming algorithms and excite all paths at all subarrays. The extension of the analog beamforming matrices from one to N-subarrays is now denoted by $\mathbf{F}_{\mathrm{RF},N} \in \mathbb{C}^{NM^2 \times NN_{\mathrm{RF}}}$, $\mathbf{W}_{\mathrm{RF},N} \in \mathbb{C}^{NM^2 \times NN_{\mathrm{RF}}}$. These matrices are related to their single subarray versions $\mathbf{F}_{\mathrm{RF}}$, $\mathbf{W}_{\mathrm{RF}}$ by

$$\mathbf{F}_{\mathrm{RF},N} = \mathbf{I}_N \otimes \mathbf{F}_{\mathrm{RF}} \quad \text{and} \quad \mathbf{W}_{\mathrm{RF},N} = \mathbf{I}_N \otimes \mathbf{W}_{\mathrm{RF}} \tag{6.6}$$

at Tx and Rx side, respectively. For practical implementation purpose, the proposed analog beamforming strategy requires no new RF designs. The conventional single subarray RF front-ends are repetitively used, while their baseband signals are combined at CBBUs of a higher dimension, i.e., $\mathbf{F}_{\mathrm{BB}} \in \mathbb{C}^{NN_{\mathrm{RF}} \times NN_{\mathrm{RF}}}$, $\mathbf{W}_{\mathrm{BB}} \in \mathbb{C}^{NN_{\mathrm{RF}} \times NN_{\mathrm{RF}}}$.

Combining analog beamforming and digital baseband processing, we write the complete hybrid beamforming transmission model for multi-subarray systems which is similar to the single subarray case as

$$\mathbf{y} = \mathbf{W}_{\mathrm{BB}}^H \underbrace{\mathbf{W}_{\mathrm{RF},N}^H \mathbf{H}\, \mathbf{F}_{\mathrm{RF},N}}_{\triangleq \mathbf{H}_{\mathrm{eff}}} \mathbf{F}_{\mathrm{BB}}\, \mathbf{s} + \mathbf{W}_{\mathrm{BB}}^H \underbrace{\mathbf{W}_{\mathrm{RF},N}^H \mathbf{n}}_{\triangleq \mathbf{n}_{\mathrm{eff}}}, \tag{6.7}$$

where $\mathbf{H}_{\mathrm{eff}} \in \mathbb{C}^{NN_{\mathrm{RF}} \times NN_{\mathrm{RF}}}$ and $\mathbf{n}_{\mathrm{eff}} \in \mathbb{C}^{NN_{\mathrm{RF}} \times 1}$ are defined as the effective channel matrix and the noise vector in the digital baseband, respectively. The noise vector $\mathbf{n}$ follows distribution $\mathbf{n} \sim \mathcal{CN}(\mathbf{0},\, \sigma_n^2\, \mathbf{I}_{NM^2})$. In this case, the number of supported data streams N_{s} is limited by the variables P, N_{RF} and N with $N_{\mathrm{s}} \leq NP$, $N_{\mathrm{s}} \leq NN_{\mathrm{RF}}$. For a better understanding of physical implementation, the baseband signal $\mathbf{z} = \mathbf{F}_{\mathrm{BB}} \cdot \mathbf{s}$ is a block vector with $\mathbf{z} = [\mathbf{z}_1^T, \mathbf{z}_2^T, \cdots, \mathbf{z}_N^T]^T$. The block $\mathbf{z}_{n_{\mathrm{t}}} \in \mathbb{C}^{N_{\mathrm{RF}} \times 1}$ represents the symbols transmitted via the n_{t}-th subarray, see Fig. 6.5.

Effective Channel: By substituting $\mathbf{H}$, $\mathbf{W}_{\mathrm{RF},N}$, $\mathbf{F}_{\mathrm{RF},N}$ in (6.7) with (6.5), (6.6) and considering the mixed-product property [Loa00] of the Kronecker product $(\mathbf{A} \otimes \mathbf{B})(\mathbf{C} \otimes \mathbf{D}) = (\mathbf{AC}) \otimes (\mathbf{BD})$, an effective channel model of multi-subarray systems similar to (6.3) can be obtained as

$$\mathbf{H}_{\mathrm{eff}} = \sum_{p=1}^{P} \underbrace{\mathbf{H}_p}_{\substack{\text{Phase} \\ \text{Couplings}}} \otimes \underbrace{\alpha_p \left[\mathbf{W}_{\mathrm{RF}}^H\, \mathbf{a}_{\mathrm{r}}(\theta_p^{\mathrm{r}}, \phi_p^{\mathrm{r}})\right] \cdot \left[\mathbf{F}_{\mathrm{RF}}^H\, \mathbf{a}_{\mathrm{t}}(\theta_p^{\mathrm{t}}, \phi_p^{\mathrm{t}})\right]^H}_{\substack{\text{Effective Channel Gains of} \\ \text{all beams along path } p}}. \tag{6.8}$$

Comparing (6.8) with (6.3) and (6.4), we find that the channel features for both spatial multiplexing kinds are combined with Kronecker products. It is capable of supporting a maximum of NP or NN_{RF} streams, as the effective channel matrix may have a *higher* rank than either of the two conventional systems [AHAS+12], [Lar05] exploiting a single spatial multiplexing kind. Meanwhile, the covariance matrix of the effective noise satisfies $\mathbf{R}_{\mathbf{n}_{\mathrm{eff}}} = \mathbb{E}[\mathbf{n}_{\mathrm{eff}} \mathbf{n}_{\mathrm{eff}}^H] = \sigma_{\mathrm{n}}^2\, [\mathbf{I}_{\mathrm{N}} \otimes (\mathbf{W}_{\mathrm{RF}}^H \mathbf{W}_{\mathrm{RF}})]$.

6.2.2 Spectral Efficiency with Total Transmit Power Constraints

In this part, we first formulate the spectral efficiency with a total transmit power constraint as the benchmark for evaluating the spatial multiplexing gains. Our spectral efficiency evaluation is carried out assuming that Gaussian symbols are transmitted. Extending the spectral efficiency for single subarray systems using hybrid beamforming [ARAS+14] to multi-subarray systems, the spectral efficiency achieved by certain hybrid beamforming scheme is formulated as

$$R = \log_2[\det(\mathbf{I}_{NN_{\mathrm{RF}}} + \mathbf{R}_{\mathrm{n}}^{-1}(\mathbf{W}_{\mathrm{BB}}^H\mathbf{W}_{\mathrm{RF},N}^H\mathbf{H}\,\mathbf{F}_{\mathrm{RF},N}\mathbf{F}_{\mathrm{BB}})\mathbf{R}_{\mathbf{s}}(\mathbf{W}_{\mathrm{BB}}^H\mathbf{W}_{\mathrm{RF},N}^H\mathbf{H}\,\mathbf{F}_{\mathrm{RF},N}\mathbf{F}_{\mathrm{BB}})^H)], \tag{6.9}$$

where $\mathbf{R}_{\mathbf{s}} \triangleq \mathbb{E}[\mathbf{s}\mathbf{s}^H]$ and $\mathbf{R}_{\mathrm{n}} \triangleq \sigma_{\mathrm{n}}^2\mathbf{W}_{\mathrm{BB}}^H\mathbf{W}_{\mathrm{RF},N}^H\mathbf{W}_{\mathrm{RF},N}\mathbf{W}_{\mathrm{BB}}$. Considering a power constraint P_{C}, the radiating power satisfies $\mathrm{tr}(\mathbf{F}_{\mathrm{RF},N}\mathbf{F}_{\mathrm{BB}}\mathbf{R}_{\mathbf{s}}\mathbf{F}_{\mathrm{BB}}^H\mathbf{F}_{\mathrm{RF},N}^H) \leq P_{\mathrm{C}}$. To simplify the discussion later, we assume that the transmitted symbols $\mathbf{s}$ are i.i.d. variables which makes $\mathbf{R}_{\mathbf{s}}$ a diagonal matrix. Without loss of generality, we assume $\mathbf{R}_{\mathbf{s}} = \mathbf{I}_{NN_{\mathrm{RF}}}$. Furthermore, also to simplify the discussion later, we assume the effective noise $\mathbf{W}_{\mathrm{BB}}^H\mathbf{W}_{\mathrm{RF},N}^H\mathbf{n}$ of the equalized symbols being white Gaussian noise with i.i.d. entries, i.e., $\mathbf{W}_{\mathrm{BB}}^H\mathbf{W}_{\mathrm{RF},N}^H\mathbf{W}_{\mathrm{RF},N}\mathbf{W}_{\mathrm{BB}} = \mathbf{I}_{\mathrm{NN}_{\mathrm{RF}}}$.

Maximizing the spectral efficiency of the hybrid beamforming systems requires a joint optimization over the matrices $\{\mathbf{W}_{\mathrm{BB}}, \mathbf{W}_{\mathrm{RF},N}, \mathbf{F}_{\mathrm{RF},N}, \mathbf{F}_{\mathrm{BB}}\}$. Considering the RF precoder and the RF equalizer are taken from quantized codebooks $\{\mathcal{F}_{\mathrm{RF}}, \mathcal{W}_{\mathrm{RF}}\}$, the mutual information achieved by Gaussian signaling can be formulated in an outer-inner problem form as

$$\tilde{I} = \max_{\mathbf{F}_{\mathrm{RF}}\in\mathcal{F}_{\mathrm{RF}},\ \mathbf{W}_{\mathrm{RF}}\in\mathcal{W}_{\mathrm{RF}}} \left\{ \begin{array}{l} \max\limits_{\mathbf{F}_{\mathrm{BB}},\ \mathbf{W}_{\mathrm{BB}}} \quad R, \\ \text{s.t.} \ \left\{ \begin{array}{l} ||\mathbf{F}_{\mathrm{RF},N}\mathbf{F}_{\mathrm{BB}}||_F^2 \leq P_{\mathrm{C}}, \\ \mathbf{W}_{\mathrm{BB}}^H\mathbf{W}_{\mathrm{RF},N}^H\mathbf{W}_{\mathrm{RF},N}\mathbf{W}_{\mathrm{BB}} = \mathbf{I}_{\mathrm{NN}_{\mathrm{RF}}}, \end{array} \right. \end{array} \right\}, \tag{6.10}$$

where the outer maximization is chosen over finite codebooks and the RF precoder and equalizer are assumed to be of N_{RF} RF chains at each subarray. The inner maximization is applied knowing the $\mathbf{F}_{\mathrm{RF}}$ and $\mathbf{W}_{\mathrm{RF}}$. Here we recall that $\mathbf{F}_{\mathrm{RF},N} = \mathbf{I}_N \otimes \mathbf{F}_{\mathrm{RF}}$ and $\mathbf{W}_{\mathrm{RF},N} = \mathbf{I}_N \otimes \mathbf{W}_{\mathrm{RF}}$.

Assuming finite sets $\mathcal{F}_{\mathrm{RF}}$ and $\mathcal{W}_{\mathrm{RF}}$, the solution of $\mathbf{F}_{\mathrm{RF}}$, $\mathbf{W}_{\mathrm{RF}}$ to the outer maximization can be found by either using exhaustive search [YCG15] or using received power based search [CRKF17]. We would like to note that, for deterministic channels like a wireless backhaul channel, finding optimal $\mathbf{W}_{\mathrm{RF}}$, $\mathbf{F}_{\mathrm{RF}}$ over a finite set is not a crucial issue. The time for this searching period can be amortized averagely within a long transmission time period, since the scenario/environment does not change significantly. Furthermore, those algorithms can be applied more time-efficiently than that of single subarray systems, since the process can be parallelized at N subarrays. In this work, we focus on the inner optimization problem, whose results can demonstrate the possibility of having intra-path multiplexing at multiple path directions in later numerical evaluations. Given certain $\mathbf{F}_{\mathrm{RF}}$, $\mathbf{W}_{\mathrm{RF}}$ and the measurement result of the corresponding $\mathbf{H}_{\mathrm{eff}}$, the mutual information I of the inner part is found as

$$\begin{aligned} I \ = \ & \max_{\mathbf{F}_{\mathrm{BB}},\ \mathbf{W}_{\mathrm{BB}}} \ \log_2[\det(\mathbf{I}_{NN_{\mathrm{RF}}} + \mathbf{F}_{\mathrm{BB}}^H\mathbf{H}_{\mathrm{eff}}^H\mathbf{W}_{\mathrm{BB}}\mathbf{R}_{\mathrm{n}}^{-1}\mathbf{W}_{\mathrm{BB}}^H\mathbf{H}_{\mathrm{eff}}\mathbf{F}_{\mathrm{BB}})], \\ & \text{s.t.} \ ||\mathbf{F}_{\mathrm{RF},N}\mathbf{F}_{\mathrm{BB}}||_F^2 \leq P_{\mathrm{C}}, \ \mathbf{W}_{\mathrm{BB}}^H\mathbf{W}_{\mathrm{RF},N}^H\mathbf{W}_{\mathrm{RF},N}\mathbf{W}_{\mathrm{BB}} = \mathbf{I}_{\mathrm{NN}_{\mathrm{RF}}}. \end{aligned} \tag{6.11}$$

In the above inner maximization problem, one baseband precoder/equalizer solution of multi-subarray systems can be found by modifying the well-known solution of the single subar-

ray systems [AH16] as

$$\mathbf{F}_{\mathrm{BB}} = (\mathbf{F}_{\mathrm{RF},N}^H \mathbf{F}_{\mathrm{RF},N})^{-\frac{1}{2}} \widetilde{\mathbf{F}} \overset{(1)}{=} [\mathbf{I}_N \otimes (\mathbf{F}_{\mathrm{RF}}^H \mathbf{F}_{\mathrm{RF}})^{-\frac{1}{2}}] \widetilde{\mathbf{F}}, \tag{6.12a}$$

$$\mathbf{W}_{\mathrm{BB}}^H = \widetilde{\mathbf{W}}^H (\mathbf{W}_{\mathrm{RF},N}^H \mathbf{W}_{\mathrm{RF},N})^{-\frac{1}{2}} \overset{(1)}{=} \widetilde{\mathbf{W}}^H [\mathbf{I}_N \otimes (\mathbf{W}_{\mathrm{RF}}^H \mathbf{W}_{\mathrm{RF}})^{-\frac{1}{2}}], \tag{6.12b}$$

where equality $\overset{(1)}{=}$ denotes an identity based on the distributive property of the inverse operation in Kronecker product [Loa00]. $\widetilde{\mathbf{F}}$ and $\widetilde{\mathbf{W}}^H$ are equivalent baseband precoder and equalizer, respectively. It is worth mentioning that the additional filters $(\mathbf{F}_{\mathrm{RF},N}^H \mathbf{F}_{\mathrm{RF},N})^{-\frac{1}{2}}$ and $(\mathbf{W}_{\mathrm{RF},N}^H \mathbf{W}_{\mathrm{RF},N})^{-\frac{1}{2}}$ in (6.12) can simplify the expressions of the two constraints in (6.11). With such a processing architecture, we form another optimization problem in the following lemma.

Lemma: Considering a processing structure with $\mathbf{F}_{\mathrm{BB}} = (\mathbf{F}_{\mathrm{RF},N}^H \mathbf{F}_{\mathrm{RF},N})^{-\frac{1}{2}} \widetilde{\mathbf{F}}$ and $\mathbf{W}_{\mathrm{BB}}^H = \widetilde{\mathbf{W}}^H (\mathbf{W}_{\mathrm{RF},N}^H \mathbf{W}_{\mathrm{RF},N})^{-\frac{1}{2}}$, the problem stated in (6.11) is equivalent to the following problem

$$\begin{aligned} \max_{\widetilde{\mathbf{F}},\, \widetilde{\mathbf{W}}} \;\; & \log_2[\det(\mathbf{I}_{NN_{\mathrm{RF}}} + \widetilde{\mathbf{F}}^H (\mathbf{F}_{\mathrm{RF},N}^H \mathbf{F}_{\mathrm{RF},N})^{-\frac{1}{2}} \mathbf{H}_{\mathrm{eff}}^H (\mathbf{W}_{\mathrm{RF},N}^H \mathbf{W}_{\mathrm{RF},N})^{-\frac{1}{2}} \widetilde{\mathbf{W}} \cdot \\ & \cdot \mathbf{R}_{\mathrm{n}}^{-1} \widetilde{\mathbf{W}}^H (\mathbf{W}_{\mathrm{RF},N}^H \mathbf{W}_{\mathrm{RF},N})^{-\frac{1}{2}} \mathbf{H}_{\mathrm{eff}} (\mathbf{F}_{\mathrm{RF},N}^H \mathbf{F}_{\mathrm{RF},N})^{-\frac{1}{2}} \widetilde{\mathbf{F}})], \\ \text{s.t. } & ||\widetilde{\mathbf{F}}||_F^2 \leq P_{\mathrm{C}},\; \widetilde{\mathbf{W}}^H \widetilde{\mathbf{W}} = \mathbf{I}_{\mathrm{NN_{RF}}}. \end{aligned} \tag{6.13}$$

Proof. Due to the linear one-to-one mapping between $\mathbf{F}_{\mathrm{BB}}$ ($\mathbf{W}_{\mathrm{BB}}$) and $\widetilde{\mathbf{F}}$ ($\widetilde{\mathbf{W}}$), the proof of the problem equivalence is the same as the proof for the single subarray systems (the proof of Lemma 5 in [AH16]), if one replaces $\mathbf{F}_{\mathrm{RF}}$ in that proof with $\mathbf{F}_{\mathrm{RF},N}$ ($\mathbf{W}_{\mathrm{RF},N}$). □

Since the problem in (6.13) can be solved via the standard MIMO precoder and equalizer design, we found $\widetilde{\mathbf{F}}$ and $\widetilde{\mathbf{W}}^H$ as

$$\widetilde{\mathbf{F}} = \mathbf{V}\boldsymbol{\Psi} \quad \text{and} \quad \widetilde{\mathbf{W}}^H = \mathbf{U}^H, \tag{6.14}$$

where the diagonal matrix $\boldsymbol{\Psi} = \mathrm{diag}\{\psi_1, \psi_2, \ldots, \psi_{NN_{\mathrm{RF}}}\}$ contains the gain coefficients that affect the power allocation. The matrices $\mathbf{U} \in \mathbb{C}^{NN_{\mathrm{RF}} \times NN_{\mathrm{RF}}}$, $\mathbf{V} \in \mathbb{C}^{NN_{\mathrm{RF}} \times NN_{\mathrm{RF}}}$ are unitary matrices given by the singular value decomposition (SVD) of an extended channel

$$[\mathbf{I}_N \otimes (\mathbf{W}_{\mathrm{RF}}^H \mathbf{W}_{\mathrm{RF}})^{-\frac{1}{2}}]\, \mathbf{H}_{\mathrm{eff}}\, [\mathbf{I}_N \otimes (\mathbf{F}_{\mathrm{RF}}^H \mathbf{F}_{\mathrm{RF}})^{-\frac{1}{2}}] = \mathbf{U}\boldsymbol{\Sigma}\mathbf{V}^H, \tag{6.15}$$

where $\boldsymbol{\Sigma} \in \mathbb{C}^{NN_{\mathrm{RF}} \times NN_{\mathrm{RF}}}$ is a diagonal matrix with singular values $\sigma_1 \geq \sigma_2 \geq \ldots \geq \sigma_{NN_{\mathrm{RF}}} \geq 0$. Then, the transmission model in (6.7) becomes

$$\mathbf{y} = \boldsymbol{\Sigma}\boldsymbol{\Psi}\mathbf{s} + \tilde{\mathbf{n}},\; s.t.\; ||\boldsymbol{\Psi}||_F^2 \leq P_{\mathrm{C}}, \tag{6.16}$$

where $\tilde{\mathbf{n}} \sim \mathcal{CN}(\mathbf{0}, \sigma_{\mathrm{n}}^2 \mathbf{I}_{NN_{\mathrm{RF}}})$. Using the water-filling algorithm [CT06] gives the solution on ψ_η, $1 \leq \eta \leq NN_{\mathrm{RF}}$ as

$$\psi_\eta = \left(\left[\kappa - \frac{\sigma_{\mathrm{n}}^2}{\sigma_\eta^2} \right]^+ \right)^{\frac{1}{2}}, \tag{6.17}$$

where κ is the 'water level' and is chosen such that $\sum_\eta \psi_\eta^2 = P_{\mathrm{C}}$. The notation $[a]^+$ is used for taking non-negative values only as $\max(a, 0)$. Consequently, if $\kappa - \sigma_{\mathrm{n}}^2/\sigma_\eta^2 < 0$, we set $\psi_\eta = 0$. In the evaluation shown later, the SNR γ_η on the η-th subchannel is defined as

$$\gamma_\eta \triangleq \sigma_\eta^2 \, \psi_\eta^2 / \sigma_{\mathrm{n}}^2. \tag{6.18}$$

The mutual information I derived in this section will be used for evaluating the performance of the proposed hybrid architecture in exploiting the combined spatial multiplexing gain in the channel (6.5). The singular values σ_η will be used for analyzing the number of subchannels and their relation with P and N under different geometry setups. Finally, the SNR γ_η on the η-th subchannel is used in demonstrating the subchannel quality under different transmit power constraints.

6.3 Performance Evaluation

In this part, we evaluate the mutual information of the multi-subarray system using a limited scattering channel model, which will be introduced in Sec. 6.3.1. The model involves the hybrid beamforming architecture for mmWave communication as described in Sec. 6.2 for exploiting the spatial multiplexing at two levels. The subarrays are sufficiently spaced apart from each other. This forms a two-subarray MIMO system with two paths, i.e., $\{N, P\} = \{2, 2\}$ supporting 4 streams. For comparison, the performance of a single subarray LoS system, i.e., an AWGN channel with $\{N, P\} = \{1, 1\}$, a *single* subarray two-path system, i.e., $\{N, P\} = \{1, 2\}$, and a LoS MIMO system with two subarrays, i.e., $\{N, P\} = \{2, 1\}$, supporting 1, 2 and 2 streams respectively, are evaluated under the same power constraints.

In this work, we denote the mutual information $\tilde{I}$ in (6.10) and I in (6.11) under different system setups $\{N,P\}$ as $\tilde{I}_{\{N,P\}}$ and $I_{\{N,P\}}$, respectively. Meanwhile, we denote their corresponding channel capacity using water-filling algorithm in (2.18) with perfect CSI at Tx as $C_{\{N,P\}}$. Here, we would like to note that, since the 2-subarray LoS MIMO system under investigation is optimally arranged, $C_{\{N,P\}=\{2,1\}}$ is equivalent to the channel capacity C_{opt} in (2.22) with beamforming gains at subarrays. Furthermore, the singular values of the 2-subarray LoS MIMO system are found equal. We denote this value as $\sigma_{\{N,P\}=\{2,1\}}$. For the single subarray LoS system, we denote its singular as $\sigma_{\{N,P\}=\{1,1\}}$.

6.3.1 A Two-Path Two-Subarray Wireless Backhaul Model

To keep things simple, we only consider a two-path model that consists of a LoS path and a ground/side-building reflected path for backhaul communications and extend it to multi-subarray systems. Emulating the multipath propagation with two resolvable paths is widely considered in the literature [Rap01] and provides a simple and effective model for analyzing the basic properties. The scenario in this part can be viewed similarly to Fig. 6.4 and, to simplify the discussion, we reduce the sketched subarray number from $N = 3$ to $N = 2$. We assume the direct connection between transceivers to be x-axis/x'-axis and it parallels to the surface of the reflecting object. The point of reflection is separated from the line connecting the centroids of Rx and Tx by a distance h meters, e.g., the transceivers are at the same height h. The transceiver arrays are parallel to each other and separated by a transmit distance D with $\lambda \ll d_{\text{sub}} \ll h < D$ following the assumptions on the geometric relations in Sec. 6.2.1. The subarrays are placed along the y-axis/y'-axis which is assumed to be perpendicular to the reflecting surface.

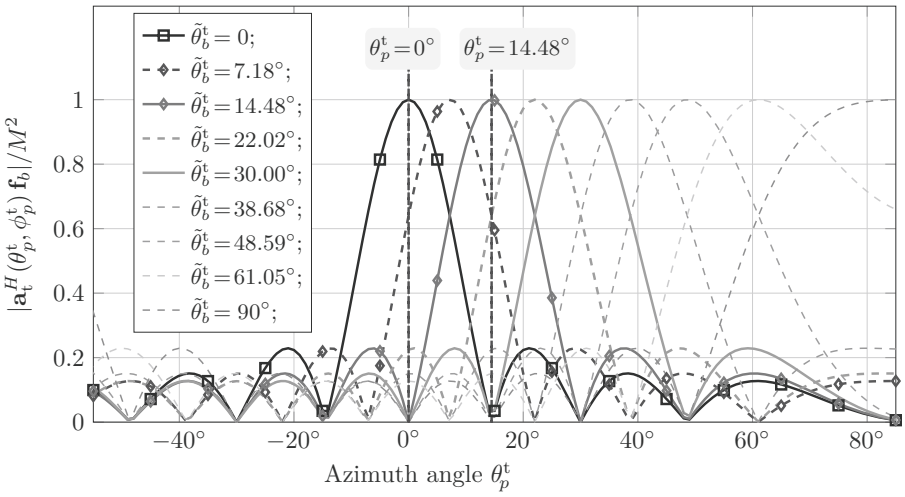

Figure 6.6: The normalized array patterns in the xy-plane ($\phi_p^{\mathrm{t}} = 90°$) at Tx side. (Source: [SRB+18] © 2018 IEEE).

The path gain α_p along path p is described as

$$\alpha_p = \Gamma_p \cdot \frac{\lambda}{4\pi D_p}, \tag{6.19}$$

with a reflection coefficient Γ_p and the Friis' free space path loss $\lambda/(4\pi D_p)$ [Rap01]. For the LoS path, we set $\Gamma_1 = 1$. The other reflected path Γ_2 is evaluated using the Fresnel equation with the angle of incidence, dielectric constant, and conductivity [Rap01]. Note that we model each reflection at a single object only, i.e., ground. For reflections with scattering clusters, more complicated models for α_p can be applied [ARAS+14].

Array patterns of the subarrays: To fully specify $\mathbf{H}_{\mathrm{eff}}$, we work out exemplary radiation patterns for subarrays. For reasonable link budget in later simulations, the subarrays are modeled as uniform square arrays with antenna element spacing $d_{\mathrm{e}} = \lambda/2$ and are consisting of M^2 isotropically radiating antenna elements each with $M = 8$. For every RF precoder $\mathbf{F}_{\mathrm{RF}}$ and RF equalizer $\mathbf{W}_{\mathrm{RF}}$, an implementation using analog phase shifters [HHN+05] is assumed. As a function of its steering angles $\{\tilde{\theta}_b^{\mathrm{t}}, \tilde{\phi}_b^{\mathrm{t}}\}$, the b-th analog beamforming vector (column vector) $\mathbf{f}_b$ of $\mathbf{F}_{\mathrm{RF}}$ is then denoted as

$$\mathbf{f}_b = \left[1,\ \ldots,\ e^{-jk_\lambda d_{\mathrm{e}}((m_{\mathrm{y}}-1)\sin\tilde{\theta}_b^{\mathrm{t}}\sin\tilde{\phi}_b^{\mathrm{t}}+(m_{\mathrm{z}}-1)\cos\tilde{\phi}_b^{\mathrm{t}})},\ \ldots,\ e^{-jk_\lambda d_{\mathrm{e}}((M-1)\sin\tilde{\theta}_b^{\mathrm{t}}\sin\tilde{\phi}_b^{\mathrm{t}}+(M-1)\cos\tilde{\phi}_b^{\mathrm{t}})}\right]^T, \tag{6.20}$$

where we recall that $1 \leq m_{\mathrm{y}},\ m_{\mathrm{z}} \leq M$ are the y, z indices of an antenna element in the subarray. The $\mathbf{w}_b$ at Rx can be written in a similar fashion w.r.t. its steering angles $\tilde{\theta}_b^{\mathrm{r}}$ and $\tilde{\phi}_b^{\mathrm{r}}$.

For simplification in later simulations, we assume $\mathbf{f}_b$, $\mathbf{w}_b$ are chosen from the same beamforming vector set $\mathcal{B}_{\mathrm{RF}}$. Thus, $\mathcal{F}_{\mathrm{RF}}$ and $\mathcal{W}_{\mathrm{RF}}$ are the same set that collects all N_{RF}-combinations from the set $\mathcal{B}_{\mathrm{RF}}$. Furthermore, as later simulations consider reflection and beamforming in the xy-plane only, see Fig. 6.4, we use $|\mathcal{B}_{\mathrm{RF}}| = 16$ predefined 'candidate beams'/'steering directions' with azimuth angles $\tilde{\theta}_b^i \in \{0°, \pm 7.18°, \pm 14.48°, \pm 22.02°, \pm 30°, \pm 38.68°, \pm 48.59°, \pm 61.05°, 90°\}$ and an elevation angle $\tilde{\phi}_b^i = 90°$. Due to the fact that the amplitudes of array patterns with negative $\tilde{\theta}_b^i$ values and ones with positive $\tilde{\theta}_b^i$ values are symmetric about the line $\theta_p^i = 0°$, only the amplitudes of array patterns $\mathbf{a}_{\mathrm{t}}^H(\theta_p^{\mathrm{t}}, \phi_p^{\mathrm{t}})\mathbf{f}_b$ with non-negative $\tilde{\theta}_b^{\mathrm{t}}$ are illustrated in Fig. 6.6 for clarity. Here, we recall that θ_p^{t} (ϕ_p^{t}) refers to azimuth

(elevation) AoD of the path p. The normalized array patterns at Rx side $|\mathbf{a}_{\mathrm{r}}^{H}(\theta_p^{\mathrm{r}}, \phi_p^{\mathrm{r}})\mathbf{w}_b|/M^2$ are similarly defined w.r.t. azimuth (elevation) AoA θ_p^{r} (ϕ_p^{r}) of the path p.

6.3.2 Results for a Deterministic 2-Subarray 2-Path Scenario

Environment parameters: The transceivers are assumed to be separated by a transmit distance $D = 100$ m, e.g., wireless backhaul, and to be at the same height, $h \in [5,\ 35]$ m. One reflected path from the ground is assumed, and the point of reflection is in the middle between the transceivers. The relative dielectric constant $\epsilon_{\mathrm{r}} = 3.6478$ and loss tangent $\tan\delta = 0.2053$ of concrete [FCF+11] are chosen to emulate ground reflection coefficient Γ_2. Those parameter settings can also be used for emulating side-building reflection in a similar scenario.

System parameters: The subarrays are assumed to be 8×8 $\lambda/2$-spaced uniform square arrays with isotropically radiating antennas, i.e., $M = 8$ with the highest array gain 18 dBi. The system uses a carrier frequency of 60 GHz, i.e., $\lambda = 5$ mm. For transceivers with 2 subarrays, this leads to an inter subarray distance $d_{\mathrm{sub}} = \sqrt{\lambda D/N} = 0.5$ m for optimizing the spectral efficiency over the LoS path. The system setup approaches the required assumption $\lambda \ll d_{\mathrm{sub}} \ll h < D$. To simplify later discussions, let us assume that the analog beamforming algorithm of subarrays steers one beam per available path, $N_{\mathrm{RF}} = P$. Furthermore, we take advantage of the mirror symmetry of the situation which allows us to use a symmetric beam set at transceivers, $\tilde{\theta}_b^{\mathrm{t}} = -\tilde{\theta}_b^{\mathrm{r}} = \tilde{\theta}_b$. The beams $\mathbf{f}_1$, $\mathbf{w}_1$ with $\tilde{\theta}_1 = 0$ are used for the LoS path, and beams $\mathbf{f}_2$, $\mathbf{w}_2$ with $\tilde{\theta}_2 \in \{7.18°, 14.48°, 22.02°, 30°\}$ are used for exciting the reflected path in the considered height range. The allowed bandwidth with 0dB loss regulated by [ISO14] is of a value $W = 1.88$ GHz. The transmit power P_{T} varies from -7 dBm to 20 dBm in later evaluations. Considering K_{c} subcarriers, the noise power for one subcarrier is assumed to be $\sigma_{\mathrm{n}}^2 = k_{\mathrm{B}} T_{\mathrm{K}} F W / K_{\mathrm{c}}$ [Fri44], where k_{B} is the Boltzmann constant, $T_{\mathrm{K}} = 300$ K is the absolute temperature in Kelvin, and $F = 5$ dB is the noise figure. For each subcarrier, the power constraint P_{C} is then calculated as $P_{\mathrm{C}} = P_{\mathrm{T}}/K_{\mathrm{c}}$. Here we assume that K_{c} is large enough and makes the subcarrier bandwidth smaller than the coherence bandwidth. The spectral efficiency is then found being independent of K_{c}. The baseband processing of such multi-carrier systems are applied per sub-carrier. For simplification, we focus our discussion on the spectral efficiency of the central sub-carrier at the carrier frequency.

Link Budget: A brief link budget is calculated here to offer a better understanding of our parameter settings. The allowed peak EIRP [FCC13] is 43 dBm at an array gain of 18 dBi. Considering a further transmit power reduction due to poor PAPR, we evaluate the average transmit power P_{T} in a range from -7 dBm to 20 dBm. The noise power for the complete bandwidth W is found as -76 dBm. The free space pathloss of the LoS path according to Friis transmission equation $(\frac{\lambda}{4\pi D})^2$ is -108 dB. Considering the AWGN channel derived from a single subarray LoS system with $P_{\mathrm{T}} = 20$ dBm, the calculated SNR on the LoS path is about 24 dB with a corresponding spectral efficiency of 8 bits/s/Hz. Accordingly considering the reflected path, the free space pathloss has additional loss up-to 2 dB w.r.t. the LoS path. In addition, the reflection power loss changes from 1 dB to 5 dB in the range of h under investigation.

Spectral Efficiency and Singular Values vs. Height: Fig. 6.7 and Fig. 6.8 compare the spectral efficiency and the singular values using different beam patterns for a 2-subarray 2-path hybrid MIMO system, $\{N,P\} = \{2, 2\}$. Their values are normalized w.r.t. the channel capacity

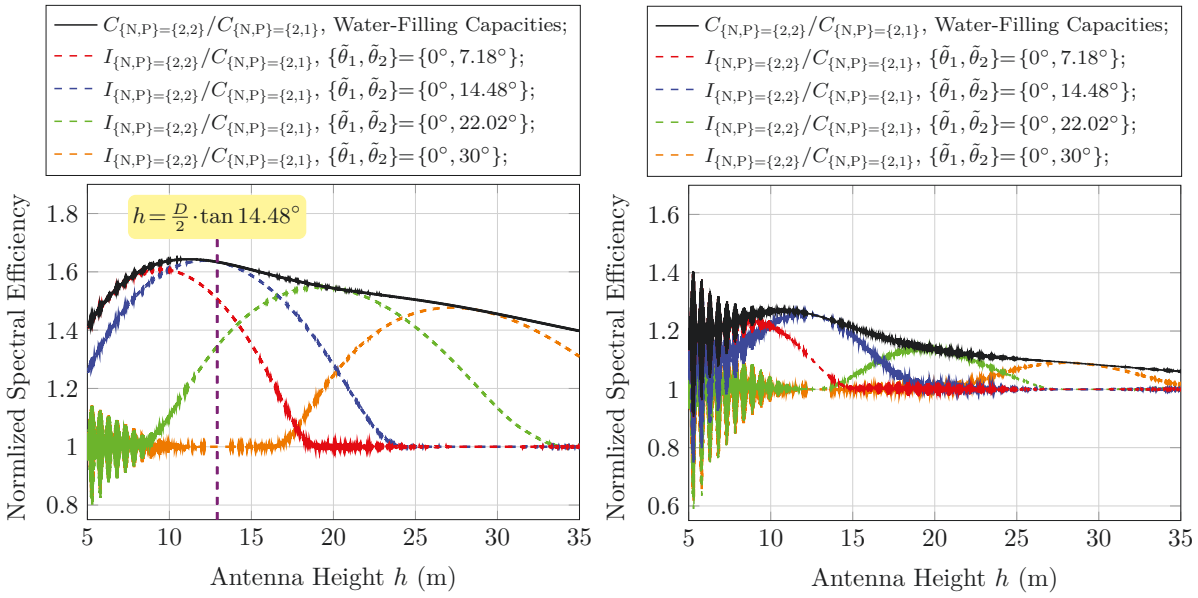

(a) $P_{\mathrm{T}} = 20$ dBm **(b)** $P_{\mathrm{T}} = 5$ dBm

Figure 6.7: Normalized spectral efficiency of a 2-subarray 2-path MIMO system w.r.t the capacity of an optimally arranged LoS MIMO system where we note that $C_{\{N,P\}=\{2,1\}} = 2 \cdot C_{\{N,P\}=\{1,1\}}$. (Parts of the results are reported in [SRB+18] © 2018 IEEE).

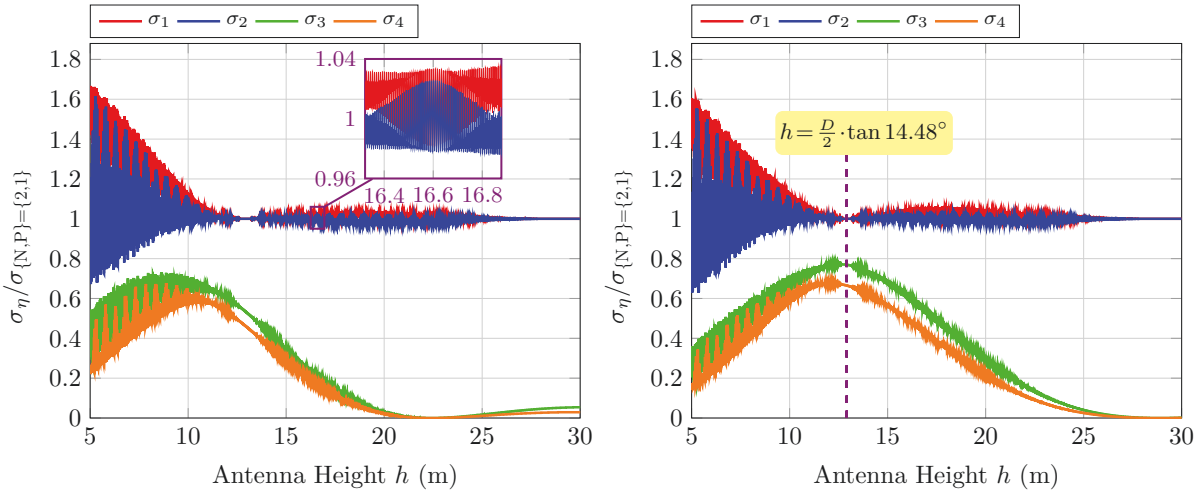

(a) $\{\tilde{\theta}_1,\tilde{\theta}_2\} = \{0°, 7.18°\}$ **(b)** $\{\tilde{\theta}_1,\tilde{\theta}_2\} = \{0°, 14.48°\}$

Figure 6.8: Normalized singular values of a 2-subarray 2-path MIMO system w.r.t the singular value of an optimally arranged LoS MIMO system where we note that $\sigma_{\{N,P\}=\{2,1\}} = \sqrt{2} \cdot \sigma_{\{N,P\}=\{1,1\}}$. (Source: [SRB+18] © 2018 IEEE).

of a corresponding 2-subarray LoS MIMO system, $C_{\{N,P\}=\{2,1\}}$ and $\sigma_{\{N,P\}=\{2,1\}}$, respectively. Varying the height changes the propagation length of the reflected path as well as its AoD and AoA simultaneously. Therefore, the spectral efficiency and the singular values using different analog beam sets are affected, especially by the resulting AoD/AoA.

Considering Fig. 6.6 and Fig. 6.7 (a), it can be found that the spectral efficiency achieves channel capacity, when there is sufficient power and the direction of the reflected path is aligned with the main lobe of the respective beam pattern. In those cases, low condition numbers are expected with small distances between singular values, see Fig. 6.8. The maximum spectral

efficiency, which is about 165 $\%$ of the spectral efficiency achieved by the LoS multi-subarray system, is found with beam pair $\{\tilde{\theta}_1, \tilde{\theta}_2\} = \{0°, 14.48°\}$ at a height about $\frac{D}{2}\tan(14.48°)$ in Fig. 6.7. Because the roots of both beam patterns roughly point along the complementary paths, the oscillation phenomenon is suppressed at this height as well. We would like to note here that there are two effects that influence the achieved peak value of the respective beam pairs, the effective gains and the condition numbers of the resulting channel matrices.

As shown in Fig. 6.7, even if the antenna arrangement is just optimized for the LoS path, a significant spectral efficiency gain in comparison with LoS MIMO systems is noticed as the normalized values are notably higher than one in most cases. From Fig. 6.8, it is observed that the singular values are grouped/clustered with corresponding paths. Singular values within each group are closer to each other than that of other groups. *The grouping phenomenon of singular values shows that the intra-path multiplexing exists at multiple path directions*. Meanwhile, it offers the potential for almost linearly increasing the spectral efficiency w.r.t. the subarray number N, as only a single curve is found for each path in single subarray scenarios with further simulations, see Appendix A.2. In Fig. 6.7, an interesting phenomenon is found that the spectral efficiency gains of all beam pairs saturate at the value one at high height range, where only the LoS path is dominating the system performance. Therefore, the system works as a LoS multi-subarray system as the second path is almost invisible to those beams under investigation.

An oscillation phenomenon due to interference is observed and is more severe in low height regions. Invoking the narrow-band assumption, i.e., assuming that the symbol duration is longer than the delay spread, we explain the oscillation phenomenon as follows: the waves of the same transmitted symbol are passing along 2 paths with different lengths. Changing the height changes the phase of the wave passing through the reflected path. The imposed wave varies periodically between constructive and destructive interference. A length difference in the order of λ is capable of causing several oscillating periods. The spatial frequency $f_h(h)$ of the oscillation is a function of h as $f_h(h) = 4\pi\sqrt{1 + (\frac{D}{2h})^2}/\lambda$. This oscillation phenomenon is also observed in Appendix A.2 with $N = 1$. But for $N = 2$ and higher, beats are found for this spatial frequency oscillation. The beats of the oscillation can also be explained by a spatial frequency offset on $f_h(h)$ since there exists a height difference between subarrays of value d_{sub}. The amplitudes of the oscillation are influenced by the path gain differences, the array gain differences, and the transmit power of the water-filling based transmission scheme. Due to the strong variation of the performance at low height values, sharper beams are recommended to suppress the oscillation and/or one should increase the height of the system.

Spectral Efficiencies and SNRs vs. Transmit Power: At one particular height, Fig. 6.9 and Fig. 6.10 illustrate the variation of the spectral efficiency and the subchannel SNRs of different systems at different transmit power values, respectively. To simplify discussions, the evaluations are carried out for a height value $h = \frac{D}{2}\tan(14.48°)$. In Fig. 6.9, the spectral efficiencies of 2-subarray 2-path hybrid MIMO systems are almost doubling the values achieved by a single subarray system and are much higher than the values of the 'LoS MIMO'/'LoS' systems.

In Fig. 6.10, it can be found that, at this given height, the SNRs for the first two subchannels of a 2-subarray 2-path system are identical to each other. With very low transmit power, e.g., $P_{\mathrm{T}} = -7\ \mathrm{dBm}$, the spectral efficiency and the SNRs of the first two subchannels are also identical to that of the 'LoS MIMO'/'LoS' systems, while the third and fourth subchannels are

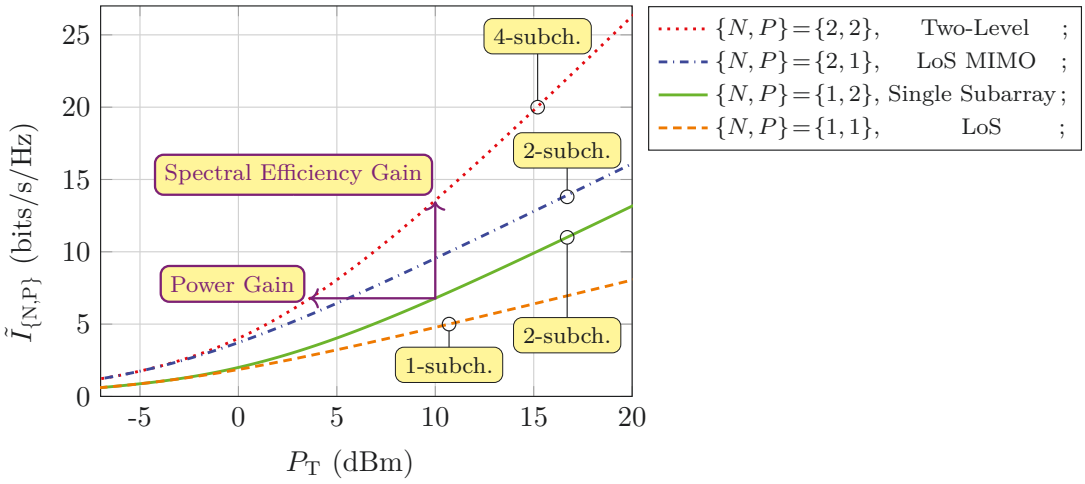

Figure 6.9: Spectral Efficiency of different mmWave MIMO systems when $h = \frac{D}{2}\tan(14.48°)$. (Source: [SRB+18] © 2018 IEEE).

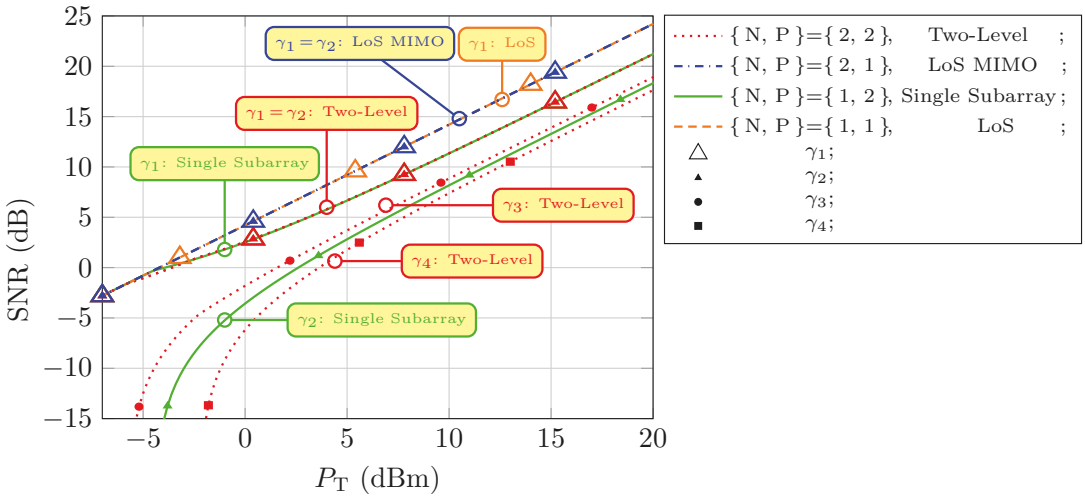

Figure 6.10: SNRs of the subchannels vs. transmit power achieved by different mmWave MIMO systems when $h = \frac{D}{2}\tan(14.48°)$. (Source: [SRB+18] © 2018 IEEE).

not bringing any benefits. This can be explained via the water-filling algorithm which exploits only the two best subchannels dominated by the LoS path.

For the LoS 2-subarray MIMO system and the single-subarray 2-path MIMO system, the number of subchannels is reduced to two as shown in Fig. 6.10. When applying the water-filling algorithm with the same amount of fill-in 'water' to the LoS MIMO system with $N_s = 2$, higher SNRs are observed in comparison with the first two subchannels of the 2-subarray 2-path hybrid MIMO system. Furthermore, SNRs of the single-subarray 2-path hybrid MIMO system are almost aligned with the SNRs of the corresponding groups of the 2-subarray 2-path system. This fits the previously observed phenomenon on grouped singular values.

6.4 Summary

In this chapter, a hierarchical system with multiple widely spaced subarrays was proposed for exploiting two different spatial multiplexing kinds jointly. The proposed system offers high spatial multiplexing gains for mmWave backhaul links in limited scattering environments. For proving

the feasibility of such joint exploitation, we started from analyzing the conventional mmWave system, which exploits spatial multiplexing provided by multipath propagation, namely inter-path spatial multiplexing. In contrast, widely spaced antenna elements are necessary for LoS MIMO systems to exploit spatial multiplexing embedded in a single path, namely intra-path spatial multiplexing. More importantly, intra-path spatial multiplexing appears not only in the LoS path but also in many resolvable propagation paths.

Attempting to harness both kinds of spatial multiplexing jointly, we proposed an array of subarrays. The subarrays aimed at inter-path spatial multiplexing. The current mmWave RF components are directly usable for them. By further putting a number of subarrays together with sufficient distance apart, it became possible to exploit the intra-path spatial multiplexing gain with respect to each prorogation path. After analyzing the array response vector, the corresponding channel model was derived with a modified hybrid beamforming architecture. Furthermore, under total transmit power constraints, we analyzed the spectral efficiency achieved by the proposed systems. In comparison to single subarray systems addressing only spatial signatures, an approximately linear scaling of the spectral efficiency is observed. In comparison with the LoS MIMO based approach, data rate increment up-to 65 $\%$ is observed by utilizing just one additional path. Those results showed that the two kinds of spatial multiplexing in mmWave studies can be jointly exploited and this significant performance gain is worth for further investigations.

In this chapter, we summarize the key learning points for engineers as:

- Using arrays of widely spaced subarrays in limited scattering environments, the aforementioned structured phase couplings in the LoS path direction can also be found in other path directions. This forms two different spatial multiplexing kinds on their two antenna topology levels.
- With reasonable costs and complexity, the advanced hybrid analog/digital beamforming architecture for the arrays of multiple subarrays can efficiently and jointly exploit the spatial multiplexing gain between different path directions and spatial multiplexing gain within a single path direction.

Chapter 7

Conclusion and Outlook

7.1 Conclusion

The main goal of this thesis was to analyze the applicability of line-of-sight (LoS) spatial multiplexing at millimeter wave (mmWave) frequencies. The channel between antenna arrays in strong LoS Multiple-Input-Multiple-Output (MIMO) systems is determined by antenna topology, and orthogonal channel matrices can be achieved in the ideal cases. By analyzing the relationship between phases and antenna positions in 3D space under spherical wave propagation, we derived a channel factorization model. This channel factorization model can be used for providing antenna topology solutions for this antenna arrangement dependent MIMO communication, mathematically proving channel properties like robustness against displacements, and reducing the complexity in signal processing with both digital and analog implementations. In addition, for this mmWave wideband communication system, a hardware-in-the-loop demonstrator was examined in this thesis. Besides identifying several hardware impairments that may decrease the performance of practical systems, initial attempts on efficiently and parallelly compensating these impairments were made. Finally, motivated by the robustness of LoS spatial multiplexing against transmit directions, we introduced the LoS spatial multiplexing to other path directions and checked the potential of further increasing the throughput of fixed wireless.

In particular, the following results were obtained:

- ▷ We introduced the basic concept of strong LoS MIMO communication in chapter 2. Such systems rely on the phase couplings between the transmit array and the receive array that are specifically and accordingly arranged. In the ideal cases with optimal antenna arrangements, the orthogonal channel matrices allowing parallel stream transmission with equal sub-channel quality can be obtained via this LoS path communication.

- ▷ We showed in section 3.1 that the strong LoS MIMO channel matrix can be factorized into a product of three matrices with two diagonal matrices at outer positions. The diagonal entries of the two diagonal matrices are of unit magnitudes and contribute most of the variations at different antenna geometry realizations. Only the middle matrix contributed by array projections in broadside relative to transmit direction determines capacity and sub-channel conditions, if the array sizes are negligible in comparison to the transmit distance.

- ▷ We used this channel factorization model to provide a general solution on antenna arrangements in point-to-point strong LoS MIMO communication in section 3.2. The state-of-the-art works have not offered a conclusive antenna topology solution, e.g., the rotation directions of the uniform planar arrays are restricted. Viewing the antenna topology from a projection point of view, we showed that the optimal antenna arrangement solution on any curved surface can be easily obtained via mapping the broadside solution to the surface. As examples, 1D and 2D antenna arrangements that compensate the degradation from any tilt angle were presented.

- ▷ The robustness of the LoS spatial multiplexing can be explained with the proposed channel factorization model (as discussed in chapter 3). The possible normalized displacement errors of the middle matrix are much less sensitive than that of the two outer diagonal matrices. This provided the insights into the robustness of LoS spatial multiplexing from a mathematical point of view, although the realizations on the matrices can be very different. Together with the simulation results (provided earlier in chapter 2), we concluded that the LoS spatial multiplexing for fixed wireless communication is quite robust against moderate displacement errors.

- ▷ To meet the growing demands on the throughput of wireless backhaul links, we outlined basic assumptions and a multi-subarray design for a mmWave LoS MIMO backhaul system in section 3.3 and section 3.4, respectively. Potentially supporting data rates well above 100 Gbit/s, this LoS multi-subarray system deploys spatial multiplexing on top of the analog beamforming scheme. The findings motivate the usage of LoS MIMO technologies at mmWave and higher frequencies with their moderate array sizes and relatively high spatial multiplexing gain.

- ▷ The second important topic in this work was the usage of the channel factorization model for signal processing. An algorithm named sequential channel equalization (SCE) was proposed for LoS MIMO processing in chapter 4. By refining the channel factorization in section 4.1, the middle matrix under sub-optimal arrangements has an inverse discrete Fourier matrix as its dominating term and is perturbed by certain displacement errors. Therefore, the proposed method in section 4.2, which is in the reverse order w.r.t. the factorization and has a fast Fourier transform matrix in the middle, became feasible and requires less complexity as discussed in section 4.3 and section 4.4.

- ▷ Since the two outer diagonal matrices of SCE can be very different at different realizations of the antenna topology, a method for setting them (the two diagonal matrices) was proposed in section 4.2. As the input of the method, only the channel matrix needs to be known (i.e., estimated) rather than its factored form, which makes the SCE algorithm implementable for practical systems. As found numerically under optimal/sub-optimal arrangements in section 4.5, the SCE using the proposed method performs as good as/nearly as good as the zero-forcing equalization (ZFE).

- ▷ By using analog equalization in LoS MIMO systems, we showed in section 4.4 that the loss of mutual information due to low resolution quantization can be reduced. When

designing the analog equalizing network with SCE, the number of fully configurable analog components scales linearly with the stream number, while the state-of-the-art works implementing the ZFE scale quadratically. Furthermore, with the use of a conventional Butler matrix, the wiring efforts and the number of fixed phase shifters can be reduced.

- We considered synchronization for the LoS MIMO systems with independent oscillators at different antennas in chapter 5. As a reaction to the observed gradually changing carrier frequency offsets (CFO), a signal model and an efficient frame structure were proposed in section 5.1 and section 5.2, respectively. They accounted for two effects, one due to the quasi-stationary physical channel, and one due to the time-varying behavior of the oscillators. Based on the frame structure and the relative small CFOs during training sequence transmission, a method for efficiently estimating the LoS MIMO channel and the CFOs was studied.

- In order to turn the mmWave LoS spatial multiplexing into practice, possible hardware imperfections with wideband signals should be considered and compensated. A systolic/pipelined structure was proposed in section 5.3 for efficiently handling multiple streams at high symbol rates. Furthermore, the proposed architecture is a viable approach that scales well with the number of MIMO streams. With the recorded data from a hardware-in-the-loop demonstrator, it was shown that, after compensating the interantenna interference (IAI, from the LoS MIMO channel) together with the CFOs, the rest of the hardware impairments, e.g., the intersymbol interference from frequency selective components, can be compensated rather independently and parallelly at different steams. The proposed low complexity architecture can achieve performance that is nearly as good as that of the highly complex baseline algorithm, as shown in section 5.4. Eventually, using SCE or ZFE for the IAI suppression results in almost the same performance, e.g., about 0.1dB difference between their error vector magnitude values.

- Considering that the reflected objects in limited scattering environments are spatially correlated, a channel model was derived for mmWave systems with widely spaced subarrays in chapter 6. The spatial multiplexing gain from the spatial signature of multiple paths and the spatial multiplexing gain from the structured phase couplings of a single path direction are found simultaneously at two different levels of the arranged antennas.

- We proposed to use an advanced hybrid analog/digital beamforming architecture to efficiently implement the proposed multi-subarray mmWave MIMO system at reasonable costs and complexity in section 6.2. Analog beamforming is applied at subarrays and excites the resolvable paths that allow signal transmission. Then, the baseband digital beamforming enhances the performance via suppressing the interferences of analog beams and exploiting the spatial multiplexing of each path direction. The proposed system can achieve a higher order of the sub-channels than that achieved by the conventional systems of either a single subarray or a single path direction, and it can overcome the low rank property brought by limited scattering.

7.2 Outlook

In this section, we would like to discuss the open research topics, especially with the insights provided by this work. Since the LoS MIMO system becomes a very promising technology in enhancing the throughput of fixed wireless, the presented topics focus more on practical concerns.

- ▷ **Polarization Diversity**: Polarization diversity can be easily added to the current setup for doubling the bandwidth efficiency. However, in the case that cross polarization discrimination factor is small, the interference between two polarized arrays are also found to be dependent on antenna arrangements. Therefore, re-modeling the LoS MIMO channel with polarized/dual-polarized antennas [Col08] and extending cross polarization interference cancellation algorithms [CCSV86, LNNS89] to these LoS MIMO scenarios are of interests.

- ▷ **Antenna Topology**: In this thesis, we have discussed that a 3D antenna arrangement allows higher throughputs in scenarios with rays from different directions compared to 2D arrangements, since the projection of the array should be jointly considered for multiple directions. Therefore, it is worth to investigate general 3D antenna topologies, which can be used to further improve the performance in scenarios like multiple access (point-to-multipoint communication in a wireless backhaul network) and multipath. Finally, migration of the system concept to higher frequency bands, which further reduces the array sizes and provides larger available bandwidths, is interesting for even higher throughput.

- ▷ **System Design**: The performance of the practical mmWave LoS MIMO systems should be further studied during system expansion with more parallel streams. Moreover, considering the complexity and the requirements on training sequences for synchronization, antennas/subarrays with shared low frequency reference clock yields the most feasible system design. In addition, since analog equalization suits well for LoS MIMO communication, analog equalizing networks that avoid possible frequency selectivity still needs to be developed by RF experts.

- ▷ **Low Resolution Quantization**: Channel estimation using low resolution ADCs with and without the analog equalizing network in MIMO communication is of interest. Initial attempts on a general 2×2 MIMO setup with quantization bits as low as one can be found in [IN07, MAN10]. Further considering that the strong LoS MIMO system has only a single tap in its physical channel, the channel state information can also be estimated with narrowband signals, for which the high resolution quantization can be easily implemented. However, for this kind of channel reciprocity between narrowband and wideband signal transmission, the reciprocity principle is fulfilled only if the effective wideband channel including circuitries is not frequency selective.

- ▷ **Practical Scenarios**: In this work, we discussed the LoS MIMO systems under a strong LoS assumption, which suits well for rooftop scenarios. However, in other front-/backhaul scenarios, e.g., links between two lamp posts in the street canyon, the dominance of the LoS path and the possibility of the Fresnel zone being partially blocked

should be characterized. Since the clustering effects may occur in LoS communication, the channel model for LoS MIMO communication with correlated post cursors [M+17] should be investigated. Moreover, according to the current channel measurements, the physical channel is found to be rather deterministic [HCGL18, CGHL17]. The variations of the propagation path in longer time periods due to weather and season changes should be analyzed. Eventually, the resizable/reconfigurable array design of practical systems for massive deployments should be carried out based on the insights from this work.

- ▷ **Channel Sparsity and Two-Level Spatial Multiplexing**: The performance and the equalization algorithms of the widely spaced multi-subarray system using wideband signals would be interesting, as the channel with multiple paths becomes sparse also in the time/delay domain. Considering intended applications like wireless backhaul, the channel is quasi-deterministic. Using time-domain equalization, avoiding the cyclic prefix as required by frequency-domain equalization, offers a great potential in improving the temporal efficiency. However, the high complexity requirement becomes a problem for standard time-domain algorithms like decision feedback equalization [ADS00]. It is noticed with some initial attempts of the author that, if there exists delay domain channel sparsity, the time-domain filters become sparse as well. Then, the complexity of the filters can be reduced without a strong negative impact on the performance and the time-domain equalization tends to be an interesting solution in mmWave backhaul systems. Eventually, due to the roughness of possible reflecting surfaces, cluster structures with angular spreads are expected for channel impulse responses. The phase couplings of the respective path would then evolve certain randomness. Modeling the channel and efficiently handling the involved additional challenges like signal processing are open research areas.

Appendix A

Appendix

A.1 SFO Estimation During Post Processing

During the post-processing, the SFO is estimated based on the training sequences with a correlation based method proposed in [GHLS02, WCS05]. Although SFO estimation and compensation is not the focus of our work, we repeat several key steps here for completeness. For an K_{o}-fold oversampled, $K_{\mathrm{o}} = 8$ in this work[1], version $y'_{n_{\mathrm{r}}}[k]$ of each received signal stream is captured and correlated with the corresponding oversampled training sequences $x_{\mathrm{T},n_{\mathrm{t}}}[k]$, i.e.,

$$\Lambda_{n_{\mathrm{r}}n_{\mathrm{t}}}[k] = \left| \sum_{l=1}^{K_{\mathrm{o}} \cdot L_T} x^*_{\mathrm{T},n_{\mathrm{t}}}[l] \cdot y'_{n_{\mathrm{r}}}[l+k-1] \right|^2, \tag{A.1}$$

where the sampling index k_q at the beginning of the q-th sub-frame are found with highest correlation peak as

$$k_q = \arg\max_k \Lambda_{n_{\mathrm{r}}n_{\mathrm{t}}}[k]. \tag{A.2}$$

Due to the fact that symmetric pulses are commonly used for transmission, the magnitude of the cross-correlation peaks is also symmetric, when sample timing is aligned and multipath is not influencing the shape significantly. Therefore, the metric $\Lambda_{n_{\mathrm{r}}n_{\mathrm{t}}}[k]$ is used for SFO estimation where the squaring is performed to reduce the effect of multipath, and typically a small window of samples K_{w} around the main peak, e.g., $K_{\mathrm{w}} = 17$ in this work, is used for the estimation. An estimate for $\varepsilon[k_q]$ of the q-th sub-frame is then obtained by using a DFT on that block of samples with

$$\hat{\varepsilon}[k_q] = \frac{-K_{\mathrm{w}}}{4\pi} \measuredangle \left\{ \sum_{l=0}^{K_{\mathrm{w}}-1} \Lambda_{n_{\mathrm{r}}n_{\mathrm{t}}} \left[k_q - l + \frac{K_{\mathrm{w}}-1}{2} \right] e^{-j\frac{4\pi l}{K_{\mathrm{w}}}} \right\}, \tag{A.3}$$

where the SFO estimate $\hat{\varepsilon}[k_q]$ is a fractional number valid for the q-th sub-frame. For data processing, downsampling to symbol rate is performed and considered after the SFO compensation in this work. We also would like to note that, since there exists only one common sampling frequency offset process between Rx and Tx, the estimation in Chapter 5 is performed using the received signal at Rx-1 and training sequences at Tx-1, i.e., $n_{\mathrm{r}} = n_{\mathrm{t}} = 1$.

[1] One can reduce the K_{o}, e.g., to 4 or 2, but a performance decrease should be expected.

A.2 Performance of a Single Subarray System in a 2-Path Scenario

This part illustrates the simulation results for single subarray systems $N = 1$ with the path number P being one and two. Other parameters of the channel model and the system setup are the same defined and set as in Sec. 6.3 including transmit distance D, the carrier frequency f_c, the height of the system h, the subarray size M, the antenna element spacing d_e, the beamforming vector set $\mathcal{B}_{\mathrm{RF}}$, the reflection coefficients Γ_p, the transmit power P_{T}, the noise power σ_n^2 and the bandwidth W.

Fig. A.1 compares the relative spectral efficiencies $I_{\{\mathrm{N,P}\}=\{1,2\}}$ of a 2-path channel when different analog beam patterns are used. The corresponding water-filling channel capacity with perfect CSI at Tx is denoted as $C_{\{\mathrm{N,P}\}=\{1,2\}}$. Meanwhile, in order to present the singular value variation of the channel, the beam pair $\{\tilde{\theta}_1, \tilde{\theta}_2\} = \{0°, 14.48°\}$ is selected as an example in Fig. A.2. All the values are normalized w.r.t. the channel capacity $C_{\{\mathrm{N,P}\}=\{1,1\}}$ or singular value $\sigma_{\{\mathrm{N,P}\}=\{1,1\}}$ of a single subarray system with a single path. The spectral efficiencies are examined with total transmit power of $20\mathrm{dBm}$ at different heights. Considering Fig. 6.6, Fig. A.1, and Fig. A.2, it can be found that when there is sufficient power and the directions of paths are aligned with the main lobe of the respective beam pattern, the spectral efficiency can be maximized, while the condition number is small.

An oscillation phenomenon due to interference is observed and is similar to that in Sec. 6.3 without the beats. The waves of the same transmitted symbol are passing along 2 paths with different lengths. Therefore, they are superimposed with varying phase differences by varying antenna height h. This causes a periodic change between constructive and destructive interference. This interference phenomenon is influenced by the pathloss differences and the array gain differences. Only if the amplitudes of the same signal from the LoS path and the reflected path are comparable, strong oscillations would occur (e.g., in low height region).

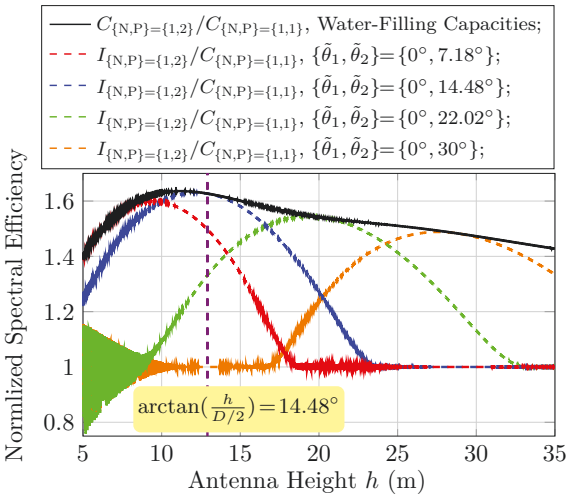

Figure A.1: Normalized spectral efficiency of a 1-subarray 2-path MIMO system w.r.t the capacity of a single path LoS system, $P_{\mathrm{T}} = 20\mathrm{dBm}$.

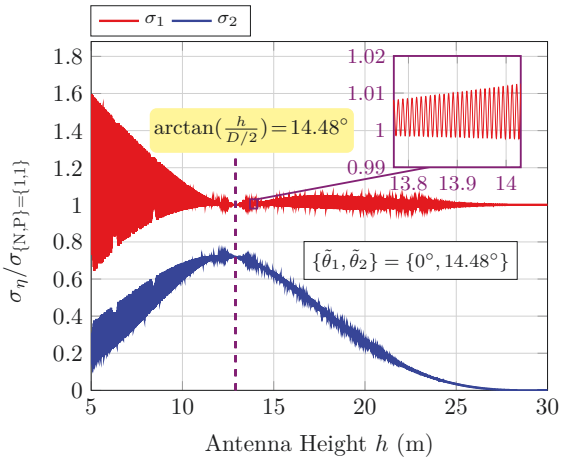

Figure A.2: Normalized singular values of a 1-subarray 2-path MIMO system w.r.t the singular value of a single path LoS system.

Bibliography

[AANS+13] S. Apostu, A. Al-Nuaimi, E. Steinbach, M. Fahrmair, X. Song, and A. Möller. Towards the Design of an Intuitive Multi-view Video Navigation Interface Based on Spatial Information. In *Proceedings of the International Conference on Human-computer Interaction with Mobile Devices and Services*, pages 103–112, New York, NY, USA, 2013. ACM.

[ABM+15] J. Antes, F. Boes, T. Messinger, U. J. Lewark, T. Mahler, A. Tessmann, R. Henneberger, T. Zwick, and I. Kallfass. Multi-Gigabit Millimeter-Wave Wireless Communication in Realistic Transmission Environments. *IEEE Transactions on Terahertz Science and Technology*, 5(6):1078–1087, Nov 2015.

[ADS00] N. Al-Dhahir and A. H. Sayed. The Finite-Length Multi-Input Multi-Output MMSE-DFE. *IEEE Transactions on Signal Processing*, 48(10):2921–2936, Oct 2000.

[AH16] A. Alkhateeb and R. W. Heath. Frequency Selective Hybrid Precoding for Limited Feedback Millimeter Wave Systems. *IEEE Transactions on Communications*, 64(5):1801–1818, May 2016.

[AHAS+12] O. E. Ayach, R. W. Heath, S. Abu-Surra, S. Rajagopal, and Z. Pi. Low Complexity Precoding for Large Millimeter Wave MIMO Systems. In *Proceedings of the IEEE International Conference on Communications*, pages 3724–3729, June 2012.

[AK15] J. Antes and I. Kallfass. Performance Estimation for Broadband Multi-Gigabit Millimeter- and Sub-Millimeter-Wave Wireless Communication Links. *IEEE Transactions on Microwave Theory and Techniques*, 63(10):3288–3299, Oct 2015.

[Ala98] S. M. Alamouti. A Simple Transmit Diversity Technique for Wireless Communications. *IEEE Journal on Selected Areas in Communications*, 16(8):1451–1458, Oct 1998.

[AMGPH14] A. Alkhateeb, J. Mo, N. Gonzalez-Prelcic, and R. W. Heath. MIMO Precoding and Combining Solutions for Millimeter-Wave Systems. *IEEE Communications Magazine*, 52(12):122–131, Dec 2014.

[ANHT+13] A. Al-Nuaimi, R. Huitl, S. Taifour, S. Sarin, X. Song, Y. X. Gu, E. Steinbach, and M. Fahrmair. Towards Location Recognition using Range Images. In *Proceedings of the IEEE International Conference on Multimedia and Expo Workshops*, pages 1–6, July 2013.

[ARAS+14] O. E. Ayach, S. Rajagopal, S. Abu-Surra, Z. Pi, and R. W. Heath. Spatially Sparse Precoding in Millimeter Wave MIMO Systems. *IEEE Transactions on Wireless Communications*, 13(3):1499–1513, March 2014.

[AVR08] L. Anttila, M. Valkama, and M. Renfors. Circularity-Based I/Q Imbalance Compensation in Wideband Direct-Conversion Receivers. *IEEE Transactions on Vehicular Technology*, 57(4):2099–2113, July 2008.

[Bal05] C. A. Balanis. *Antenna Theory: Analysis and Design, 3rd Edition*. Wiley-Interscience, 2005.

[BBS13] J. Brady, N. Behdad, and A. M. Sayeed. Beamspace MIMO for Millimeter-Wave Communications: System Architecture, Modeling, Analysis, and Measurements. *IEEE Transactions on Antennas and Propagation*, 61(7):3814–3827, July 2013.

[BLM+14] N. Bhushan, J. Li, D. Malladi, R. Gilmore, D. Brenner, A. Damnjanovic, R. T. Sukhavasi, C. Patel, and S. Geirhofer. Network Densification: The Dominant Theme for Wireless Evolution into 5G. *IEEE Communications Magazine*, 52(2):82–89, Feb 2014.

[BOO05] F. Bohagen, P. Orten, and G.E. Oien. Construction and Capacity Analysis of High-rank Line-of-sight MIMO Channels. In *Proceedings of the IEEE Wireless Communications and Networking Conference*, volume 1, pages 432–437, March 2005.

[BOO06] F. Bohagen, P. Orten, and G.E. Oien. Optimal Design of Uniform Planar Antenna Arrays for Strong Line-of-Sight MIMO Channels. In *Proceedings of the IEEE Workshop on Signal Processing Advances in Wireless Communications*, pages 1–5, July 2006.

[BOO09] F. Bohagen, P. Orten, and G. E. Oien. On Spherical vs. Plane Wave Modeling of Line-of-Sight MIMO Channels. *IEEE Transactions on Communications*, 57(3):841–849, March 2009.

[BS03] O. Besson and P. Stoica. On Parameter Estimation of MIMO Flat-Fading Channels with Frequency Offsets. *IEEE Transactions on Signal Processing*, 51(3):602–613, March 2003.

[CCSV86] J. Chamberlain, F. Clayton, H. Sari, and P. Vandamme. Receiver Techniques for Microwave Digital Radio. *IEEE Communications Magazine*, 24(11):43–54, Nov 1986.

[CFV00] D. Chizhik, G. J. Foschini, and R. A. Valenzuela. Capacities of Multi-Element Transmit and Receive Antennas: Correlations and Keyholes. *Electronics Letters*, 36(13):1099–1100, June 2000.

[CGHL17] D. Cvetkovski, E. Grass, T. Hälsig, and B. Lankl. Hardware-in-the-loop demonstration of a 60GHz line-of-sight 2x2 MIMO link. In *Proceedings of the IEEE International Conference on Smart Technologies*, pages 631–636, July 2017.

[CHT+12] W. Y. Chen, Y. R. Hsieh, C. C. Tsai, Y. M. Chen, C. C. Chang, and S. F. Chang. A Compact Two-Dimensional Phased Array Using Grounded Coplanar-Waveguides Butler Matrices. In *Proceedings of European Radar Conference*, pages 421–424, Oct 2012.

[CLS04] S. Calabrò, B. Lankl, and G. Sebald. Multiple Co-Polar Co-Channel Point-to-Point Radio Transmission. *AEU - International Journal of Electronics and Communications*, 58(1):51 – 57, 2004.

[Col08] M. Coldrey. Modeling and Capacity of Polarized MIMO Channels. In *Proceedings of the IEEE Vehicular Technology Conference*, pages 440–444, May 2008.

[CRKF17] H. L. Chiang, W. Rave, T. Kadur, and G. Fettweis. A Low-Complexity Beamforming Method by Orthogonal Codebooks for Millimeter Wave Links. In *Proceedings of the IEEE International Conference on Acoustics, Speech and Signal Processing*, March 2017.

[CT65] J. Cooley and J. Tukey. An Algorithm for the Machine Calculation of Complex Fourier Series. *Mathematics of Computation*, 19(90):297–301, April 1965.

[CT06] T. M. Cover and J. A. Thomas. *Elements of Information Theory*. John Wiley & Sons, 2nd edition, 2006.

[DF98] P. F. Driessen and G. J. Foschini. On the Capacity Formula for Multiple Input-multiple Output Wireless Channels: A Geometric Interpretation. *IEEE Transactions on Communications*, 47(2):173–176, Feb 1998.

[DOA+17] Z. Du, E. Ohlmer, K. Aronkyt, J. Putkonen, J. Kapanen, and D. Swist. 5G E-band Backhaul System Measurements in Urban Street-Level Scenarios. In *Proceedings of the European Microwave Conference*, pages 372–375, Oct 2017.

[Dra16] DragonWave Inc. Multi-Gigabit Microwave Backhaul with Enhanced$^{\mathrm{MC}}$, 2016. White Paper.

[ECC09] ECC. Use of the 57 - 64 GHz frequency band for point-to-point Fixed Wireless Systems. *CEPT/ECC Recommendation (09)01 (02-2009)*, Jan 2009.

[ECC17] ECC. Guidelines on how to plan LoS MIMO for Point-to-Point Fixed Service Links. *CEPT/ECC Report 258*, Jan 2017.

[ERI17] ERICSSON. Ericsson Microwave Outlook 2017, Dec 2017.

[FCC13] FCC. Part 15 of the Commissions Rules Regarding Operation in the 57-64 GHz Band. *Federal Communications Commission (FCC) document ET Docket No. 07-113 and RM-11104*, Aug 2013.

[FCF+11] B. Feitor, R. Caldeirinha, T. Fernandes, D. Ferreira, and N. Leonor. Estimation of Dielectric Concrete Properties from Power Measurements at 18.7 and 60 GHz. In *Proceedings of the Loughborough Antennas and Propagation Conference*, pages 1–5, Nov 2011.

[Fet14a] G. Fettweis. LTE: The Move to Global Cellular Broadband. *Intel Technical Journal, special issue on LTE*, 18:7–10, Feb 2014.

[Fet14b] G. Fettweis. The Tactile Internet: Applications and Challenges. *IEEE Vehicular Technology Magazine*, 9(1):64–70, March 2014.

[FG98] G. J. Foschini and M. J. Gans. On Limits of Wireless Communications in a Fading Environment when Using Multiple Antennas. *Wireless Personal Communications*, 6(3):311–335, March 1998.

[Fos96] G. J. Foschini. Layered Space-Time Architecture for Wireless Communication in a Fading Environment when Using Multi-element Antennas. *Bell Labs Technical Journal*, 1(2):41–59, Autumn 1996.

[Fri44] H. T. Friis. Noise Figures of Radio Receivers. *Proceedings of the IRE*, 32(7):419–422, July 1944.

[Fri46] H. T. Friis. A Note on a Simple Transmission Formula. *Proceedings of the IRE*, 34(5):254–256, May 1946.

[GBGP02] D. Gesbert, H. Bolcskei, D. A. Gore, and A. J. Paulraj. Outdoor MIMO Wireless Channels: Models and Performance Prediction. *IEEE Transactions on Communications*, 50(12):1926–1934, Dec 2002.

[GDM+15] Z. Gao, L. Dai, D. Mi, Z. Wang, M. A. Imran, and M. Z. Shakir. MmWave Massive-MIMO-Based Wireless Backhaul for the 5G Ultra-Dense Network. *IEEE Wireless Communications*, 22(5):13–21, Oct 2015.

[GHLS02] A. Gesell, J. Huber, B. Lankl, and G. Sebald. Data-Aided Symbol Timing Estimation for Linear Modulation. *AEU - International Journal of Electronics and Communications*, 56(5):303 – 311, 2002.

[GS06] M. Ghogho and A. Swami. Training Design for Multipath Channel and Frequency-Offset Estimation in MIMO Systems. *IEEE Transactions on Signal Processing*, 54(10):3957–3965, Oct 2006.

[GSCK17] Y. Ghasempour, C. Silva, C. Cordeiro, and E. Knightly. IEEE 802.11ay: Next-Generation 60 GHz Communication for 100 Gb/s Wi-Fi. *IEEE Communications Magazine*, 55(12):186–192, Dec 2017.

[GSS+03] D. Gesbert, M. Shafi, D. Shiu, P. J. Smith, and A. Naguib. From Theory to Practice: an Overview of MIMO Space-Time Coded Wireless Systems. *IEEE Journal on Selected Areas in Communications*, 21(3):281–302, April 2003.

[Han09] R. C. Hansen. *Phased Array Antennas*. John Wiley & Sons, Inc., 2nd edition, 2009.

[HCGL17] T. Hälsig, D. Cvetkovski, E. Grass, and B. Lankl. Measurement Results for Millimeter Wave Pure LOS MIMO Channels. In *Proceedings of the IEEE Wireless Communications and Networking Conference*, pages 1–6, March 2017.

[HCGL18] T. Hälsig, D. Cvetkovski, E. Grass, and B. Lankl. Statistical Properties and Variations of LOS MIMO Channels at Millimeter Wave Frequencies. In *Proceedings of the International ITG Workshop on Smart Antennas*, pages 1–6, March 2018.

[HGPR+16] R. W. Heath, N. Gonzalez-Prelcic, S. Rangan, W. Roh, and A. M. Sayeed. An overview of signal processing techniques for millimeter wave mimo systems. *IEEE Journal of Selected Topics in Signal Processing*, 10(3):436–453, April 2016.

[HHN+05] A. Hajimiri, H. Hashemi, A. Natarajan, Xiang Guan, and A. Komijani. Integrated Phased Array Systems in Silicon. *Proceedings of the IEEE*, 93(9):1637–1655, Sep 2005.

[Hil76] J. E. Hill. Gain of Directional Antennas. *Watkins-Johnson Tech-note*, 3(4), July/Aug 1976.

[HK03] T. Haustein and U. Kruger. Smart Geometrical Antenna Design Exploiting the LOS Component to Enhance a MIMO System Based on Rayleigh-fading in Indoor Scenarios. In *Proceedings of the IEEE Proceedings on Personal, Indoor and Mobile Radio Communications*, volume 2, pages 1144–1148, Sep 2003.

[HKL+13] S. Hur, T. Kim, D. J. Love, J. V. Krogmeier, T. A. Thomas, and A. Ghosh. Millimeter Wave Beamforming for Wireless Backhaul and Access in Small Cell Networks. *IEEE Transactions on Communications*, 61(10):4391–4403, Oct 2013.

[HL16] T. Hälsig and B. Lankl. Channel Parameter Estimation for LOS MIMO Systems. In *Proceedings of the International ITG Workshop on Smart Antennas*, pages 1–5, March 2016.

[HRA10] K. Hassan, T. S. Rappaport, and J. G. Andrews. Analog Equalization for Low Power 60 GHz Receivers in Realistic Multipath Channels. In *Proceedings of IEEE Global Telecommunications Conference*, pages 1–5, Dec 2010.

[HSS+13] K. Hiraga, K. Sakamoto, T. Seki, T. Nakagawa, and K. Uehara. Effects of Weight Errors on Capacity in Simple Decoding of Short-Range MIMO Transmission. *IEICE Communications Express*, 2(5):193–199, 2013.

[HSS+14] K. Hiraga, K. Sakamoto, T. Seki, T. Tsubaki, H. Toshinaga, and T. Nakagawa. Performance Measurement of Broadband Simple Decoding in Short-Range MIMO. In *Proceedings of the IEEE International Symposium on Personal, Indoor and Mobile Radio Communications*, pages 213–216, Sep 2014.

[IN07] M. T. Ivrlac and J. A. Nossek. On Channel Estimation in Quantized MIMO Systems. In *Proceedings of International ITG Workshop on Smart Antennas*, Feb 2007.

[ISO14] ISO/IEC/IEEE. International Standard for Information technology–Telecommunications and information exchange between systems–Local and metropolitan area networks–Specific requirements-Part 11: Wireless LAN Medium Access Control (MAC) and Physical Layer (PHY) Specifications Amendment 3: Enhancements for Very High Throughput in the 60 GHz Band (adoption of IEEE Std 802.11ad-2012). *ISO/IEC/IEEE document 8802-11:2012/Amd.3:2014(E)*, March 2014.

[KAM+15] R. Kalimulin, A. Artemenko, R. Maslennikov, J. Putkonen, and J. Salmelin. Impact of Mounting Structures Twists and Sways on Point-to-Point Millimeter-Wave Backhaul Links. In *Proceedings of the IEEE International Conference on Communication Workshop*, pages 19–24, June 2015.

[KKK15] Y. K. Kim, K. S. Kim, and S. Kim. A Portable and Remote 6-DOF Pose Sensor System With a Long Measurement Range Based on 1-D Laser Sensors. *IEEE Transactions on Industrial Electronics*, 62(9):5722–5729, Sep 2015.

[KLN+11] D. G. Kam, D. Liu, A. Natarajan, S. Reynolds, H. C. Chen, and B. A. Floyd. LTCC Packages With Embedded Phased-Array Antennas for 60 GHz Communications. *IEEE Microwave and Wireless Components Letters*, 21(3):142–144, March 2011.

[KS17] N. Kishore Kumar and J. Schneider. Literature Survey on Low Rank Approximation of Matrices. *Linear and Multilinear Algebra*, 65(11):2212–2244, 2017.

[Kui99] J. B. Kuipers. *Quaternions and Rotation Sequences: A Primer with Applications to Orbits, Aerospace, and Virtual Reality*. Princeton University Press, 1999.

[Lar05] P. Larsson. Lattice Array Receiver and Sender for Spatially Orthonormal MIMO Communication. In *Proceedings of the IEEE Vehicular Technology Conference*, pages 192–196, May 2005.

[Lee72] W. Lee. Effect of Mutual Coupling on a Mobile-Radio Maximum Ratio Diversity Combiner With a Large Number of Branches. *IEEE Transactions on Communications*, 20(6):1188–1193, Dec 1972.

[LLWC09] T. LaRocca, J. Liu, F. Wang, and F. Chang. Embedded DiCAD Linear Phase Shifter for 57-65GHz Reconfigurable Direct Frequency Modulation in 90nm

CMOS. In *Proceedings of the IEEE Radio Frequency Integrated Circuits Symposium*, pages 219–222, June 2009.

[LN11] J. Löfgren and P. Nilsson. On Hardware Implementation of Radix 3 and Radix 5 FFT Kernels for LTE Systems. In *Proceedings of the NORCHIP*, pages 1–4, Nov 2011.

[LNNS89] B. Lankl, A. Nist, J. A. Nossek, and G. Sebald. Fully Digital ATDE's and XPIC's for a STM-1 Cochannel Radio System Family. In *Proceedings of the IEEE International Conference on Communications, World Prosperity Through Communications,*, pages 1013–1019 vol.2, June 1989.

[Loa00] C. F.Van Loan. The Ubiquitous Kronecker Product. *Journal of Computational and Applied Mathematics*, 123(12):85 – 100, Nov 2000.

[M+17] A. Maltsev et al. Channel Models for IEEE 802.11ay. *IEEE doc. 11-15/1150r9*, March 2017.

[MAN10] A. Mezghani, F. Antreich, and J. A. Nossek. Multiple Parameter Estimation with Quantized Channel Output. In *Proceedings of International ITG Workshop on Smart Antennas*, pages 143–150, Feb 2010.

[MH14] J. Mo and R. W. Heath. High SNR Capacity of Millimeter Wave MIMO Systems with One-bit Quantization. In *Proceedings of Information Theory and Applications Workshop*, pages 1–5, Feb 2014.

[MMS+09] A. Maltsev, R. Maslennikov, A. Sevastyanov, A. Khoryaev, and A. Lomayev. Experimental Investigations of 60 GHz WLAN Systems in Office Environment. *IEEE Journal on Selected Areas in Communications*, 27(8):1488–1499, Oct 2009.

[MNB+12] H. Mehrpouyan, A. A. Nasir, S. D. Blostein, T. Eriksson, G. K. Karagiannidis, and T. Svensson. Joint Estimation of Channel and Oscillator Phase Noise in MIMO Systems. *IEEE Transactions on Signal Processing*, 60(9):4790–4807, Sep 2012.

[MSAM15] B. Mamandipoor, M. Sawaby, A. Arbabian, and U. Madhow. Hardware-Constrained Signal Processing for mm-Wave LoS MIMO. In *Proceedings of the Asilomar Conference on Signals, Systems and Computers*, pages 1427–1431, Nov 2015.

[MZ08] X. Ma and W. Zhang. Performance Analysis for MIMO Systems with Lattice-Reduction Aided Linear Equalization. *IEEE Transactions on Communications*, 56(2):309–318, Feb 2008.

[NI06] J. A. Nossek and M. T. Ivrlač. Capacity and Coding for Quantized MIMO Systems. In *Proceedings of the International Conference on Wireless Communications and Mobile Computing*, pages 1387–1392. ACM, July 2006. Invited paper.

[PC95] B. Picinbono and P. Chevalier. Widely Linear Estimation with Complex Data. *IEEE Transactions on Signal Processing*, 43(8):2030–2033, Aug 1995.

[PCH16] Z. Pi, J. Choi, and R. W. Heath. Millimeter-wave Gigabit Broadband Evolution Toward 5G: Fixed Access and Backhaul. *IEEE Communications Magazine*, 54(4):138–144, April 2016.

[PSDT15] X. Pu, S. Shao, K. Deng, and Y. Tang. Analysis of the Capacity Statistics for 2×2 3D MIMO Channels in Short-Range Communications. *IEEE Communications Letters*, 19(2):219–222, Feb 2015.

[PTL+16] A. Puglielli, A. Townley, G. LaCaille, V. Milovanovic, P. Lu, K. Trotskovsky, A. Whitcombe, N. Narevsky, G. Wright, T. Courtade, E. Alon, B. Nikolic, and A. M. Niknejad. Design of Energy- and Cost-Efficient Massive MIMO Arrays. *Proceedings IEEE*, 104(3):586–606, March 2016.

[Rap01] T. S. Rappaport. *Wireless Communications: Principles and Practice*. Prentice Hall PTR, Upper Saddle River, NJ, USA, 2nd edition, 2001.

[RHDM15] T. S. Rappaport, R. W. Heath, R. C. Daniels, and J. N. Murdock. *Millimeter Wave Wireless Communications*. Prentice Hall, 2015.

[RSM+13] T. S. Rappaport, S. Sun, R. Mayzus, H. Zhao, Y. Azar, K. Wang, G. N. Wong, J. K. Schulz, M. Samimi, and F. Gutierrez. Millimeter Wave Mobile Communications for 5G Cellular: It Will Work! *IEEE Access*, 1:335–349, May 2013.

[Rup98] M. Rupp. LMS Tracking Behavior under Periodically Changing Systems. In *Proceedings of the European Signal Processing Conference*, pages 1–4, Sep 1998.

[Say02] A. M. Sayeed. Deconstructing Multiantenna Fading Channels. *IEEE Transactions on Signal Processing*, 50(10):2563–2579, Oct 2002.

[Say08] A. H. Sayed. *Adaptive filters*. John Wiley & Sons, Inc., 2008.

[Say10] A. H. Sayed. *Fundamentals of Adaptive Filtering*. Wiley India Pvt. Limited, 2010.

[SB09] D. A. Sobel and R. W. Brodersen. A 1 Gb/s Mixed-Signal Baseband Analog Front-End for a 60 GHz Wireless Receiver. *IEEE Journal of Solid-State Circuits*, 44(4):1281–1289, April 2009.

[SC97] P. F. M. Smulders and L. M. Correia. Characterisation of Propagation in 60 GHz Radio Channels. *Electronics Communication Engineering Journal*, 9(2):73–80, Apr 1997.

[SCH+17] X. Song, D. Cvetkovski, T. Hälsig, W. Rave, G. Fettweis, E. Grass, and B. Lankl. High Throughput Line-of-Sight MIMO Systems for Next Generation Backhaul Applications. *Frequenz*, 71(9-10):389–398, Sep 2017.

[SCR+18] X. Song, D. Cvetkovski, W. Rave, E. Grass, and G. Fettweis. Sequential Channel Equalization in Strong Line-of-Sight MIMO Communication. *IEEE Transactions on Wireless Communications*, 2018. Accepted.

[SF15] X. Song and G. Fettweis. On Spatial Multiplexing of Strong Line-of-Sight MIMO with 3D Antenna Arrangements. *IEEE Wireless Communications Letters*, 4(4):393–396, Aug 2015.

[Sha48] C. E. Shannon. A Mathematical Theory of Communication. *The Bell System Technical Journal*, 27(4):623–656, Oct 1948.

[SHC+18] X. Song, T. Hälsig, D. Cvetkovski, W. Rave, B. Lankl, E. Grass, and G. Fettweis. Design and Experimental Evaluation of Equalization Algorithms for Line-of-Sight Spatial Multiplexing at 60 GHz. *IEEE Journal on Selected Areas in Communications*, 36(11):2570–2580, Nov 2018.

[SHR+16] X. Song, T. Hälsig, W. Rave, B. Lankl, and G. Fettweis. Analog Equalization and Low Resolution Quantization in Strong Line-of-Sight MIMO Communication. In *Proceedings of the IEEE International Conference on Communications*, pages 1–7, May 2016.

[SI12] X. Song and O. Iscan. Network Coding for the Broadcast Rayleigh Fading Channel with Feedback. In *Proceedings of the IEEE International Symposium on Information Theory Proceedings*, pages 2057–2061, July 2012.

[SJL+15] X. Song, C. Jans, L. Landau, D. Cvetkovski, and G. Fettweis. A 60GHz LOS MIMO Backhaul Design Combining Spatial Multiplexing and Beamforming for a 100Gbps Throughput. In *Proceedings of the IEEE Global Communications Conference*, Dec 2015.

[SLIF15] X. Song, L. Landau, J. Israel, and G. Fettweis. Strong LOS MIMO for Short Range mmWave Communication - Towards 1 Tbps Wireless Data Bus. In *Proceedings of the IEEE International Conference on Ubiquitous Wireless Broadband*, pages 1–5, Oct 2015.

[SMMA16] M. Sawaby, B. Mamandipoor, U. Madhow, and A. Arbabian. Analog Processing to Enable Scalable High-Throughput mm-Wave Wireless Fiber Systems. In *Proceedings of the Asilomar Conference on Signals, Systems and Computers*, pages 1658–1662, Nov 2016.

[SRB+18] X. Song, W. Rave, N. Babu, S. Majhi, and G. Fettweis. Two-Level Spatial Multiplexing Using Hybrid Beamforming for Millimeter-Wave Backhaul. *IEEE Transactions on Wireless Communications*, 17(7):4830–4844, July 2018.

[SRF16] X. Song, W. Rave, and G. Fettweis. Analog and Successive Channel Equalization in Strong Line-of-Sight MIMO Communication. In *Proceedings of the IEEE International Conference on Communications*, pages 1–7, May 2016.

[SSF16] T. Seifert, X. Song, and G. Fettweis. Interference-Aware Multi-Iterative Equalization and Detection for Frequency-Selective MIMO Channels. In *Proceedings of the IEEE International Conference on Communications*, pages 1–6, May 2016.

[SST+09] C. Sheldon, M. Seo, E. Torkildson, M. Rodwell, and U. Madhow. Four-channel Spatial Multiplexing over a Millimeter-Wave Line-of-Sight Link. In *Proceedings of the IEEE MTT-S International Microwave Symposium Digest*, pages 389–392, June 2009.

[STS+08a] C. Sheldon, E. Torkildson, M. Seo, C. P. Yue, U. Madhow, and M. Rodwell. A 60GHz Line-of-sight 2x2 MIMO Link Operating at 1.2Gbps. In *Proceedings of the IEEE International Antennas and Propagation Society Symposium*, July 2008.

[STS+08b] C. Sheldon, E. Torkildson, M. Seo, C. P. Yue, M. Rodwell, and U. Madhow. Spatial Multiplexing over a Line-of-Sight Millimeter-wave MIMO Link: A Two-Channel Hardware Demonstration at 1.2Gbps over 41m Range. In *Proceedings of the European Conference on Wireless Technology*, pages 198–201, Oct 2008.

[Tel99] E. Telatar. Capacity of Multi-antenna Gaussian Channels. *European Transactions on Telecommunications*, 10(6):585–595, 1999.

[TSC98] V. Tarokh, N. Seshadri, and A. R. Calderbank. Space-Time Codes for High Data Rate Wireless Communication: Performance Criterion and Code Construction. *IEEE Transactions on Information Theory*, 44(2):744–765, March 1998.

[TSMR09] E. Torkildson, C. Sheldon, U. Madhow, and M. Rodwell. Nonuniform Array Design for Robust Millimeter-Wave MIMO Links. In *Proceedings of the IEEE Global Telecommunications Conference*, pages 1–7, Nov 2009.

[TV05] D. Tse and P. Viswanath. *Fundamentals of Wireless Communication*. Cambridge University Press, 2005.

[VvdV10] V. Venkateswaran and A. J. van der Veen. Analog Beamforming in MIMO Communications With Phase Shift Networks and Online Channel Estimation. *IEEE Transactions on Signal Processing*, 58(8):4131–4143, Aug 2010.

[WBKK03] D. Wubben, R. Bohnke, V. Kuhn, and K. D. Kammeyer. MMSE Extension of V-BLAST Based on Sorted QR Decomposition. In *Proceedings of the IEEE Vehicular Technology Conference*, pages 508–512, Oct 2003.

[WCS05] Y. Wu, S. C. Chan, and E. Serpedin. Symbol-Timing Estimation in Space-Time Coding Systems Based on Orthogonal Training Sequences. *IEEE Transactions on Wireless Communication*, 4(2):603–613, March 2005.

[Win78] S. Winograd. On Computing the Discrete Fourier Transform. *Mathematics of Computation*, 32(141):175–199, Jan 1978.

[WMT+17] R. Wu, R. Minami, Y. Tsukui, S. Kawai, Y. Seo, S. Sato, K. Kimura, S. Kondo, T. Ueno, N. Fajri, S. Maki, N. Nagashima, Y. Takeuchi, T. Yamaguchi, A. Musa, K. K. Tokgoz, T. Siriburanon, B. Liu, Y. Wang, J. Pang, N. Li, M. Miyahara, K. Okada, and A. Matsuzawa. 64-QAM 60-GHz CMOS Transceivers for IEEE 802.11ad/ay. *IEEE Journal of Solid-State Circuits*, 52(11):2871–2891, Nov 2017.

[XRBS00] H. Xu, T. S. Rappaport, R. J. Boyle, and J. H. Schaffner. Measurements and Models for 38-GHz Point-to-Multipoint Radiowave Propagation. *IEEE Journal on Selected Areas in Communications*, 18(3):310–321, March 2000.

[YCG15] C. H. Yu, M. P. Chang, and J. C. Guey. Beam Space Selection for High Rank Millimeter Wave Communication. In *Proceedings of the IEEE Vehicular Technology Conference*, May 2015.

[YDKP14] W. Yang, G. Durisi, T. Koch, and Y. Polyanskiy. Quasi-Static Multiple-Antenna Fading Channels at Finite Blocklength. *IEEE Transactions on Information Theory*, 60(7):4232–4265, July 2014.

[ZCZ+12] C. Zhou, X. Chen, X. Zhang, S. Zhou, M. Zhao, and J. Wang. Antenna Array Design for LOS-MIMO and Gigabit Ethernet Switch-Based Gbps Radio System. *International Journal of Antennas and Propagation*, 2012.

[ZMB+14] X. Zhang, M. Matthaiou, E. Björnson, M. Coldrey, and M. Debbah. On the MIMO Capacity with Residual Transceiver Hardware Impairments. In *Proceedings of the IEEE International Conference on Communications*, pages 5299–5305, June 2014.

[ZMK05] X. Zhang, A. F. Molisch, and S.-Y. Kung. Variable-Phase-Shift-Based RF-Baseband Codesign for MIMO Antenna Selection. *IEEE Transactions on Signal Processing*, 53(11):4091–4103, Nov 2005.

[ZO13] L. Zhou and Y. Ohashi. Design of Non-uniform Antenna Arrays for Robust Millimeter-Wave LOS MIMO Communications. In *Proceeding of the IEEE Annual International Symposium on Personal, Indoor, and Mobile Radio Communications*, pages 1397–1401, Sep 2013.

[ZSS+14] G. Zhang, B.-H. Sun, L. Sun, J.-P. Zhao, Y. Geng, and R. Lian. Design and Implementation of a 3 X 3 Orthogonal Beam-Forming Network for Pattern-Diversity Applications. *Progress In Electromagnetics Research C*, 53:1926, 2014.

[ZVM10] H. Zhang, S. Venkateswaran, and U. Madhow. Channel Modeling and MIMO Capacity for Outdoor Millimeter Wave Links. In *proceedings of the IEEE Wireless Communication and Networking Conference*, pages 1–6, April 2010.

[ZWG15] Y. P. Zhang, P. Wang, and A. Goldsmith. Rainfall Effect on the Performance of Millimeter-Wave MIMO Systems. *IEEE Translations on Wireless Communications*, 14(9):4857–4866, Sep 2015.